Machining Chatter in Flank Milling and Investigation of Process Damping in Surface Generation

by

Keivan Ahmadi

A thesis
presented to the University of Waterloo
in fulfillment of the
thesis requirement for the degree of
Doctor of Philosophy
in
Mechanical Engineering

Waterloo, Ontario, Canada, 2011

AUTHOR'S DECLARATION

I hereby declare that I am the sole author of this thesis. This is a true copy of the thesis, including any required final revisions, as accepted by my examiners.

I understand that my thesis may be made electronically available to the public.

Abstract

Although a considerable amount of research exists on geometrical aspects of 5-axis flank milling, the dynamics of this efficient milling operation have not yet been given proper attention. In particular, investigating machining chatter in 5-axis flank milling remains as an open problem in the literature. The axial depth of cut in this operation is typically quite large, which makes it prone to machining chatter. In this thesis, chatter in 5-axis flank milling is studied by developing analytical methods of examining vibration stability, generating numerical simulations of the process, and conducting experimental investigations.

The typical application of 5-axis milling includes the machining of thermal resistant steel alloys at low cutting speeds, where the process damping dominates the machining vibration. The results of experimental study in this thesis showed that the effect of process damping is even stronger in flank milling due to the long axial engagement. Accordingly, the first part of the thesis is devoted to studying process damping, and in the second part, the modeling of chatter in flank milling is presented.

Linear and nonlinear models have been reported in the literature that account for process damping. Although linear models are easier to implement in predicting stability limits, they could lead to misinterpretation of the actual status of the cut. On the other hand, nonlinear damping models are difficult to implement for stability estimation analytically, yet they allow the prediction of "finite amplitude stability" from time domain simulations. This phenomenon of "finite amplitude stability" has been demonstrated in the literature using numerical simulations. In this thesis, that phenomenon is investigated experimentally. The experimental work focuses on uninterrupted cutting, in particular plunge turning, to avoid unduly complications associated with transient vibration. The experiments confirm that, because of the nonlinearity of the process damping, the transition from fully stable to fully unstable cutting occurs gradually over a range of width of cut. The experimental investigation is followed by developing a new formulation for process damping based on the indentation force model. Then, the presented formulation is used to compute the stability lobes in plunge turning, taking into account the effect of nonlinear process damping. The developed lobes could be established for different amplitudes of vibration. This is a departure from the traditional notion that the stability lobes represent a single boundary between fully stable and fully unstable cutting conditions.

Moreover, the process damping model is integrated into the Multi-Frequency Solution and the Semi Discretization Method to establish the stability lobes in milling. The basic formulations are presented along with comparisons between the two approaches, using examples from the literature. A non-shallow cut is employed in the comparisons. Assessing the performance of the two methods is conducted using time domain simulations. It is shown that the Semi Discretization Method provides accurate results over the whole tested range of cutting speed, whereas higher harmonics are required to achieve the same accuracy when applying the Multi Frequency Solution at low speeds. Semi Discretization method is modified further to calculate the stability lobes in flank milling with tools with helical teeth. In addition to the tool helix angle and long axial immersion, the effect of instantaneous chip thickness on the cutting force coefficients is considered in the modified formulation of Semi Discretization as well.

Considering the effect of chip thickness variation on the cutting force coefficients is even more important in the modeling of 5-axis flank milling, where the feedrate, and consequently the chip thickness, varies at each cutter location. It also varies along the tool axis due to the additional rotary and tilt axis. In addition to the feedrate, the tool and workpiece engagement geometry varies at each cutter location as well. The actual feedrate at each cutter location is calculated by the dynamic processing of the toolpath. The tool and workpiece engagement geometry is calculated analytically using the parametric formulation of grazing surface at the previous and current passes. After calculating the instantaneous chip thickness and tool/workpiece engagement geometry, they are integrated into the Semi Discretization Method in 5-axis flank milling to examine the stability of vibration at each cutter location. While the presented chatter analysis results in establishing stability lobes in 3-axis flank milling, it results in developing a novel approach in presenting the stability of the cut in 5-axis flank milling. The new approach, namely “stability maps”, determines the unstable cutter locations of the toolpath at each spindle speed. The accuracy of established 3-axis flank milling stability lobes and 5-axis stability maps is verified by conducting a set of cutting experiments and numerical simulations.

Acknowledgements

I extend my sincerest thanks to my supervisor, Professor Fathy Ismail, for his invaluable support, inspiring ideas, and exceptional mentorship throughout my PhD. The lessons I learned from him are priceless.

In various parts of this thesis, I have been aided by Robert Wagner, of the Mechanical Engineering Machine Shop. His expertise and experience was a great help in conducting the cutting experiments. He is also a wonderful friend. I am grateful for his help and friendship.

During my stay in Waterloo, I have made fantastic friends. I would like to thank them for the joyful moments and precious memories. I would also like to thank the faculty members, staff, and students of the University of Waterloo. I have had an amazing time since 2007, when I joined this community.

I express my gratitude to the National Sciences and Engineering Research Council of Canada for funding this research.

Above all, I would like to thank my beloved family, specially my parents, brothers, and my sister. This accomplishment would not be possible without their support and encouragement.

Dedication

To my family

Table of Contents

List of Figures

List of Tables

Nomenclature

In the list below, the units of a quantity is shown as a combination of the base units, *i.e.* FMLT. Although angles are dimensionless, they are shown in [°]. Because the indexes used in the text are understandable from the context, they are not explained in this list.

Scalars

$\bar{\alpha}$	Tool rake angle [°]
$\bar{\beta}$	Friction angle [°]
ω	Angular velocity [°/T]
ω_c	Chatter angular velocity [°/T]
f	Frequency [1/T]
f_c	Chatter frequency [1/T]
r	Radial deflection [L]
v	Cutting speed [L/T]
N_c	Number of cutting teeth [-]
u	Surface parameter [-]
v	Surface parameter [-]
Ω	Spindle rotation speed [°/T]
s_t	Feedrate [L/tooth]
b, b_{cr}	Width of cut, and critical width of cut [L]
h	Chip thickness [L]
F_x, F_y	Cutting force components in Cartesian coordinate [F]
φ	Cutting edge angular position[°]
φ_c	Shear plane angle [°]
$\varphi_{st}, \varphi_{ex}$	Start and exit angles [°]
R	Tool radius [L]
C_{eq}	Equivalent viscous damper [FT/L]

C_d	Damping shape factor [L^2]
ε	Phase difference between the undulations generated in the present and previous passes [°]
K_{sp}	Specific indentation force [F/L^3]
K_x, K_y	Structural stiffness in Cartesian coordinate [F/L]
$\mathbb{A}$	Tilt angle [°]
$\mathbb{C}$	Rotation angle [°]
F_{xs}, F_{ys}	Shearing components of cutting forces in the Cartesian coordinate [F]
F_{xp}, F_{yp}	ploughing components of cutting forces in the Cartesian coordinate [F]
$\Delta\theta$	Numerical simulation resolution [°]
A_{cr}	Critical amplitude of vibration at which the tool disengages from the cut [L]
α	Constant coefficient used to formulate damping shape factor[L]
p	Constant coefficient used to formulate damping shape factor [L]
α_t, α_r	Constant coefficients used to formulate nonlinear cutting force coefficients [-]
θ	Angular immersion of cutting tooth [°]
M_x, M_y	Mass [M]
C_x, C_y	Structural damping coefficient in Cartesian coordinate [FT/L]
ζ_x, ζ_y	Structural damping ratio in Cartesian coordinate [-]
n	Number of stability lobe [-]
t	Time [T]
V	Volume of the extruded material [L^3]
μ	Coulomb friction coefficient [-]
β_1	Angle used to define the tool top point position in toolpath planning [°]
β_2	Angle used to define the tool bottom point position in toolpath planning [°]
L	Wave length [L]
W	Tool wear [L]
γ	Tool clearance angle [°]
A	Vibration amplitude [L]

F_t, F_r	Cutting force components in the tangential and radial directions [F]
T	Tooth passing period [T]
ψ	Tool helix angle [°]
K_t, K_r	Cutting force coefficients in the tangential and radial directions [F/L^2]
x, y	Tool deflection in Cartesian coordinate [L]
η	Slope of the wave [°]
υ	Poisson ratio [-]
E	Young's modulus of elasticity [F/L^2]
ρ	Extent of the deformation zone [L]
ds	Pseudo distance [-]
β	Angle [°]
κ	Tool rake angle [°]
i	Index- Complex number
S	Area, projection of extruded volume on XY plane [L^2]
c_p	Process damping coefficient [F]
h^H, h^{reg}	Harmonic and regenerative components of the chip thickness [L]
f_a	Actual feedrate [L/tooth]
Δz	Thickness of the axial disks [L]
$f_{program}$	Programmed feedrate [L/T]

Points, Vectors, and Matrices

C_{wp}, C_{tr}, C_t	The origins of workpiece, tilt/rotary, and tool coordinate systems
$\mathbf{p}^H, \mathbf{p}^{reg}$	Harmonic and regeneration components of the tool deflection [L]
$\mathbf{S}(\mathrm{u}, \mathrm{v})$	Surface swept by the tool axis [L]
$\mathbf{G}(\mathrm{u}, \mathrm{v})$	Grazing surface [L]
$\mathbf{G}_p(\mathrm{u}, \mathrm{v})$	Grazing surface generated at the previous pass [L]
$\mathbf{\Pi}$	Transition matrix [-]

$\mathbf{f}$	Feed vector [L/T]
$\mathbf{V}_1, \mathbf{V}_2$	Vectors defining the tool position [L]
$\mathbf{r}$	Rotation vector [°]
$\mathbf{q}$	Tool vibration state vector
$\mathbf{R}(v)$	Upper guiding curve [L]
$\mathbf{S}(v)$	Lower guiding curve [L]
$\mathbf{R}_b, \mathbf{R}_m, \mathbf{R}_t$	Frenet frame elements on the upper guiding curve
$\mathbf{S}_b, \mathbf{S}_m, \mathbf{S}_t$	Frenet frame elements on the lower guiding curve
$\mathbf{F}$	Force vector [F]
$\mathbf{T}$	Homogenous rotation matrix [-]
$\mathbf{a}$	Tool orientation vector [L]
$\mathbf{K}, \mathbf{M}, \mathbf{C}$	Stiffness, mass, and damping matrices
$\mathbf{A}, \mathbf{B}$	Matrices of directional coefficients
$\mathbf{p}, \dot{\mathbf{p}}, \ddot{\mathbf{p}}$	Tool deflection vector and its time derivatives in the Cartesian coordinate
$\mathbf{I}$	Identity matrix

Chapter 1
Introduction

Machining of curved surfaces is a critical stage in the production of many industrial parts such as dies, molds and jet engine turbine blades. Because of the high dimensional accuracy and surface finish requirements, the machining cost of such surfaces is high, typically $15,000 to $50,000 for a small impeller. Flank milling leads to higher efficiency in the production of curved surfaces, where the machined surface is cusp-free and the material removal rate is high due to the large axial immersion. Nevertheless, the low radial immersion, thin chip thickness, and flexible workpiece make the process highly prone to machining chatter in the finishing passes. The excessive vibration of the tool and/or workpiece can result in damage or bad surface finish of such expensive parts. Accordingly, a good measure to reduce the production cost would be to avoid machining chatter while maintaining or even increasing the material removal rate.

Because of simplicity in programming, 3-axis machining is commonly used to machine curve surfaces. However, 5-axis machining brings more efficiency to the process by adding increased flexibility to the toolpath planning. This is due to the possibility of matching the curvatures of the tool and surface in a 5-axis toolpath, leading to a shorter toolpath and scallop height. Therefore, 5-axis machining has been a topic of interest for researchers over the past few decades, especially for those concerned with the geometrical aspects of the process. Many methods have been presented in the literature for the determination of the tool's position and orientation on the surface. These methods employ the geometric properties of the tool and surface, such as the tangent planes and curvatures, to find the optimum orientation of the tool at each cutter location.

Mechanistic modeling of 3-axis flank milling has been developed extensively in the literature, including methods to improve dimensional accuracy by minimizing tool deflection. Yet little research exists about the mechanics and dynamics, especially chatter in 5-axis flank milling. Without chatter predictive models, one would most likely use conservative removal rates, which result in lower productivity. In other words, including the dynamics in the planning of 5-axis flank milling appears to be a necessity if productivity in the machining of curved surfaces is to be enhanced.

1.1 Thesis Objective

The main objective of the thesis is to establish a chatter predictive model for 5-axis flank milling. The model will be used to predict the stability of vibration at each cutter location along the toolpath. As well, the stability analysis method needs to be computationally cost effective to be applicable in the stability analysis of toolpaths at different cutting parameters, such as spindle speed and feedrate. This goal will be achieved by extending the chatter predictive models already in the literature. However, several research goals must be met to prepare the necessary tools for extending these models.

Because of the large axial immersion in flank milling, ploughing forces are an important ingredient of this operation. These forces are recognized as the major source of process damping in machining. Empirical models of process damping are applicable only for the tested tool geometry and vibration amplitude. Therefore, in this thesis, an analytical process damping model is developed and then employed in the modeling of 5-axis flank milling.

Due to the tilt and rotary motions in 5-axis milling, the tool/workpiece engagement geometry varies at each cutter location. Indeed, calculating the tool/workpiece engagement geometry has been a favorite topic for many researchers. However, the existing methods are not efficient in the finishing passes where the chip thickness is thin. In this thesis, an analytical method is developed to calculate the tool/workpiece engagement geometry in the finishing passes. The calculated geometry will be employed in the mechanistic modeling of cutting forces and in formulating chatter in 5-axis flank milling.

1.2 Thesis Organization

This thesis is divided into two parts. The first part includes the development of the process damping model, which is implemented in the modeling of chatter in milling in the second part. The first part is presented in Chapters 3 and 4, and the second part in Chapters 5 and 6.

In Chapter 2, the main literature and background associated with modeling regenerative chatter, process damping, and 5-axis flank milling is reviewed. In Chapter 3, an experimental study is carried out to investigate the effect of process damping on machining chatter. In Chapter 4, an analytical process damping model is developed and used in the frequency domain calculation of stability borders in plunge turning. In Chapter 5, the process damping model is employed in the frequency and time domain calculations of stability borders in milling. The efficiency and accuracy of the time and frequency domains are compared to each other in this chapter as well. In Chapter 6, the chatter

predictive model of flank milling is developed. The instantaneous chip thickness and tool/workpiece engagement geometry are calculated by post processing the toolpath; these are then employed in the time domain analysis and numerical simulation of 5-axis flank milling. In the final chapter, Chapter 7, some concluding remarks and suggestions for future work are provided.

Chapter 2
Background and Literature Review

In this chapter, some geometric parameters of turning and milling that are used throughout this thesis are defined. Then, the various cutting force models and methods of combining them with the dynamic model of machine tools to formulate the regenerative chatter model are reviewed. This is followed by a study of the geometry and dynamics of 5-axis flank milling.

2.1 Geometry of Turning and Milling Operations

In this section the machining parameters used in this thesis are defined. Geometry of plunge turning is explained first, followed by milling with helical teeth.

2.1.1 Turning

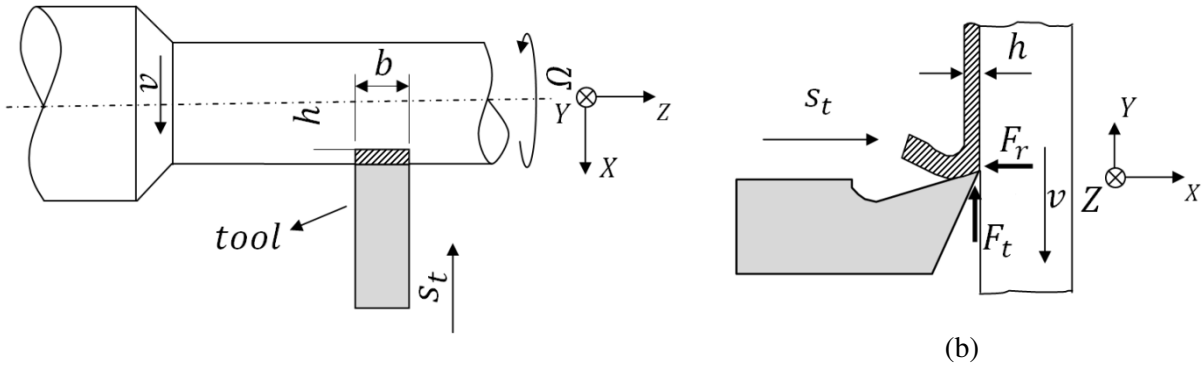

Figure 2-1: Schematic of plunge turning

A schematic of plunge turning is shown in Figure 2-1. The tool moves in the X direction with a constant feedrate, s_t, provided by the machine tool servo motor. The cutting speed, v, depends on the spindle rotational speed, Ω, and cuter radius, R: $v=\Omega R$. The hatched areas in Figure 2-1 (a, b) show the uncut chip. h designates uncut chip thickness, and b its width. According to Figure 2-1, the chip thickness in plunge turning is equal to the feedrate, s_t. The shown plunge turning follows the orthogonal cutting geometry where the cutting edge is perpendicular to the cutting velocity. In most of the common machining operations, the cutting edge is not perpendicular to the cutting velocity; in such cases, it is described by the oblique cutting geometry [1].

2.1.2 Milling

Figure 2-2 shows the schematic of flank milling with a cylindrical tool with helical teeth. The helix angle is denoted by ψ. In this operation, the cutting speed is determined by the tool rotation speed, Ω, and its radius, R. Unlike the single cutting edge of turning, the cutter has several cutting edges in milling; $j=1..n$. The location of each cutting edge is determined by the angle φ measured clockwise from Y direction. Each cutter is engaged with the workpiece only for some part of its rotation period, between the start and exit angles: $\varphi_{st}<\varphi<\varphi_{ex}$. The start and exit angles are determined by the radial immersion, b_r. Moreover, the chip thickness varies at each rotation angle, unlike turning where it is constant. Mertolutti [2] showed that the real tooth path is trochoidal, but it can be approximated by a circular path if the feedrate is negligible compared to the cutting speed. Assuming a circular tooth path, according to Figure 2-2, the chip thickness at each rotation angle is

$$h = s_t \sin(\varphi) \tag{2.1}$$

According to Equation (2.1), the chip thickness in Figure 2-2(b) varies between $s_t sin\varphi_{st}$ at the start and zero at the exit. This type of milling is known as climb or down-milling, where the cutting speed and feed are in the same direction. When these vectors oppose each other, the process is called up-milling or conventional, for which the chip thickness starts from zero and finishes at $s_t sin\varphi_{ex}$.

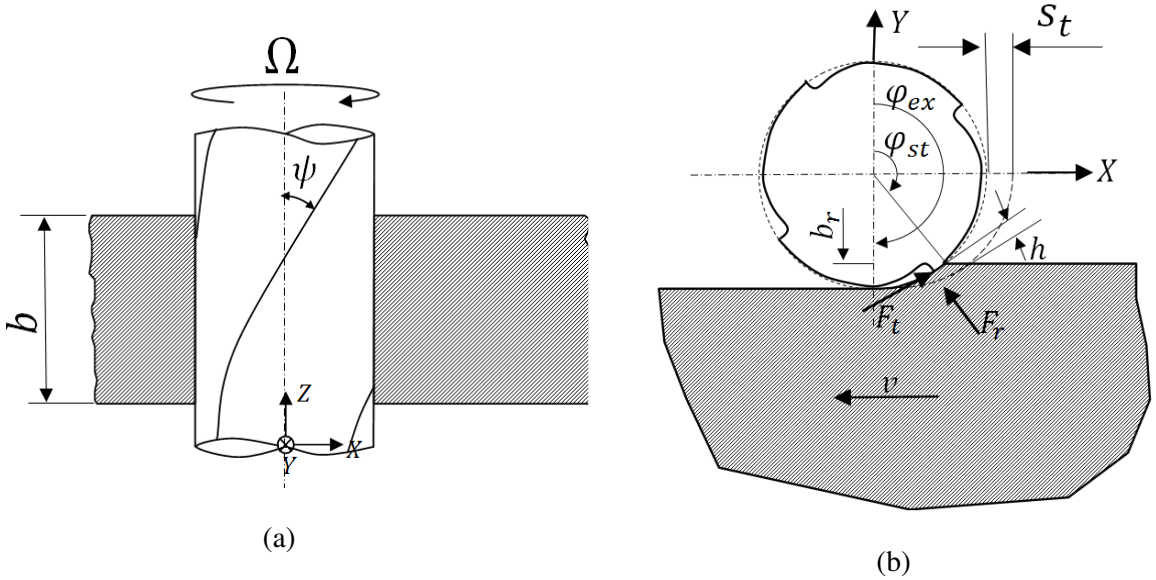

Figure 2-2: Schematic of down-milling with endmills with helical teeth.

Following the notation of plunge turning, the cutting forces at the tool/workpiece interface are resolved into the normal to the machined surface direction, F_r, and tangent to it, F_t. In addition to these two elements, the cutting force has another component in the direction parallel to the tool axis (the Z direction), due to the oblique cutting geometry.

2.2 Cutting Forces

2.2.1 Analytical Modeling

Merchant [3] assumed the orthogonal cutting shear zone to be a thin plane, shear plane. The cutting forces were then computed by applying the laws of plasticity on the shear plane:

$$F_t = bh\left[\tau_s \frac{\cos\left(\bar{\beta}-\bar{\alpha}\right)}{\sin\varphi_c \cos\left(\varphi_c+\bar{\beta}-\bar{\alpha}\right)}\right],\quad F_r = bh\left[\tau_s \frac{\sin\left(\bar{\beta}-\bar{\alpha}\right)}{\sin\varphi_c \cos\left(\varphi_c+\bar{\beta}-\bar{\alpha}\right)}\right] \tag{2.2}$$

In Equation (2.2), τ_s, $\bar{\alpha}$, $\bar{\beta}$, and φ_c are the shear stress on the shear plane, tool rake angle, friction angle and shear angle, respectively. The shear angle, φ_c, is calculated analytically [3] or measured experimentally [1]. Likewise, Lee and Shaffer [4] and Palmer and Oxly [5] developed the cutting forces based on the thick shear plane assumption.

According to Equation (2.2), the cutting forces are a function of the uncut chip area, bh. In the next section, the cutting force models are briefly presented.

2.2.2 Mechanistic modeling

In the mechanistic modeling, the cutting forces are related to the uncut chip thickness through empirical cutting force coefficients, K_t and K_r [6 and 7].

$$F_t = K_t bh, F_r = K_r bh \tag{2.3}$$

This cutting force model is adopted for various machining operations in the literature [8-10]. The cutting force coefficients are specific to each machining operation and are extracted from cutting experiments. For example, in turning the cutting forces in the X and Y directions are measured at different feedrates, h, and constant chip width, b. Then the cutting coefficients are extracted by linear curve fitting of the recorded forces at different chip thicknesses, h. In milling, the linear curve fitting is performed on the average magnitude of cutting forces.

Although the established models are employed successfully in the analysis of machine tool dynamics, surface error, etc., they have to be repeated for each machining operation with different

cutter geometry and workpiece material. To avoid such costly experiments, the cutting force coefficients in a variety of practical machining operations such as turning, drilling and milling are calculated by mathematically incorporating the experimentally measured orthogonal cutting force coefficients in the oblique cutting mechanics of them [1 and 11-13].

Koenigsberger and Sabberwal [14] showed that the cutting force coefficients are actually exponential functions of uncut chip thickness, *h*. Considering the exponential relation between the cutting force coefficients and uncut chip thickness, one can rephrase the linear cutting forces model of Equation (2.3) to the following exponential model [15]:

$$\begin{aligned} F_t &= bK_t h^{\alpha_t} \\ F_r &= bK_r h^{\alpha_r} \end{aligned} \tag{2.4}$$

Since the uncut chip thickness varies around the cutting arc in milling, application of the exponential cutting force model results in a more accurate simulation of this process. Many investigations have been carried out in the literature to study the effect of variable cutting force coefficients on the predicted cutting forces and milling dynamics [16-19].

2.3 Machining Chatter

2.3.1 Stability Lobes

Tobias and Fishwick in [20] and Tlusty and Polacek in [21] identified the feedback between subsequent cuts – regeneration – as the main source of vibration instability in machining. To briefly explain the mechanism of regeneration, the uncut chip thickness in plunge turning shown in Figure 2-1(b) is modified by considering the tool dynamic deflection in the feed direction, *X(t)*, as demonstrated in Figure 2-3. The total uncut chip thickness consists of not only the feed-generated part, s_t, but also the part generated due to the phase difference between the surface waviness produced during the previous and present tool passes:

$$h = s_t + X\left(t\right) - X\left(t - T\right) \tag{2.5}$$

X(t) is the tool deflection and *T* is the tool passing period. The phase difference between the two consecutive waves is denoted by ε in Figure 2-3.

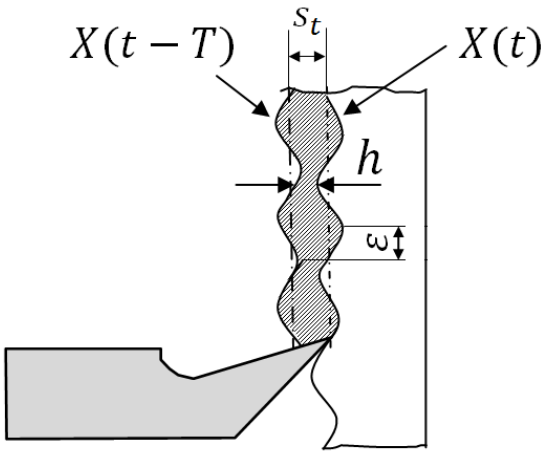

Figure 2-3: Regeneration of waviness on the machined surface

The authors of [20] and [21] also formulated the dynamics of regenerative chatter by combining the structural dynamics of the machine tool and the mechanics of orthogonal cutting, resulting in a linear Delay Differential Equation, DDE, with constant coefficients. They solved the DDE to determine the border of stable width of cut at each spindle speed and established the "stability lobes". A schematic of stability lobe diagram is demonstrated in Figure 2-4. These lobes determine the width of cut at which the vibration becomes unstable for each spindle speed. The gray area above the lobes shows the unstable region, and the white area below them shows the stable region. At the widths of cut below the critical width of cut, b_{cr}, the cut is stable for any spindle speed.

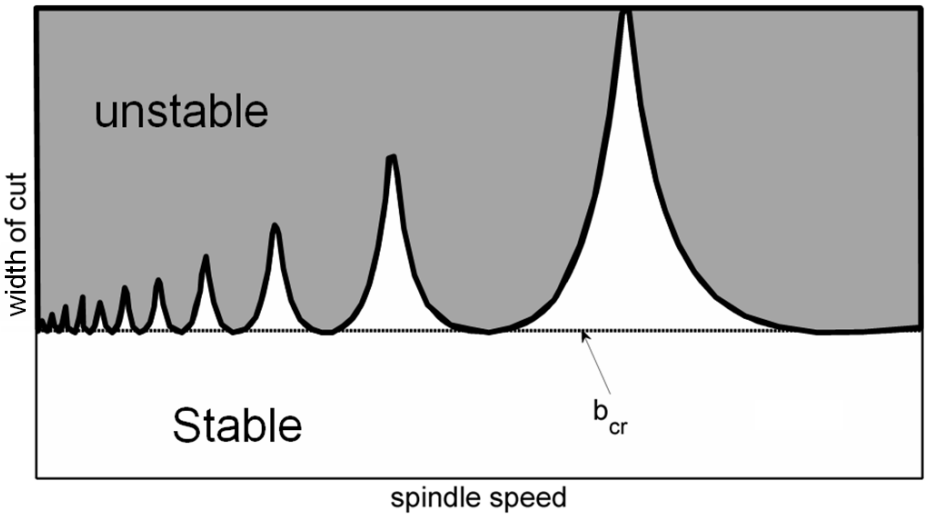

Figure 2-4: Stability lobe diagram

The critical width of cut corresponding to the plunge turning of Figure 2-3 depends on the tangential cutting force coefficients and on the real part of the frequency response function between the tool and workpiece, *Re(G)*:

$$b_{cr} = \frac{-1}{2K_t \min\left(\mathrm{Re}\left(G\right)\right)} \tag{2.6}$$

The stability diagram is a practical tool to achieving higher productivity. In milling operations, the cutting force direction and chip thickness vary around the arc of cut due to tool rotation. Therefore, the dynamics of regeneration is described by a DDE with time varying coefficients [22]. In [23], the average direction was used and the single point chatter analysis approach was applied to milling. Opitz and Bemardi [24] also used the average value of the coefficients to calculate the stability borders. Recently, Budak and Altintas [25] approximated the coefficients by a finite number of Fourier expansion coefficients. Although they formulated the Multi Frequency Solution, MFS, they showed that only the first term of the Fourier expansion, the zero order, suffices for most of the milling operations. Insperger and Stepan [26] used the Semi Discretization Method, SDM, to examine the stability of milling. These authors showed that neglecting the higher orders of the Fourier expansion coefficients in [25] results in the elimination of period-doubling instability in highly interrupted milling operations. Merdol and Altintas [27] obtained results similar to [26] by using a large number of higher harmonics in the MFS of [27].

2.3.2 Process damping

The results of cutting experiments in the literature confirm the accuracy of predicted stability borders at high cutting speed, but the theoretical predictions at low speed were significantly lower than those observed in actual cutting tests. Figure 2-5 shows the stability lobes which agree better with experimental evidence.

Sisson and Keg [28] recognized that the damping generated at the cutter/workpiece interface is the main source of the high stability at low speed. Recently, Huang and Wang [29] carried out a theoretical and empirical study to detect the sources of process damping and evaluated their participation in the dissipation of energy at low cutting speed. They summarized the sources of process damping as deriving from the change in direction and magnitude of shear and ploughing forces. According to their study, the energy dissipated by the change in the magnitude of ploughing force is ten times greater than for other sources. Ploughing forces are generated from the interaction of the tool cutting edge and flank face with workpiece surface undulations.

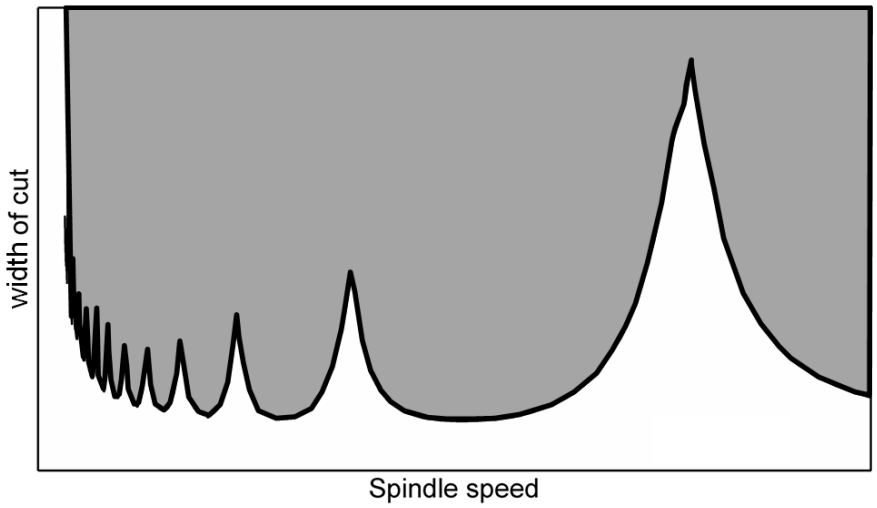

Figure 2-5: Increased stability at low cutting speed due to process damping

To enhance the accuracy of stability estimation at low speed, Peters *et al.* [30] modeled the inner and outer Dynamic Cutting Force Coefficients, DCFC, as complex numbers to include the process damping in the prediction model. These coefficients were obtained experimentally using sinusoidal excitations while executing turning operations. Tlusty [31] analyzed the DCFC measurements carried out in several laboratories in a CIRP keynote paper. It was realized by all laboratories that the imaginary part of the inner modulation of DCFC represents the process damping; it depends strongly on the material being cut, tool clearance angle, tool wear, cutting speed and feedrate. Tlusty and Heczko [32] estimated the inner modulation coefficient from transient vibration instead of sinusoidal excitation. By using complex cutting coefficients instead of real numbers at each cutting speed, independent of the instantaneous vibration amplitude, the process damping model remains linear. Recently, Altintas *et al.* [33] measured the damping in the cut also using sinusoidal excitation. They identified the damping value by explicitly representing the process damping as an additional dashpot in the vibratory model whose coefficient is inversely proportional to the cutting speed.

Although the experimentally determined damping models are linear and accordingly simple to use in the analytical prediction of process stability, the identification process should be repeated for different workpiece materials, tool geometries and feedrates. Indeed, Tlusty in his critical review [31] found significant discrepancies in the measured imaginary part of the DCFE. Perhaps such discrepancies can be attributed to variations in the amplitude of excitation or tool conditions.

Wu [34] presented a model in which the tool and workpiece interaction is represented by an indentation of the workpiece surface undulations by the tool. In this model, the ploughing force is

assumed to be proportional to the volume of the material extruded under the cutting edge and flank face. Elbestawi *et al.* [35] and Lee *et al.* [36] applied this ploughing force model in numerical simulations and showed that the ploughing force acts like an additional damper. This model was employed in other numerical simulations of machining chatter in ball-end milling [37] and [38] and was shown to represent reality more closely. It should be noted, however, that the numerical computations of the extruded volume requires high resolution in discretizing the surface undulations, which makes establishing the stability lobes diagram a time-consuming task. In addition, the indentation model is nonlinear, since the extruded volume is computed only for the part of the vibratory cycle when the tool is moving into the workpiece; otherwise, it is zero when the tool is moving away from the workpiece. It is also nonlinear because it depends on the surface undulations amplitude. Chiou *et al.* [39 and 40] represented the indentation pulse with its first order Fourier transform and thus managed to approximate the nonlinear damping model with a linear model. A basic assumption of small amplitude vibration was made in that approximation. The authors in [39] and [40] integrated that approximate linear model into their analytical development for establishing the stability lobes.

While the viscous model of process damping has been implemented in several works to establish the lobes in turning (e.g., [41] and [33]), few cases have been reported for milling. Budak and Tunc [42] considered the effect of process damping as an additional damper in the zero order MFS. They identified the additional damping coefficients by measuring the stability limits experimentally and fitting the results to the stability model. Kurata *et al*. [43] identified the process damping coefficient through inverse chatter analysis of plunge turning, and then used it in the prediction of stability lobes in milling. Eynian and Altintas [44] integrated the experimentally identified viscous dampers in the zero order MFS as well, but they used rotating tool modes to alleviate the effect of neglecting higher harmonics. Bachrathy and Stepan [45] used Liang's piecewise linear damper in SDM to calculate the stability lobes, linearizing the damping model around the periodic solution of the vibratory system.

2.4 5-axis Flank Milling

2.4.1 Tool Placement

A considerable amount of research has been reported in the literature that aims at increasing the geometrical accuracy of surfaces produced by flank milling [46]. Most of these efforts have focused on developing tool placement and movement strategies to machine ruled surfaces [47-54].

The primary methods of tool placement [51] in flank milling employ the ruled line, L_r, on the surface to orient the tool, as shown in Figure 2-6. For this reason, the tool's axis is planned to be parallel to L_r while it is tangent to a point on the ruled line. Figure 2-7 shows the projections of the tool and workpiece on the plane perpendicular to L_r. The machined surface will be exact only at the tangent point, A, and overcut happens at the other points along L_r due to the natural twist of the surface. Moving the tangent point along the ruled line results in the distribution of error along the ruled line. Rubio *et al.* [51] chose the contact point to be at the middle L_r.

Several methods have been developed to decrease the maximum overcut by shifting the tool or by twisting it around the surface normal at the contact point [52, 48, 55 and 56]. Stute *et al.* [57], giving up the idea of orienting the tool parallel to the ruled line, defined the tool position using the coordinates of two points on its axis. These coordinates are obtained by shifting the intersection points of the ruled line with the guiding rails in the direction of surface normal. Liu [47] chose the two contact points to be at the quarter and three quarter distance from the guiding rails. Rubio *et al.* [58, 59 and 50] first placed the tool parallel to the ruled line while it touches its middle point. Then, by twisting the tool around the surface normal, they found two points on the guiding rails that the tool could touch. Mathematically, it is achieved by numerical solution of a system of seven algebraic equations. The method provides smaller overcuts at a higher computational cost.

Due to the high computational cost of the Rubio's method, it could not be used in commercial programs. Bedi *et al.* [54], neglecting the ruled line on the surface, placed a cylindrical tool tangent to both the guiding curves at the same parametric value. This way, the tool's axis sweeps a ruled surface. They further improved their method using an optimization scheme to place the tool tangent to three points on the surface [53]. Using these methods, they also calculated the grazing surface analytically as an offset surface to the ruled surface swept by the tool's axis. This method will be further discussed in Chapter 6. Recently, some methods employed the swept surface formulation to minimize the overcut in the tool path planning [60 and 61].

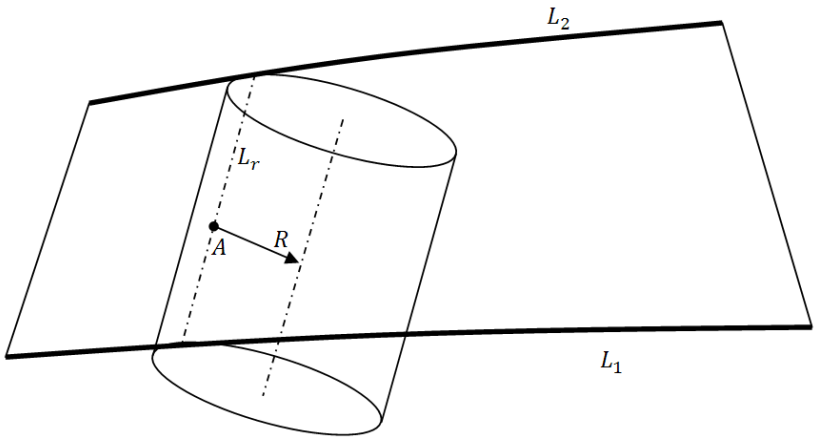

Figure 2-6: Placing a cylindrical tool on a ruled surface parallel to the ruled line, L_r

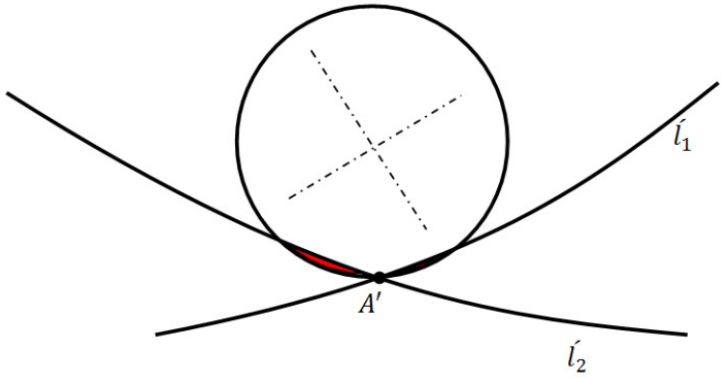

Figure 2-7: Projection of a cylindrical tool and a ruled surface on a ruled line, showing the overcut along the ruled line

2.4.2 Mechanics and Dynamics of 5-axis Flank Milling

Besides the geometric improvement of toolpath, increasing productivity of machining curved surfaces by optimizing the cutting parameters has been of great interest. For this reason, predictive models have been established to analyze the mechanics and dynamics of 5-axis machining. The predictive models calculate the actual feedrate and tool/workpiece engagement by kinematic and geometric analysis of the toolpath, respectively. Then they incorporate the calculated feedrate and tool/workpiece engagement in the mechanistic models of cutting forces. In the following two sections, the variation of actual feedrate and calculation of the tool/workpiece engagement are reviewed, after which the mechanistic modeling of 5-axis milling is addressed.

2.4.2.1 Variation of feedrate

The rotational motion of the tool results in different feedrates along the cutter axis. Also, depending on the rotational to translational motion ratio at each point along the toolpath, the actual feedrate will be smaller than the programmed feedrate. Altintas and Ferry in [62], and Larue and Altintas in [63], calculated the different feedrates along the cutter axis by the dynamic analysis of the 5-axis motion. They showed the effect of the feedrate variation on the cutting force level but did not study its effect on chatter. Ismail and Ziaei [64] conducted some cutting experiments to investigate the effect of feedrate variation on chatter. They used offline feedrate scheduling for chatter suppression in 5-axis milling of a turbine blade. Although a significant improvement in stability is observed in their experiments, they did not provide any mathematical chatter prediction method in 5-axis milling.

2.4.2.2 Calculation of tool/workpiece engagement

The tool/workpiece engagement calculation has been one of the interesting topics in the literature. The presented methods for tool/workpiece engagement calculation can be categorized into: analytical methods, vector-based methods, solid modelers and image-based methods.

El-Mounayri *et al*. [65] obtained the engagement area by applying a spline representation of the cutting edge. They determined the engaged points by calculating the intersection of the cutting edge's curve with the solid model of the workpiece, and then used the engaged area approximation in a mechanistic model to predict the cutting forces in a 3-axis ball end milling. Their method can be used for general 3-D milling operations. Fussell *et al.* [66] used the Z-map method to approximate the tool/workpiece engagement area. In this method, the part is represented by a set of vectors parallel to the Z axis. The vector set is updated at each tool movement according to its intersection with the tool's swept envelope. Later, they generalized the method using a vector set parallel to the surface normal [67]. In these methods, the ray tracing methods are implemented to calculate the intersection of the vectors with the tool swept envelope. Bailey *et al.* [68] employed a solid modeler method to predict the cutting forces in 3-axis machining of dies and molds. Roth *et al.* [69] employed the rendering engine of computer graphics to track the cutting geometry. Ferry and Altintas [62] also used a solid-modeler to determine the engagement condition in flank milling of engine impellers. While numerical methods for tool/workpiece engagement are useful in roughing operations where the radial immersion is large, they may not be efficient in the finishing cut where that immersion is low and essentially uniform. Such low immersion would necessitate high resolution in discretizing the tool and stock to achieve reasonable accuracy in the computed cutting forces.

2.4.2.3 Mechanistic modeling of 5-axis flank milling

In the above works, dynamic cutting force modeling has been neglected. Budak and Ozturk [70] developed a mechanistic cutting force model in 5-axis ball end milling. They calculated the engagement condition analytically due to the straight forward formulation of the ball part of the tool. They extended their work later to simulate the dynamic cutting force in the same process [71]. They also calculated the stability lobes for 5-axis ball end milling of sculptured surfaces. Recently, Ferry and Altintas [62] presented a mechanistic cutting force model to calculate the static force in flank milling. They later developed their model to study the chatter in flank milling [72]. Although they used the Nyquest criterion to determine whether the process is stable or not, they did not calculate the stability lobes.

2.5 Summary

The feedback between the subsequent cuts causes regenerative chatter and vibration instability in machining. Regenerative chatter has been formulated by delay differential equations in the literature. These equations are obtained by combining the mechanistic models of cutting forces and the dynamic models of machine tools. For the stability analysis of the delay differential equations, both time and frequency domain methods are presented in the literature. The result of the analysis is presented in the form of stability lobe diagrams that determine the border between stable and unstable depth of cuts at each spindle speed. Stability lobes provide a useful tool for optimizing the cutting parameters and increasing the productivity while avoiding adverse effects of machining chatter.

Recently, the mechanistic models of cutting forces have been extended to simulate 5-axis flank milling. To extend the existing mechanistic models to 5-axis flank milling, most of the investigations in the literature have focused on complicated tool/workpiece engagement and chip thickness calculations due to the tilt and rotary axis. Yet, the established models are limited to the simulation of cutting forces without considering machining chatter. Most recently, the frequency domain solution of machining chatter has been extended to 5-axis flank milling, but the model under-estimated the stability borders due to neglecting the process damping; the long axial immersion results in a significant source of process damping. Therefore, in addition to the calculation of tool/workpiece engagement and instantaneous chip thickness, an accurate modeling of process damping is required to model chatter in 5-axis flank milling.

The indentation of material under the flank face of the tool has been recognized as the main source of process damping. This model has been employed in the numerical simulation of several machining

operations. A few empirical and analytical damping models have also been presented in the literature based on the indentation force. These models have been used in the time and frequency domain methods of stability analysis. Nonetheless, the empirical models are applicable only for the tested tool geometry and vibration amplitude, and the analytical models have been developed based on the small amplitude assumption.

In this thesis, the indentation force is approximated by an equivalent viscous damper to simulate process damping. The coefficient of presented damper is calculated analytically in terms of the tool clearance angle, amplitude of vibration, the length of generated waves, tool wear and workpiece material. Having developed the equivalent viscous model of process damping, this is integrated into the time and frequency domain methods of modeling chatter in turning and milling, leading to the development of an accurate and efficient time domain model of chatter in 5-axis flank milling. The presented model is used to establish the stability diagrams for 5-axis flank milling toolpaths, as they determine the stable and unstable cutter locations throughout these paths.

Chapter 3
Experimental Investigation of Process Damping Nonlinearity in Machining Chatter

In this chapter, the indentation model of ploughing force is integrated into the numerical simulation of turning operation to investigate the effect of process damping on the stability of machining chatter.

In the next section, the vibratory model used to simulate the machine tool dynamics is explained. The indentation model of ploughing forces is given in Section 3.2. The numerical calculation of extruded material volume and the effect of simulation resolution on the calculated volume are discussed in Section 3.3. Then, the presented numerical simulation scheme is used to examine the accuracy of the stability lobes established using two linear process damping models from the literature: the empirical model of [33] and the analytical model of [39]. While the steady state of tool vibration is either stable or unstable, according to the linear process damping model, the numerical simulation shows an intermediate situation of finite amplitude stability due to the increased process damping at higher vibration amplitude. The experimental results presented in Section 3.5 confirm the state of finite amplitude of stability and the effect of process damping on its development.

3.1 Dynamic Model

The vibratory model used in this chapter to describe the dynamics of turning is shown in Figure 3-1. To simplify the simulation and concentrate on the modeling of process damping, the tool is assumed to be rigid in the tangential direction, *X*, and is modeled by a single degree of freedom system in the feed direction, *Y*. The workpiece is assumed rigid in both directions. The equation governing the motion of the tool in the feed direction, normal to the cut, is:

$$M\ddot{y} + Ky + C\dot{y} = F_y \qquad (3.1)$$

M, K, and *C* are the modal mass, stiffness, and damping of the tool, respectively. s_t in Figure 3-1 stands for feed per revolution, *y(t)* is current vibration, *y(t-T)* is the vibration in the previous revolution, *T* is the time of one revolution, *R* is the workpiece radius, and ε is the phase angle between the current vibration displacement and the vibration displacement in the previous revolution.

The tool oscillatory motion in the feed direction, *y(t)*, along with its transition motion in the cutting direction, *x(t)*, generate waviness on the machined surface, as shown in Figure 3-1. The generated wavelength, *L,* depends on the chatter frequency f_c and the cutting velocity, *v*:

$$L = \frac{v}{f_c} \tag{3.2}$$

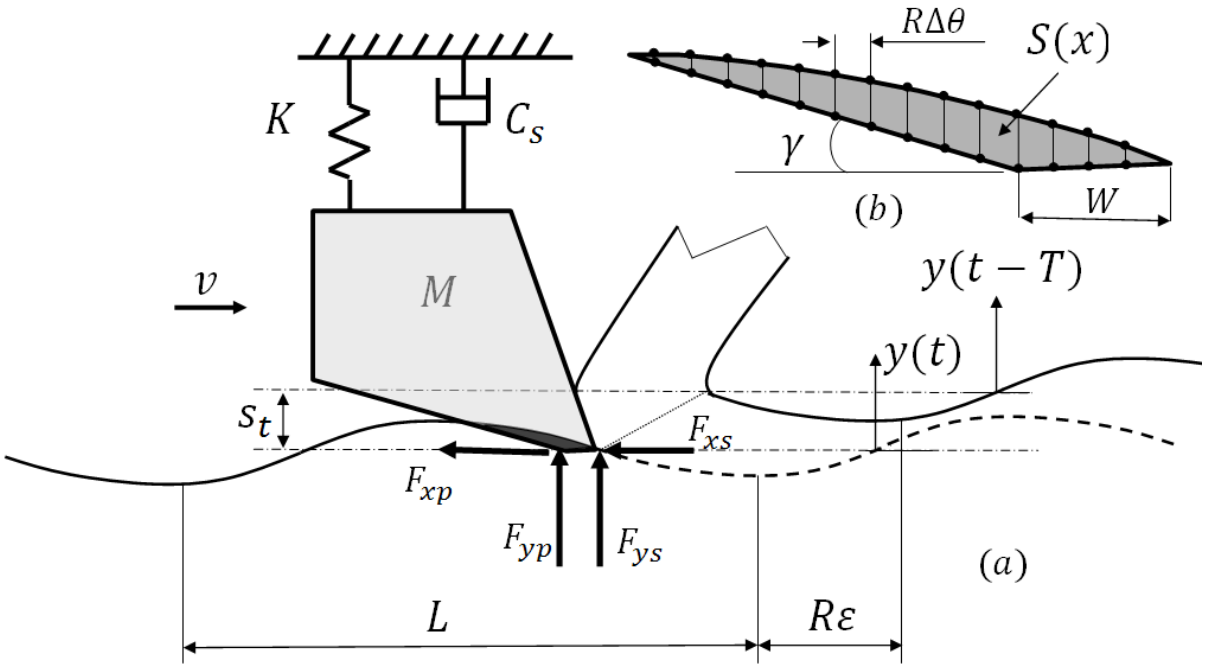

Figure 3-1: Vibratory model and regeneration of waviness

The chatter frequency is usually close to the natural frequency of the system. The cutting forces exerted on the tool in the feed, F_y and cutting, F_x, directions consist of shearing and ploughing forces.

$$\begin{aligned} F_y &= F_{ys} + F_{yp} \\ F_x &= F_{xs} + F_{xp} \end{aligned} \tag{3.3}$$

In Equation (3.3), the index *p* stands for ploughing and the index *s* designates shearing. The shearing forces are obtained using the mechanistic regenerative force model, as follows:

$$F_{xs} = bK_t h \text{ , and } F_{ys} = K_r F_{xs} \text{ ; } \qquad h = s_t + y(t-T) - y(t) \tag{3.4}$$

In Equation (3.4), *b, K_r, K_t,* and *h* are the width of cut, radial, and tangential cutting force coefficients, and chip thickness, respectively. The chip thickness consists of the feed per revolution s_t and the regenerative term *(y(t-T)-y(t))*. The chip thickness cannot be negative because it implies tool disengagement. In this case, *h=0*.

The ploughing forces are added using the indentation force model presented by Wu [34]. The mechanism of the indentation and the numerical calculation of these forces are given in the next section.

3.2 Ploughing Force Model

The ploughing forces in [34] and [35] arise due to the indentation of the tool into the workpiece undulations. The material extruded under the flank face and wear land of the tool, as it moves into the generated undulation, is shown in Figure 3-1 and Figure 3-2. The radial ploughing force is proportional to the extruded volume according to:

$$F_{yp}(x) = K_{sp} V(x); \quad V(x) = S(x) b \qquad (3.5)$$

S(x), the dark area in Figure 3-1, is the cross-sectional area of the extruded volume. For a unit width of cut, *b=1* and *S(x) =V(x).* In the tangential direction, the ploughing force is computed assuming coulomb friction with coefficient μ from:

$$F_{xp}(x) = \mu F_{yp}(x) \qquad (3.6)$$

K_{sp} is a constant coefficient that depends on the physical properties of the material. Wu [34] estimated this coefficient using an analogy with the force required for the indentation of unit volume of similar material under a cylindrical indenter. Using this analogy, K_{sp} was determined from:

$$K_{sp} = \frac{E}{1.29\rho\,(1-2\upsilon)} \qquad (3.7)$$

where E and υ are the Young modulus and Poisson ratio, respectively. ρ is the extent of the deformation zone, which is obtained by measuring the residual stresses resulting from the plastic deformation of the material. This value is usually between 0.2 and 2 mm; for AISA 1018 steel (the material employed in this work), it was measured at 1mm. Taking E=207 GPa and υ=0.3, K_{sp} will be 4×10^{14} N/m^3. The volume of the extruded material is either calculated by numerical integration or approximated analytically.

3.3 Numerical Calculation of the Extruded Volume

A considerable task in the application of the indentation model is to calculate the volume of the extruded material accurately. A numerical chatter simulation example is provided here in which the indentation force model is used to represent the ploughing forces. Although similar time domain simulations exist in the literature [35-38], the numerical procedure is briefly explained here for the sake of completeness and to highlight the parameters that affect the indentation force.

In a numerical simulation of machining chatter in the time domain, at each time step Δt, the chip thickness and consequently the cutting forces are calculated using Equation (3.4). To compute the indentation forces at time step i, one needs to keep track of the tool displacements at previous time steps, from *(i-1)* to *(i-J)*. The shaded area, $S(x_i)$, shown in Figure 3-2 at time step i is calculated from:

$$S(x_i) = \sum_{j=0}^{J-1} (z_j + z_{j+1}) \frac{v\Delta t}{2} \qquad (3.8)$$

J is the number of points on the surface undulation involved in the computation of the extruded volume; they are indicated by solid circles in Figure 3-2. The J points are obtained by numerical search of the differences, $z's$, between the coordinates on the surface undulation and the corresponding coordinates on the flank face and wear land.

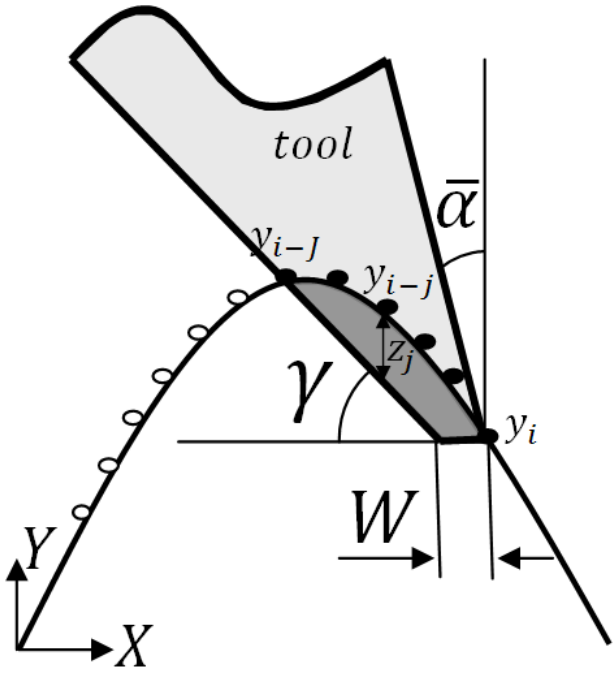

Figure 3-2: Numerical computation of extruded volume due to indentation of the tool into surface undulations

Elbestawi *et al.* [35] showed that the ploughing force acts as a damper. It was shown that the extruded volume wave has 90° phase difference with the displacement, and it was non-zero for the negative range of the vibration velocity where the tool was moving into the workpiece undulation. Outside that range, it was zero. The 90° phase difference with the displacement makes it act as a damping force, and having a non-zero value over a portion of the vibratory cycle makes it nonlinear.

Figure 3-3 shows several cases of S_{max} computed for different values of: a) clearance angle γ, b) wave length L, c) vibration amplitude A, and d) wear land W. As expected, S_{max}, and hence process damping, increases for: smaller γ, shorter L, and larger W. Such behavior is indeed intuitive and agrees with experimental observations. The relationship with the amplitude A, however, needs some discussion. Figure 3-3c shows the strong dependency of the process damping on the vibration amplitude: it increases rapidly at higher amplitudes. This strong relationship shows the limitation of the linear damping representations, whether complex DCFC or explicit viscous damper, obtained from cutting tests using sinusoidal excitations at particular amplitudes. It also shows the limitation of the linear approximation developed by Chiou *et al.* [39] by assuming small amplitude vibration. The adequacy of linearization of the nonlinear process damping "pulse" is demonstrated in Section 3.4. Also examined in Section 3.4 is the performance of linear and the nonlinear damping models in assessing the stability of the cut. The comparison will be conducted using the experimental data and vibratory model of Altintas *et al.* [33].

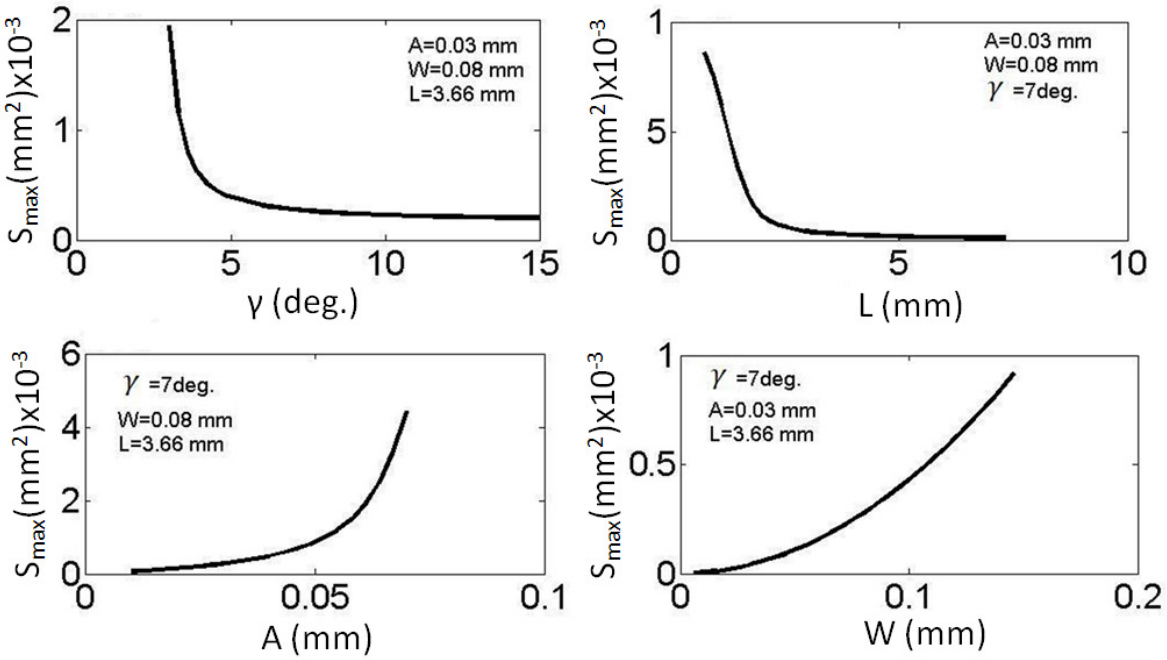

Figure 3-3: The effect of γ, A, L and W on the volume of the extruded material per unit width of cut

3.3.1 The Effect of Simulation Resolution on the Calculated Ploughing Force

The biggest portion of time in the numerical simulation of chatter is consumed in calculating the indentation area at each simulation time step. It is important to investigate the resolution $\Delta\theta$, shown in Figure 3-1, required to represent the indentation pulse accurately. This investigation is described below.

Figure 3-4 shows the numerically calculated $S(x)$, while the tool indents a sinusoidal undulation of length L=3.7 mm and amplitude A=0.03 mm, for $\Delta\theta$ = 0.1, 0 .07, 0.05, 0.03, and 0.01^{o}. They are drawn in solid lines with increasing thickness, with the thickest being associated with the highest resolution of 0.01 ^{o}. Also shown in Figure 3-4 is the analytically calculated $S(x)$ as a broken line. The procedure used for computing $S(x)$ analytically is explained in the next chapter. By increasing the simulation resolution $\Delta\theta$ from 0.1 ^{o} to 0.01 ^{o}, the numerically computed $S(x)$ converges to that obtained analytically. The figure shows that, at the coarse resolution of 0.1^{o}, only a small fraction of the pulse is captured, which would translate into gross underestimation of the process damping. The situation improves as the resolution increases to 0.07, 0.05, and then to 0.03 ^{o}. It is only with the highest resolution of 0.01 ^{o} that the numerically computed area is practically identical to that evaluated analytically. To put things in perspective, for the $\Delta\theta = 0.01^{0}$ resolution required to achieve accurate results, the number of simulation steps for a single revolution of the workpiece will be 36,000. At each simulation step, the indentation area needs to be computed, which involves searching for the engaged section of the tool into the surface undulation, computing the elemental areas, and summing them up. This is a lengthy procedure that takes a considerable amount of time.

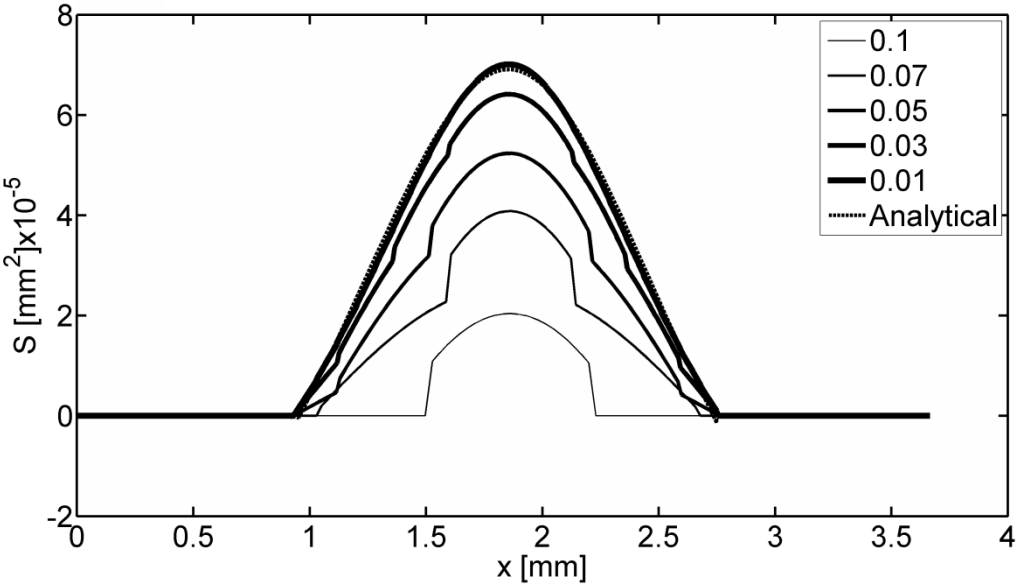

Figure 3-4: Effect of discretization resolution on the accuracy of numerically computed indentation areas for L=3.7mm, γ=7°, W=0.04mm, and A=0.03mm

3.4 . Linear versus Nonlinear Process Damping

In this section, two linear process damping models are studied and compared with the [34] nonlinear indentation model. The first (approximate) linear model was developed by Chiou *et al.* [39], assuming small amplitude vibration, which allowed computing the extruded volume analytically. Accordingly, the volume of the extruded material per unit width of cut is computed from:

$$S = \begin{cases} 0 & ;\dot{y} > 0 \\ \dfrac{-W^2}{2v}\dot{y} & ;\dot{y} \le 0 \end{cases} \qquad (3.9)$$

This model will be referred to as Model 1 in this chapter. Equation (3.9) shows the damping to be proportional to the square of the wear land W and inversely proportional to the cutting speed v. Figure 3-5 compares the extruded volume per unit width of cut, S, computed from Equation (3.9) with that calculated numerically for two waves of different amplitudes – namely, a small amplitude of A= 0.003 mm and a large amplitude of A=0.03 mm. Figure 3-5 shows that the extruded volume from Equation (3.9) is close to reality at the small amplitude, whereas it deviates significantly from the actual volume at the larger amplitude. As will be seen later in this section, the amplitude of vibration

at the stability limit depends on the feed per revolution, s_t; accordingly, the assumption of small amplitude could lead to underestimating process damping for typical feedrates.

In addition to the small amplitude assumption, Chiou *et al.* [39] approximated the nonlinear process damping "pulse" with its Fourier transform first harmonic term. This, in effect, linearized the process damping and allowed the authors to use a linear model in establishing the stability lobes analytically. Figure 3-6 shows this approximation as a broken line. It is a crude approximation, and deviates significantly from the actual pulse in the outer regions.

The other linear model considered here is that of Altintas *et al.* [33], which will here be designated as Model 2. In this model, the process damping is expressed as:

$$F_{yp} = \frac{c_p \dot{y}}{v} b \qquad (3.10)$$

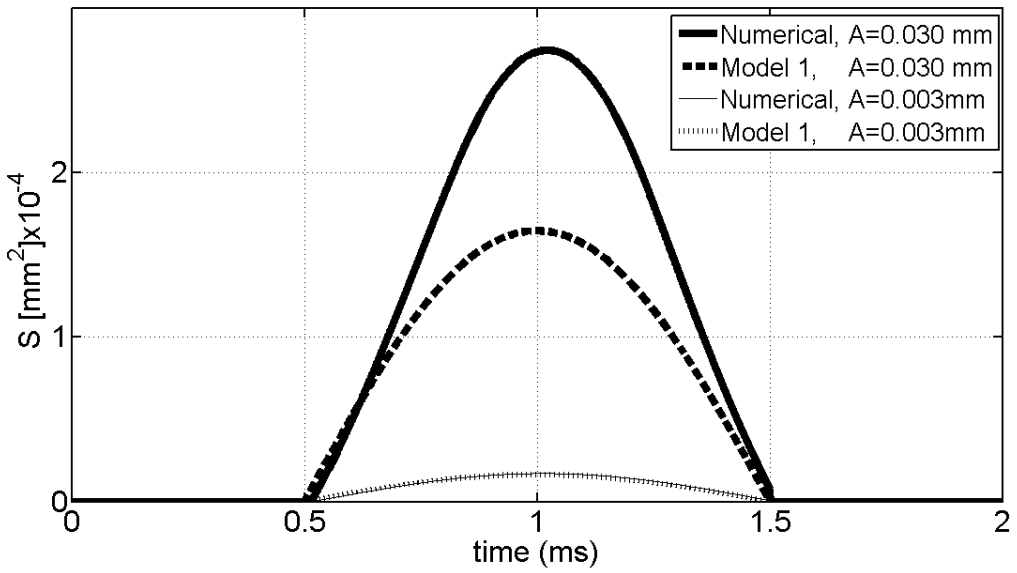

Figure 3-5: The indentation area calculated numerically and using Model 1 [39] approximation for two waves with different amplitudes

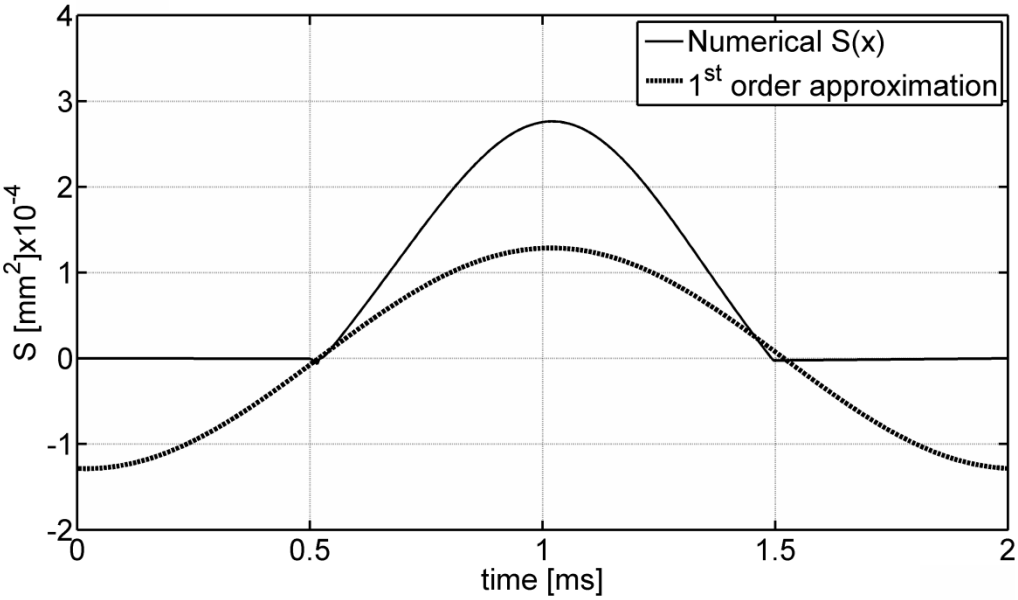

Figure 3-6: Indentation area computed numerically and its approximation using the first harmonic term of its Fourier Transform

Equation (3.10) shows the damping term as an additional viscous dashpot whose value bc_p/v is inversely proportional to the velocity v. c_p was named by the authors as the "process damping coefficient" and was determined experimentally from sinusoidal excitation. The tools used had a flank clearance angle of 7^o. c_p was obtained for different materials using tools with varying amounts of flank wear. The experiments in [33] showed a linear relationship between the wear land and the process damping, unlike the model presented in [39] that considered the relationship to be quadratic. The results from cutting tests of AISI 1045 steel using sinusoidal excitation at an amplitude A= 0.035 mm yielded $c_p = 0.611\times10^6$ (N/m).

Next, a case study is presented that compares the stability predictions from Model 1 and Model 2. The vibratory model is that of [33], whose parameters were: $K = 6.48\times10^6$ (N/m), M = 0.56 (Kg), and C = 145 (N.s/m). The cutting force coefficient for AISI 1045 in the normal to the cut direction was estimated at K_r = 1384 MPa. The operation was a plunge turning of a 35 mm diameter shaft at a feedrate of s_t = 0.05 (mm/rev). A small W = 0.04 mm is assumed to account for tool edge radius and to allow comparing between the two models. It should be mentioned that the assumption of such a wear land does not affect the prediction from Model 2, since $c_p = 0.611\times10^6$ (N/m) associated with a new tool will be used. On the other hand, as will be seen, in the range of examined speed, the effect of that wear land is small on the stability prediction from Model 1.

The established stability lobes from Models 1 and 2 are shown in Figure 3-7.The details regarding establishing these lobes can be found in [39] and [7], respectively. Figure 3-7 also shows results of experiments conducted in [33], where a solid circle indicates a stable cut and + indicates an unstable cut. The following observations can be made from this figure:

- Model 1 fails to identify the status of the cut almost in all cases, especially for speeds below 1500 RPM. The assumption of a wear land of only 0.04 mm helped increase the lower stability slightly at the lower speed, but in general, the lower stability border is close to what would have been obtained had the damping been ignored altogether.
- Model 2 succeeds in identifying the status of the cut in most cases. Apparently, it fails to identify that the process is unstable in four cases at and below 1000 RPM. This apparent failure might be due to misjudging the process as unstable, whereas in reality it is in a state of "finite amplitude stability", as explained below.

In establishing stability lobes using a linear chatter model, the amplitude of vibration is assumed to stay constant at the border of stability, decreases to zero below the border, and increases till the tool starts jumping out of the cut beyond the border. The amplitude of vibration at the border of stability is not defined. The amplitude at which the tool starts jumping out of the cut was considered by Shin and Tobias [73] as the critical amplitude A_{cr} that, from geometry, could be obtained from:

$$A_{cr} = \frac{s_t}{2\sin(\varepsilon/2)} \qquad (3.11)$$

To examine the amplitudes of vibration associated with linear models, numerical simulations were conducted of Model 2 at 1000 RPM. As can be seen from Figure 3-7, at 1000 RPM, the limit width of cut is 1.1mm. The simulations were conducted below and above that limit at b=0.7 and 1.2 mm, respectively. The results at b=0.7 mm showed the vibration y died down to zero, the force normal to the cut F_y reached a steady, DC, value of 45 N, and the thickness h reached a steady value of 0.05 mm, which is equal to the feedrate s_t =0.05 mm/rev. At b=1.2 mm, the vibration y continued to grow until it stabilized close to the end of the cut at a constant value of 0.033 mm, the chip thickness h at that latter section dropped to zero periodically, and the corresponding F_y also dropped to zero periodically. The picture just described has been known for a long time (see, for example, Tlusty and Ismail [74]). The important issue here is the amplitude at which the vibration stabilizes. This amplitude is actually A_{cr}, which could be computed from Equation (3.11), and in the current case, is 0.033 mm. If we assume that the amplitude of vibration at the boundary of stability is A_{cr}, then we can see the potential source of error in employing a process damping coefficient, like c_p, obtained

from sinusoidal excitation at a different amplitude. c_p would be accurate if it has also been estimated using excitation amplitude A_{cr}. Needless to say, estimating c_p from sinusoidal excitation at amplitudes that would cover one lobe for a range of feedrates would be an arduous and time-consuming task. Addressing such a task could be a subject for future research.

Numerical simulations were also conducted using the nonlinear indentation force model. The same vibratory model, feedrate and cutting coefficient of Altintas *et al.* [33] were used. A wear land of 0.04 mm was assumed and $K_{sp}= 4\times10^{14}$ N/m^3 was utilized. The extruded volume at each time step was computed numerically following the procedure described in Section 3.3. Figure 3-8(a), (b), and (c) show the simulation results at 1000 RPM and feedrate 0.05 mm/ rev., for b=0.5, 0.7 and 1.0 mm, respectively. At b=0.5 mm, Figure 3-8(a), the cut is stable, the vibration oscillation dies down to zero, the corresponding F_y stabilized at 30 N, and h reached a static value of 0.05 mm. At b=0.7 mm, Figure 3-8(b), the vibration grows and stabilizes close to the end of the cut at an amplitude of 0.02 mm, the corresponding F_y had a strong AC component but did not drop to zero, and h also stabilized and did not drop to zero. This is a case of finite amplitude stability. At b=1 mm, Figure 3-8(c), the vibration grows and stabilizes at an amplitude of 0.033 mm (which is equal to A_{cr}), the corresponding F_y grew and dropped to zero periodically, and h grew and also dropped periodically to zero, signaling the tool jumping out of the cut. The behavior in Figure 3-8(a) and (c) for the nonlinear damping model are similar to that observed employing the linear model for fully stable and fully unstable, respectively. The difference between the linear model and nonlinear model is the case of finite amplitude stability in Figure 3-8(b) associated with the nonlinear model.

Many simulation runs were conducted for the nonlinear model at 1000 RPM. Figure 3-9 summarizes the results obtained expressed in terms of the amplitude of vibration. The blank circles are associated with the cuts using a tool with wear land of W=0.04 mm. Plotted in the figure, solid circles are also the results of simulations where process damping was neglected altogether. From Figure 3-9, the following observations can be made:

- For both cases, with and without process damping, A_{cr} at which the tool jumps out of the cut is the same. Actually, A_{cr} is also the same when a linear process damping model was employed.
- When process damping is neglected, the transition from fully stable, where the vibration is zero, to fully unstable, where the tool jumps out of the cut with amplitude A_{cr}, is sharp.
- Including the process damping effect with W=0.04 mm shifted the limit of full stability from b=0.4 mm to b=0.5 mm.

- For the worn tool, the transition from fully stable to fully unstable occurs gradually over a range of width of cut from b=0.5 mm to b=1 mm. This gradual transition was also reported by Chandiramani and Pathala [75] and Jemielniak and Widota [76].

The comparisons conducted above between the linear damping models showed the deficiency in Model 1 where small amplitude vibration was assumed, as well as a potential source of error in Model 2, due to estimating the process damping parameter from sinusoidal excitation at particular amplitude. It also showed the ability of the nonlinear damping model to predict cases of finite amplitude stability. These finite amplitude cases were demonstrated using numerical simulations. Cutting experiments are presented next to verify the occurrence of these cases of finite amplitude stability.

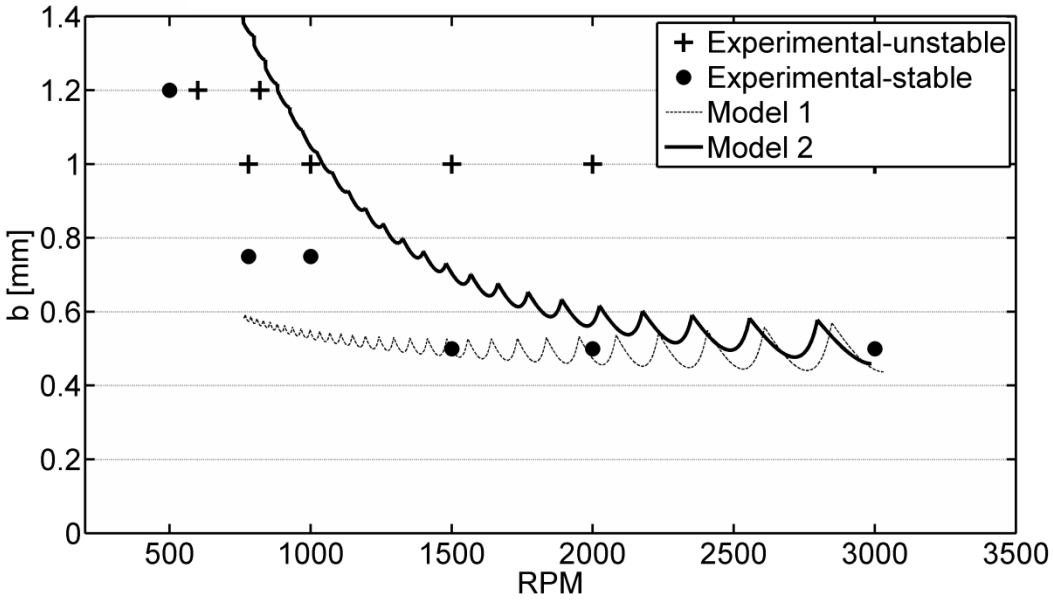

Figure 3-7: Stability lobes established from Model 1 [39] and Model 2 [33], and experimental results: circles stable and + unstable from [33]

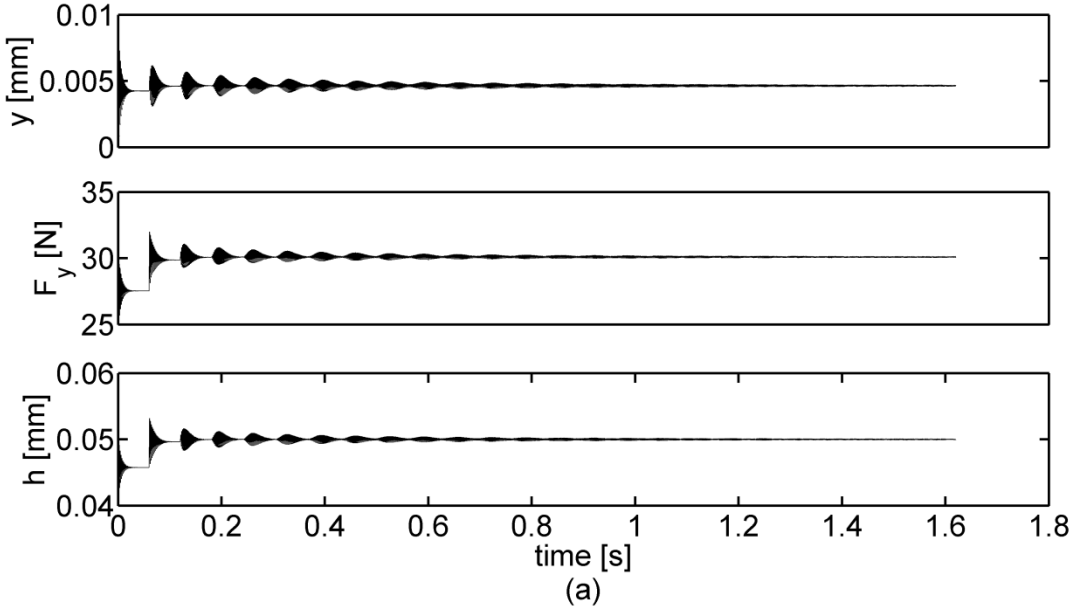
0.01
0.005
0
y [mm]
35
30
25
F_y [N]
0.06
0.05
0.04
h [mm]
0
0.2
0.4
0.6
0.8
1
1.2
1.4
1.6
1.8
time [s]

(a)

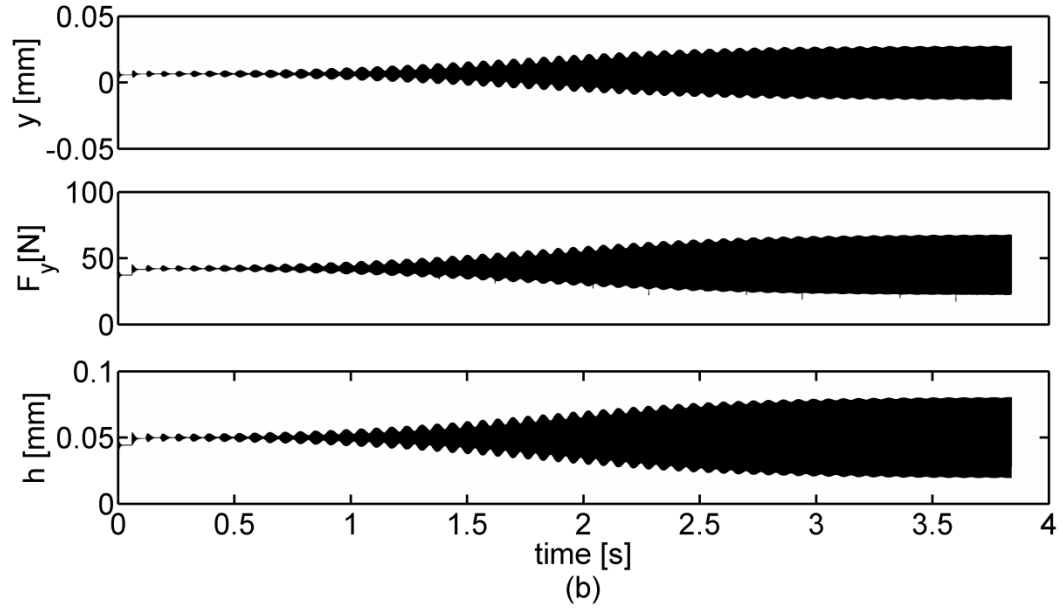
0.05
0
-0.05
y [mm]
100
50
0
F_y [N]
0.1
0.05
0
h [mm]
0
0.5
1
1.5
2
2.5
3
3.5
4
time [s]

(b)

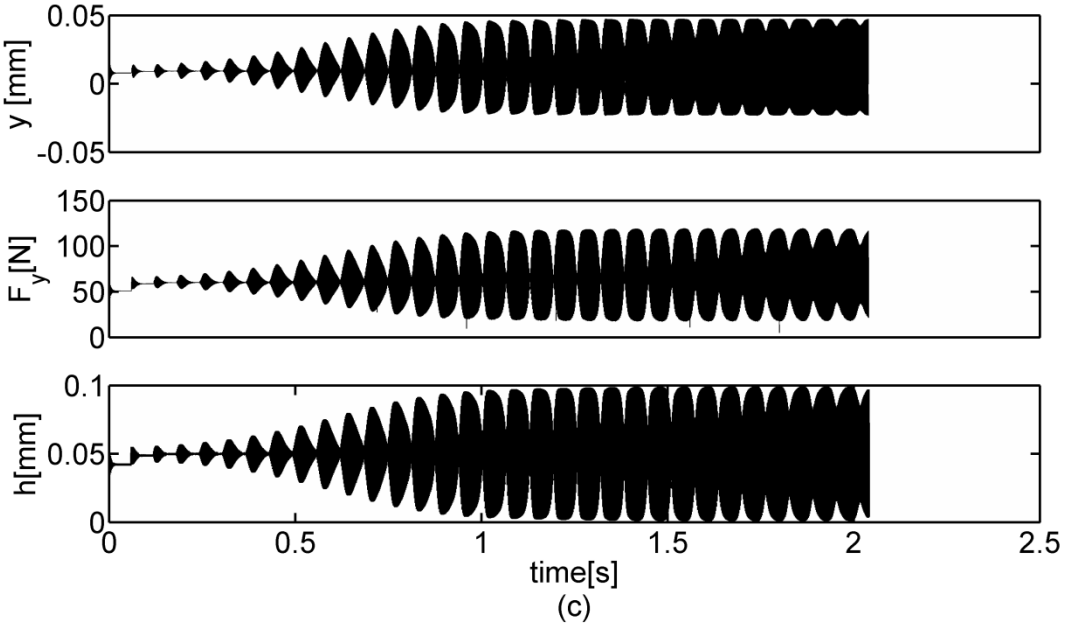

Figure 3-8: Numerical simulations using the nonlinear model at 1000 RPM for a) *b*=0.5 mm, b) *b*=0.7 mm, and c) *b*=1.0 mm

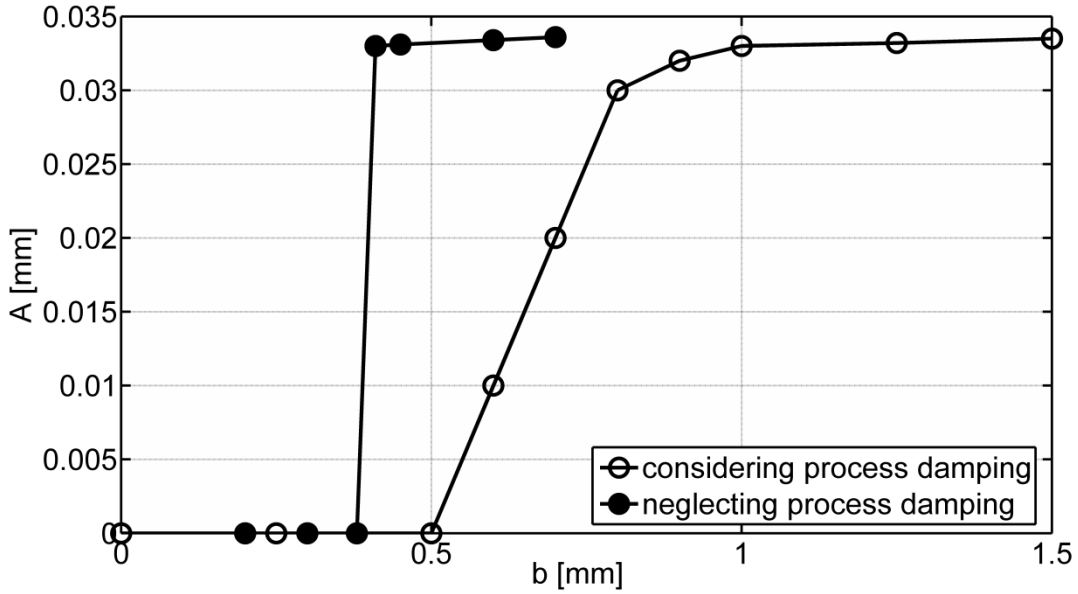

Figure 3-9: Steady state vibration amplitude obtained from numerical simulations with nonlinear process damping and with no damping

3.5 Experimental Evidences of Finite Amplitude Stability

Numerical simulations employing the process damping nonlinear model demonstrated the occurrence of "finite amplitude stability" [75, 76]. This finite amplitude stability implies that, over a range of width of cut, the vibration amplitude stabilize at values between zero and the critical amplitude, A_{cr}, given in Equation (3.11), at which point the tool starts jumping out of the cut. There has been some experimental evidence of gradual increase in surface roughness and peak spectral value of measured acceleration [77], as the cut went from (according to the definition of the authors) stable, to marginal, to unstable. The experiments of Clancy and Shin [77] showed the peak spectral acceleration to increase more gradually for a sharp tool compared to that recorded for worn tools. This inconsistency might have been due to the finite frequency resolution used in measuring the acceleration spectra, or to the width of cut not increasing sufficiently for the vibration amplitude to reach A_{cr}. It should be mentioned, however, that the objective of Clancy and Shin [77] was to develop a multi-dimension chatter model in turning rather than to study the effect of process damping on the vibration amplitude. To the best knowledge of the current author, there has not been a study reported in the literature that explicitly investigated the phenomenon of finite amplitude stability experimentally. Such a study is conducted in this work.

A schematic of the experimental setup is depicted in Figure 3-10. Because of equipment availability, the experiments were conducted on a 3-axis milling machine rather than on a lathe. The workpiece was clamped in a tool holder that was mounted in the spindle. The tool was clamped in a fixture mounted on a Kistler 9255 table dynamometer, which in turn was clamped to the machine table. In effect, the required plunge turning configuration was achieved, in which the workpiece rotates and the tool executes the feed motion in the radial direction.

A parting tool with a TiN insert of a 4mm edge and a 7^{o} clearance angle was used. The tool was mounted on the table dynamometer such that the edge was parallel to the spindle axis in the Y-Z plane of the machine. The AISI 1018 steel workpiece had a 100 mm (4") diameter for a length of 50 mm and a 25.4 mm (1") diameter for 76 mm length. It was clamped in a 1" collet chuck and the overhang length could be adjusted to achieve the required modal parameters.

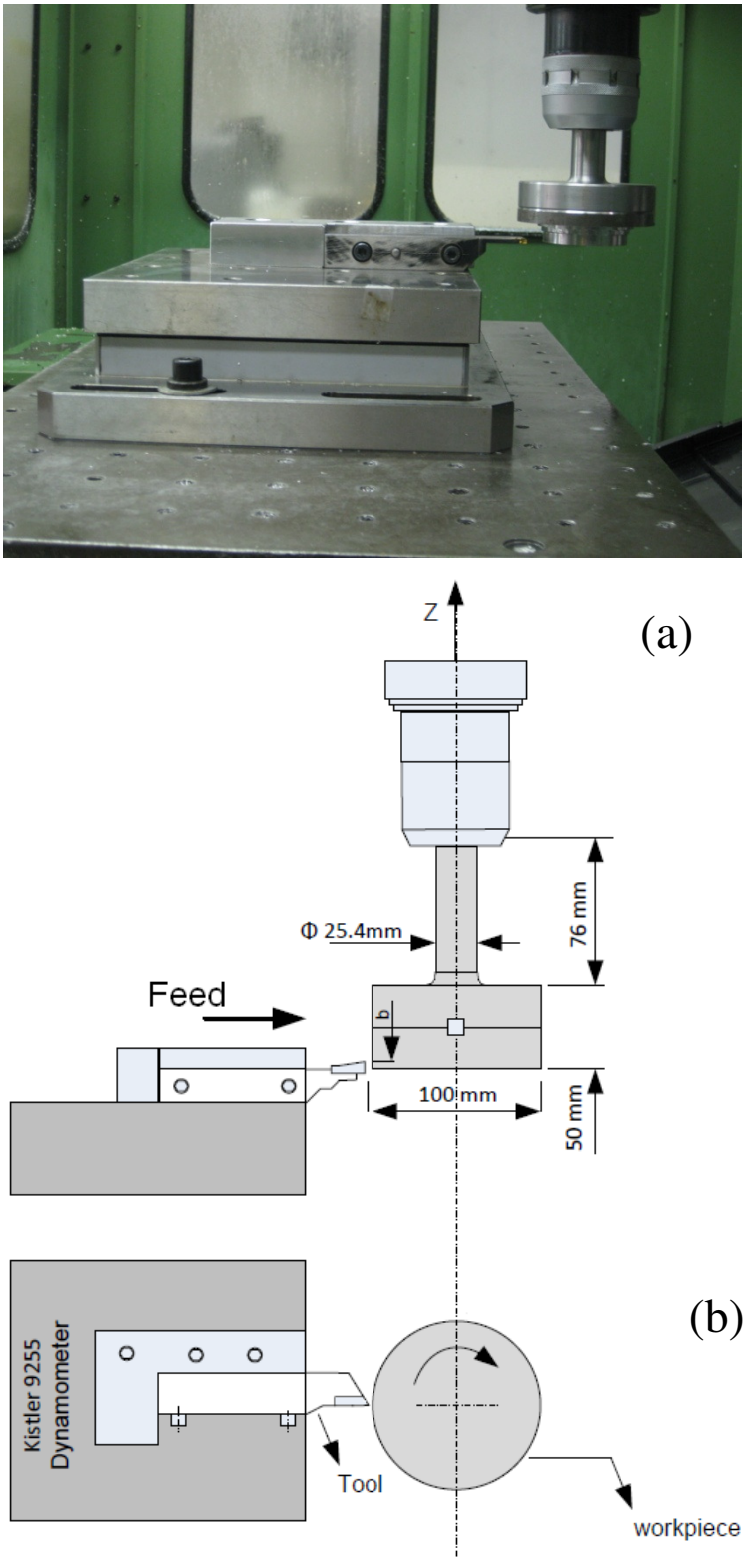

Figure 3-10: (a) Experimental setup, (b) Schematic of the experimental setup

For an overhang length of 90 mm, the measured FRF in the Y direction at the bottom end of the workpiece is shown in Figure 3-11. It shows a strong mode at 390 Hz. The flexibility on the tool side was negligible compared to that on the workpiece. All cutting tests were conducted with the feed in the Y direction. This direction is also normal to the cut surface, and accordingly the vibratory model could be represented by a single degree of freedom system. By curve-fitting the Frequency Response Function (FRF) in Figure 3-11, the modal parameters were found to be:

$$K = 2.2\times10^{7}\,\frac{N}{m}, M = 3.8\,Kg, C = 731.5\,\frac{N.sec}{m}$$

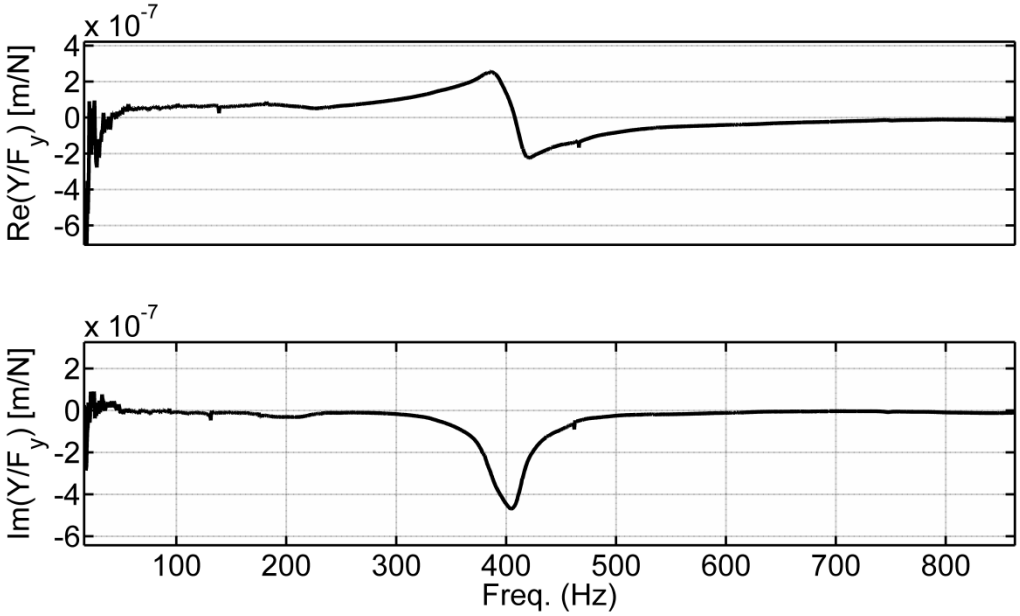

Figure 3-11: Measured frequency response function at the end of workpiece in the feed direction

All tests presented here were conducted at a feedrate of 0.05 mm/rev. Instead of measuring the vibration displacement using, for instance, a proximity probe, the cutting force signal was employed to assess the finite amplitude stability phenomenon. Recall that when the tool starts jumping out of the cut, the amplitude of vibration is A_{cr} or greater, the chip thickness is h = 0 mm, and the cutting force becomes zero. A low-pass filter was applied to the measured forces to attenuate frequencies higher than 700 Hz. To illustrate the effect of implementing the filter, the measured force and its spectrum for filtered and un-filtered signals are shown in Figure 3-12. The cut was conducted at 300

RPM with a sharp tool and width of cut b=1.8mm. As can be seen, the filtering does not affect the signal at 390 Hz, whereas it attenuates the signal at frequencies higher than 700 Hz.

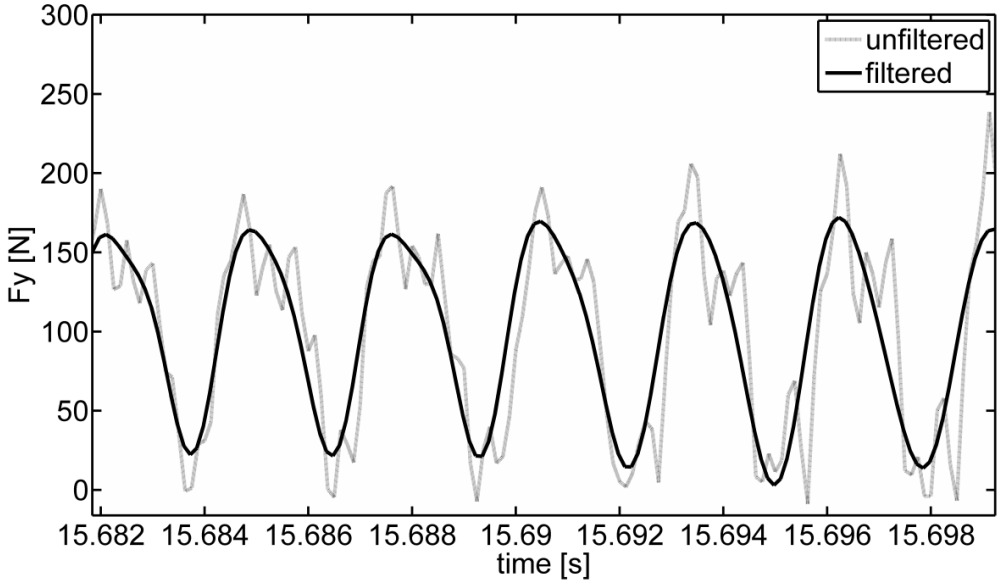

(a)

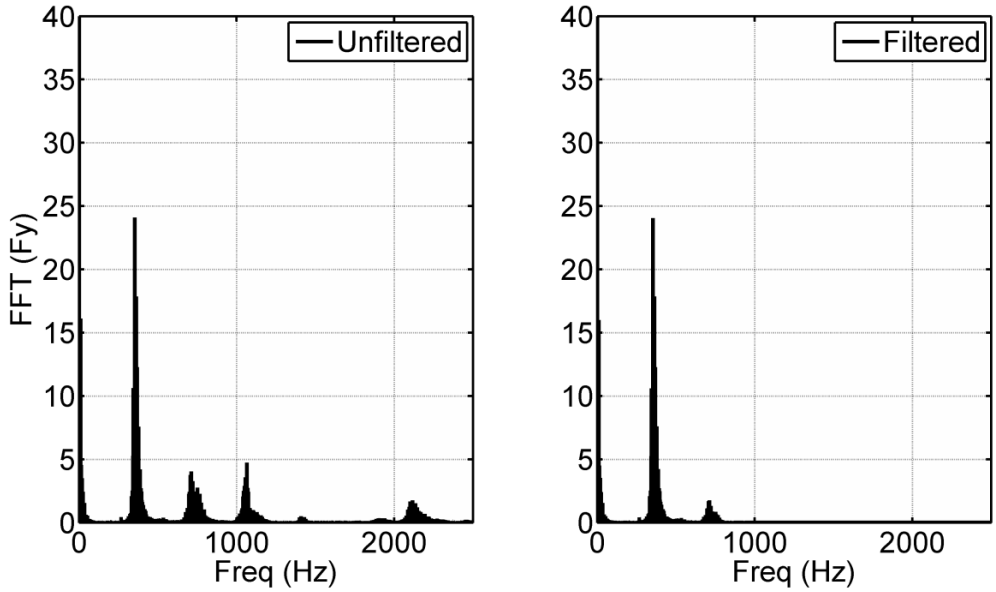

(b)

Figure 3-12: a) Filtered and unfiltered measured cutting forces at 300 RPM and b=1.8mm, using a sharp tool; b) the corresponding frequency spectra

A set of cutting experiments was conducted at 550 RPM. The feed was in the Y direction in the Y-Z plane, which meant that the feed was in the radial direction of the workpiece. The average length of cut was 18 mm. For the 550 RPM and 4”diameter, this meant that the cutting speed varied from 175.5 m/min on the outside to 113.3 m/min at the end of the cut closer to the center of the workpiece. This variation in speed, as the cut progressed towards the center, translates at the 390 Hz frequency into variation in surface wave length from 7.5 mm at the outside to 4.8 mm at the inside. Two tools were used, a sharp tool and a worn tool with a wear land of 0.08 mm. Figure 3-13 shows the measured forces for the sharp tool for widths of cut: 1.5 mm in Figure 3-13(a) and 1.6 mm in Figure 3-13(b). In Figure 3-13(a), the cut was stable and we can hardly see any oscillatory component in the signal. However, in Figure 3-13(b), the cut was unstable, the oscillatory component dominates the signal, and the force fluctuates over the whole cut between zero and 130 N. The chip was broken into small pieces due to the tool jumping out of the cut repeatedly. Figure 3-13 indicates that the process damping associated with this sharp tool for surface undulations 4.8-7.5 mm in length was negligible, and that the transition from completely stable at 1.5 mm to completely unstable at 1.6 mm was steep. This picture will change for the worn tool, as presented next.

For the worn tool, the cutting tests were conducted at widths of cut: b=2.7, 3.0, 3.1, 3.3, 3.4, and 3.5 mm. Figure 3-14(a), (b), and (c) show the measured forces at b=2.7, 3.3, and 3.4 mm, respectively. The cut at 2.7 mm in Figure 3-14(a) is completely stable. The cut at 3.4 mm in Figure 3-14(c) is completely unstable, where the force periodically drops to zero and the chip is in the form of small pieces associated with the tool’s repeated disengagement. Figure 3-14(b) shows the force in the first 10 seconds of the cut to contain an oscillatory component; however, it is not big enough for the force to drop to zero. The collected chip over the first 10 seconds shows variation in thickness, yet it is small and does not cause the chip to break into small pieces. The remainder of the cut in Figure 3-14(b) shows it to be completely stable. Over the first 10 seconds of the cut, the wave length of surface undulations varies from 7.5 mm to 6.8 mm. For this range of wave length, the process damping was insufficient to make the cut completely stable, and thus the process can be classified as a case of “finite amplitude stability”. The measured force profiles obtained at b= 3, and 3.1 mm were similar to that in Figure 3-14(b).

The amplitudes of the oscillatory (AC) components of the measured forces at 550 RPM were divided by the corresponding widths of cut and plotted in Figure 3-15 to help assess the change profile of the vibration amplitude as the process went from completely, o7r fully, stable to completely unstable. The solid triangles show the normalized values for the sharp tool, whereas the solid circles

show the normalized values for the worn tool. As can be seen, the transition associated with the sharp tool is steep, from fully stable at b=1.5 mm to fully unstable at b=1.6 mm. On the other hand, the transition is gradual for the worn tool, from fully stable at b=2.7 mm to fully unstable at b= 3.4 mm; in between, the process is in a state of "finite amplitude stability". It is interesting to see that, for both tools, the normalized AC component of the force reaches the same value of 63 N at full instability. This should be expected, since both occur at the same vibration amplitude A_{cr}.

Computer simulations were also conducted for the cases at 550 RPM. The measured modal parameters at the end of the workpiece given above, together with the cutting force coefficient in the direction normal to the cut of K_{rc}=1330 MPa and K_{sp} =4×10^{14} N/m^3, were utilized. The normalized amplitudes of AC forces obtained from simulations are also plotted in Figure 3-15. The blank triangles correspond to the sharp tool and the blank circles to the worn tool. The simulations agree with the experimental results for the sharp tool, and they also show the same sharp transition from fully stable to fully unstable. The simulations associated with the worn tool show the transition to be more uniform and smooth than that obtained from experiments. This smooth behavior agrees with the numerical simulations reported in [75] as well as those shown above in Figure 3-9. The discrepancy in behavior over the transition region between simulation and experiment could be due to the underlying assumptions of the indentation force model, especially those employed in Equation(3.7); this discrepancy warrants further investigation. Nevertheless, both simulations and experiments show the transition from fully stable to fully unstable for the worn tool to occur over a range of width of cut. For the worn tool, the process damping is significant, and it is the nonlinearity of this damping model that causes such gradual transition from fully stable to fully unstable.

A further experimental proof of the "finite amplitude stability" is shown in Figure 3-16 and Figure 3-17. The cutting experiment was conducted at 300 RPM (width of cut, b= 1.8 mm), using a sharp tool. It should be mentioned here that an attempt was made to use a worn tool and, due to excessive process damping, the cut was completely stable at the full width of the cutting edge. Because of the shorter wave lengths associated with the lower speed of 300 RPM, process damping did arise with the sharp tool, and it increased as the cut progressed closer to the center of the workpiece. Figure 3-16 shows the measured force over 47 seconds. There are four darkened sections of the force time trace, labeled: A, B, C and D. The corresponding surface undulation wave lengths are: 3.9, 3.5, 3.4 and 3.3 mm, respectively. Figure 3-17 shows photographs of the collected chips corresponding to sections A, C and D. In section A, the force periodically drops to zero, indicating a fully developed chatter. In the photograph the corresponding chip is broken into small pieces, clearly showing the result of the tool

jumping out of the cut at the chatter frequency. The force in section D and the corresponding smooth chip show a fully stable cut. In this section, the process damping is high enough to make the cut fully stable. In section B, the AC component of the force is large but not large enough to cause the force to drop to zero periodically. In section C, the AC component is smaller than that in section B, but is still significant. The chip corresponding to section C shows strong undulations due to the large vibration amplitude, yet this amplitude is not large enough to cause the chip to break into small pieces similar to that in section A. To summarize: the measured forces and the collected chip clearly show the cut to be fully stable in D, fully unstable in A, and in a state of finite amplitude stability in sections B and C.

The frequency spectra corresponding to the different sections of the measured force in Figure 3-16 are shown in Figure 3-18. The spectral line at 390 Hz increases in amplitude, from zero at section D, to 6 at B, to 25 at C, and finally to 90 at A. The spectra in B, C and D might lead one to assess the status of cut as simply unstable, and that chatter has taken place. From a practical point of view, this would be a reasonable conclusion, since the produced surfaces in the three cases are unacceptable. The problem arises, however, when cutting experiments are conducted to verify a linear chatter model. If, for instance, the cut is judged unstable according to the spectrum in B, it would mean that the linear model has predicted the stability limit incorrectly. This example accentuates the difficulties encountered in discerning the boundary of instability and in verifying linear chatter models at low cutting speeds where process damping is prominent. It also demonstrates the importance of properly addressing the nonlinearity of that damping in establishing chatter models.

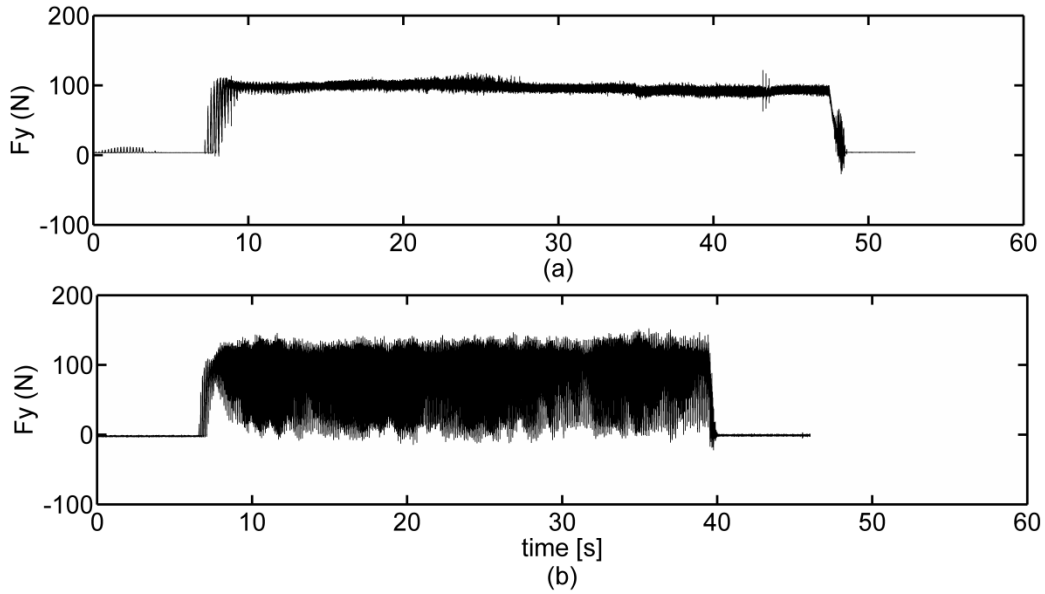

Figure 3-13: Measured cutting forces at 550 RPM using a sharp tool: a) *b*=1.5 mm, and b) *b*=1.6mm

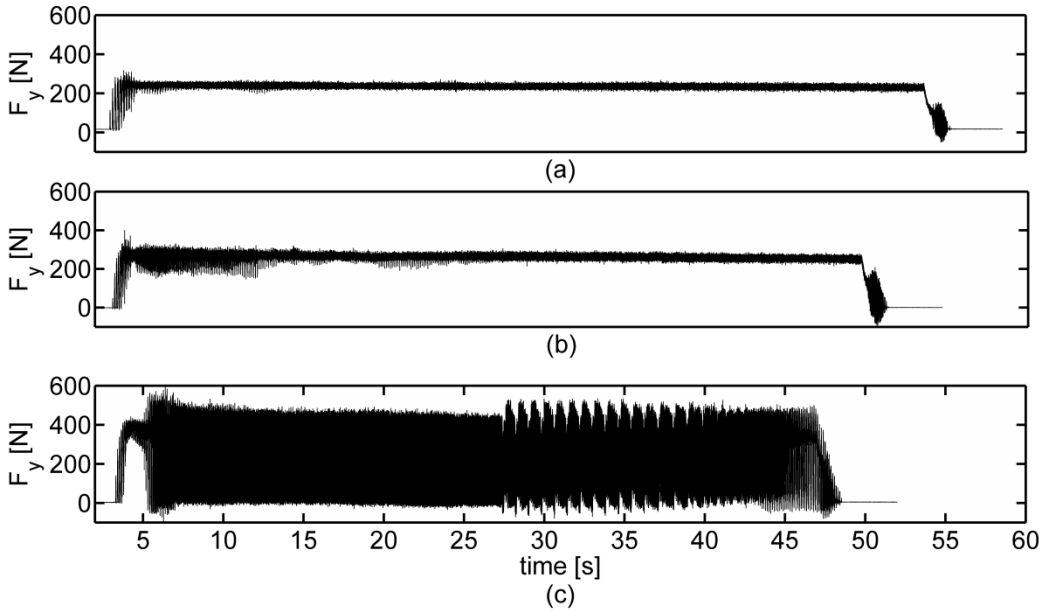

Figure 3-14: Measured cutting forces at 550 RPM with worn tool: a) *b*=2.7mm, b) *b*=3.3 mm, and c) *b*=3.4 mm

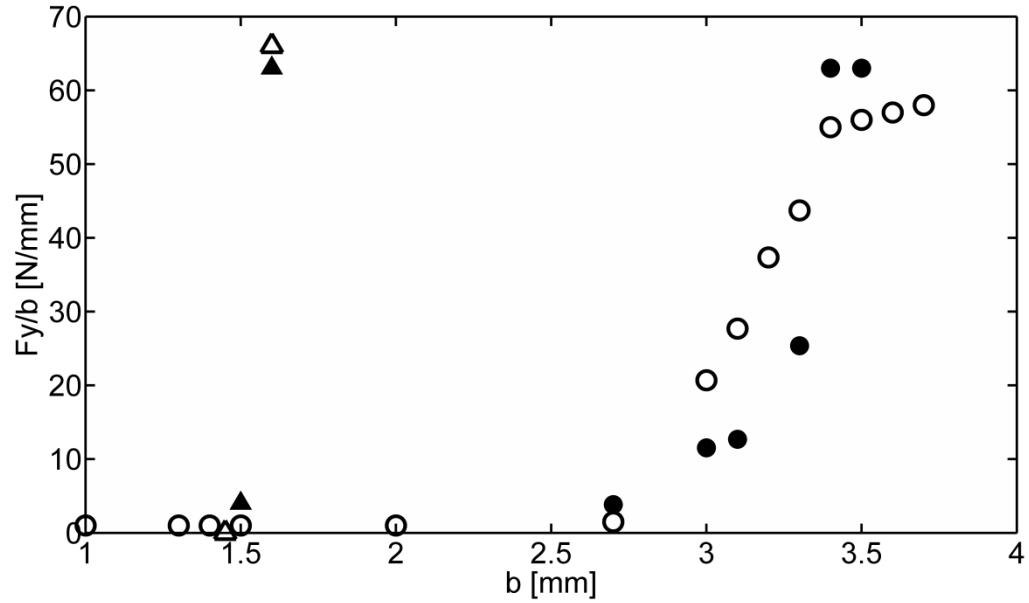

Figure 3-15: The measured and simulated amplitude of AC component of the cutting force normalized by its corresponding width of cut: ● Measured with the worn tool, ○ simulated with the worn tool, ▲ measured with a sharp tool, and Δ simulated with a sharp tool

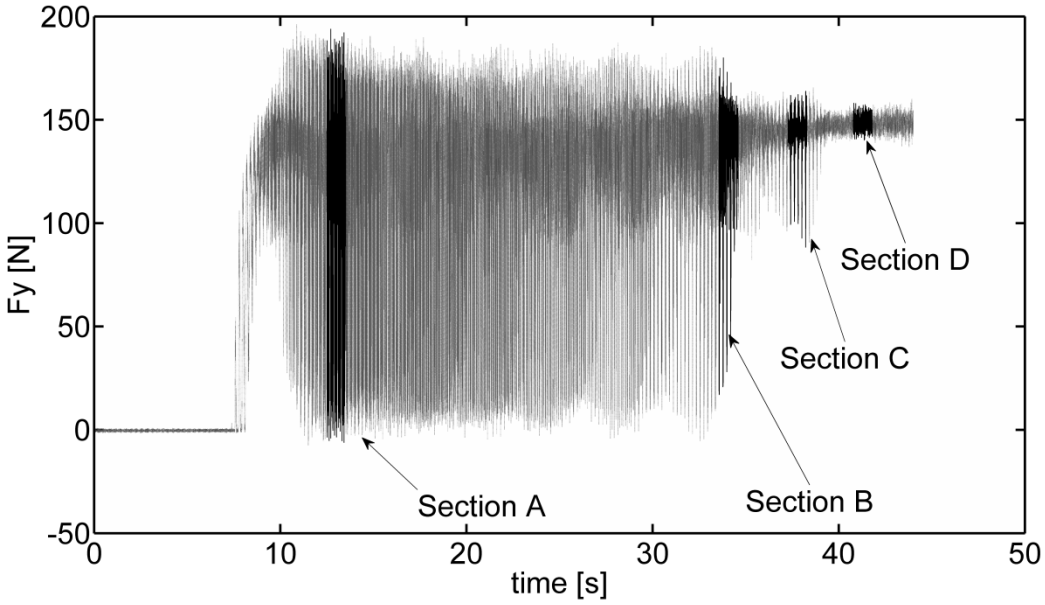

Figure 3-16: Measured cutting force at 300 RPM with sharp tool and *b*=1.8mm

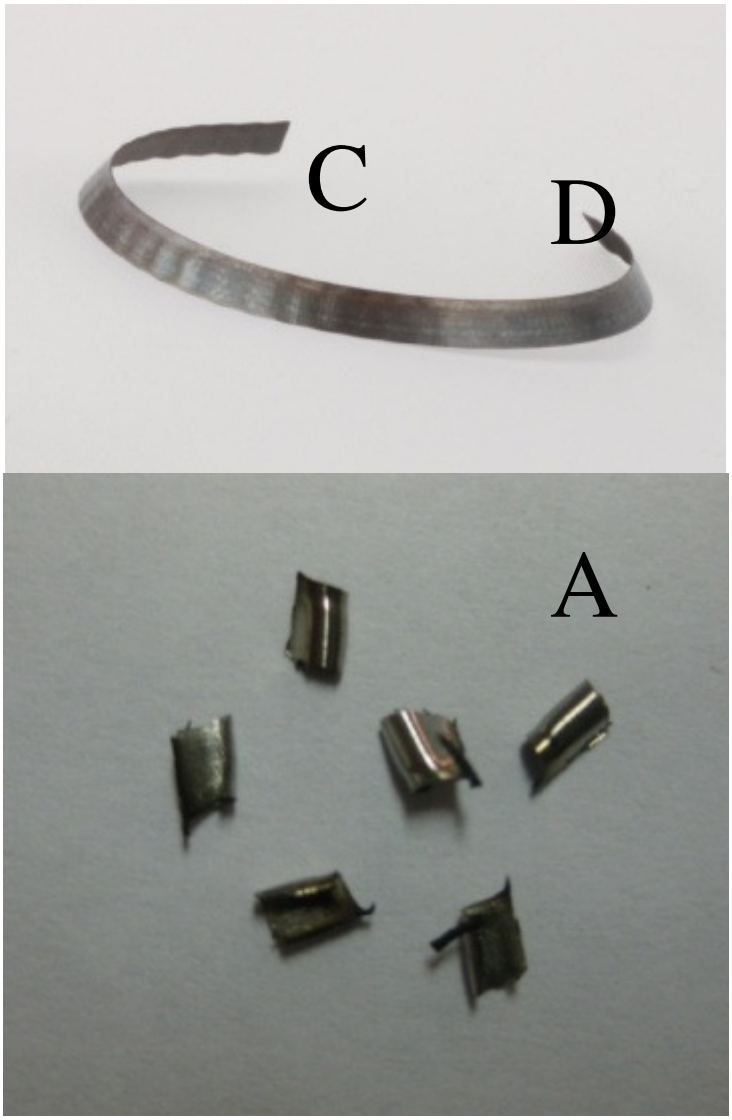

Figure 3-17: Produced chip at 300 RPM: A) unstable, C) Finite amplitude vibration, D) stable cuts

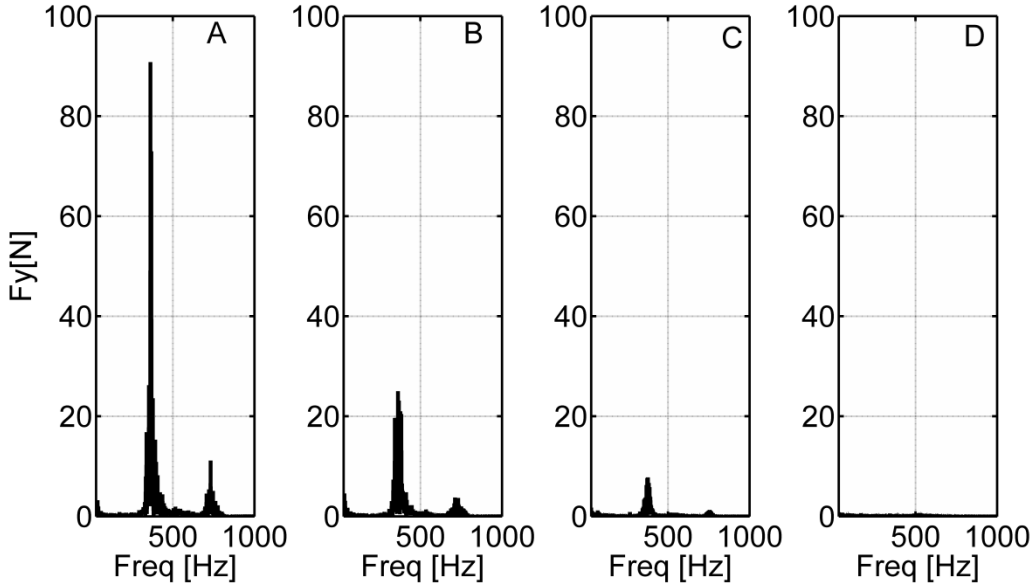

Figure 3-18: Measured frequency spectra corresponding to sections A, B, C and D given in Figure 3-16

3.6 Summary

The two linear process damping models investigated here showed that the model based on small amplitude vibration leads to underestimating the stability limit, and that the accuracy of a damping model obtained from sinusoidal excitation depends on the amplitude of excitation in relationship to the feedrate employed in the verification experiments. The experimental work conducted in this chapter confirmed the finite amplitude stability phenomenon associated with nonlinear process damping. This phenomenon makes it difficult to discern the boundary of stability in verification experiments of linear damping models. The experiments also showed that, in the presence of process damping, the transition from fully stable to fully unstable conditions occurs gradually over a range of width of cut. This is in agreement with numerical simulations reported in the literature as well as those conducted in the current work. The numerical simulations, however, showed gradual change to be smoother than that observed here experimentally. This discrepancy might be due to the underlying assumptions in the ploughing force model, which warrants further investigation. Nevertheless, the general behavior from experiments was consistent with simulations in terms of the change in

vibration amplitude from zero to a critical value for cases where process damping was negligible as well as for cases where it was significant.

Although numerical simulations have allowed the integration of nonlinear indentation force into machining chatter models, it requires high discretization resolution for accurate numerical simulation, as has been shown in this chapter. Needless to say, establishing the stability lobes in this way over a typical range of cutting speed using time domain simulation would be a lengthy task. Developing a new process damping model that can be employed in the analytical methods of calculating stability lobes and preserves finite amplitude stability is addressed in the next chapter.

Chapter 4
Analytical Stability Lobes Including Nonlinear Process Damping Effect on Machining Chatter

The objective of the current chapter is to develop a linearized model of the process damping while preserving the vibration-amplitude dependence of the indentation pulse on the resulting stability. The developed process damping model will be used to establish the stability lobes analytically taking into account the effect of nonlinear process damping. The developed lobes could be established for different amplitudes of vibration. This is a departure from the traditional notion that the stability lobes represent a single boundary between fully stable and fully unstable cutting conditions.

The analytical computations of the new process damping model are described in the next section. These involve the computations of the indentation area and equivalent viscous damping of the indentation force. A faster method for computing this equivalent damping will also be presented; it will be shown to greatly speed up the establishment of stability lobes. Section 4.2 will present an approach to establishing the lobes at particular amplitudes of vibration as well as boundary lobes analytically. For this reason, the established process damping model is integrated into the frequency domain calculation of stability lobes. The analytically established lobes will be tested in the subsequent section against time domain simulations as well as against the lobes presented by Altintas *et al.* [33], using an empirical damping model. This will be followed by experimental verifications of the proposed approach using plunge turning of steel and employing sharp and worn tools. It will be shown that the analytically established lobes yield practically the same results obtained from time domain simulations, and that they are in good agreement with results obtained from cutting tests.

4.1 Analytical Representation of Process Damping

In this section, the geometry of the indentation area will be discussed, along with the analytical computation of that area. This is utilized in formulating the equivalent viscous damping that will be employed in establishing the stability lobes. An analytical formula to compute the equivalent damping will also be presented.

4.1.1 Analytical Computation of Indentation Area

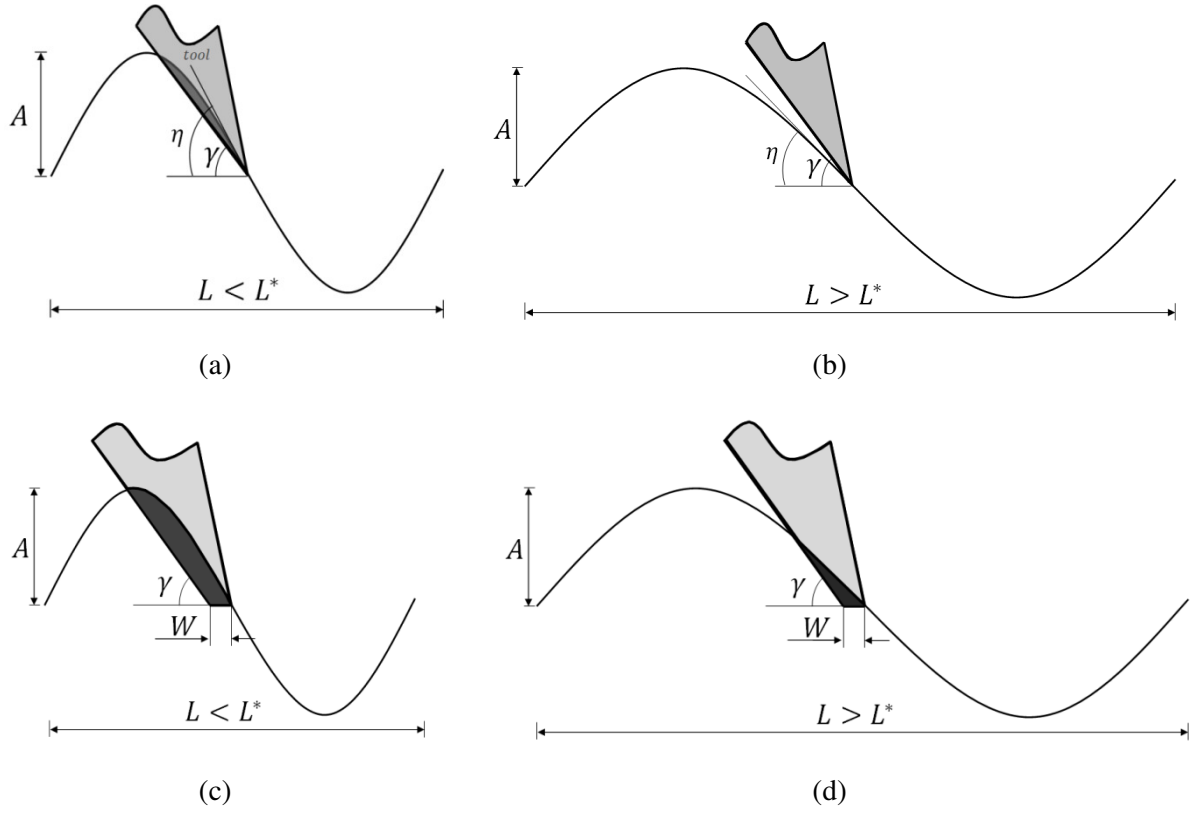

Figure 4-1: Geometry of indentation area: a) W=0, L<L*, b) W=0, L>L*, c) W≠ o, L<L*, and d) W≠ o, L>L*

Figure 4-1 shows the indentation areas for different situations: (a) and (b) are for sharp tools, whereas (c) and (d) are for a worn tool with wear land W. In (a) and (c), the clearance angle γ is greater than the maximum magnitude of slope η of the wave, which is smaller than the slope in (b) and (d). Cases associated with sharp tools were discussed previously [78]; clearly, in Figure 4-1(b), there is no indentation and thus process damping is not involved. This situation will occur at wave lengths equal to or greater than L^*, for which η becomes equal to γ:

$$\tan(\eta) = \tan(\gamma) = A\frac{2\pi}{L^*} \qquad (4.1)$$

Below L^*, even for a sharp tool, the process damping would contribute to the stability of the system. In Figure 4-1(c), the flank face intersects with the back side, (0-L/4), of surface undulation, whereas in Figure 4-1(d), it intersects with the front side, (L/4-3L/4), creating a triangular shape.

Liang and co-workers [39, 40] treated the case (d), for which they assumed small amplitude vibration and expressed the indentation area by the equation:

$$F_{py} = \begin{cases} 0 & ;\dot{y} > 0 \\ K_{sp} b \dfrac{-w^2}{2v} \dot{y} & ;\dot{y} \le 0 \end{cases} \qquad (4.2)$$

where v is the cutting speed in the tangential direction. The approximation in Equation (4.2) will be utilized in the current work in establishing the lower bound stability lobes, where the vibration amplitude is close to zero. Notice that Equation (4.2) is only valid for $W>0$ and accordingly does not deal with sharp tools. In time domain simulations, all the possibilities of indentations in Figure 4-1 are treated in the same way which, as mentioned earlier, consumes considerable time. Here, the area of indentations will be computed analytically, and therefore one must recognize the different scenarios above and compute that area, $S(x)$, accordingly.

Figure 4-2 shows a cross-sectional area in the XY plane of the extruded volume at tool position (x,y). The indentation area $S(x)$ (dark area) is surrounded by three geometries: surface undulation (y_s), wear land (y_w), and flank face of the tool (y_f). Each of these boundaries can be described as a function of χ and x, as follows:

$$\begin{aligned} y_s(\chi) &= A\sin\lambda\chi \;;\; \lambda = 2\pi / \mathrm{L} \\ y_f(\chi) &= y_w + \beta(x - W - \chi) \;, \beta = \tan\gamma \\ y_w(\chi) &= y_s(x) \end{aligned} \qquad (4.3)$$

The flank face is shown to intersect with the back side of the wave at the point (x', y'). Hence, the area bounded by these geometries is

$$S(x) = \int_{x'(x)}^{x_w(x)} (y_s(\chi) - y_f(\chi))d\chi + \int_{x_w(x)}^{x} (y_s(\chi) - y_w(\chi))d\chi, \quad \frac{L}{4} < x < \frac{3L}{4} \qquad (4.4)$$

To perform the integrals in Equation (4.4), the intersection point (x',y') must first be found. To simplify finding this intersection, the sine was is replaced by two 3rd order polynomials, one for the back side, in the range $-L/4$ to $L/4$, and the other for the front side, in the range $L/4$ to $3L/4$. These two polynomials are

$$y_s(\chi) = \begin{cases} a_3\chi^3 + a_1\chi; & \dfrac{-L}{4} < \chi < \dfrac{L}{4} \\ -a_3\left(\chi - \dfrac{L}{2}\right)^3 - a_1\left(\chi - \dfrac{L}{2}\right); & \dfrac{L}{4} \le \chi < \dfrac{3L}{4} \end{cases} \qquad (4.5)$$

Note that a_o and a_2 =0, because the back side is asymmetric around the X and Y axes. The front side of the wave is a mirror image of the back side around x= L/4. The coefficients a_3 and a_1 were found by equating the original sine with the polynomial representing the back side at two points (e.g., at x=L/6 and L/12). They were found to be: a_3 = - 38.58 A/L^3 and a_1= 6.27 A/L. Figure 4-3 shows the polynomials superimposed on the original sine wave for a wave of amplitude A=0.03mm and wave length L=3.7 mm.

The intersection point *(x',y')* between the flank face and the surface wave at a tool position x will be obtained from:

$$y_s(\chi) = y_f(\chi) \tag{4.6}$$

The intersection point is obtained by simply finding the roots of the cubic equation Equation (4.6). The intersection will be assumed first to occur with the back side of the wave, but if x'> L/4, then the polynomial in Equation (4.6) will be switched to that of the front side. With the tool position *(x,y)* and intersection point *(x',y')* now available, the integrals in Equation (4.4) are performed to obtain the indentation area *S(x)* analytically.

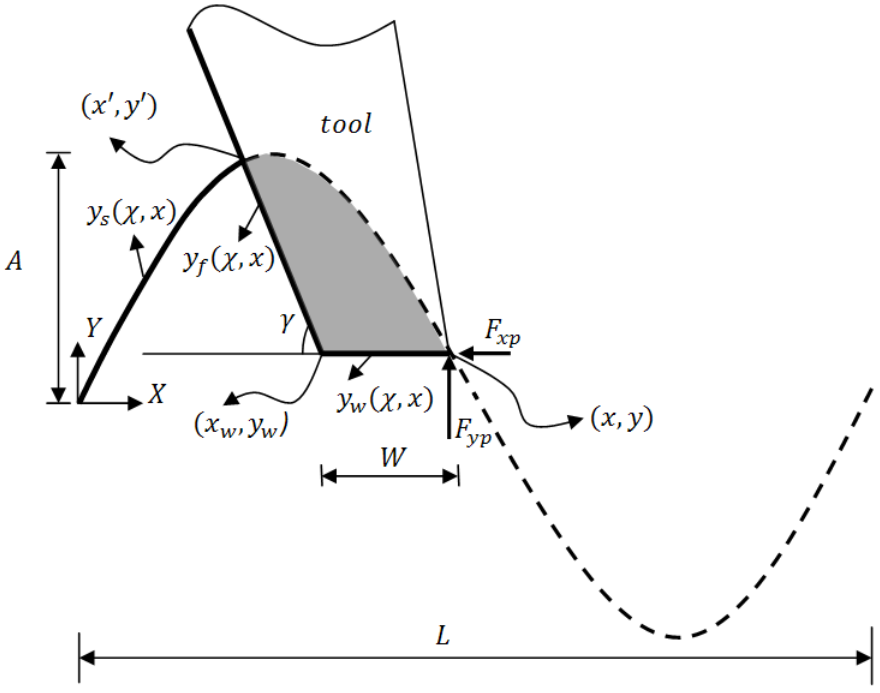

Figure 4-2: Geometry of tool indentation into surface undulations

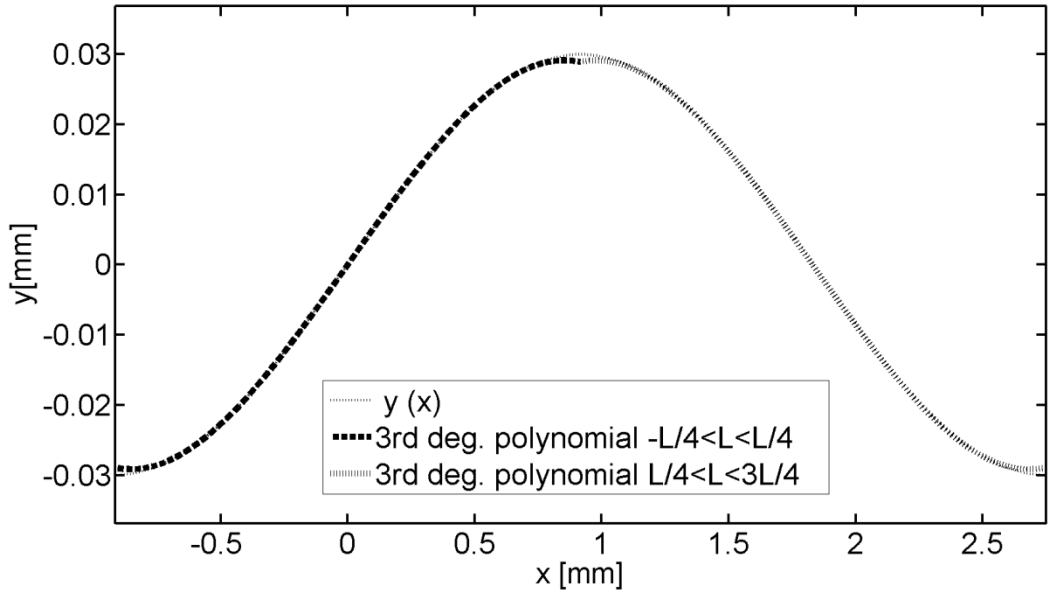

Figure 4-3: Polynomials used to approximate a sine wave of L=3.7mm, A=0.03mm

The indentation area is updated for the tool positions during the downward motion of the tool in the range of $x=L/4$ to $3L/4$. Thus, multiplying by the width of cut b and K_{sp}, we get the indentation force pulse responsible for process damping. The damping in this way is nonlinear, since it operates over a portion of the vibratory cycle and is zero over the remainder of the cycle. Presented next is the development to replace this nonlinear damper by an equivalent linear viscous damper that will allow establishing the stability lobes analytically.

4.1.2 Equivalent Viscous Damping

The idea of replacing a nonlinear damper, for example a coulomb friction, by an equivalent linear viscous damper, C_{eq}, is well accepted [79] in evaluating the steady state response of a vibratory system under harmonic excitation. This idea is utilized here to replace the nonlinear process damper by a viscous damper to establish the stability lobes analytically. In these lobes, the response of the system in the frequency domain will be employed. Implicit in establishing the lobes from the behavior of the vibratory system in the frequency domain is that the system is vibrating at steady amplitude at the chatter frequency. Recently, Budak and Tunc [41 and 42] used the equivalent viscous damping approach to estimate K_{sp} from chatter experiments. In the current work, K_{sp} is assumed available and the objective is to develop a method to establish the lobes that account for different states of the cut, namely fully stable, fully unstable, and finite amplitude stability. The development

of C_{eq} was described in [42]. It is also described next to maintain consistency in the terminology utilized throughout the current work.

The energy dissipated by the indentation force in one vibration cycle of amplitude A and wavelength L is E_i:

$$\mathrm{E}_i = \int_{L/4}^{3L/4} K_{sp} b S(x) \frac{dy}{dx} dx \tag{4.7}$$

Since the toolpath is assumed to be a sinusoidal wave of amplitude A and length L, $y(x)$ and, consequently, $\frac{dy}{dx}$ are

$$y = A\sin(\lambda x);\quad \frac{dy}{dx} = A\lambda\cos(\lambda x);\quad \lambda = \frac{2\pi}{L}$$

substituting dy/dx in Equation (4.7), E_i will be:

$$\mathrm{E}_i = A\lambda K_{sp} b\overline{\mathrm{E}_i}:\quad \overline{\mathrm{E}_i}(A,\gamma,W,L) = \int_{L/4}^{3L/4} S(x)\cos\lambda x dx$$

On the other hand, the energy dissipated by a viscous damper with coefficient C_{eq} on a similar wave is

$$\mathrm{E}_\mathrm{d} = \int_0^L C_{eq}\frac{dy}{dt}dy = v\int_0^L C_{eq}\left(\frac{dy}{dx}\right)^2 dx = vA^2\lambda^2 C_{eq}\int_0^L(\cos\lambda x)^2 dx = \frac{L}{2}vA^2\lambda^2 C_{eq}$$

By equating E_i and E_d, one can find C_{eq} in terms of A, L, γ *and* W:

$$C_{eq} = \left(\frac{K_{sp}b}{v}\right)C_d;\quad C_d = \frac{\overline{\mathrm{E}_i}(A,\gamma,W,L)}{A\pi} \tag{4.8}$$

The effect of A, L, W, and γ on C_d is shown in Figure 4-4 for a range of tool and vibration wave parameters. C_d depends on tool and vibration wave geometry and therefore can be considered the "shape damping factor". As expected, C_d increases by increasing A and W, but decreases by increasing γ and L. It is interesting to see the decline in damping accompanying the increase in clearance angle. That might explain the decrease in stability associated with the presence of a stable built-up edge that could increase the effective clearance angle. It is also important to see the strong dependence of the damping on the amplitude of vibration.

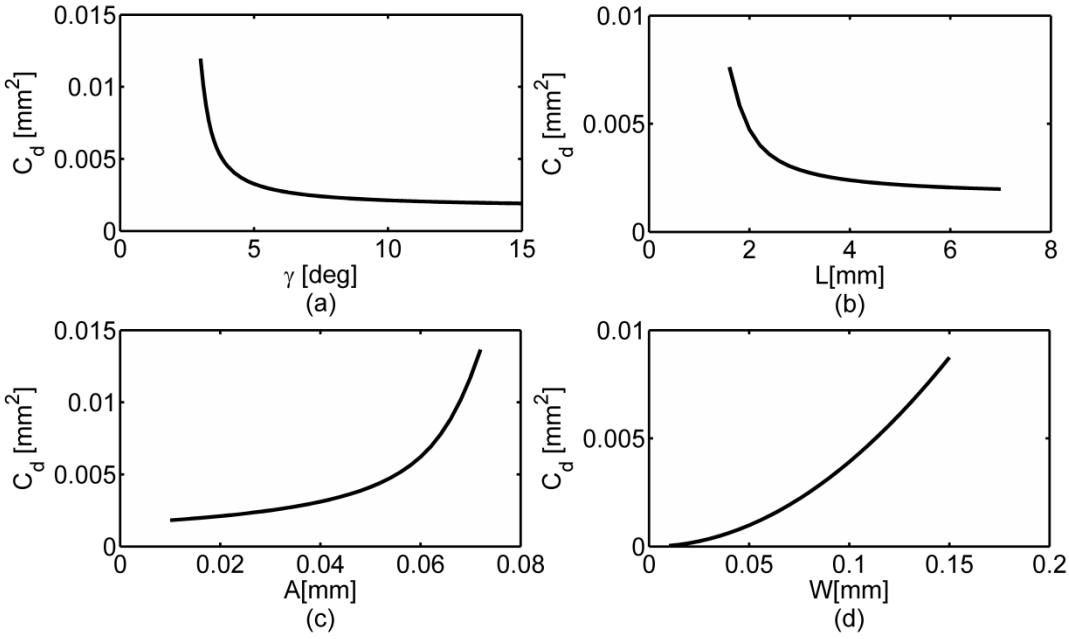

Figure 4-4: Variation of C_d in relation to: a) clearance angle γ, b) wave length L, (c)vibration amplitude A, and (d) wear land width W

Although Equation (4.8) represents an analytical formulation for C_d, it is not a closed-form equation explicit in terms of *A, γ, L* and *W*. It relies on the computations of the indentation area *S(x)* that in turn depends on the intersection point between the tool flank or wear land and surface undulations. The intersection point, in case of the flank face, is obtained from solution of a cubic equation, as described earlier. All in all, expressing *S(x)* explicitly in the above parameters that would lead to performing the integral in Equation (4.8) analytically proved unmanageable. Instead, the integral was evaluated numerically by using $\Delta x = L/50$. This process also consumes time, albeit much shorter than that used in time domain simulations. To address this shortcoming, it was decided that a data base for C_d that covers a typical range of the parameters involved should be generated. This data base was envisioned to be in the form of look-up tables that would circumvent the need to perform the computational elements required to find C_d , in every iteration, in the course of establishing the lobes. Fortunately, the effort to generate such a data base has resulted in a concise expression of C_d, as described next.

4.1.3 Analytical Formulation of Equivalent Damping

The analytical and empirical process damping models in the literature, [40] and [33], took the form:

$$C_d = \alpha W^{\beta_w} \tag{4.9}$$

Equation (4.9) shows the effect of tool wear W. However, it is evident from the behavior of C_d in Figure 4-4 that the strong effect of the clearance angle γ and especially the vibration amplitude A cannot be overlooked. For this reason, computations of C_d were conducted for all of the following parameters:

- Clearance angle γ at 5, 7 and 9°.
- Wear land width W: 0.02-0.12 mm at increments of 0.02 mm. W=0 was also computed for cases where $L<L^*$.
- Wave length L: 0.6 L^*-$2L^*$ at increments of 0.2L^*, and 3L* -10L* at increments of 1L*.
- Amplitude of vibration A: 0.01-0.10 mm at increments of 0.01 mm. The case of A=0.005 mm was also computed to demonstrate that the model presented here approaches that of Liang and co-workers [39 and 40], as the vibration amplitude approaches zero.

In total, 2046 computations were performed to obtain the shape damping factor C_d using the procedure described in Section 4.1.1. Initially, attempts were made to have a single expression of C_d through curve fitting all of the generated data that include L, W, γ and A. The correlation coefficient was poor and the decision was made to have C_d (that is, a function of L and W) for a particular γ and a particular level of vibration amplitude. An example of computed data and their curve fitting is shown in Figure 4-5. The circles show the computed values for different L for the case A=0.03 mm, W=0.06 mm and γ = 7°. It shows C_d to behave differently in the region $L>L^*$ from that where $L<L^*$. This behavior was consistent for all other cases, and accordingly the data was fitted into two different functions: linear for $L<L^*$ and exponential for $L>L^*$. The solid line in Figure 4-5 shows the results of curve fitting. Although there is discontinuity in slope at $L=L^*$, the fitting in the two regions is excellent. The expressions for C_d are given in Equation (4.10).

$$C_d = \begin{cases} \alpha\left(L+W-L^*\right)^{\beta_L} W^{\beta_w}, & L > L^* \\ p(L^*-L)+\alpha W^{\beta_L+\beta_w}, & L \le L^* \end{cases} \tag{4.10}$$

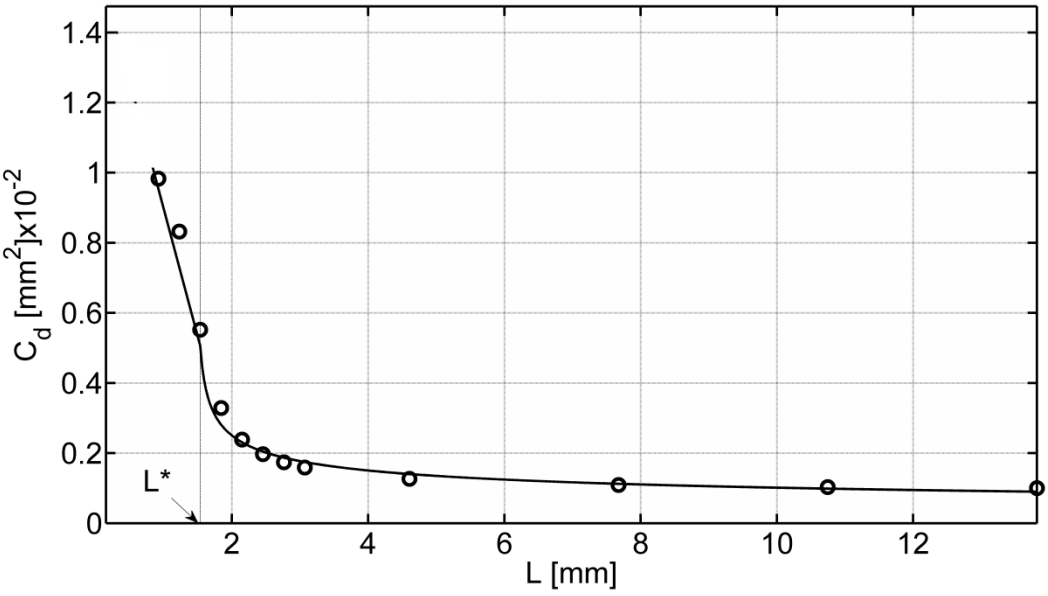

Figure 4-5: Computed data and curve fitting results of C_d at A=0.03mm, γ=7°, and W=0.06 mm

W and *L* in Equation (4.10) are in millimeters. For $L>L^*$, C_d takes the same form as that suggested by Liang and coworkers [39 and 40], except that the exponent for *L* is now β_L instead of zero. For $L<L^*$, the linear expression for C_d is new and, to the best of my knowledge, has not been reported in the literature. The values of coefficients and exponents obtained from curve-fitting of the different cases are listed in Table 4-1. Also listed in Table 4-1 are the values of the coefficient α and the exponent β_W associated with the Liang model, where the assumption of small amplitude vibration was made.

The following observations can be made from Table 4-1:

- β_W is practically 2 for all cases, which is consistent with Liang's model.
- The absolute value of β_L reaches a steady value of -0.33 for large amplitudes, while for smaller amplitudes it diminishes in the direction towards A=0.
- The absolute values of the coefficients p and α exhibit a consistent trend of increasing with the increase in the amplitude of vibration *A*. They also show a consistent decreasing trend with the increase in the clearance angle γ.

The consistent increase in absolute values of p and α in the direction of increased vibration amplitude is of particular interest. It led to curve-fitting these coefficients over the amplitude range in

Table 4-1, and excellent results were obtained by fitting p into a linear relationship with A, whereas α was fitted into a quadratic relationship. The correlation coefficients were 0.99 for both fittings. Accordingly, p and α are expressed as:

$$p = a_p^1 A + a_p^0$$
$$\alpha = a_\alpha^2 A^2 + a_\alpha^1 A + a_\alpha^0 \quad (4.11)$$

The coefficient a^1_p and a^0_p associated with p, and a^2_α, a^2_α and a^2_α associated with α are listed in Table 4-2 for γ=5, 7 and 9°.

Table 4-1: Computed α, β_W, β_L and p for different combinations of tool clearance angle and vibration amplitude

γ / A(mm)	5°				7°				9°			
	α	β_W	β_L	p(×10^{-2})	α	β_W	β_L	p(×10^{-2})	α	β_W	β_L	p(×10^{-2})
Liang[39]	0.250	2.00	0.00	-	0.250	2.00	0.00	-	0.250	2.00	0.00	-
0.005	0.254	1.98	-0.21	0.17	0.270	1.97	-0.16	0.12	0.296	1.99	-0.14	0.09
0.01	0.410	1.98	-0.28	0.34	0.331	1.97	-0.25	0.24	0.308	1.98	-0.20	0.19
0.02	0.540	1.99	-0.32	0.68	0.459	1.98	-0.31	0.49	0.401	1.97	-0.30	0.38
0.03	0.625	2.00	-0.33	1.03	0.554	1.99	-0.32	0.73	0.496	1.99	-0.32	0.57
0.04	0.670	2.00	-0.33	1.37	0.618	2.00	-0.33	0.97	0.561	1.99	-0.32	0.75
0.05	0.756	2.00	-0.33	1.71	0.667	2.00	-0.33	1.22	0.609	2.00	-0.33	0.94
0.06	0.805	2.00	-0.33	2.05	0.714	2.00	-0.33	1.46	0.651	2.00	-0.33	1.13
0.07	0.848	2.00	-0.33	2.39	0.755	2.00	-0.33	1.70	0.688	2.00	-0.33	1.32
0.08	0.881	2.00	-0.33	2.74	0.791	2.00	-0.33	1.95	0.723	2.00	-0.33	1.51
0.09	0.924	2.00	-0.33	3.08	0.824	2.00	-0.33	2.19	0.7.54	2.00	-0.33	1.70
0.10	0.957	2.00	-0.33	3.42	0.854	2.00	-0.33	2.44	0.783	2.00	-0.33	1.89

Table 4-2: Coefficients of Equation (4.11)

a / γ	a^0_p (x10^{-2})	a^1_p (x10^{-2})	a^0_α	a^1_α	a^2_α
5°	-0.0044	34.26	0.254	13.300	-65.140
7°	-0.002	24.38	0.231	11.580	-55.210
9°	0.0015	18.87	0.238	9.333	-39.760

Equation (4.10) and Equation (4.11) along with Table 4-1 and Table 4-2 provide a much simpler and faster approach for computing C_d at different amplitudes, wavelengths, clearance angles and flank wear widths. Obtaining C_d in this way provides a great advantage in establishing the stability lobes using the iterative approach described next.

4.2 Establishing Stability Lobes Including Process Damping

In establishing the lobes in this work, other sources of process damping such as changes in the magnitude and direction of the shear force are neglected in comparison with the indentation of material underneath the flank face of the tool. This is a reasonable assumption, based on the study conducted by Huang and Wang [29], where the authors showed that the energy dissipated by the other sources is small compared to that dissipated by the indentation.

The dynamic model used in this part is the same as the one presented in Chapter 3. A similar shear force model is also used, but the ploughing force is represented by the equivalent viscous damper developed in this chapter. Thus, the equation of motion is

$$M\ddot{y} + Ky + C\dot{y} = K_r b\ (s_t + y - y^T); \qquad C = C_s + C_{eq}(A, L, b) \tag{4.12}$$

According to Equation (4.10), C_{eq} is a function of *A, L, W*, *b* and γ, but only *A, b* and *L* depend on the cutting conditions. γ and *W* are parameters of the tool and are known a priori. For this reason, C_{eq} appears in Equation (4.12) as a function of only *A, b* and *L*.

If there is no process damping and $C_{eq.}$=0, then Equation (4.12) will be the classic regenerative chatter formulation, which is well developed in the literature [7]. In this case, the stability lobes are obtained by sweeping the chatter frequency, ω_c, (rad/s) in the vicinity of the system's natural frequency, and calculating the depth of cut *b* and spindle speed at the border of stability from

$$\begin{aligned} & b = \frac{-|\Lambda|^2}{2K_r \,\mathrm{Re}(\Lambda)}, \qquad \Lambda = K - M\omega_c^2 + Ci\omega_c \\ & T = 2n\pi + \varepsilon, \qquad n = 0,1,2,..., \varepsilon = \pi - 2\varphi \\ & , \bar{\varphi} = \tan^{-1}\frac{\mathrm{Im}(\Lambda)}{\mathrm{Re}(\Lambda)} \end{aligned} \tag{4.13}$$

In Equation (4.13), *n* is the lobe number, which is actually the number of full vibration waves over one revolution of the workpiece, ε is the phase angle between waves in subsequent revolutions, *T* is the time of one revolution, and $\bar{\varphi}$ is the phase angle between the displacement of the vibratory

system and the exciting force. *Re (Λ)* and *Im (Λ)* are the real and imaginary parts of the frequency response function, FRF, of the vibratory system, respectively. In this section, Equation (4.13) will be employed in an iterative solution to find the stability lobes in the presence of C_{eq}, which is a function of *A, b* and *L*.

Before describing the iterative procedure, it is worthwhile recalling that, due to the nonlinear nature of process damping, the process can be in three states: fully stable, where the amplitude of vibration is zero; fully unstable, where the amplitude of vibration is A_{cr} or slightly larger; and finite amplitude stability, where the vibration stabilizes at an amplitude between zero and A_{cr}. This suggests that there are two distinct outer boundaries: one between fully stable and finite amplitude stability, and the other between finite amplitude stability and fully unstable. In theory, one might even have a particular boundary within the finite stability region at specified amplitude, say A_s, below which the amplitude is smaller than A_s, whereas it is greater than A_s above that boundary. The procedure to establish the lobes at a particular amplitude is designated here as "Fixed Amplitude Lobes", while the procedure to establish the lobes for the upper bound or lower bound stability lobes will be designated "Boundary Lobes". The former is described first.

Fixed Amplitude Lobes:

1- Choose a chatter frequency, ω_c, in the vicinity of the tool natural frequency and *n* the lobe number.
2- Set C_{eq}=0.
3- Calculate *b* and *T* from Equation (4.13).
4- Update $L = \frac{v}{f_c}$, where f_c is chatter frequency in Hz. The speed *v* is obtained from *T* and the radius of the workpiece.
5- Update $C_{eq}(A_s,L,b)$ using new *L*, *b* and Equation (4.8) or Equation (4.10).
6- Repeat steps 3-5 until *b* converges to the desirable tolerance.

The tolerance for convergence will be discussed in Section 4.3. The procedure above is repeated using increments of $\Delta\omega_c$ over a frequency range that depends on the wave number *n*, and then the whole procedure is repeated for different *n*.

Boundary Lobes:

Lower bound: amplitude $A \approx 0$;

In this case, the same procedure described above for fixed amplitude lobes is followed with the provision that C_{eq} is what would be obtained from Liang's model, first line in Table 4-1. Notice that

this model is only applicable for $L>L^*$. This is fine, since for small amplitude of vibration, Equation (4.1) shows that L^* also becomes small. This situation could only materialize at extremely low cutting speed combined with high frequency of vibration, which is not the focus of this work.

Upper bound: amplitude $A= A_{cr}$.

Equation (3.11) shows A_{cr} to be a function of ε, which is obtained from Equation (4.13). Consequently, in addition to L and b, the amplitude A should be updated as well in each iteration.

1. Choose a chatter frequency, ω_c, in the vicinity of the tool natural frequency, and the lobe number n.
2. Set C_{eq}=0.
3. Calculate b, ε and T from Equation (4.13).
4. Update $L = \dfrac{v}{f_c}$.
5. Update A_{cr} using Equation (3.11).
6. Update $C_{eq}(A_{cr},L,b)$ using Equation (4.8) or Equation (4.10) for new L, A_{cr} and b.
7. Repeat steps 3-6 until b converges to the desirable tolerance.

Similar to the procedure above, steps 1-7 are repeated using the increments of $\Delta\omega_c$, and the whole procedure is repeated for different wave number n.

Assessing the performance of the above procedures is conducted in the next section. The assessment is done against numerical simulations as well as the lobes established using an empirical process damping model [33]. The vibratory system parameters given in [33] will be utilized along with the cutting coefficients. The specific indentation coefficient $K_{sp} = 4\times10^5$ N/mm^3 will be utilized.

4.3 Comparisons With Time Domain Simulation and Empirical Model

Altintas *et al.* [33] conducted plunge turning experiments to develop an empirical model for the process damping. They represented the process damping effect by an additional dashpot acting on the vibratory system. Accordingly, they expressed the process damper for AISI 1045 steel in the following form:

$$C_p = \frac{6.11\times10^6}{v} b \qquad N.s/m \qquad (4.14)$$

The authors obtained C_p by harmonic excitation at 0.035 mm amplitude. The parameters of the vibratory model in [33] were: $K = 6.48\times10^6$ (N/m), $M = 0.56$ (Kg), and $C_s = 145$ (N.s/m). The cutting force coefficient for AISI 1045 in the feed direction was estimated at K_r=1380 MPa. The workpiece was a 35 mm diameter shaft cut at a feedrate $s_t = 0.05$ (mm/rev). The tool had a clearance angle γ of

7°. The above parameters will be employed in this section to establish the lobes following the developed procedures above and to compare with the lobes computed using the empirical damping factor in Equation (4.14). Although the tool used in [33] was sharp, a small $W = 0.04$ mm is assumed here to account for tool edge radius (hone radius).

Before comparing the lobes obtained using the procedures developed here with the Lobes and experimental results in [33], it is important first to test the accuracy in determining the equivalent damping using Equation (4.10) with that following the detailed computations described in sections 3.1 and 3.2. Notice that the equivalent damping is updated in each iteration involved in establishing the width of cut at a particular chatter frequency ω_c and wave number n. For this test, we will establish the upper bound lobes at A_{cr} and fixed amplitude lobes at A_s =0.020 mm. Notice that, from Equation (3.11), the minimum value of A_{cr} occurs at $A_{cr}=\frac{s_t}{\sqrt{2}}$; and accordingly, for s_t=0.05 mm/rev, the minimum A_{cr} will be 0.035 mm. Figure 4-6 shows the computed lobes using the fast (section 4.1.3) and detailed method (section 4.1.2), the former is drawn in a broken line, whereas the latter is drawn in a solid line. The lobes from the two methods coincide for 20 μm and A_{cr} amplitudes. With such excellent agreement, the fast method will be employed for the remainder of this chapter.

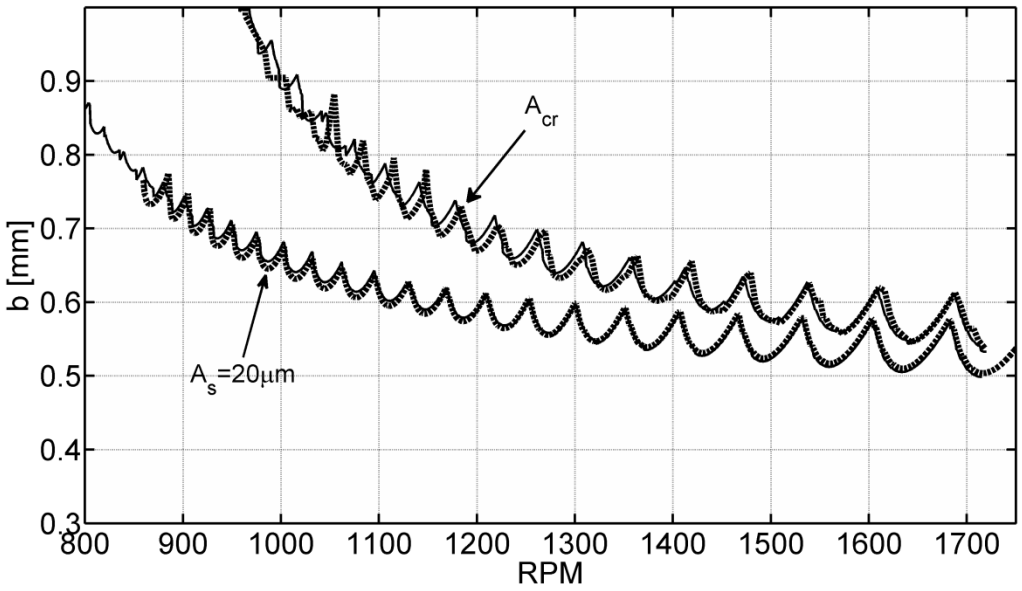

Figure 4-6: Upper bound and fixed amplitude lobes computed using equivalent damping from quick method of Equation (4.10), (broken lines) and detailed method of Section 4.1.2 (solid line)

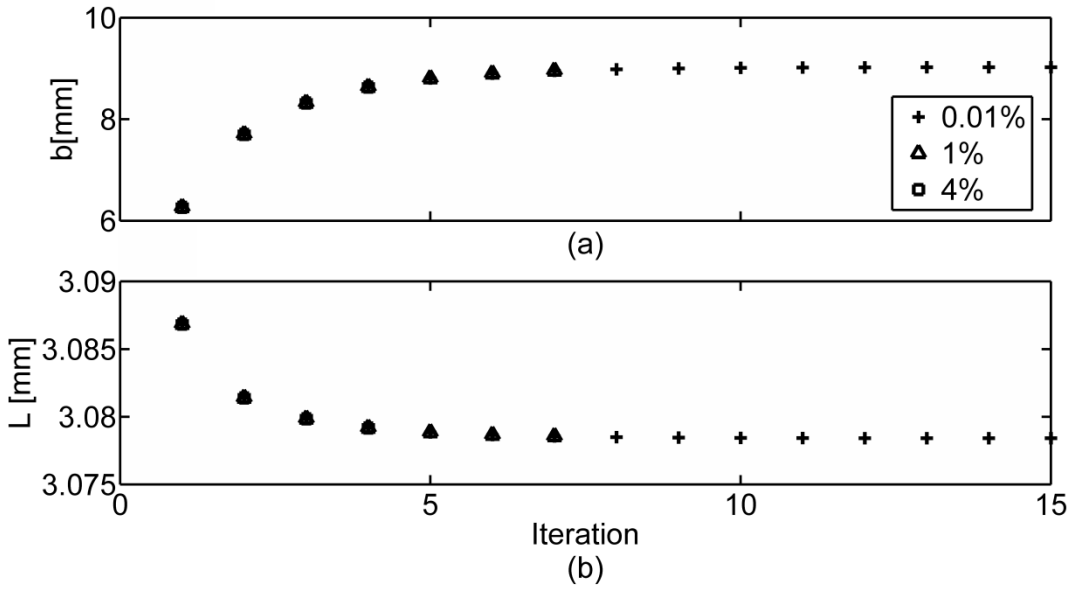

Figure 4-7: Convergence of b and L at 1000 RPM when computing the lobes shown in Figure 4-6

Another issue should also be resolved before conducting the comparisons with [33], namely the convergence tolerance allowed in the iterative procedure. Figure 4-7shows the convergence of the width of cut *b* and wave length *L* for a point at 1000 RPM on the upper bound lobes in Figure 4-6. The criterion used was for the percentage change in *b* in two subsequent iterations not to exceed a set value. The figure shows the effect of tightening the tolerance from 4% to 1% to 0.01%. It shows that 1% is sufficient, that insignificant improvement was gained by using 0.01 %, and thus 1% was chosen as the convergence tolerance. Figure 4-7shows that it took only 7 iterations for *b* and *L* to stabilize.

An important test of the proposed method is to compare it with the time domain simulation. In the time domain simulation, the nonlinear nature of the indentation pulse is treated directly, while in the proposed method the nonlinear pulse is replaced by an equivalent viscous damper. The test is now described by comparing with the lobes in Figure 4-9. The results of this simulation are presented in Figure 3-8 to explain finite amplitude stability qualitatively. However, they are repeated here to compare the results with the developed stability lobes, quantitatively. The simulations were conducted at 1000 RPM for three depths of cuts: *b*=0.5, 0.7 and 1.0 mm. The results of simulations are shown in Figure 4-8. For *b*=0.5mm, which is below the stability lobes, the vibration dies down to zero. For *b*=1.0 mm, which is above the upper stability lobes, the vibration amplitude stabilizes at 0.035 mm, which is equal to A_{cr}. For *b*=0.7mm, the vibration stabilizes at 0.02 mm. As a matter of

fact, the point at 0.7 mm width of cut is close to the fixed amplitude stability lobes shown in Figure 4-9 that were established at A_s =0.02 mm. This test demonstrates the viability of employing the equivalent damping approach in establishing the lobes from the frequency domain and establishing lobes at a particular amplitude of vibration.

Having demonstrated the accuracy of the iterative approach, it is also important to compare the times needed for the different methods of computing the stability including process damping: time domain simulation, iterative approach using the detailed computation method described in sections 3.2, and the iterative approach using the quick computation method of section 3.3. On a PC with a 2.2 GHz processor, it took three hours to compute the steady state vibration of case (b) in Figure 4-8 in the time domain simulation using 36,000 steps/revolution; it took ten minutes to compute one single lobe at a frequency resolution of 0.5 Hz using the detailed method; and it took only two seconds to compute the entire, upper or lower, bound stability lobes using the quick method. This is a drastic reduction in computation time.

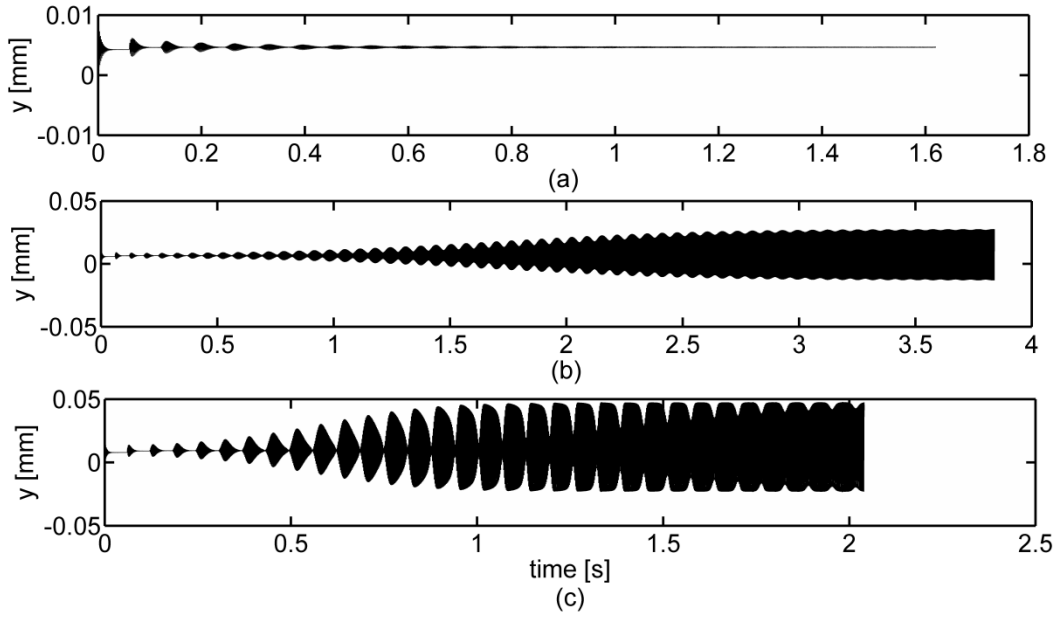

Figure 4-8: Tool vibration from numerical simulations in the time domain at 1000 RPM and: a) b=0.5 mm, fully stable, (b) b=0.7 mm, finite amplitude stability at A_s =0.02 mm, and (c) b=1.0 mm, fully unstable (Repeated from Chapter 3)

Figure 4-9 shows the upper and lower bound stability lobes established using the current procedures and those established using the empirical damping model of Altintas [33]. Recall that the

damping factor in [33] was determined from harmonic excitation at amplitude of 0.035mm. Accordingly, this coefficient would be most accurate if the vibration amplitude during cutting is also 0.035mm, as it could lead to inaccuracies at other amplitudes. In the present case, the feedrate is 0.05 mm/rev, and A_{cr} will be close to 0.035 mm. This makes the comparison at this feedrate between [33] and the upper bound lobes associated with A_{cr} more meaningful. Figure 4-9 shows the lobes established using C_p to be higher, especially below 1500 RPM, than the upper bound lobes established using the procedure developed in this work. This difference could be attributed to the fact that, in our procedure, the indentation of the tool into the workpiece is considered to be the only source of process damping, whereas the empirical model includes all potential sources. The results of cutting tests conducted in [33] are also included in Figure 4-9, where + designates cases that were considered unstable and o designates those considered stable. It is interesting to see that four of the unstable cases are below the empirical lobes but only two of them are below the upper bound lobes. Figure 4-9 also shows the lower bound lobes in thin line. It shows four experimental cases that were judged stable to be above these lobes. Since it was not mentioned in [33] how the stability condition was recognized, it is difficult to make a reasonable conclusion in terms of accuracy of the lobes established using the indentation equivalent damping and those using empirically determined damper. For instance, some of the points within the upper and lower lobes could be cases of finite amplitude stability that were misclassified one way or the other. To illustrate this point, lobes at fixed amplitude of 0.01 mm are also included in Figure 4-9. Two of the cases considered to be stable are below these lobes, with a third point being close to the border.

Further comparisons with time domain simulations are given in Figure 4-10(a). The objective of this figure is to further prove that the analytical stability lobes can be established at specific amplitude of vibration, say A_s, other than those associated with the lower bound and $A_{cr.}$ The figure shows the lobes established at A_s= 10 μm over the speed range 500- 1400 RPM. The figure also shows the lobes at A_s = 20 μm, as well as the lower bound lobes for comparison. Four sets of points $(P_i, Q_i), i$ =1-4, are chosen above and below A_s=10 μm for time domain simulations. They are chosen at 550, 625, 750 and 1000 RPM. The widths of cut at these point sets are close to the corresponding widths on the lobes A_s=10 μm but none of them lies exactly on lobes themselves. It should be realized that the closer the test point gets to the analytical lobes the longer simulation times it takes for the vibration to stabilize at constant amplitude. Having the points exactly on the lobes would make the simulation time unmanageable. The simulation results are shown in Figure 4-10(b) for the four sets. The corresponding amplitudes of vibration at steady state are listed in Table 4-3. Also listed in Table 3 are

the widths of cut b_0's at the lower bound as well as the widths of cut b_{10}'s at the A_s = 10 μm lobes. From the table, it can be seen that the resulting amplitudes at the four sets of points, regardless of the differences in speed and width of cut, are indeed close to 10 μm. At 1000 RPM, the deviation in amplitudes from10 μm appears larger at P_4 and Q_4, 0.31 and 15.15 μm, respectively. At this speed, due to the large wavelength, the area between lower bound, A_s=10 μm, and A_s=20 μm is narrow, and the slightest shift in width of cut leads to large deviation in vibration amplitude. Figure 4-10(a) shows P_4 located closer to A_s=20 μm lobes, and its amplitude of 15.15 μm is thus closer to 20 μm, as it should be. Q_4 point on the other hand is below the lower bound and its vibration amplitude of 0.31μm is negligible compared to the vibration amplitudes computed at the other test cases.

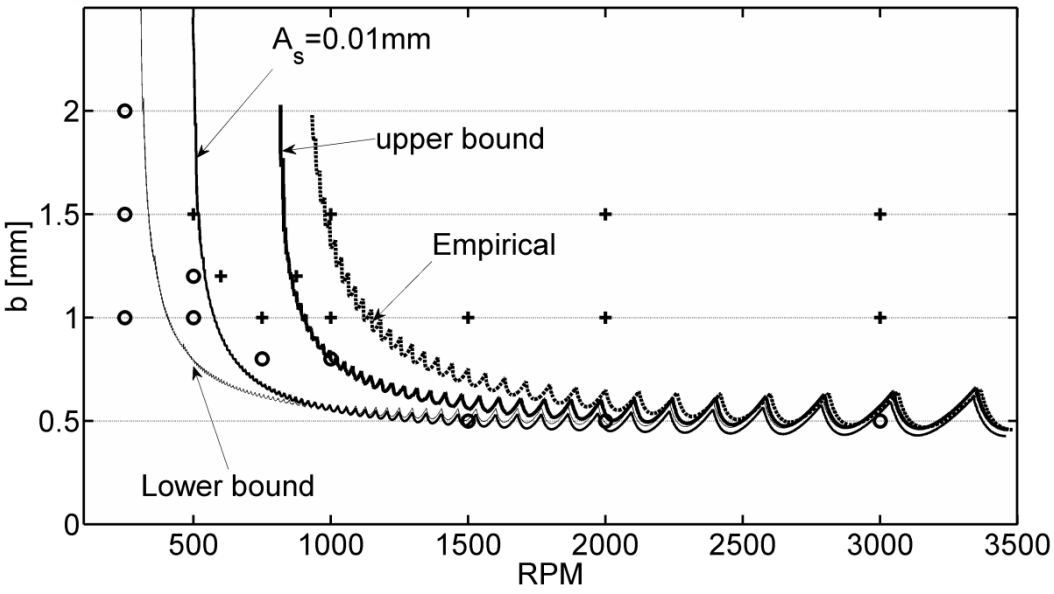

Figure 4-9: Stability lobes computed using the empirical damping model in [33] and the developed iterative method: Experimental results reproduced from [33]: + judged fully unstable, o judged fully stable

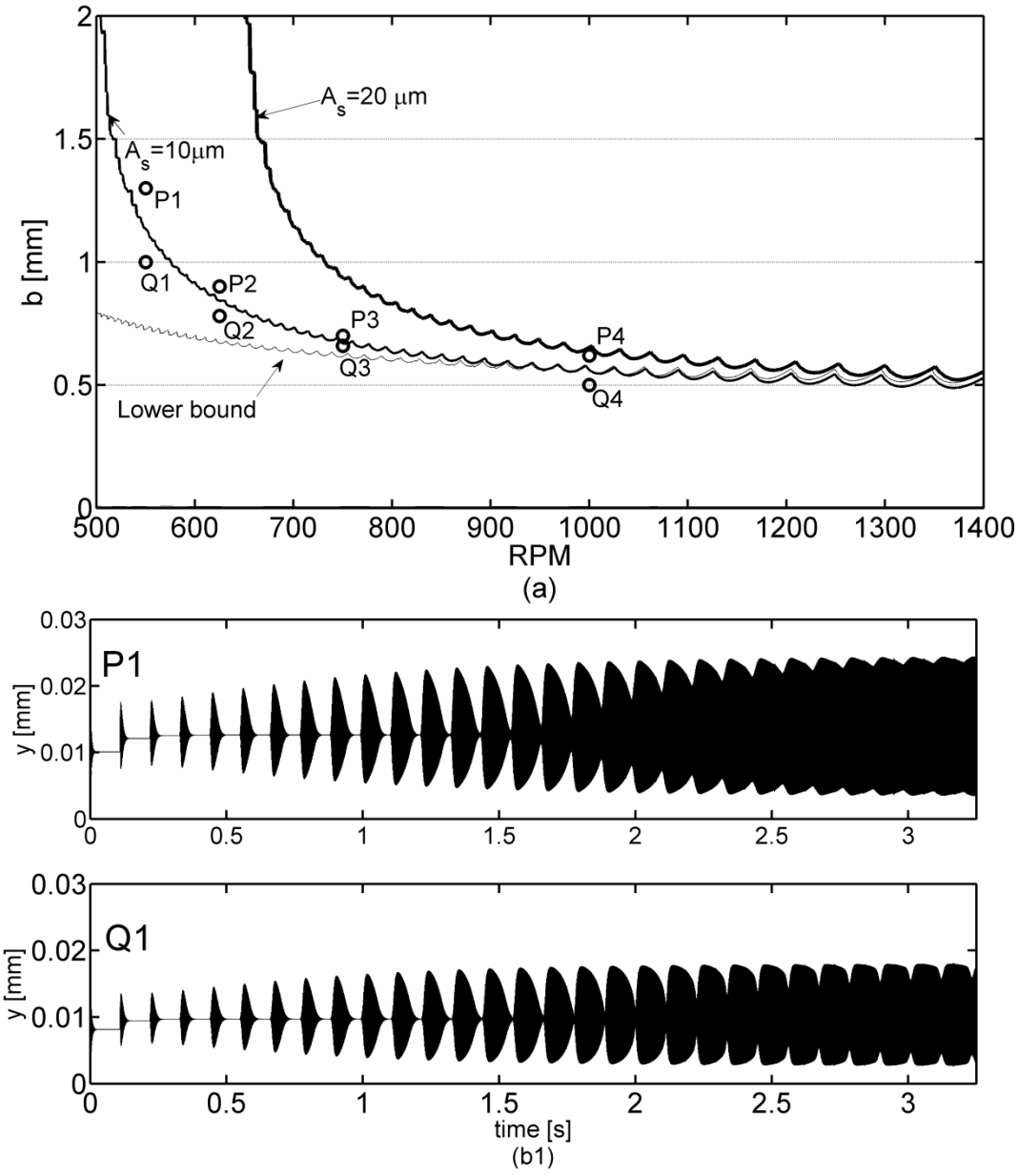
b [mm]
RPM
A_s=20 μm
A_s=10μm
P1
Q1
P2
Q2
P3
Q3
P4
Q4
Lower bound
(a)
P1
Q1
y [mm]
time [s]
(b1)

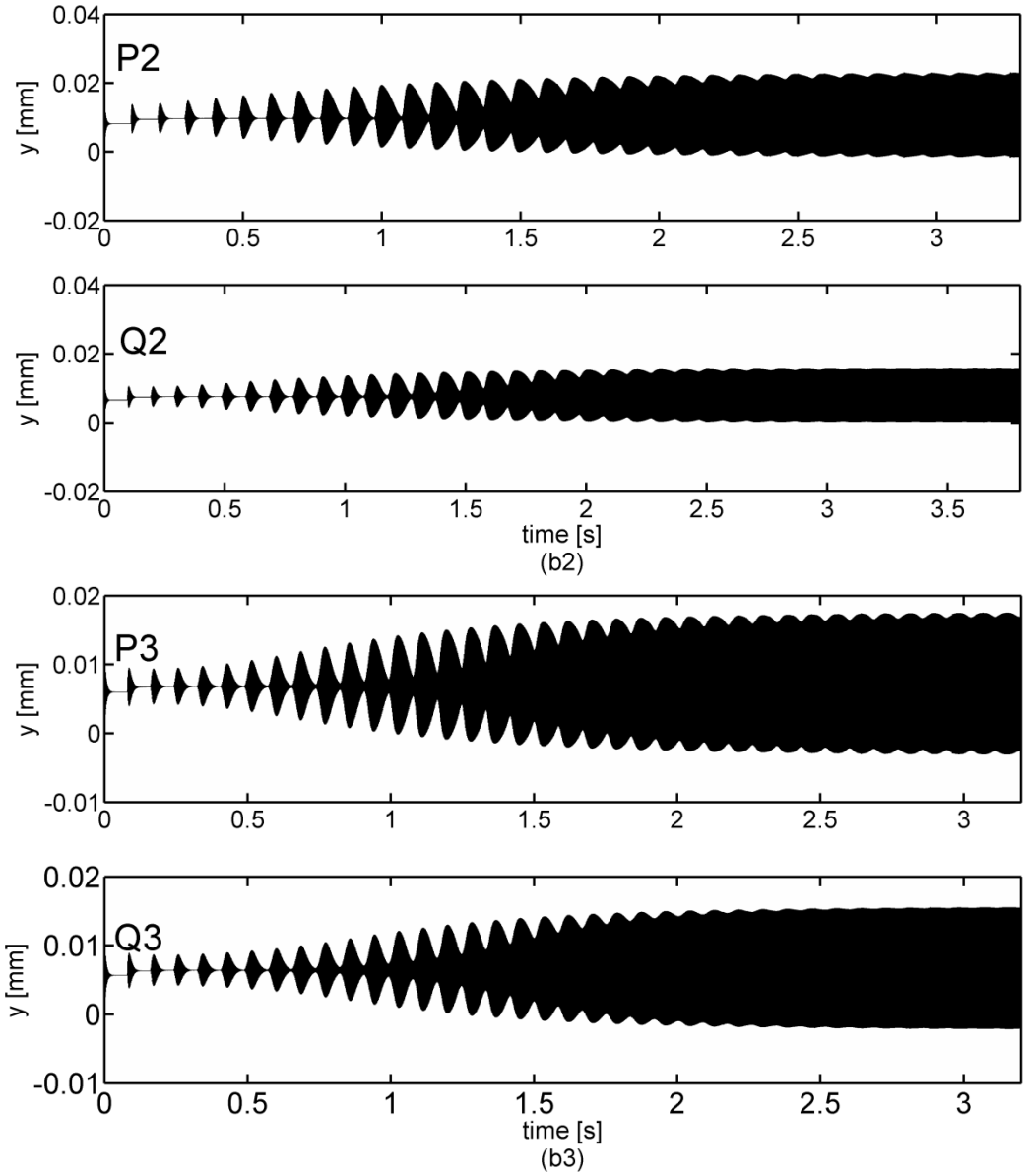
P2
Q2
P3
Q3
y [mm]
time [s]
(b2)
(b3)

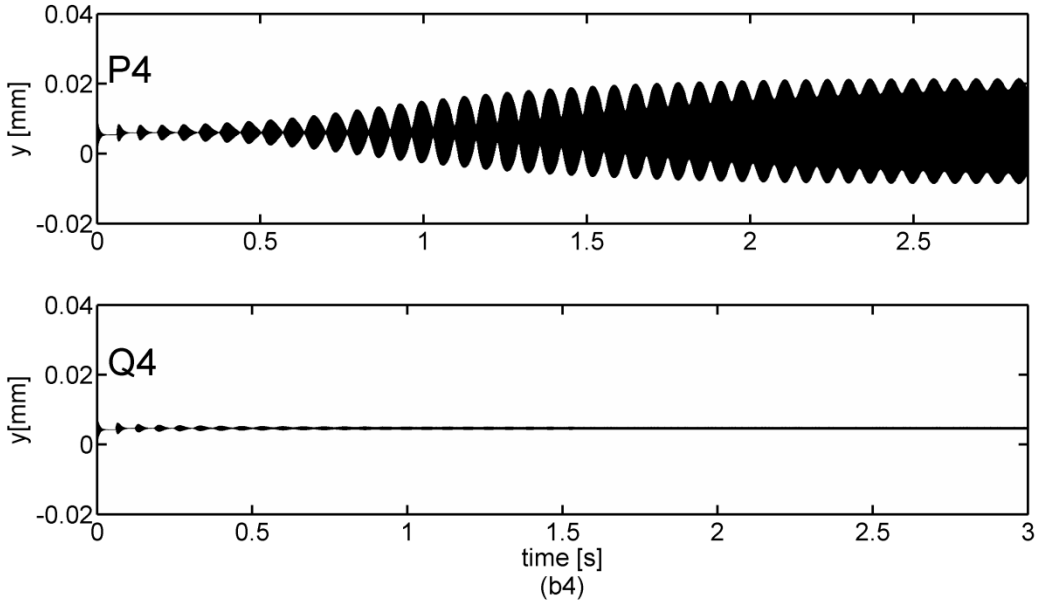

Figure 4-10: a) A_s=10 µm and A_s=20 µm specific amplitude, and lower bound analytical lobes; b) numerical simulation results at P_i and Q_i , i=1..4

Table 4-3: Widths of cut at points P and Q and their corresponding amplitudes of vibration obtained from time domain simulations.

		Width of cut [mm]				Vibration amplitude [µm]		
I	RPM	b_0	Q_i	b_{10}	P_i	Q_i	A_{10}	P_i
1	550	0.7266	1.00	1.1350	1.30	7.65	10	10.43
2	625	0.6698	0.78	0.8421	0.90	7.85	10	12.25
3	750	0.6166	0.66	0.6691	0.70	8.85	10	10.28
4	1000	0.5607	0.50	0.5611	0.62	0.31	10	15.15

Presented next are experimental results to further verify the proposed method of constructing the stability bands.

4.4 Experimental Verification

The experimental setup of Section 3.5 is used in this section to verify the accuracy of the established stability boundaries. The force signal was utilized in assessing the status of the cut. The experiments were conducted at moderate speeds mainly to allow comparisons between the sharp and

worn tools. Such comparisons are important in demonstrating the viability of the iterative approach to establishing the lobes analytically including process damping.

The cutting force coefficients in the feed direction were estimated from stable cutting to be: K_r= 1800, 1330 and 1130 MPa for s_t=0.035, 0.05 and 0.075 mm/rev, respectively. Also for each feedrate, two different tools were used in the experiments, a sharp and a worn tool with W=0.08 mm wear land. For the sharp tool, a wear land of W=0.04 mm was assumed to account for the tool edge radius.

The boundary lobes calculated for each feedrate are shown in Figure 4-11, Figure 4-12, and Figure 4-13. Each figure consists of two subfigures: (a) for the worn tool and (b) for the sharp tool. These figures also show the results of the experimental cutting tests: + for fully unstable, o for fully stable, and Δ for finite amplitude stability. When the measured cutting force signal at steady state stayed above zero, the cut was judged to be either fully stable or at a state of finite amplitude stability. It was fully stable when the force signal showed no appreciable oscillations; otherwise, it was a state of finite amplitude stability. When the measured steady state force dropped to zero at some portion of its vibration cycle, the cut was judged fully unstable. Zero cutting force is an indicator of tool/workpiece separation due to vibration amplitude exceeding A_{cr}. In this case, the produced chip is broken into small pieces due to the periodic tool/workpiece disengagement. While the chip is continuous for stable and finite amplitude stability cases, in the latter case, it shows significant thickness variation. Examples of measured forces and their spectra as well as photographs of the chip can be found in the investigation of the nonlinearity of process damping reported in Section 3.5.

In Figure 4-11, for s_t=0.035 mm/rev, the lower and upper bound stability lobes are close to each other with a narrow region of finite amplitude stability. For s_t=0.05 mm/rev in Figure 4-12, the finite amplitude stability region is wider than that associated with the 0.035 feed in Figure 4-11. Now, cases of finite amplitude stability can be seen between the upper and lower bound lobes, even for the sharp tool. For s_t=0.075 mm/rev, in Figure 4-13, the region of finite amplitude stability is even larger than that at 0.05 mm/rev. Although the cutting test results are inconsistent with the calculated lobes in some cases, the agreement is good between experimental measurements and the analytical lobes. The discrepancy between experimental points and calculated lobes is more visible for s_t=0.035. It seems that, at this low feedrate the contribution of other factors (e.g., workpiece runout) cannot be ignored in determining the stability of the cut.

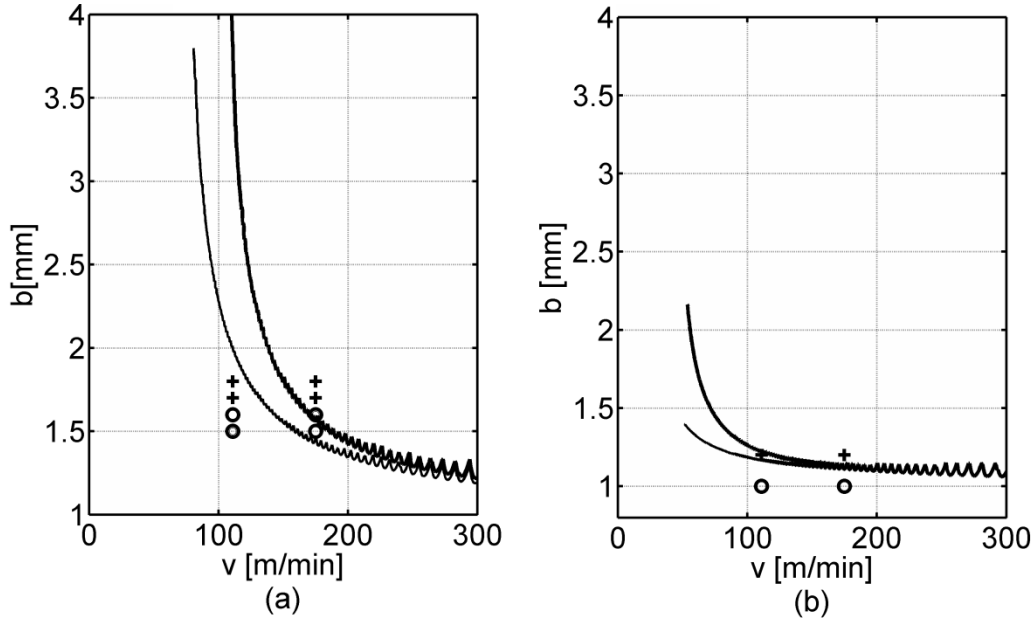

Figure 4-11: Upper bound (thick line) and lower bound (thin line) lobes for S_t=0.035 mm/rev; cutting test results: + fully unstable, o fully stable, Δ finite amplitude stability

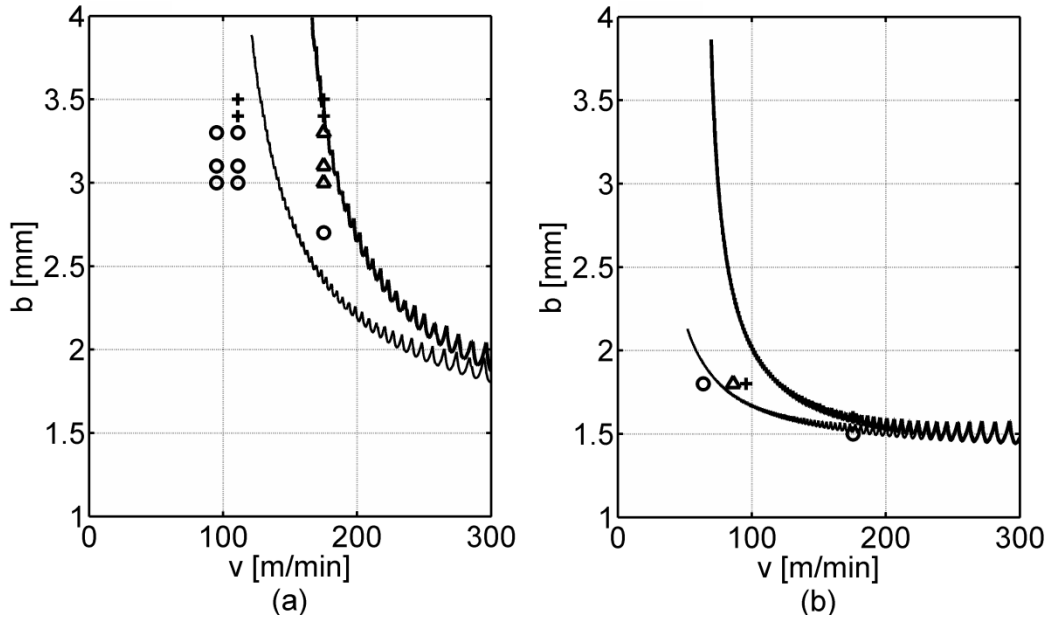

Figure 4-12: Upper bound (thick line) and lower bound (thin line) lobes for S_t=0.05 mm/rev; cutting test results: + fully unstable, o fully stable, Δ finite amplitude stability

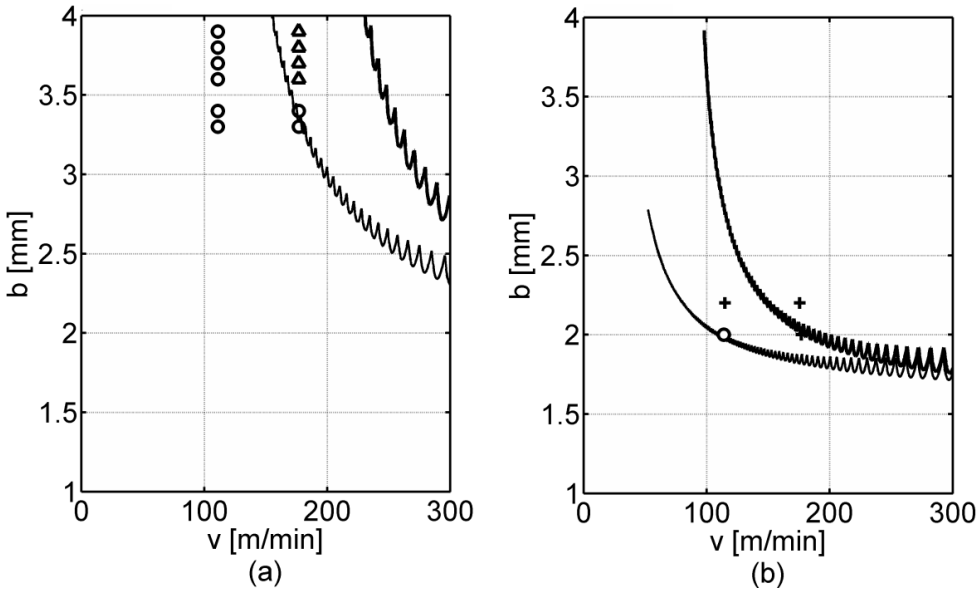

Figure 4-13: Upper bound (thick line) and lower bound (thin line) lobes for S_t=0.075 mm/rev; cutting test results: + fully unstable, o fully stable, Δ finite amplitude stability

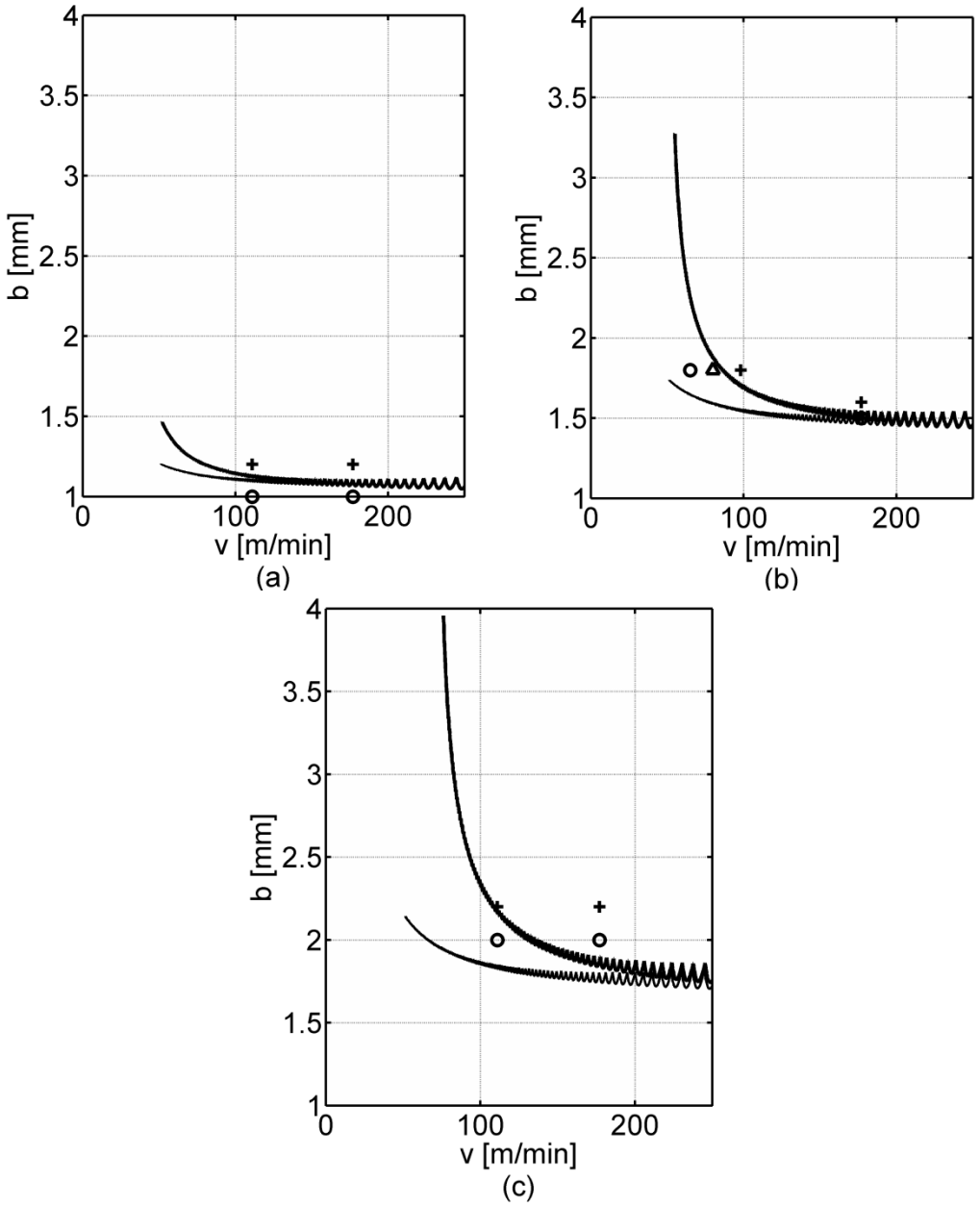

Figure 4-14: Upper and lower stability lobes computed for a sharp tool assuming W=0.03 mm at a) s_t=0.035 mm/rev, b) s_t =0.05 mm/rev, and c) s_t =0.075 mm/rev

To explain some of the discrepancies observed above with the sharp tools, recall that a small wear land W=0.04 mm was assumed to account for the effect of cutting edge radius. As observed by Budak and Tunc [41], the existence of edge radius affects the chip formation process as well as the process damping. Moreover, the edge radius results in a static indentation component [34] that operates along

the full length of the surface undulation, $0<x<L$, whereas in the presented model, only the dynamic part in the range $L/4<x<3L/4$ is considered. For the sharp tool in our experiments, this radius was measured at 50 μm. Further work is needed to better integrate the effect of the edge radius into the stability lobes computations. Nevertheless, the assumption of having a small wear land was based on observations of cutting tests conducted at high speed when compared with the analytical lobes established with and without wear. The 0.04mm value leads to reasonable results, except for the cases mentioned above. However, the stability lobes were redone assuming W=0.02 and 0.03 mm. The 0.02mm led to lower stability lobes that were in bigger disagreement with the experimental results, while W=0.03 mm, on the other hand, led to better agreement in several cases. Figure 4-14(a), (b) and (c) show the lobes associated with the sharp tools, re-established with W=0.03 mm for the three feederates 0.035, 0.05 and 0.075 mm, respectively. By comparing these figures with those established with W=0.04 mm, the following observations can be made.

- In Figure 4-14(a), the fully unstable case at b=1.2mm and v=111 m/min is now above the upper bound stability lobes as it should be, instead of being in the region of finite amplitude stability in Figure 4-11(b).
- In Figure 4-14(b), the fully unstable case at b=1.8mm and v=97m/min is now above the upper bound stability lobes, as it should be, instead of being in the region of finite amplitude stability in Figure 4-12(b). However, the fully stable case in Figure 4-12(b) has now moved inside the finite stability region in Figure 4-14(b).
- In Figure 4-14(c), the two fully unstable cases at b=2mm, v=177m/min, b=2.2mm and v=177min are now above the upper bound stability lobes, as they should be. However, the case of fully stable in Figure 4-13(b) has now moved inside the region of finite amplitude stability in Figure 4-14(c).

The above discussion shows W in the range 0.03-0.04mm accounts reasonably well for the effect of edge radius. It is one potential source of uncertainty. Another source of uncertainty in establishing the lobes including process damping, whether for sharp or worn tools, is the value of the specific indentation coefficient K_{sp}. In the current work, $K_{sp} = 4\times10^5$ N/mm^3 was chosen for AISI 1018 steel. This value was obtained from [34], and as could be seen from the experimental results described herein, it led to good agreement with the analytical stability lobes. Budak and Tunc [41] conducted chatter experiments and in a reverse approach estimated K_{sp} at 0.7×10^5 N/mm^3 for AISI 1050 steel. The physical and mechanical properties of 1018 and 1050 are close, which would not explain the

large difference between the two values. Nevertheless, one must recognize potential sources of uncertainty and assess the impact of changing values of some parameters on the resulting stability. The iterative procedure developed here should help assess such impact, as it is concise and fast.

4.5 Summary

An iterative procedure was developed to establish the stability lobes analytically including process damping. Upper and lower bound stability lobes were established instead of the traditional stability lobes that represent a single boundary between stable and unstable regions. Having two boundaries of stability allowed having a region in between where the process is in a state of finite amplitude stability. In this way, the effect of process damping nonlinearity was preserved. It was also shown that stability lobes can be established for specified amplitudes of vibration. The developed approach produced the same results obtained from time domain simulations and agreed reasonably well with cutting experiments. The developed approach relied on replacing the nonlinear damping pulse by an equivalent viscous damper. A compact expression of this damper was developed, whose coefficients were computed from tables. While a large number of computations were conducted to compile these tables, further work will be needed to expand the tables to cutting speeds lower than those covered here; further work will also be need to determine more values of tool clearance angle and larger amplitudes of vibration. A drastic reduction in computations time was achieved with the developed iterative approach when compared with time domain simulations. On a PC with 2.2 GHz processor, it took three hours of simulation time to compute the steady state vibration of case (b) in Figure 4-8, but only two seconds of computation time to establish the entire stability lobes over a wide range of cutting speeds. This drastic time reduction was the main achievement of this work.

In the next chapter, the developed damping model will be employed in time and frequency domain methods of calculating the stability lobes in milling.

Chapter 5
Stability Lobes in Milling Including Process Damping

In this chapter, the equivalent viscous model of process damping is integrated into two well accepted methods of calculating the stability lobes in milling: the Multi-Frequency Solution (MFS) and the Semi Discretization Method (SDM). Assessing the performance of the two methods is conducted using time domain simulations. It is shown that the Semi Discretization Method provides accurate results over the whole tested range of cutting speed, whereas higher harmonics are required to achieve the same accuracy when applying the Multi Frequency Solution at low speeds.

Moreover, the finite amplitude stability is shown to occur in milling, as well. The amplitude dependent equivalent viscous damper model is used in SDM to calculate the upper stability lobes. A set of cutting experiments are conducted to verify the accuracy of the predicted upper and lower stability lobes.

The 2DOF dynamic model used in this investigation is described in the next section. Since numerical simulations are used to compare the performance of MFS and SDM, a brief description of the numerical simulation model is presented in Section 5.2. In this section, a more effective approach to identifying the onset of instability from the simulation results will be presented. The formulations and computation steps of MFS and SDM are given in Sections 5.3 and 5.4, respectively. Section 5.5 will present the results of examples conducted to compare the two approaches in establishing the lobes. Moreover, the effect of including higher harmonics in MFS and choosing a proper discretization size in SDM will be discussed in that section. In these examples, the cut is not highly interrupted (non-shallow immersion). It will be shown that the zero order MFS stability lobes agree well with the ones obtained from SDM at high cutting speeds. The two methods, however, disagree considerably at low speeds and high damping when the zero order is utilized. This disagreement diminishes by adding higher harmonics to MFS at the expense of longer simulation time. The occurrence of finite amplitude stability in milling is investigated in Section 5.6. Having demonstrated that finite amplitude stability also happens in milling, computing the lower and upper stability lobes in milling is addressed in the subsequent section. Experimental verifications of upper and lower stability lobes will be presented in Section 5.7. These experiments show the close agreement between the lobes from SDM and the actual cutting tests.

5.1 Dynamic Model

The 2DOF system, shown in Figure 5-1, is used to describe the dynamics of the vibratory model. The modal stiffness, mass and damping in the cutting, Y, and feed, X, directions, K_y, K_x, M_y, M_x, C_y and C_x, are usually obtained from experimental modal analysis. The tool has N cutting edges and the immersion angle of the jth tooth, φ_j, $j=1..N$, is measured clockwise from the Y direction. One can express the immersion angle as a function of time and tool rotational speed, Ω, as

$$\varphi_j = \Omega t + (j-1)\frac{2\pi}{N} \qquad (5.1).$$

The cutting force components on the jth tooth are F_r and F_t in the radial and tangential directions, respectively. The forces arise due to the shearing and ploughing mechanisms. Therefore, the tangential and radial cutting forces are composed of the shearing, with subscript s, and ploughing with subscript p, according to:

$$F_t(t) = F_{ts}(t) + F_{tp}(t); F_r(t) = F_{rs}(t) + F_{rp}(t) \qquad (5.2)$$

The shear forces are computed from:

$$F_{ts} = K_t g(\varphi_j) bh, F_{rs} = K_r F_{ts}; g(\varphi_j) = \begin{cases} 0 & \varphi_j > \varphi_{ex} \ or \ \varphi_j < \varphi_{st} \\ 1 & \varphi_{st} < \varphi_j < \varphi_{ex} \end{cases} \qquad (5.3)$$

where b is the axial depth of cut and K_t and K_r are the tangential and radial cutting force coefficients measured experimentally. In Equation (5.3), $g(\varphi_j)$ is a window function between the tool engagement start and exit angles: φ_{st} , and φ_{ex} . In Figure 5-1(b), the uncut chip thickness consists of the part produced by the tool rotation and feed motion, and the other part by the regeneration of surface waves:

$$h(t) = s_t \sin(\varphi_j) + (r(t) - r(t-T)) \qquad (5.4)$$

where $r(t)$ is the tool displacement in the radial direction, and T is the tooth passing period:

$T = 2\pi / N\Omega$.

In Equation (5.4), negative chip thickness implies disengagement of the tool from the workpiece due to the vibration amplitude reaching high values. In this case, the chip thickness is actually zero. The tangential and radial forces are divided into “harmonic”, F^H, and “regenerative”, F^{reg}, parts as follows:

$$F_{ts} = F_{ts}^{H} + F_{ts}^{reg}$$
$$F_{ts}^{H} = g\left(\varphi_j\right) K_t b s_t \sin\varphi_j ; F_{ts}^{reg} = g\left(\varphi_j\right) K_t b\left(r(t) - r(t-T)\right) \tag{5.5}$$

The regenerative part is associated with the vibration in subsequent cuts, while the harmonic part is associated with the rotational angle and the feed per tooth. It is called "harmonic" because the static force "pulse" could contain a significant number of harmonics, depending on the cut geometry.

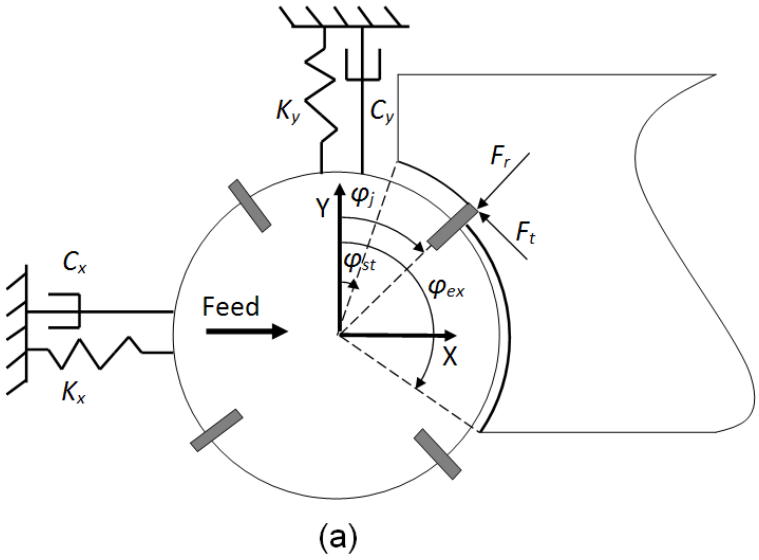

(a)

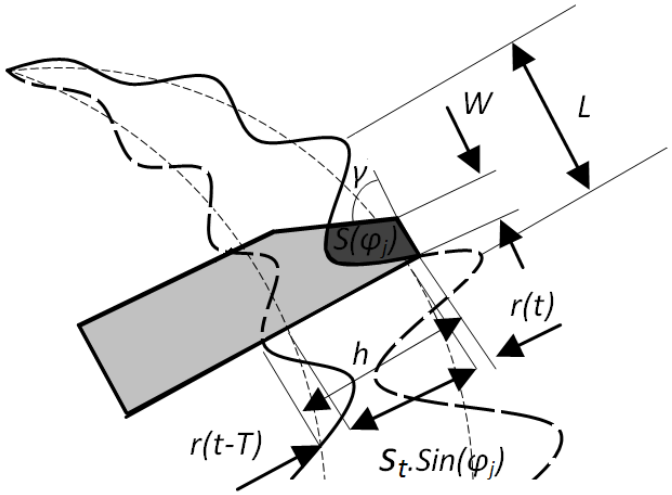

(b)

Figure 5-1: (a) 2DOF vibratory model, (b) uncut chip thickness, and indentation of undulations under the flank face of the tool

The ploughing force is calculated using Wu's indentation model [34], where the radial ploughing force is assumed to be proportional to the volume, V, of the material extruded underneath the flank face:

$$F_{rp} = g\left(\varphi_j\right) K_{sp}.V; V = bS \tag{5.6}$$

where K_{sp} is the specific indentation force; it is measured experimentally [39, 43] or computed analytically [34]. The tangential ploughing force is modeled using the Coulomb friction:

$F_{tp} = \mu F_{rp}$,

where μ is the Coulomb friction coefficient. In Equation (5.6), S, shown in Figure 5-1(b), is the area of the cross section of the extruded material. Following the development in Chapter 4, the process damping effect is represented by an equivalent linear viscous damper. It is expressed as:

$$F_{rp} \approx C_{eq}\dot{r}; C_{eq} = \frac{K_{sp} b C_d}{v} \tag{5.7}$$

where v is the tangential velocity and C_d is designated as the "shape damping factor", since it is computed from the geometrical parameters of the tool and surface undulations. In this section, small amplitude vibration will be assumed, and thus C_d will be obtained from:

$C_d = 0.25W^2$

where W is the wear land width shown in Figure 5-1(b). This leads to the following expression for the equivalent damper:

$$C_{eq} = K_{sp} b \ \frac{W^2}{4v}$$

The small amplitude vibration assumption is justified in establishing stability boundaries below which the vibrations die down. Above these boundaries, the vibrations grow and eventually stabilize at finite amplitudes. In fact, such boundaries are commonly used in the literature to define stability limits.

The summation of radial and tangential forces acting on all teeth engaged in the cut results in the total cutting forces acting on the tool in the X and Y directions:

$$\mathbf{F} = \begin{Bmatrix} F_x \\ F_y \end{Bmatrix} = \sum_{j=1}^{N} \mathbf{T}_j \begin{Bmatrix} F_t \\ F_r \end{Bmatrix}; \ \ \mathbf{T}_j = \begin{bmatrix} -\cos\varphi_j & -\sin\varphi_j \\ \sin\varphi_j & -\cos\varphi_j \end{bmatrix} \tag{5.8}$$

Substituting the chip thickness from Equation (5.4) in the mechanistic force model of Equation (5.3), the radial and tangential shearing forces are obtained in terms of tool deflections in the radial

direction. Also, the ploughing forces are obtained in terms of the tool radial velocity in Equation (5.7). The radial deflection of the tool can be expressed in terms of its components in the X and Y directions:

$$r = \mathbf{r}_j \mathbf{p}; \mathbf{r}_j = \begin{bmatrix} \sin\varphi_j & \cos\varphi_j \end{bmatrix}; \quad \mathbf{p} = \begin{bmatrix} x(t) \\ y(t) \end{bmatrix} \tag{5.9}$$

Therefore, one can express the tangential and radial forces in terms of tool deflections in the X and Y directions as:

$$\begin{bmatrix} F_t \\ F_r \end{bmatrix} = g(\varphi_j) K_t b \begin{bmatrix} 1 \\ K_r \end{bmatrix} \mathbf{r}_j \left(\begin{bmatrix} s_t \\ 0 \end{bmatrix} + \mathbf{p}(t) - \mathbf{p}(t-T) \right) + g(\varphi_j) C_{eq} \begin{bmatrix} \mu \\ 1 \end{bmatrix} \mathbf{r}_j \dot{\mathbf{p}}(t) \tag{5.10}$$

Substituting Equation (5.10) into Equation (5.8), the total cutting forces are obtained:

$$\begin{aligned} &\mathbf{F} = b\mathbf{A} \left(\begin{bmatrix} s_t \\ 0 \end{bmatrix} + \Delta\mathbf{p} \right) + \mathbf{B}\dot{\mathbf{p}} \\ &\Delta\mathbf{p} = \mathbf{p}(t) - \mathbf{p}(t-T) \\ &\mathbf{A}_j = g(\varphi_j) K_t \mathbf{T}_j \begin{bmatrix} 1 \\ K_r \end{bmatrix} \mathbf{r}_j; \quad \mathbf{B}_j = g(\varphi_j) C_{eq} \mathbf{T}_j \begin{bmatrix} \mu \\ 1 \end{bmatrix} \mathbf{r}_j; \quad \mathbf{A} = \sum_{j=1}^{N} \mathbf{A}_j, \quad \mathbf{B} = \sum_{j=1}^{N} \mathbf{B}_j \end{aligned} \tag{5.11}$$

Having calculated the cutting forces, the governing equation of the system is expressed as:

$$\begin{aligned} &\mathbf{M}\ddot{\mathbf{p}} + \mathbf{K}\mathbf{p} + \mathbf{C}\dot{\mathbf{p}} = b\mathbf{A} \left(\begin{bmatrix} s_t \\ 0 \end{bmatrix} + \Delta\mathbf{p} \right) + \mathbf{B}\dot{\mathbf{p}} \\ &\mathbf{M} = \begin{bmatrix} M_x & 0 \\ 0 & M_y \end{bmatrix}; \mathbf{K} = \begin{bmatrix} K_x & 0 \\ 0 & K_y \end{bmatrix}; \mathbf{C} = \begin{bmatrix} C_x & 0 \\ 0 & C_y \end{bmatrix} \end{aligned} \tag{5.12}$$

which is a linear DDE with time varying coefficients.

Presented next is a procedure to accentuate the identification of the onset of process instability from the results of time domain simulations of Equation (5.12).

5.2 Numerical Simulation

In this part, Wu's indentation force model, Equation (5.6), is used in a numerical scheme to simulate the tool vibration. The 2DOF vibratory system and the cutting force model described in the previous section is used in the simulation.

The total simulation time is divided into finite time intervals of Δt. The tool deflection at each time step, $\mathbf{p}_q = \mathbf{p}(q\Delta t)$, is then calculated by employing the cutting forces computed at the previous time step in Equation (5.12) . The entire procedure is described in the following steps:

1- Divide the tool revolution period into N_t divisions: $\Delta t = NT/N_t$.

2- Record the undulation height at each discrete point in a vector of N_t elements, **z,** assuming that all of the elements of **z** are zero at q=0. Also, assume that the tool vibration starts from

$$\mathbf{p}_0 = \dot{\mathbf{p}}_0 = 0$$

3- At each time step, q, calculate the immersion angle for each tooth, $j=1..N$, from

$$\varphi_j = q\Delta t\Omega + (j-1)\frac{2\pi}{N}$$

4- If $\varphi_{st} < \varphi_j < \varphi_{ex}$, calculate the regenerated chip thickness as $\mathbf{rp}_q$-z_n, where z_n is the undulation height associated with φ_j and extracted from vector **z**. Add the feed produced chip thickness, $s_t \sin(\varphi_j)$, to the regenerated part to obtain the total chip thickness, h. Also, calculate the indentation force using the numerical search explained in Section 5.2.1. If $\varphi_{st} > \varphi_j$, $\varphi_j > \varphi_{ex}$, or $h<0$, then the total cutting forces are zero.

5- Substitute the calculated chip thickness and extruded volume in Equation (5.5) and Equation (5.6), respectively, to obtain F_t and F_r. Then, resolve them into X and Y directions, and add them together for $j=1..N$ to obtain the total cutting forces at time step q.

6- Having calculated the total cutting forces at time step q, the tool deflection at the following time step $q+1$ is estimated from

$$\ddot{\mathbf{p}}_q = -\mathbf{M}^{-1}\mathbf{K}\mathbf{p}_q - \mathbf{M}^{-1}\mathbf{C}\dot{\mathbf{p}}_q + \mathbf{F}_q$$
$$\dot{\mathbf{p}}_{q+1} = \ddot{\mathbf{p}}_q \Delta t$$
$$\mathbf{p}_{q+1} = \dot{\mathbf{p}}_q \Delta t .$$

Update the undulation height in the corresponding element of vector **z**. If $h>0$, then update it with $\mathbf{rp}_{q+1}$. If $h<0$, deduct $s_t \sin(\varphi_j)$ from the current height.

5.2.1 Computation of Extruded Volume

The volume of the extruded material is calculated from the shaded area shown in Figure 5-1(b) and the axial depth of cut, b. The shaded area is bounded by the tool flank face and the workpiece surface undulations. This area is calculated at each simulation time step numerically. Figure 5-2 illustrates how the shaded area is calculated. The tool edge is at point A, whereas B is the point on the surface undulation generated by the tool edge in the previous time step. The corresponding point on the flank

is point C. The distance d = (B – C) is checked; if greater than zero, then there is penetration and the area ABC is calculated and multiplied by the axial depth of cut. The points $B^{-2}B^{-1}$, etc. are the points on the workpiece surface at (t-2Δt), (t-3Δt), .., where Δt is the simulation time step. The corresponding points on the flank face are $C^{-2}C^{-1}$, ... The elemental shaded area, say $B^{-2}B^{-1}$ $C^{-1}C^{-2}$, is calculated from $B^{-2}B^{-1}C^{-1}C^{-2} = \left(\frac{d^{-1}+d^{-2}}{2}\right)R\Delta\varphi$, where R is the radius of the cutter, and $\Delta\varphi$ is the incremental cutter rotational angle corresponding to Δt. Note that $R\Delta\varphi$ is an approximation of the length of the elemental area, which necessitates that $\Delta\varphi$ be kept small. This would mean the simulation takes longer when taking into account process damping. For more details on computing the indentation area, also see [37].

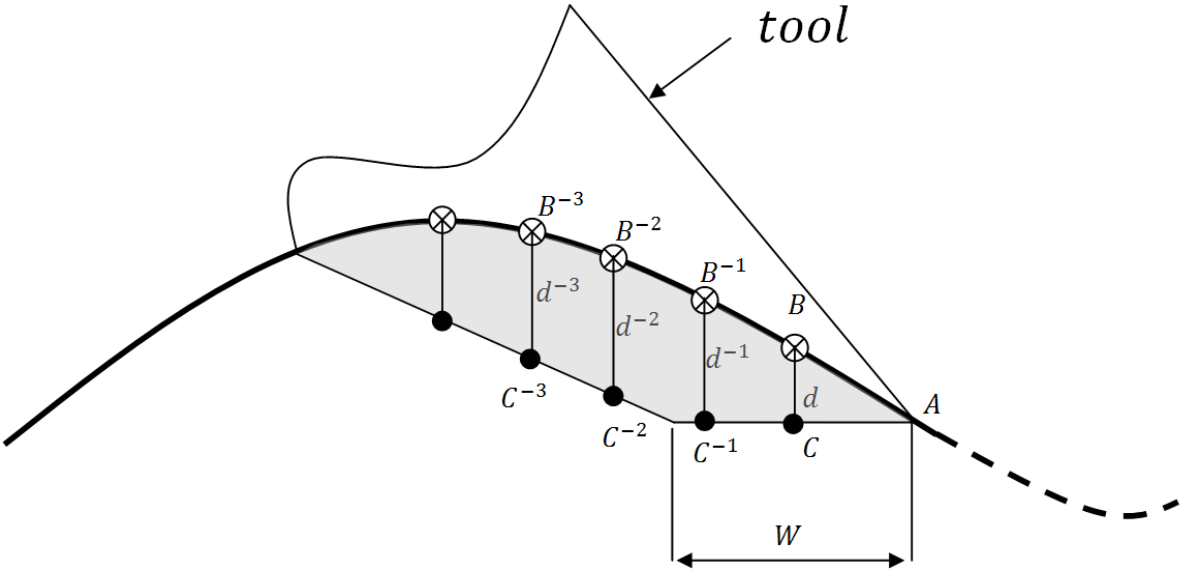

Figure 5-2: Calculation of the extruded material volume

We should mention that the indentation forces are applied when the cutting tooth is penetrating into the workpiece, and that they are zero when the tooth is moving out from the workpiece. The above model of process damping is a simplification of a more complicated interaction between the cutting edge, the flank face and the workpiece material. This interaction is highly dependent on the edge condition and, in particular, on tool wear.

5.2.2 Case Study

The parameters of the 2DOF system given in [25] will be utlized in the current simulations. The modal stiffnesses, natural frequencies and damping coefficients in the X and Y directions are:

$$K_x = 5.6\times10^6\, N/m, f_x = 603Hz, C_{x=}115.29N.s/m$$

$$K_y = 5.7\times10^6\, N/m, f_y = 666Hz, C_{y=}95.35N.s/m$$

The cutting force coefficients for the Aluminum workpiece are K_t=700 Mpa and K_r=0.07. The specific indentation force for Aluminum is reported at K_{sp}=1.5×10^5 N/mm^2 in [35]. The friction coefficient is 0.3. The tool is a 25.4mm diameter endmill with three straight (nonhelical) teeth. The clearance angle of the tooth is 7^0. The simulation is conducted at feedrate s_t=0.07 mm/tooth, ½ immersion up-milling, and speed 1500 RPM. Two different axial depths of cut are employed: 2 and 2.5 mm. The total tool displacements in the feed direction for both depths of cut are shown in Figure 5-3(a) and(b). All traces are normalized by the corresponding axial depth of cut. These normalized displacements seem to be the same at b=2 and 2.5 mm. However, by looking closely at the components of the total displacement, a dramatic difference emerges. According to Equation (5.5), the cutting force, and consequently the total tool deflection, consists of the harmonic and regenerative parts:

$$\mathbf{p} = \mathbf{p}^H + \mathbf{p}^{reg}$$

The harmonic component, $\boldsymbol{P}^H$, is independent of tool vibration, and the regenerative part, $\boldsymbol{P}^{reg}$, determines the stability of the cut. $\boldsymbol{P}^{reg}$ is comprised of the vibrations in subsequent cuts. If the amplitude of $\boldsymbol{P}^{reg}$ dies down to zero, the system will be stable; otherwise, it will be unstable. To extract $\boldsymbol{P}^{reg}$ from the total displacement, the simulation is repeated by leaving out the regenerative part of the chip thickness. In other words, the simulation is run once to compute the total displacement $\boldsymbol{P}$, and a second time without the inclusion of the regenrative part of the chip, to obtain $\boldsymbol{P}^H$. $\boldsymbol{P}^{reg}$ is obtained by subtracting $\boldsymbol{P}^H$ from $\boldsymbol{P}$. This procedure was followed to obtain the normalized displacement components at the depths of cut b=2 and b=2.5 mm. They are shown in Figure 5-3(c) and (d). Now the difference between the two cases is clear: the regenrative component $\boldsymbol{P}^{reg}$ dies down to zero at b=2mm (it is a stable cut), while, on the other hand, $\boldsymbol{P}^{reg}$ grows at b=2.5 mm (it is an unstable cut). Eventually, $\boldsymbol{P}^{reg}$ stabilizes at a finite amplitude due to nonlinearities in the system [74].

Figure 5-4 shows the frequency spectra of the time traces shown in Figure 5-3. The triangles show the tooth passing frequency ω_s and its harmonics, the bold circle shows the chatter frequency, ω_c, and the thin circles indicate side bands at the tooth passing frequency around the chatter frequency, *e.g.*

$\omega_c \pm \omega_s$. The tooth passing frequency, 75 Hz, dominates the tool total vibration signals in Figure 5-4 (a) and (b). In (b), however, the chatter frequency at 643 Hz is also visible, albiet much smaller than the spectral line at the tooth-passing frequency. The situation is completely different when the spectra of the regenerative components in Figure 5-4(c) and (d) are examined. The distiction between the stable cut in (c), where the chatter frequency is hardly visible, and the unstable cut in (d), where the chatter frequency dominates, is indeed very clear. With this enhaced method of identifying stability boundaries, the comparison between MFS and SDM will be presented in Section 5.5. The algorithms of MFS and SDM including process damping are presented first in the following two sections.As MFS and SDM algorithms are already available in the literature [25 and 26], the emphasis in the next two sections will be on including the viscous damping model into these algorithms.

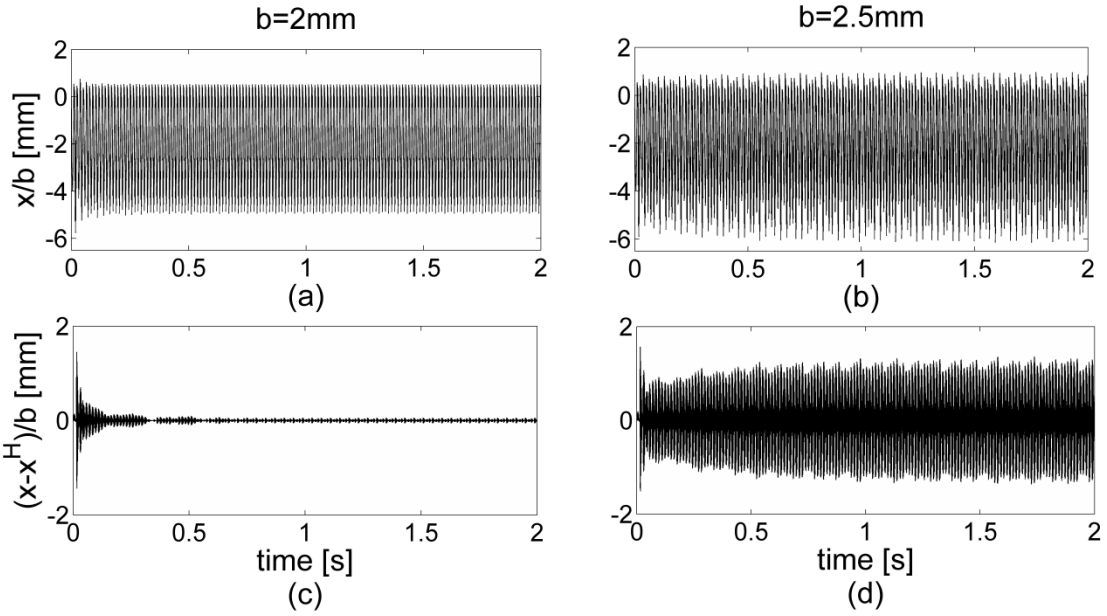

Figure 5-3: The total deflection and regenerative part in the feed direction, normalized by the depth of cut at 1500 RPM and *b*=2mm (a and c), and *b*=2.5mm (b and d)

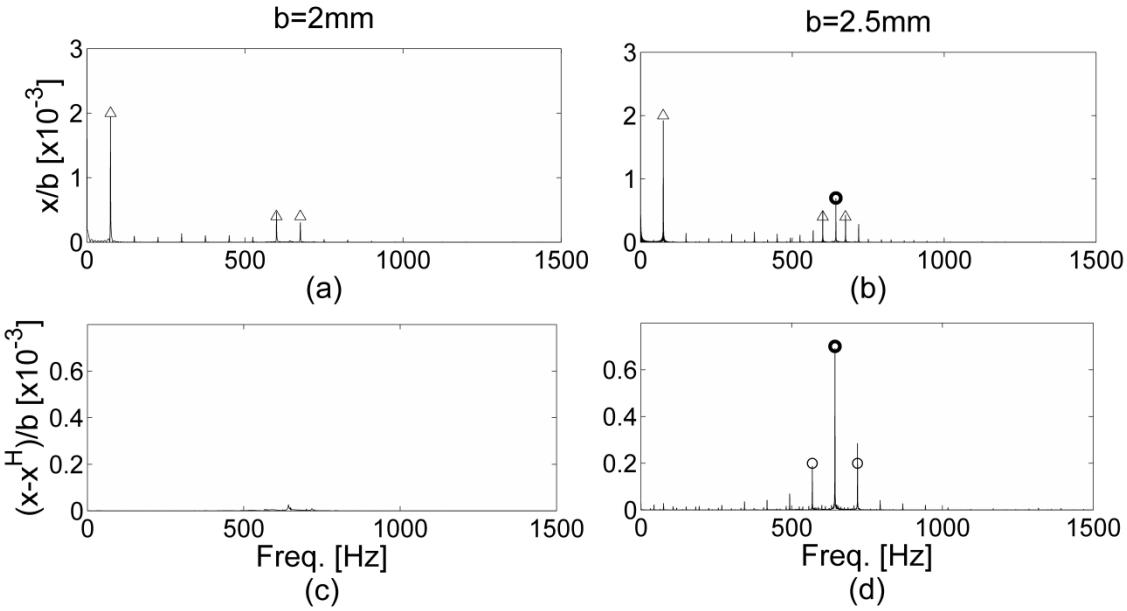

Figure 5-4: Frequency spectra of the time traces in Figure 5-3

5.3 Multi-Frequency Solution (MFS)

In this section, the equivalent viscous damper model of Equation (5.7) is integrated into the MFS of [25] to calculate the milling stability lobes. Since the chip component associated with the feedrate and tool rotation is not involved in the stability process, it is not included in the cutting forces in Equation (5.11), which leads to:

$$\mathbf{F} = b\mathbf{A}\Delta\mathbf{p} + \mathbf{B}\dot{\mathbf{p}} \tag{5.13}$$

The directional coefficient matrices ***A*** and ***B*** are periodic with the tooth passing period, *T*. Therefore, they can be expressed in the Fourier expansion form:

$$\mathbf{A} = \sum_{l=-\infty}^{\infty} \mathbf{A}_l e^{il\omega_s t}; \mathbf{B} = \sum_{l=-\infty}^{\infty} \mathbf{B}_l e^{il\omega_s t}; \mathbf{A}_l = \frac{1}{T}\int_0^T \mathbf{A} e^{-il\omega_s T} dt; \mathbf{B}_l = \frac{1}{T}\int_0^T \mathbf{B} e^{-il\omega_s T} dt \tag{5.14}$$

At the border of stability, assume a harmonic solution at the chatter frequency ω_c:

$$\mathbf{p} = \bar{\mathbf{p}} e^{i\omega_c t} \tag{5.15}$$

Consequently, the delay term in Equation (5.13) is

$$\Delta\mathbf{p} = \bar{\mathbf{p}}\left(1 - e^{-i\omega_c T}\right) e^{i\omega_c t} \tag{5.16}$$

Substituting Equations(5.14), (5.15) and (5.16) in Equation (5.13), the cutting forces can be expressed in the Fourier expansion form, as well:

$$\mathbf{F} = \sum_{k=-\infty}^{\infty} \mathbf{F}_k e^{i(\omega_c + k\omega_s)t} \tag{5.17}$$

Moreover, the response of the linear system of Equation (5.12) to the harmonic excitation of Equation (5.17) can be expressed in terms of the system frequency response function, *G(ω),* at the frequencies of excitation:

$$\mathbf{p} = \sum_{k=-\infty}^{\infty} \mathbf{F}_k \mathbf{G}\left(\omega_c + k\omega_s\right) e^{i(\omega_c + k\omega_s)t}; \mathbf{G}\left(\omega\right) = \left(\mathbf{K} - \mathbf{M}\omega^2 + \mathbf{C}i\omega\right)^{-1} \tag{5.18}$$

By substituting Equations (5.17) and (5.18) into Equation (5.13)**,** the following expression is obtained:

$$\begin{aligned} &\sum_{k=-\infty}^{\infty} \mathbf{F}_k e^{i(\omega_c + k\omega_s)t} = \\ &b\left(1 - e^{-i\omega_c T}\right) \sum_{l=-\infty}^{\infty} \sum_{k=-\infty}^{\infty} \mathbf{A}_l \mathbf{F}_k \mathbf{G}\left(\omega_c + k\omega_s\right) e^{i(l+k)\omega_s t} + \sum_{l=-\infty}^{\infty} \sum_{k=-\infty}^{\infty} \mathbf{B}_l \mathbf{F}_k i\left(\omega_c + k\omega_s\right) \mathbf{G}\left(\omega_c + k\omega_s\right) e^{i(l+k)\omega_s t} \end{aligned} \tag{5.19}$$

Applying the orthogonality property to both sides of Equation (5.19), the coefficients of the cutting force, $\boldsymbol{F_k}$, are expressed in the following recursive equation:

$$\mathbf{F}_p = b\left(1 - e^{-i\omega_c T}\right) \sum_{k=-\infty}^{\infty} \mathbf{A}_{p-k} \mathbf{F}_k \mathbf{G}\left(\omega_c + k\omega_s\right) + \sum_{k=-\infty}^{\infty} \mathbf{B}_{p-k} \mathbf{F}_k i\left(\omega_c + k\omega_s\right) \mathbf{G}\left(\omega_c + k\omega_s\right); p = 0, \pm 1, \pm 2, \ldots \tag{5.20}$$

Equation (5.20) can be cast in the following matrix equation:

$$\bar{\mathbf{F}} = \Lambda \bar{\mathbf{A}} \bar{\mathbf{F}} + \bar{\mathbf{B}} \bar{\mathbf{F}}, \Lambda = b\left(1 - e^{-i\omega_c T}\right)$$

$$\bar{\mathbf{F}} = \begin{Bmatrix} F_0 \\ F_1 \\ F_{-1} \\ \vdots \\ F_Q \\ F_{-Q} \end{Bmatrix}, \bar{\mathbf{A}} = \begin{bmatrix} \mathbf{A}_0\mathbf{G}_0 & \mathbf{A}_{-1}\mathbf{G}_1 & \mathbf{A}_1\mathbf{G}_{-1} & \cdots & \mathbf{A}_{-Q}\mathbf{G}_Q & \mathbf{A}_Q\mathbf{G}_{-Q} \\ \mathbf{A}_1\mathbf{G}_0 & \mathbf{A}_0\mathbf{G}_1 & \mathbf{A}_2\mathbf{G}_{-1} & \cdots & \mathbf{A}_{1-Q}\mathbf{G}_Q & \mathbf{A}_{1+Q}\mathbf{G}_{-Q} \\ \mathbf{A}_{-1}\mathbf{G}_0 & \mathbf{A}_{-2}\mathbf{G}_1 & \mathbf{A}_0\mathbf{G}_{-1} & \cdots & \mathbf{A}_{-1-Q}\mathbf{G}_Q & \mathbf{A}_{-1+Q}\mathbf{G}_{-Q} \\ \vdots & \vdots & \vdots & \ddots & \vdots & \vdots \\ \mathbf{A}_Q\mathbf{G}_0 & \mathbf{A}_{Q-1}\mathbf{G}_1 & \mathbf{A}_{Q+1}\mathbf{G}_{-1} & \cdots & \mathbf{A}_0\mathbf{G}_Q & \mathbf{A}_{2Q}\mathbf{G}_{-Q} \\ \mathbf{A}_{-Q}\mathbf{G}_0 & \mathbf{A}_{-Q-1}\mathbf{G}_1 & \mathbf{A}_{-Q+1}\mathbf{G}_{-1} & \cdots & \mathbf{A}_{-2Q}\mathbf{G}_Q & \mathbf{A}_0\mathbf{G}_{-Q} \end{bmatrix}_{2(2Q+1)\times 2(2Q+1)}$$

$$\mathbf{G}_k = \mathbf{G}\left(\omega_c + k\omega_s\right)$$

$$\bar{\mathbf{B}} = \begin{bmatrix} \mathbf{B}_0\mathbf{G}_0 i(\omega_c) & \mathbf{B}_{-1}\mathbf{G}_1 i(\omega_c+\omega_s) & \mathbf{B}_1\mathbf{G}_{-1} i(\omega_c-\omega_s) & \cdots & \mathbf{B}_{-Q}\mathbf{G}_Q i(\omega_c+Q\omega_s) & \mathbf{B}_Q\mathbf{G}_{-Q} i(\omega_c-Q\omega_s) \\ \mathbf{B}_1\mathbf{G}_0 i(\omega_c) & \mathbf{B}_0\mathbf{G}_1 i(\omega_c+\omega_s) & \mathbf{B}_2\mathbf{G}_{-1} i(\omega_c-\omega_s) & \cdots & \mathbf{B}_{1-Q}\mathbf{G}_Q i(\omega_c+Q\omega_s) & \mathbf{B}_{1+Q}\mathbf{G}_{-Q} i(\omega_c-Q\omega_s) \\ \mathbf{B}_{-1}\mathbf{G}_0 i(\omega_c) & \mathbf{B}_{-2}\mathbf{G}_1 i(\omega_c+\omega_s) & \mathbf{B}_0\mathbf{G}_{-1} i(\omega_c-\omega_s) & \cdots & \mathbf{B}_{-1-Q}\mathbf{G}_Q i(\omega_c+Q\omega_s) & \mathbf{B}_{-1+Q}\mathbf{G}_{-Q} i(\omega_c-Q\omega_s) \\ \vdots & \vdots & \vdots & \ddots & \vdots & \vdots \\ \mathbf{B}_Q\mathbf{G}_0 i(\omega_c) & \mathbf{B}_{Q-1}\mathbf{G}_1 i(\omega_c+\omega_s) & \mathbf{B}_{Q+1}\mathbf{G}_{-1} i(\omega_c-\omega_s) & \cdots & \mathbf{B}_0\mathbf{G}_Q i(\omega_c+Q\omega_s) & \mathbf{B}_{2Q}\mathbf{G}_{-Q} i(\omega_c-Q\omega_s) \\ \mathbf{B}_{-Q}\mathbf{G}_0 i(\omega_c) & \mathbf{B}_{-Q-1}\mathbf{G}_1 i(\omega_c+\omega_s) & \mathbf{B}_{-Q+1}\mathbf{G}_{-1} i(\omega_c-\omega_s) & \cdots & \mathbf{B}_{-2Q}\mathbf{G}_Q i(\omega_c+Q\omega_s) & \mathbf{B}_0\mathbf{G}_{-Q} i(\omega_c-Q\omega_s) \end{bmatrix} \tag{5.21}$$

where Q is the number of harmonics considered in the solution. Equation (5.21) is rearranged into the following eigenvalue problem:

$$\begin{aligned} &\bar{\mathbf{F}} = \Lambda\bar{\mathbf{C}}\bar{\mathbf{F}}, \\ &\bar{\mathbf{C}} = \left(\mathbf{I} - \bar{\mathbf{B}}\right)^{-1}\bar{\mathbf{A}}, \Lambda = b\left(1 - e^{-i\omega_c T}\right) \end{aligned} \tag{5.22}$$

Having calculated Λ from the eigenvalues of $\bar{\mathbf{C}}$, b will be the real part of

$$\frac{\Lambda_R + \Lambda_I i}{\left(1 - e^{-i\omega_c T}\right)} \tag{5.23}$$

where Λ_R and Λ_I are the real and imaginary parts of Λ. Also, because the width of cut b is a real quantity, the imaginary part of Equation (5.23) has to be zero. Applying these two conditions, the axial depth of cut at the border of stability is:

$$b = -\frac{\Lambda_R^2 + \Lambda_I^2}{K_t \Lambda_R} \tag{5.24}$$

Since C_{eq} in matrix $\bar{\mathbf{C}}$ depends on the axial depth of cut itself, at each spindle speed the following iterative procedure is performed to determine the axial depth of cut at the border of stability:

1- Choose a frequency grid for ω_c in the vicinity of tool dominant natural frequency.

2- Set initial axial depth of cut, $b=0$.

3- Calculate $\bar{\mathbf{A}}$, $\bar{\mathbf{B}}$ and $\bar{\mathbf{C}}$ from Equations (5.21) and (5.22), respectively. Then calculate Λ corresponding to each eigenvalue of $\bar{\mathbf{C}}$. For all of the Λ with negative real part and $\mathrm{Im}\left(\frac{\Lambda}{1 - e^{-i\omega_c T}}\right) = 0$, calculate the depth of cut from Equation (5.24).

4- Update the initial b with the minimum value obtained from the entire frequency grid.

5- Repeat steps 3 and 4 until the change in the obtained depth of cut becomes smaller than a pre-defined tolerance. To calculate the stability lobes, this procedure is executed for a span of spindle speeds.

5.4 Semi-Discretization Method (SDM)

In this section, the equivalent viscous damper of Chapter 4 given in Equation (5.7) is integrated into the SDM of [26] to calculate the stability lobes. Similar to MFS, the harmonic part of the cutting force is neglected. Accordingly, Equation (5.12) can be re-written in the state space form:

$$\dot{\mathbf{q}} = \mathbf{L}\mathbf{q}(t) + \mathbf{R}\mathbf{q}(t-T); \mathbf{q} = \begin{Bmatrix} \mathbf{p} \\ \dot{\mathbf{p}} \end{Bmatrix}$$

$$\mathbf{L} = \begin{bmatrix} \mathbf{0} & \mathbf{I} \\ b\mathbf{M}^{-1}\mathbf{A} - \mathbf{\Omega} & \mathbf{M}^{-1}\mathbf{B} - \xi \end{bmatrix}; \mathbf{R} = \begin{bmatrix} \mathbf{0} & \mathbf{0} \\ b\mathbf{M}^{-1}\mathbf{A} & \mathbf{0} \end{bmatrix}; \xi = \begin{bmatrix} \frac{C_x}{M_x} & 0 \\ 0 & \frac{C_y}{M_y} \end{bmatrix}; \mathbf{\Omega} = \begin{bmatrix} \frac{K_x}{M_x} & 0 \\ 0 & \frac{K_y}{M_y} \end{bmatrix} \quad (5.25)$$

This equation can be transformed into the discretized time domain. To do so, the state of tool vibration, $\boldsymbol{q}(t)$, during one delay period, T, is represented by m discrete time intervals of length $\Delta t = T/m$. In the following derivation, the system state at each discrete time, $\boldsymbol{q}(i\Delta t)$, and the time varying coefficients at each discrete time, $\boldsymbol{L}(i\Delta t)$ and $\boldsymbol{R}(i\Delta t)$, will be denoted by $\boldsymbol{q}_i$, $\boldsymbol{L}_i$ and $\boldsymbol{R}_i$, respectively.

At each interval, the time varying coefficients are assumed to stay constant; for example, during the i^{th} interval, $\boldsymbol{L}(t)$ and $\boldsymbol{R}(t)$ are approximated by $\boldsymbol{L}_i$ and $\boldsymbol{R}_i$, respectively. Also, if the time interval length is small enough, the system delay term, $\boldsymbol{q}(t-T)$, during the i^{th} interval can be estimated by $0.5(\mathbf{q}_{i-m}+\mathbf{q}_{i-m+1})$. Applying these approximations, the DDE of Equation (5.25) is transformed into the following linear ordinary differential equation in the $[i\Delta t, (i+1)\Delta t]$ time interval:

$$\dot{\mathbf{q}}_i = \mathbf{L}_i\mathbf{q}_i + \frac{1}{2}\mathbf{R}_i\left(\mathbf{q}_{i-m} + \mathbf{q}_{i-m+1}\right) \quad (5.26)$$

By combining the homogeneous and particular solutions of Equation (5.26), the system state during the i^{th} time interval is obtained as

$$\mathbf{q}_i(t) = e^{\mathbf{L}_i(t-t_i)}\mathbf{C}_0 - \frac{1}{2}\mathbf{L}_i^{-1}\mathbf{R}_i\left(\mathbf{q}_{i-m+1} + \mathbf{q}_{i-m}\right) \quad (5.27)$$

where $\boldsymbol{C}_0$ is a constant depending on the initial condition of tool vibration and is determined by applying the continuity condition at $t = i\Delta t$:

$$\mathbf{q}_i = \mathbf{C}_0 - \frac{1}{2}\mathbf{L}_i^{-1}\mathbf{R}_i\left(\mathbf{q}_{i-m+1} + \mathbf{q}_{i-m}\right) \rightarrow \mathbf{C}_0 = \mathbf{q}_i + \frac{1}{2}\mathbf{L}_i^{-1}\mathbf{R}_i\left(\mathbf{q}_{i-m+1} + \mathbf{q}_{i-m}\right) \tag{5.28}$$

Moreover, by applying the continuity condition at the other end of interval, $t=(i+1)\Delta t$, the system state at the $(i+1)^{th}$ discrete point is obtained in terms of its state at the i^{th}, $(i-m+1)^{th}$, and $(i-m)^{th}$ time steps:

$$\mathbf{q}_{i+1} = e^{\mathbf{L}_i\Delta t}\mathbf{q}_i + \frac{1}{2}\left(e^{\mathbf{L}_i\Delta t} - \mathbf{I}\right)\mathbf{L}_i^{-1}\mathbf{R}_i\left(\mathbf{q}_{i-m+1} + \mathbf{q}_{i-m}\right) \tag{5.29}$$

One can rearrange Equation (5.29) into the following matrix form:

$$\mathbf{\Pi}_{i+1} = \mathbf{\Phi}_i'\mathbf{\Pi}_i ; \mathbf{\Phi}_i' = \begin{bmatrix} e^{\mathbf{L}_i\Delta t} & \mathbf{0} & \cdots & \frac{1}{2}\left(e^{\mathbf{L}_i\Delta t} - \mathbf{I}\right)\mathbf{L}_i^{-1}\mathbf{R}_i & \frac{1}{2}\left(e^{\mathbf{L}_i\Delta t} - \mathbf{I}\right)\mathbf{L}_i^{-1}\mathbf{R}_i \\ \mathbf{0} & \mathbf{I} & \mathbf{0} & \cdots & \mathbf{0} \\ \mathbf{0} & \mathbf{0} & \mathbf{I} & \mathbf{0} & \mathbf{0} \\ \vdots & \vdots & \vdots & \vdots & \vdots \\ \mathbf{0} & \mathbf{0} & \mathbf{0} & \mathbf{I} & \mathbf{0} \end{bmatrix} ; \mathbf{\Pi}_i = \begin{Bmatrix} \mathbf{q}_i \\ \mathbf{q}_{i-1} \\ \mathbf{q}_{i-2} \\ \vdots \\ \mathbf{q}_{i-m+1} \\ \mathbf{q}_{i-m} \end{Bmatrix} \tag{5.30}$$

which, in turn, leads to the following recursive equation, mapping the system state during one delay period to its state during the following delay period through the system transition matrix, $\mathbf{\Phi}$:

$$\mathbf{\Pi}_{i+m} = \mathbf{\Phi}\mathbf{\Pi}_i ; \mathbf{\Phi} = \mathbf{\Phi}_1'\mathbf{\Phi}_2'\mathbf{\Phi}_3'...\mathbf{\Phi}_m' \tag{5.31}$$

According to the Floquet theorem, if all of the eigenvalues of the transition matrix were located inside a unit circle in the complex plane, the system is stable; otherwise, it is unstable. Applying this theory, the stability of the cut at a certain spindle rotational speed, $\Omega=1/N_cT$, and axial depth of cut is examined. At each spindle speed, this criterion needs to be applied on a grid of depths of cut to determine the border of stability. This is in contrast to MFS, where the limit width is calculated following an iterative procedure. To plot the stability lobes in SDM, the falling inside the unit circle criterion is applied on a grid of spindle speeds and depths of cut.

Presented next are examples comparing the performance of MFS and SDM in establishing the stability lobes in milling including the linear viscous model of process damping.

5.5 Stability Lobes from MFS and SDM

In this section, the lobes computed using SDM and MFS will be compared for the ½immersion up-milling example given in [25]. The dynamic and cutting coeficients of this example were given in Section 5.2.

In the first case, a tool wear width W=0.08 mm will be assumed to account for process damping. The stability lobes computed using SDM are shown in Figure 5-5. Also shown in this figure are the results of numerical simulations at several spindle speeds; the circles designate stable cut, whereas crosses indicate unstable cuts. An excellent agreement can be observed between the lobes computed using SDM and the numerical simulations. All circles fall below the stability boundaries and all crosses fall above these boundaries. This agreement verifies that the SDM algorithm including the linear viscous damping model of process damping is accurate in predicting stability over the whole tested speed range. Having said that, it must be realized that the accuracy of SDM depends on the resolution of discretization represnted by the parameter m. According to Equation (5.30), a higher number of divisions results in a bigger transition matrix, Φ, and consequently lengthier computations to extract its eigenvalues. Therefore, choosing the minimum number of devisions, m, to achieve the desired accuracy is critical for enhancing the efficiency of SDM. To illustrate this point, Figure 5-6 shows the calculated limit depth of cut at 1000 RPM using different values of m. By increasing the number of divisions from m=30, in increments of 5, the calculated limit depth of cut decreases from 14 mm and converges to 5.5 mm. Increasing of the number of devisions was stopped when the percentage change in the calculated depth of cut dropped below 1%. Figure 5-7 shows the results of investigating the effect of m at different spindle speeds, for the worn tool with W= 0.08 mm as well as for a sharp tool with W=0 mm. At each spindle speed, the minimum number of divisions to meet the 1% criterion was determined. Figure 5-7 shows that higher number of divisions, m, is required for:

1. Lower spindle speed.
2. Higher level of process damping.

The first reason is understandable, since a lower speed means a larger tooth-passing period, and thus a larger m would be needed to cover that period accurately. The second reason to increase m, the higher process damping, is not obvious: is it the increase in process damping or the increase in damping in general that neccessitates using a larger m? Attempts to answer this question will be given later.

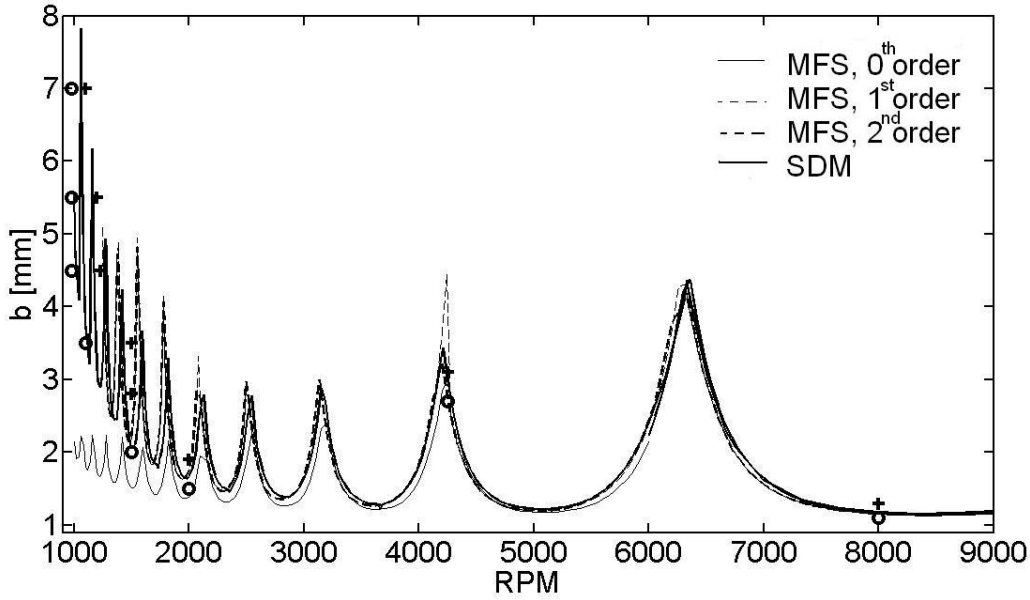

Figure 5-5: Stability lobes computed using SDM and MFS; numerical simulation results: stable (circles) and unstable (crosses)

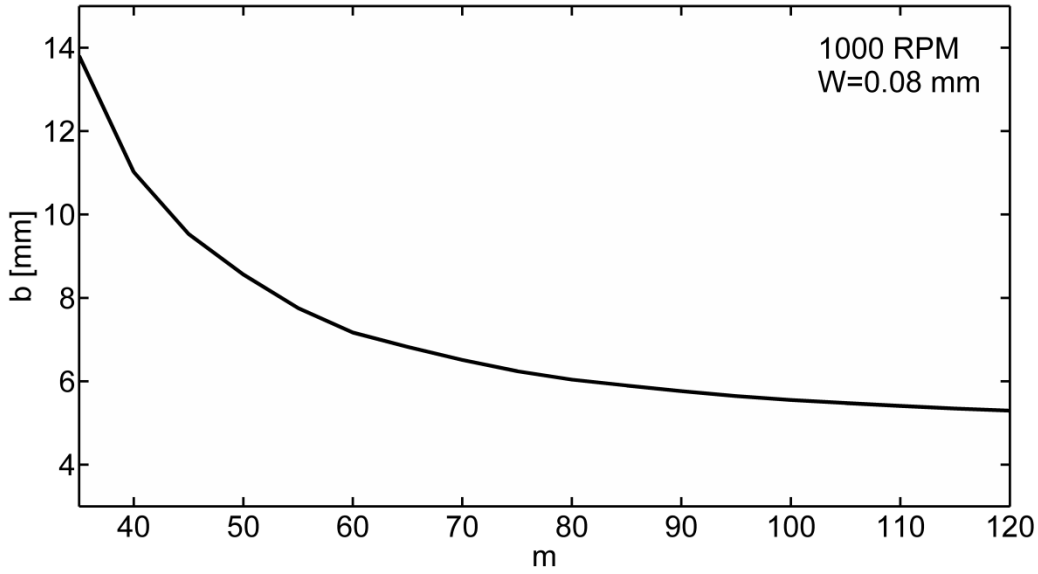

Figure 5-6: Depth of cut at stability border computed using SDM with different numbers of division

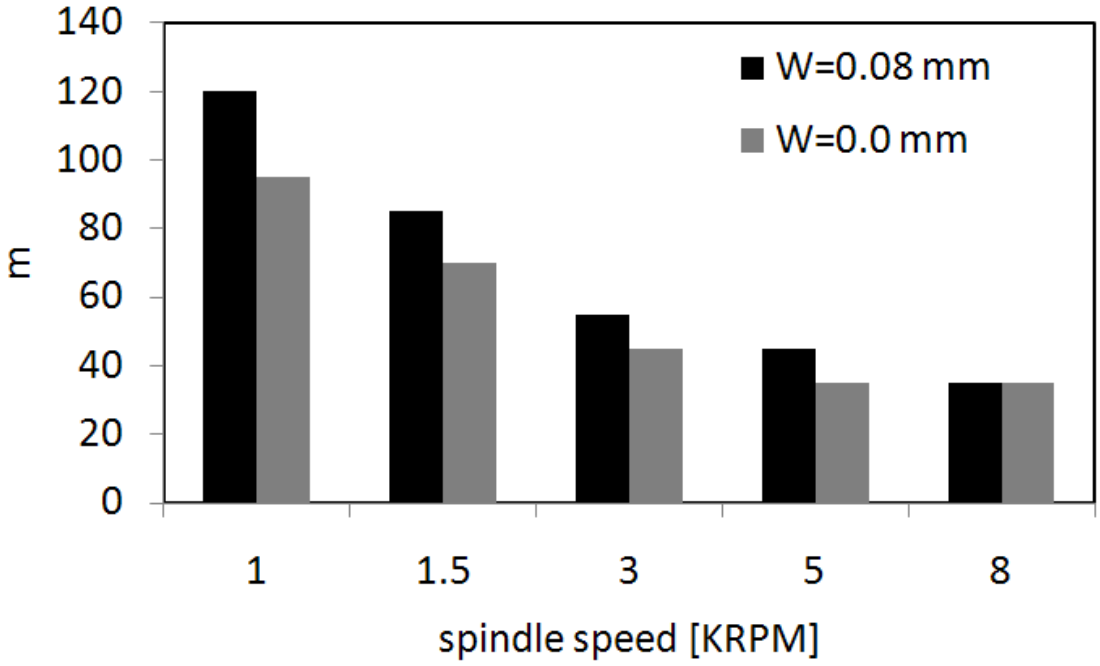

Figure 5-7: Minimum number of divisions required to achieve 1% accuracy in the prediction of axial depth of cut using SDM

The stability lobes computed using the zero order MFS are also shown in Figure 5-5; the lobes agree closely with those computed from SDM at the higher speed range above 2300 RPM. Below 2300 RPM, however, the zero order solution deviates significantly from the lobes obtained from SDM. Below 2300 RPM, the zero order solution also yields lobes that are in disagreement with the simulation results; all of the circles are above these lobes. This disagreement clearly shows that even for this non-shallow cut, the zero order solution underestimates the boundary limits at the low speed range. The MFS approach improves drastically by including the first and then both the first and second harmonics. By adding these harmonics, the lobes obtained from MFS converge to those obtained from SDM and get closer to the time domain simulations.

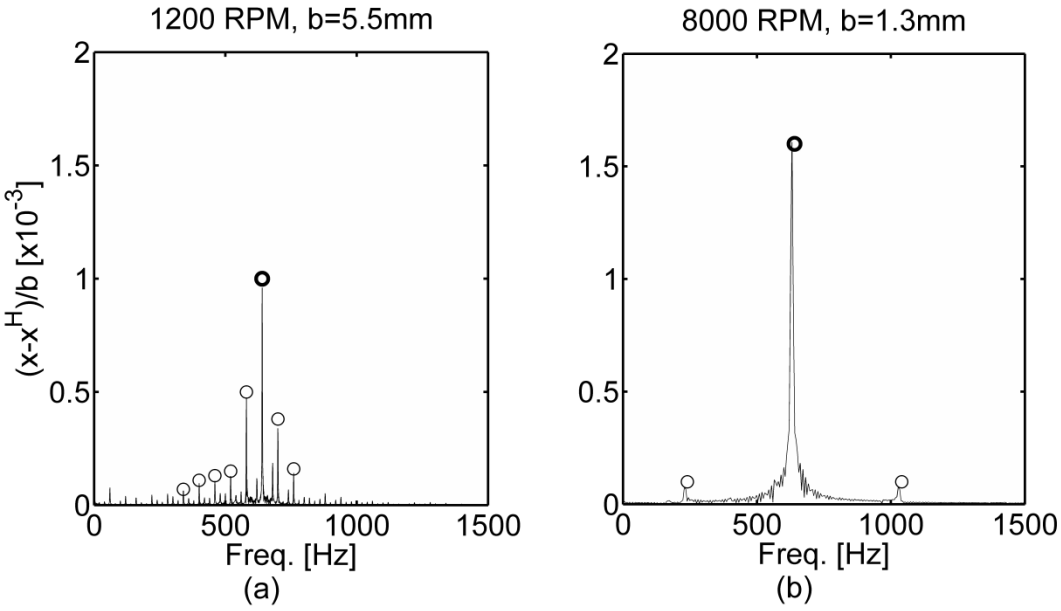

Figure 5-8: Frequency spectra of the regenerative parts of tool displacement normalized by the axial depth of cut: (a) at 1200 RPM and b=5.5 mm, and (b) 8000 RPM and 1.3 mm

Figure 5-8 shows frequency spectra of the regenerative parts of the tool displacement in the X direction, normalized by the axial depth of cut for the cases: (a) 1200 RPM and depth of cut b=5.5 mm, and (b) 8000 RPM and b=1.3 mm. The cut in both cases is unstable. Figure 5-8(b) shows a high spectral line at the chatter frequency, and the side bands at the tooth passing frequency corresponding to 8000 RPM to be small. In comparison, the spectrum of the tool displacement at the low cutting speed of 1200 RPM shows the spectral line at the chatter frequency to be smaller and the side bands at the tooth passing frequency to be much more significant. Whereas the vibration energy is concentrated at a single frequeny for the higher speed of 8000 RPM, it is spread over several frequencies dictated by the tooth-passing frequency at the lower speed of 1200 RPM. This explains the need to include higher harmonics in MFS at low speed, even for the current non-shallow immersion cut. This may also explain the need to use higher resolution, bigger m, in SDM to discern among close eigenvalues resulting from the solution of the transfer matrix.

It is also examining if the need for higher harmonics in MFS and larger m in SDM is associated with increased damping in general. For this reason an example is given here where process damping is excluded by using a sharp tool with W=0 mm. The example will show two cases: (a) using the same parameters given in Section 5.2 where the modal damping ratios are ξ_x=0.039 and ξ_y=0.035., (b) using the same parameters in (a), except the damping ratios are artificially doubled to ξ_x=0.078 and

ξ_y=0.070. Figure 5-9 shows that the computed lobes from the zero order MFS agree closely with those obtained from SDM over the entire tested speed range for the low damping case. These lobes also agree well with the numerical simulations conducted at several speeds. Figure 5-10, at twice the damping ratios, shows that the zero order solution is inaccurate at low speed and two harmonics had to be included to bring the lobes closer to those obtained from SDM and to the simulation results. In other words, it is the increase in damping, irrespective of the source, that dictates including higher harmonics in the MFS approach. For the SDM approach, m=120 was used throughout the entire speed range based on the results presented in Figure 5-7. Obviously, that was an overly conservative approach, and a better procedure should be developed to automate the selection of m at different speed intervals. Such a procedure was not attempted here and could be a subject for future reseach.

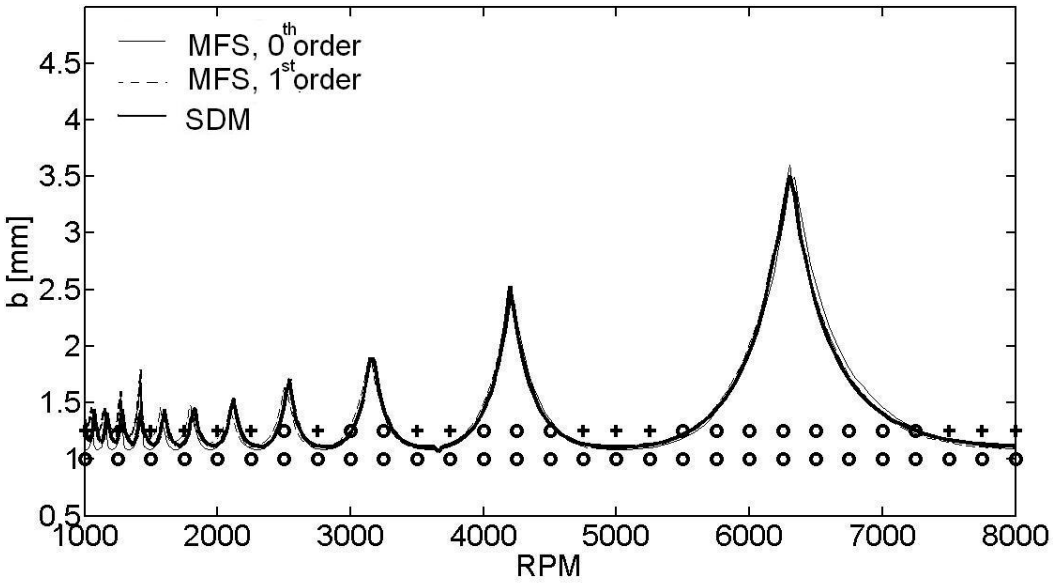

Figure 5-9: Stability lobes without process damping, ξ_x=0.039 and ξ_y=0.035; stable (circles) and unstable (crosses) obtained from numerical simulations

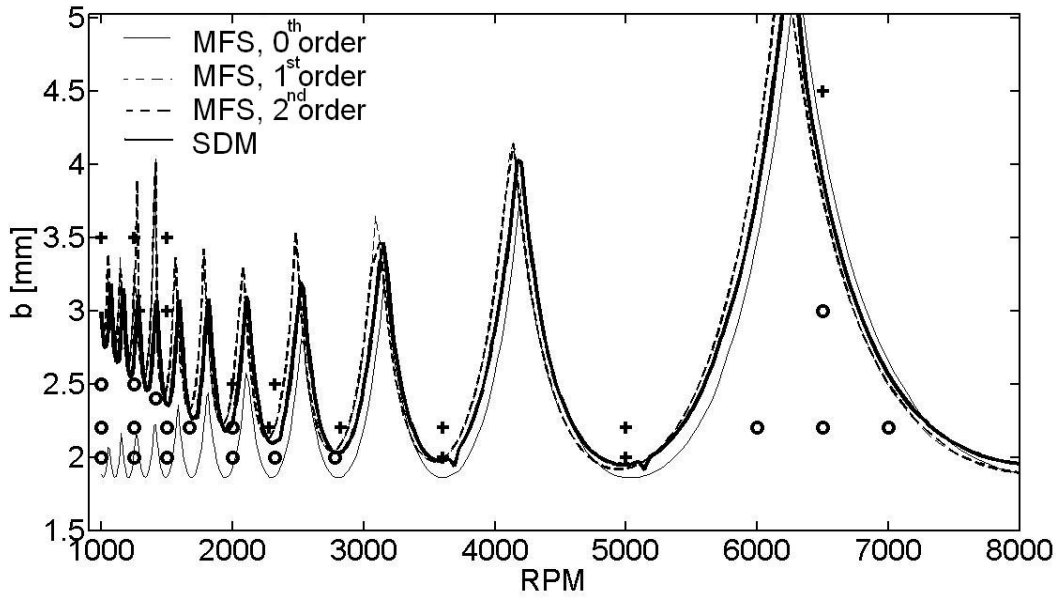

Figure 5-10: Stability lobes without process damping but with double structural damping, ξ_x=0.078 and ξ_y=0.070; stable (circles) and unstable (crosses) obtained from numerical simulations

Figure 5-11 further explains the need to include higher harmonics in the MFS at increased damping and low speed. It is an adaptation of the explanation given by Merdol and Altintas [27]. In [27], however, the explanation was illustrated using the real part of the frequency response function of the vibratory system. For better visual impact, the imaginary part of $G(\omega)$ is utilized here.

Figure 5-11(a) and (b) correspond to the lightly damped system, whereas (c) and (d) correspond to the highly damped system. (a) and (c) are associated with the low speed of 1200 RPM, while (b) and (d) are associated with the high speed of 8000 RPM. In all cases, G is evaluated at the chatter frequency ω_c (thick line) as well as by shifting it to $\omega_c \pm \omega_s$ (thin lines), where ω_s is the tooth-passing frequency. At high speed, Figures (b) and (d), there is practically no interference between the side response functions and the middle one. This explains the accurate results from the zero order solution at high speed, regardless whether the damping was low or high. At low speed and light damping, in (a) there is some interference, which increases significantly in (c) when the damping is doubled. This example clearly shows the reason for the need to include higher harmonics in the MFS approach at low speed and high damping, as these harmonics contribute significantly to the dynamics of the system.

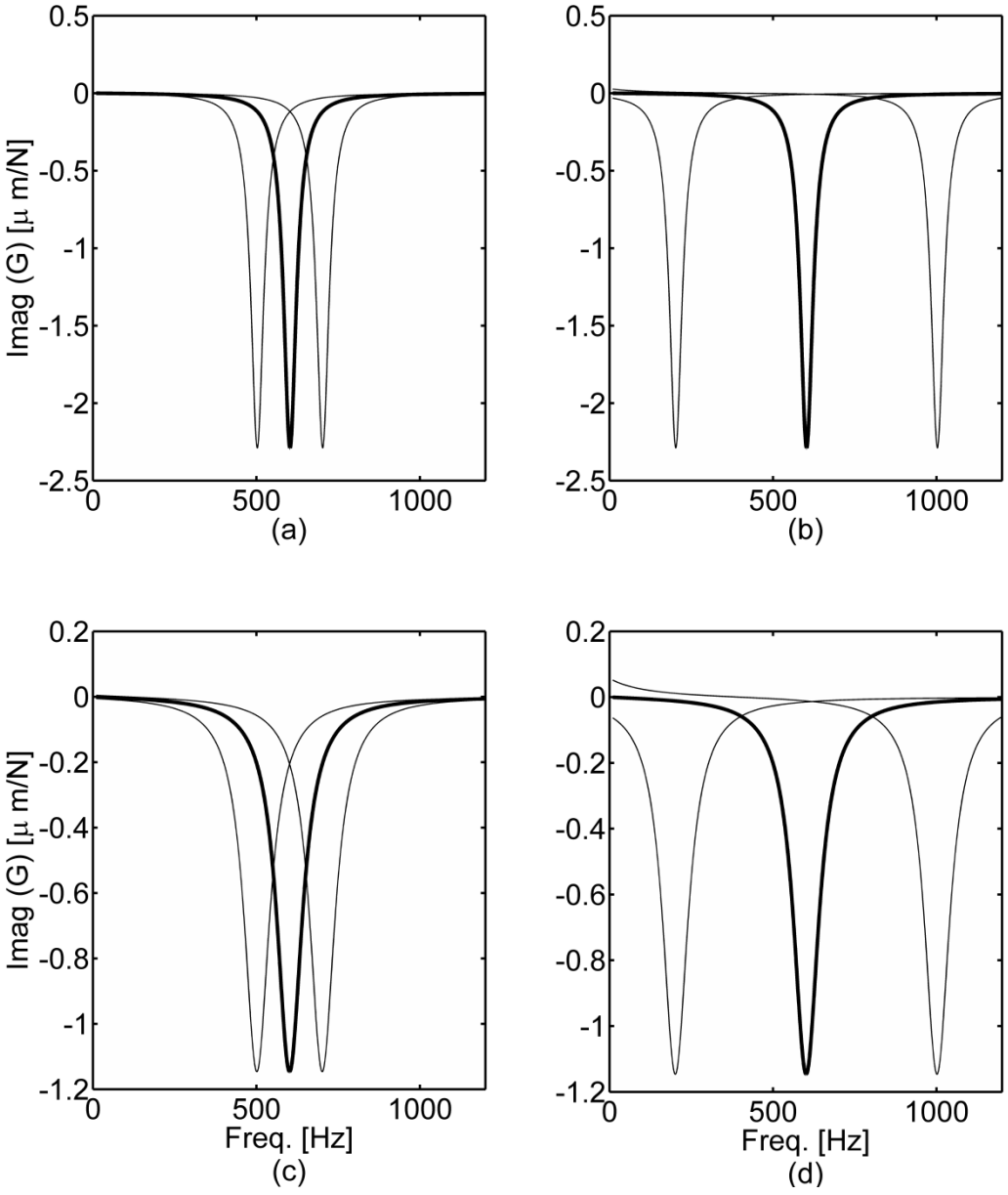

Figure 5-11: The imaginary part of frequency response functions *G(ω),* thick line, and *G(ω ± ω$_s$),* thin line*:* (a) ξ_x=0.039 and ξ_y=0.035 , 1200 RPM, (b) ξ_x=0.039 and ξ_y=0.035, 8000 RPM, (c) ξ_x=0.078 and ξ_y=0.070, 1200 RPM, and (d) ξ_x=0.078 and ξ_y=0.070, 8000 RPM

It is intersting to see that Figure 5-10 shows the lower border of stability to increase below 2500 RPM. The computed stability from the three independent methods, MFS with two harmonics, SDM and the time domain simulation agree on this increasing trend. It is an example where the only source

of damping is that associated with the vibratory model. This increasing trend of stability at the low speed can be attributed to the strong modulation of the system vibration by the tooth harmonics. Such modulation could prevent the concentration of vibration energy at any particular frequency and thus lead to higher stability. It should be realized, however, that the damping ratios in this theoretical example, ξ_x=0.078 and ξ_y=0.070 were made unusually high and not typical of those measured on machine tools. Perhaps, for this reason, the increasing trend in stability at low speed independent of process damping has not been reported in the literature, to the best knowledge of the current author.

The above comparisons show that SDM is consistantly closer to the simulation results, and accordingly will be adopted in the remainder of this chapter.

5.6 Finite Amplitude Stability in Milling

Figure 5-12(a) shows a schematic of chip thickness variation during ½immersion up-milling operation, which was addressed in Section 5.1. In this operation, h^H (shown as the gray area) varies from zero at φ_j=0^0 to s_t at φ_j=90^0. Because of the zero h^H at the beginning of the cut, the tool jumps out of the cut even for the smallest vibration amplitude. Therefore, finite amplitude stability due to process damping nonlinearity is not possible in this operation. In other words, when the minimum magnitude of h^H is zero, the lower stability lobes separate the two states: stable and unstable. However, if the minimum h^H is greater than zero, finite amplitude stability due to process damping nonlinearity may occur in milling. Figure 5-12(b) shows a schematic of chip thickness variation when the tool enters the cut at φ_{st}=45^0 and exits at φ_{ex}=135^0. In this operation, the chip thickness varies between $\frac{s_t}{\sqrt{2}}$ and s_t, and the amplitude of vibration can stabilize due to the additional process damping, without the tool jumping out of the cut.

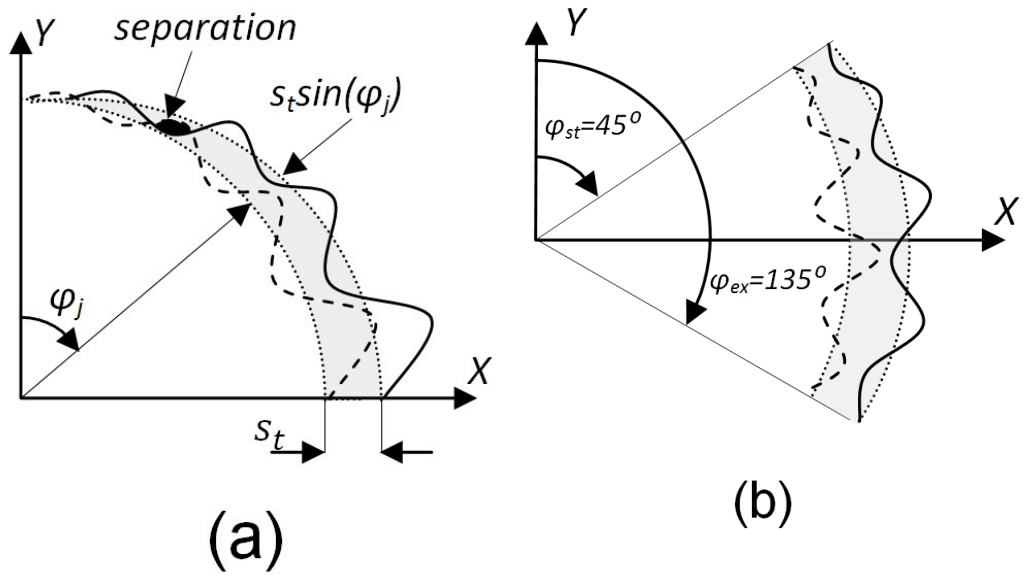

Figure 5-12: Schematic of the total chip thickness in (a) ½ immersion up-milling operation, and (b) arc of cut between $\varphi_{st}=45^0$ and $\varphi_{ex}=135^0$

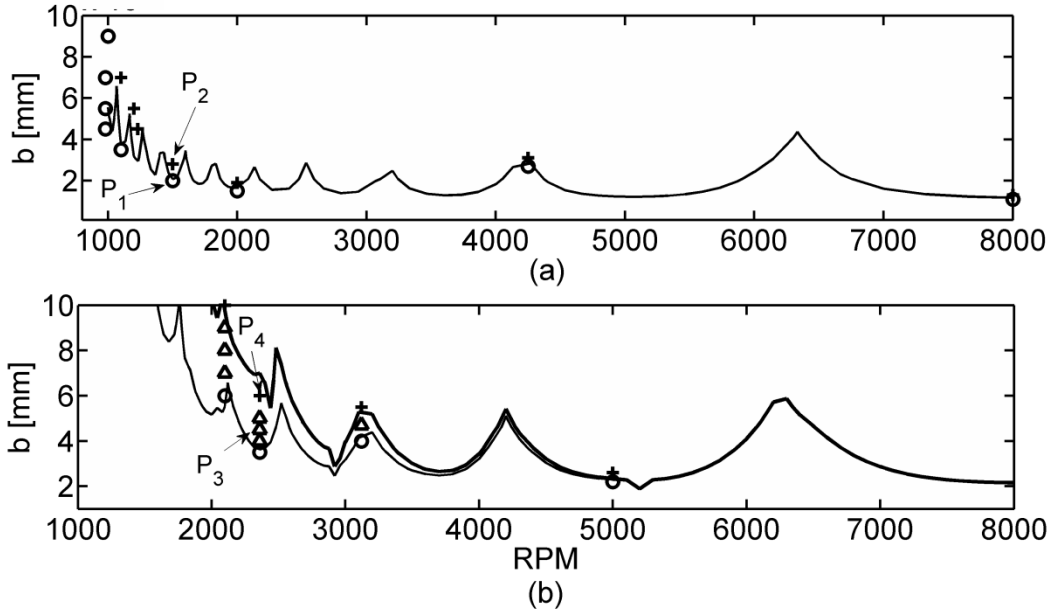

Figure 5-13: (a) Lower lobes calculated for ½immersion up-milling (b) lower (thin line), and upper (thick line) lobes for $\varphi_{st}=45^0$, and $\varphi_{st}=135^0$; numerically simulated stable (circles), unstable (crosses) and finite amplitude stability (triangles) points

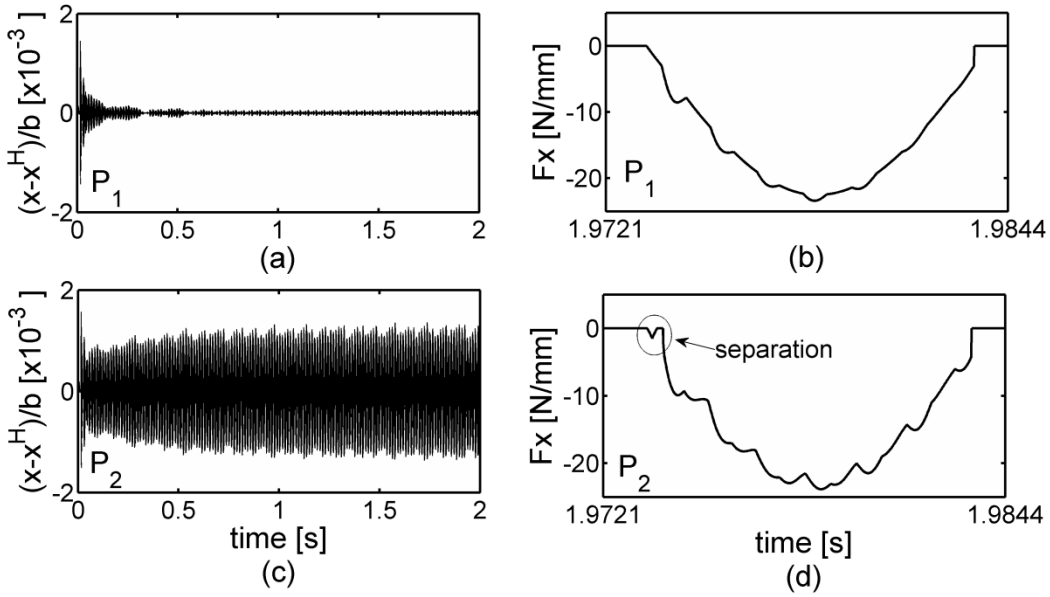

Figure 5-14: The regeneration component of tool deflection in the feed direction, and total cutting forces resulting from simulation at P_1 (a and b) and P_2 (c and d) for ½ immersion up-milling

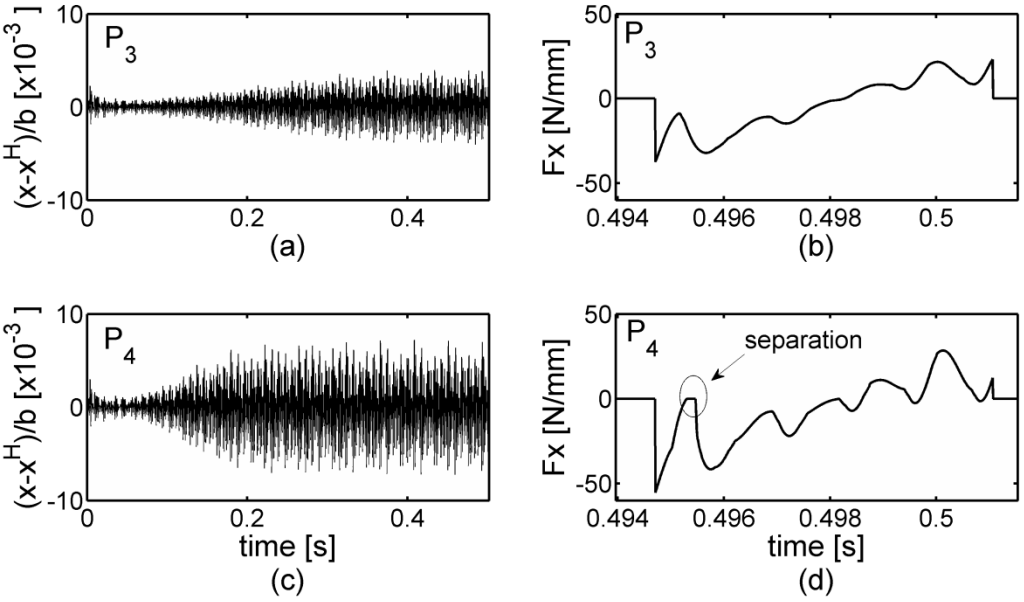

Figure 5-15: The regeneration component of tool deflection in the feed direction, and total cutting forces resulting from simulation at P_3 (a and b) and P_4 (c and d), where the cutting arc is between $\varphi_{st}=45^0$ and $\varphi_{ex}=135^0$

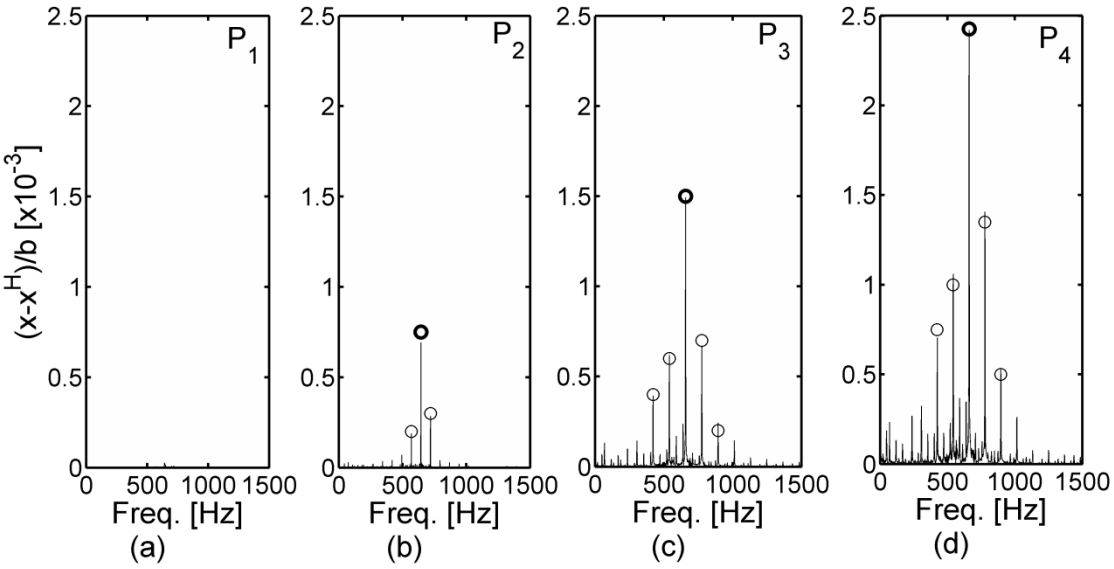

Figure 5-16: The regeneration component of tool deflection in the feed direction, and total cutting forces resulting from simulation at P_3 (a and b) and P_4 (c and d), where the cutting arc is between $\varphi_{st}=45^0$ and $\varphi_{ex}=135^0$

The lower lobes, calculated using SDM for ½immersion up-milling, are reproduced from Section 5.5 in Figure 5-13(a). Also shown in this figure are the numerically simulated stable and unstable cases. According to this figure, at the same speed, the unstable and stable points are close but at opposite sides of lower stability lobes. No finite amplitude stability is detected between the stable and unstable points. For illustration purposes, the results of simulation at P_1 and P_2 are shown in Figure 5-14. The regeneration component of tool deflection and cutting force are normalized by the axial depth of cut. The amplitude of regeneration component dies down to zero at P_1, below the lower stability lobes, and grows at P_2, above the lobes. The vibration amplitude stabilizes at 3 μm due to the tool periodic disengagement from the cut. The drop of the cutting force to zero is an indication of tool disengagement.

The lower lobes are computed also for milling between $\varphi_{st}=45^0$, and $\varphi_{ex}=135^0$. The lower bound lobes are shown in Figure 5-13(b). Numerical simulations are carried out to examine the steady state of a set of cutting points; in this figure, the status of the cut is demonstrated with circles, triangles, and crosses. The circles stand for stable, the triangles for finite amplitude stability due to process damping nonlinearity, and the crosses for the unstable points. The amplitude of regeneration component dies down to zero at the stable points, similar to P_1 in Figure 5-13(a), but it increases at

the unstable and finite amplitude stability points. To compare the finite amplitude stable points with the unstable ones, the results of numerical simulation at P_3 and P_4 are shown in Figure 5-15. The amplitude of regenerated vibration at P_4 stabilizes at 100 μm, and the cutting force drops to zero due to tool disengagement. At P_3, the amplitude of vibration stabilizes at 30 μm, but the steady state cutting force never drops to zero during any tooth-passing period. At P_3, the amplitude of vibration is even larger than the amplitude of unstable point, P_2, in ½immersion up-milling. The frequency spectra of the regeneration component of tool deflection at P_1, P_2, P_3 and P_4 are shown in Figure 5-16. The amplitude of regeneration at the chatter frequency at P_1 is almost zero. At the rest of the points, the amplitude increases from P_2 to P_4. Although the amplitude at P_3 is twice its magnitude at P_2, the tool does not jump out of the cut at P_3. That is why the cut at this point is regarded as finite amplitude stable due to process damping, whereas it is unstable at P_2. Accordingly, the finite amplitude stability due to process damping occurs in this particular cut where the minimum thickness of the harmonic component of chip is greater than zero.

5.6.1 Upper Bound Lobes in Milling

The region of finite amplitude stability due to process damping falls between the lower and upper stability lobes. Having calculated the lower stability lobes in Section 5.5 and demonstrated the feasibility of finite amplitude stability in milling in the previous section, the calculation of upper stability lobes in milling is presented in this section. Apart from calculating the coefficient of equivalent viscous damper, the rest of the procedure is similar to that of the lower lobes presented in Section 5.5.

The upper lobes determine the axial depth of cut at which the tool jumps out of the cut. The amplitude of vibration in the radial direction at the moment of disengagement depends on h^H. In turning, h^H equals the feed per revolution, s_t, but in milling, it changes according to

$$h^H = s_t \sin(\varphi) \tag{5.32}$$

where φ is the angular position of the engaged tooth. Consequently, depending on the angular position of the cutting tooth at the moment of separation, the amplitude of vibration varies. In this work, however, the disengagement is assumed to happen at the angular position corresponding to the minimum value of h^H between φ_{st} and φ_{ex}; for example, in ½immersion up-milling, this angle is 0^0, and in down-milling, it is 180^0. Substituting the minimum value of h^H into Equation (3.11), the amplitude of vibration in the radial direction at the point of separation is obtained as

$$A_{cr} = \frac{\min\left(s_t \sin(\varphi)\right)}{\sqrt{2}}; \varphi_{st} < \varphi < \varphi_{ex} \tag{5.33}$$

This amplitude, unlike in turning, does not stay constant during any one tooth-passing period at steady state. The amplitude of vibration varies due to the cutting interruption and harmonic excitation at the tooth-passing frequency. The variation of vibration amplitude, in turn, results in the variation of the viscous damping coefficient. To simplify the computation of the damping coefficient in Equation (4.10), the amplitude of vibration in the radial direction is assumed to stay constant during one tooth passing period. For instance, in the case of Figure 5-13(b), the minimum h^H is 0.05mm and happens at φ=45^0 or φ=135^0. Accordingly, A_{cr} is calculated at 0.035mm from Equation (3.11). The amplitude of vibration in the radial direction is assumed to stay constant at 35 μm during one tooth engagement, and the following steps are executed to calculate the upper stability lobes shown in Figure 5-13(b):

1- For A_{cr}=35 μm, and γ=7^0, the constants in Equation (4.10) are extracted from Table 4-1 at α=0.586, β_w=2, and β_L=-0.33.

2- The natural frequency and modal stiffness of the tool in the X and Y directions are typically close to each other. Therefore, the chatter frequency is assumed to be equal to the average natural frequency: $f_c=(f_x+f_y)/2$. If the tool structural stiffness in the X and Y directions were different, the chatter frequency would be selected equal to the natural frequency of the compliant mode.

3- Having calculated the chatter frequency in step 2, the wavelength is obtained from $L=\Omega R/f_c$

4- By substituting L from step 3, and α=0.586, β_w=2, β_L=-0.33, and W=0.08mm in Equation (4.10), C_{eq} is calculated at each spindle speed.

The calculated C_{eq} is employed in the SDM, presented in Section 5.4, to calculate the upper bound lobes. The computed finite amplitude region reasonably agrees with the results of numerical simulation. The slight over-estimation of the upper lobes is associated with the assumption made about the amplitude of vibration. Tool deflection in the radial direction during one tooth-passing period at P_4 is shown in Figure 5-17. In the beginning of engagement, where the tool jumps out of the cut, the amplitude of vibration is close to 35μm. Although the amplitude stays fairly constant during the rest of the tooth-passing period, it is less than 35 μm. In the next section, this issue will be further elaborated.

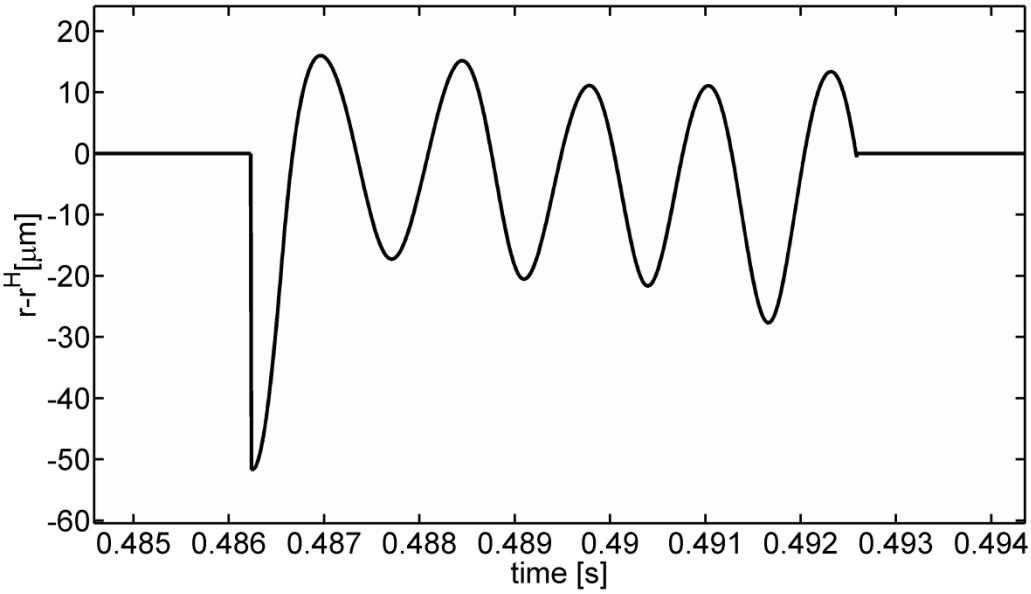

Figure 5-17: The regeneration component of tool deflection in the radial direction during one tooth-passing period at the steady state for P_4, shown in Figure 5-13(b)

5.7 Experimental Verification

In this section, a set of milling experiments are presented to verify the accuracy of the developed methods in the prediction of stability borders. A 25.4mm diameter endmill with a single carbide insert was used to eliminate the effect of runout. The clearance angle was 7^0, and a flank wear width of 0.08 mm was generated by grinding. The feedrate, s_t, was kept constant at 0.05 mm/tooth. Impact tests at the free end of the tool in the X and Y directions were performed. The following modal parameters were obtained:

$$K_x = 4.74\frac{N}{\mu m},\ K_y = 4.27\frac{N}{\mu m},\ \ f_x = 346\ Hz,\ f_y = 336 Hz,\ \ C_x = 65.30 N.s/m,$$

$$C_y = 60.78 N.s/m,$$

$$\zeta_x = \zeta_y = 0.015$$

The cutting force coefficients for the Aluminum workpiece were obtained from a set of cutting tests using a sharp insert:

$$K_t = 900 MPa,\ \ K_r = 0.6$$

The specific indentation force, K_{sp} , and the coulomb friction coefficient, μ, for the Aluminum workpiece were reported at 1.5×10^{14} N/m^3 and 0.3, respectively, in [35]. The workpiece was clamped on a Kistler 9255 table dynamometer, which in turn was clamped to the DCKEL-MAHO 5-axis milling center. Impact tests were also conducted on the workpiece in the X and Y directions. These tests showed the rigidity on the workpiece side to be much higher than that measured on the tool, and thus the flexibility of the workpiece as mounted on the machine table could be neglected.

The cutting forces were recorded at each axial depth of cut and spindle speed. Chatter development was identified from the force time plots.

5.7.1 Half and Full Immersion Cuts

Two cut geometries are utilized in this section: ½ immersion up-milling and full immersion. Because the minimum chip thickness is zero in both of these cases, a finite amplitude stability region due to process damping will not exist, and a single boundary lobes is established. Figure 5-18 shows the measured forces for the ½ immersion cutting and speed 1500 RPM; (a) at axial depth of cut 1mm (a stable cut) and (b) at 1.5 mm (an unstable cut).

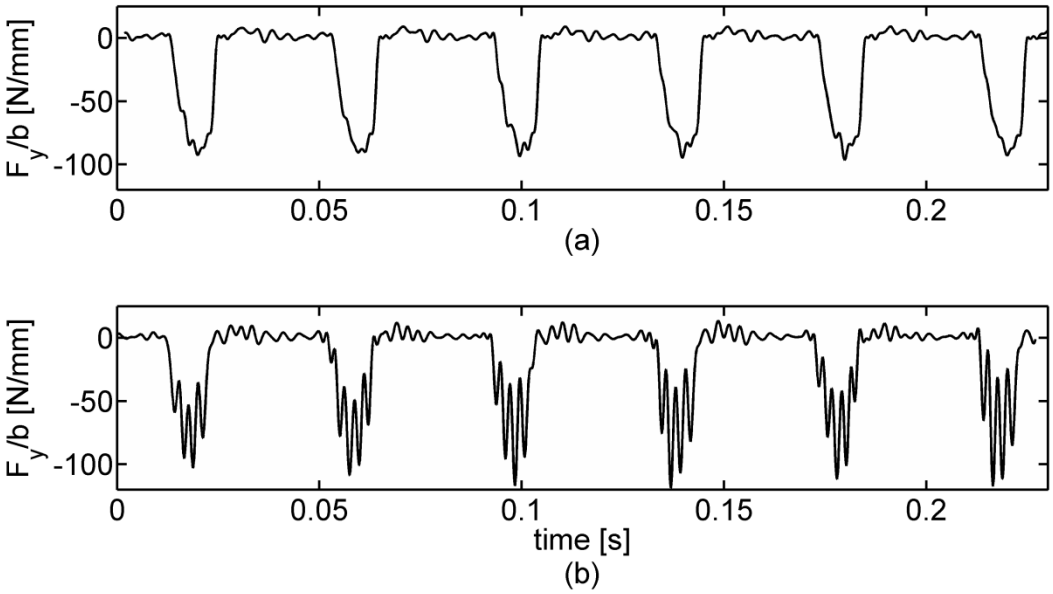

Figure 5-18: Samples of measured cutting forces in ½ immersion up-milling test: (a) stable point, 1500 RPM, b=1 mm, (b) unstable point, 1500 RPM, b=1.5 mm

Figure 5-19 and Figure 5-20 show the stability lobes computed using SDM for the ½ immersion up-milling and full immersion, respectively. The results from experimental tests are also shown in these figures. In both cases the experimental results are in close agreement with the SDM lobes. This further verifies the SDM as an accurate and effective way for establishing the lobes in milling using the viscous damping model of process damping.

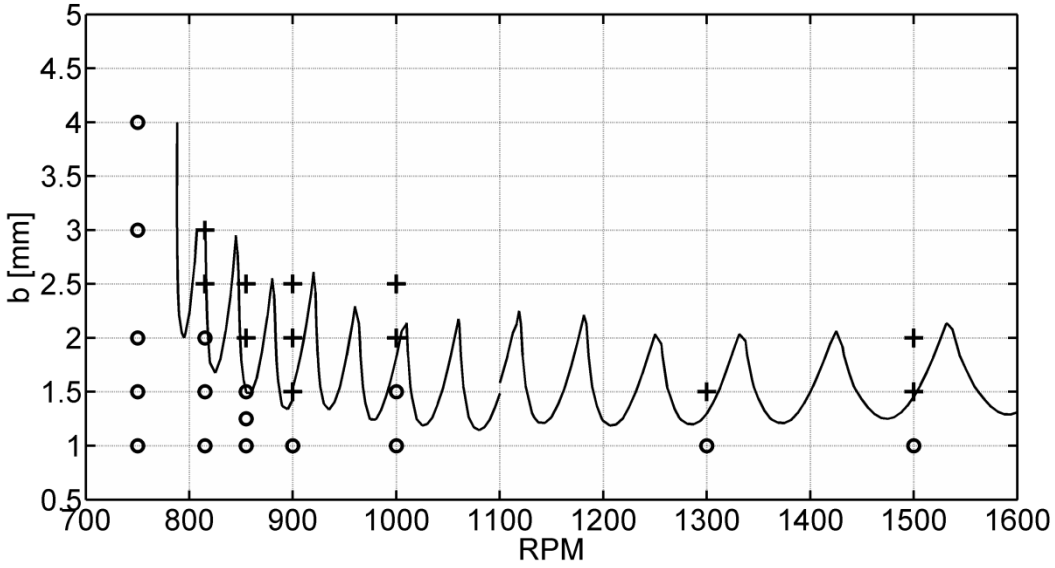

Figure 5-19: Stability lobes computed using SDM, and experimentally measured stable (circles) and unstable (crosses) points for ½ immersion up-milling

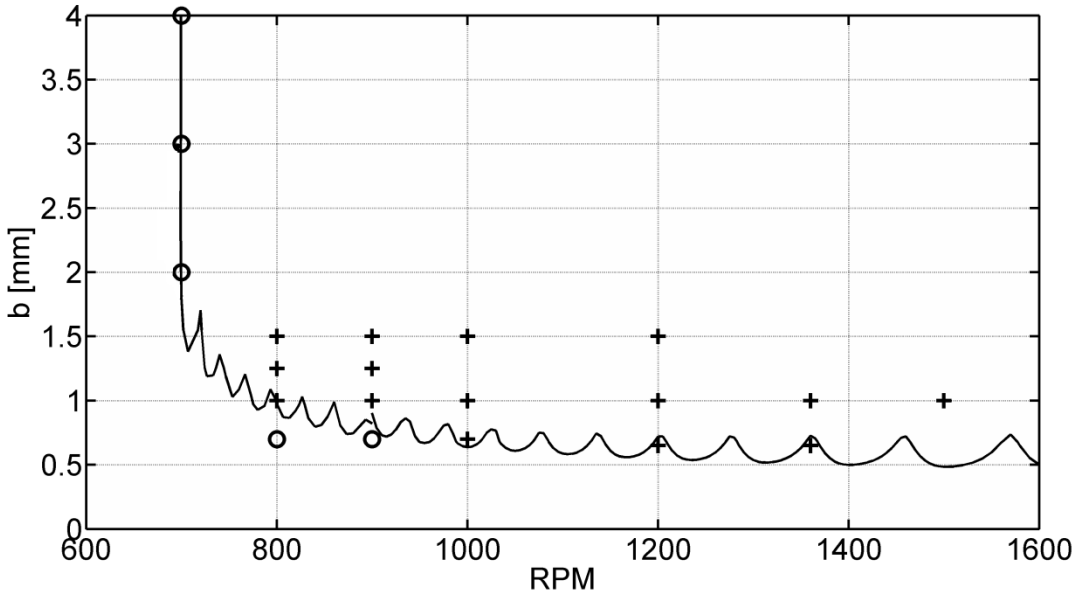

Figure 5-20: Stability lobes computed using SDM, and experimentally measured stable (circles) and unstable (crosses) points for full immersion

5.7.2 Cutting Between $\varphi_{st}=45^0$ and $\varphi_{ex}=145^0$

This test is designed to study the occurrence of finite amplitude stability due to process damping when the minimum h^H is nonzero. The upper and lower stability lobes shown in Figure 5-21 are computed using SDM. To compute the upper stability lobes, the procedure of Section 5.6.1 is employed, and the amplitude of vibration during one tooth engagement is assumed to remain constant at A_{cr}=25μm. Since the feedrate in this test is 0.05 mm/tooth, A_{cr} associated with the minimum chip thickness is calculated at 25μm. Also shown in this figure are the experimentally measured stable, unstable and finite amplitude stability cuts demonstrated by circles, crosses and triangles, respectively. Some samples of the measured stable, unstable and finite amplitude stability cutting forces are shown in Figure 5-22. The drop of the cutting forces to zero, depicted in Figure 5-22(c), is regarded as an indication of tool disengagement and unstable cuts. All of the stable points are located below the lower lobes. However, many unstable points fall below the upper lobes. To investigate the reason of stability over-estimation, numerical simulation is conducted at 950 rpm and b=2.5 mm, which is an unstable point according to the experiments and finite amplitude stability point according to the computed upper bound. The regeneration component of the radial deflection of tool during one tooth-passing period at the steady state is shown in Figure 5-23. According to this figure, the

amplitude of vibration gradually grows and reaches 25 μm at the end of engagement where the tool jumps out of the cut. Thus, assuming 25 μm for the amplitude of vibration during the entire tooth-passing period will result in the over-estimation of vibration amplitude and increased process damping. The upper bound lobes computed using A_{cr}=10 μm and A_{cr}=15 μm are shown in Figure 5-21. The lobes calculated using A_{cr}=15 μm still over-estimate the finite amplitude stability borders, but the ones at A_{cr}=10 μm seem to be close to the experimental evidence.

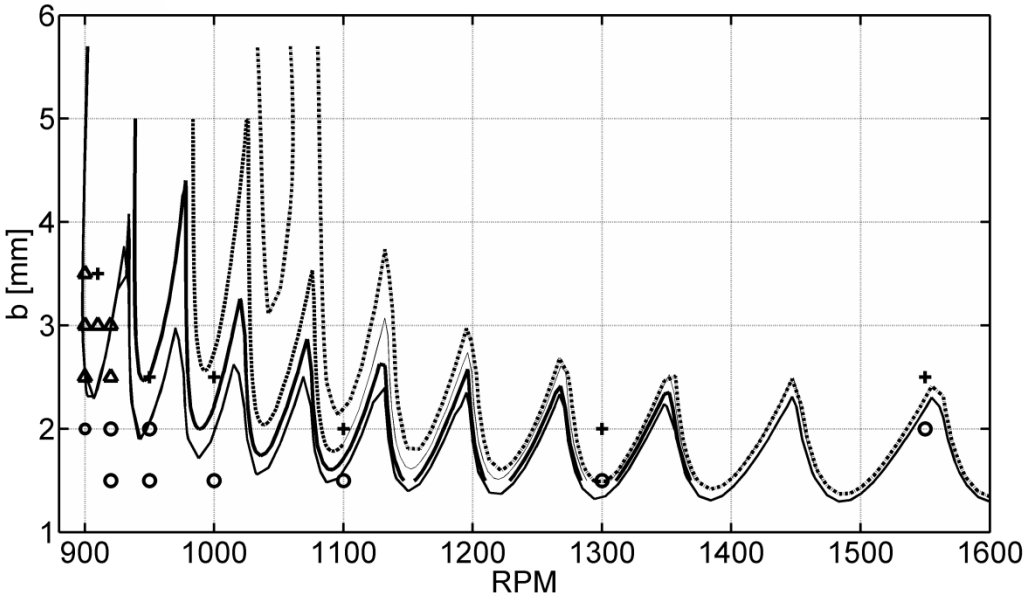

Figure 5-21: Calculated lower bound lobes (thin line), upper bound lobes using A_{cr}=25 μm (dotted line), upper bound lobes using A_{cr} =15 μm (dashed line) and upper bound lobes using A_{cr} =10 μm (thick solid line) for φ_{st}=45^0, and φ_{ex}=145^0; experimentally measured stable (circles), unstable (crosses) and finite amplitude stability (triangles)

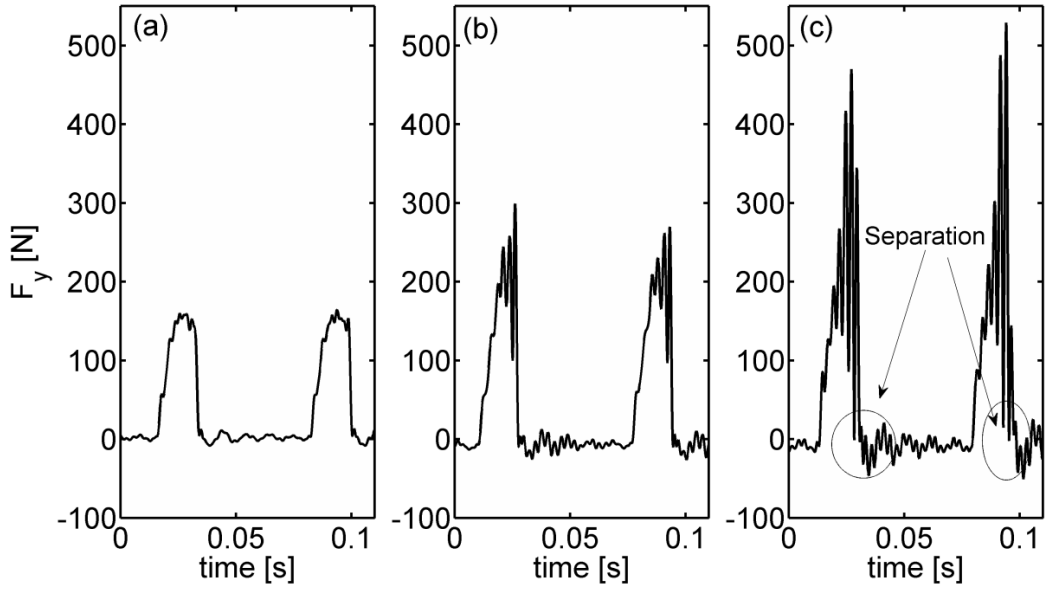

Figure 5-22: Samples of (a) stable, (b) finite amplitude stability, and (c) unstable cutting forces measured in $\varphi_{st}=45^0$ and $\varphi_{ex}=145^0$; (a) 920 rpm b=2mm, (b) 920 rpm b=3mm, and (c) 910 rpm b=3.5mm

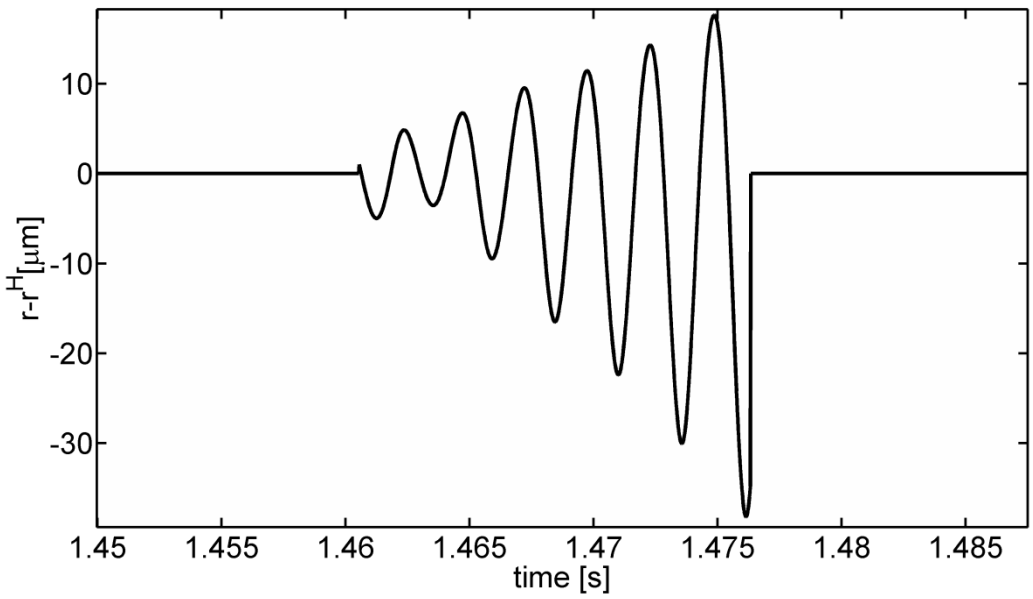

Figure 5-23: The regeneration component of tool deflection in the radial direction during one tooth-passing period at steady state: 950 rpm, b=2.5mm of $\varphi_{st}=45^0$, and $\varphi_{ex}=145^0$.

For further investigation, the stability lobes are calculated for the same cutting system, but with four cutting teeth and no runout. Figure 5-24 shows the lower and upper bound lobes obtained for a

system similar to Figure 5-21, except that the number of cutting teeth is now four. By increasing the number of teeth, the cut becomes less interrupted and the amplitude of vibration stays relatively constant during the tooth engagement. Figure 5-25 shows the regeneration component of the tool deflection in the radial direction simulated at 750 RPM, b=1mm, and N=4 during one tooth passing period; the amplitude of vibration stays close to 25μm during the entire period. The stability of the cut at a set of spindle speed and depth of cuts is examined using numerical simulations and the results are shown in Figure 5-24. In this case, the upper bound lobes obtained from A_{cr}=25μm accurately predict the border between finite amplitude stability and unstable cuts.

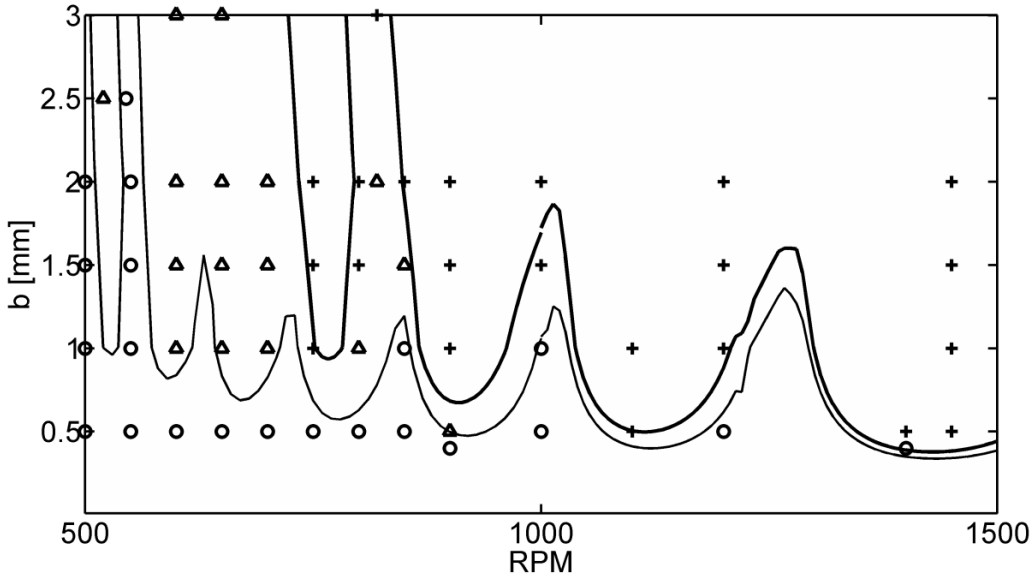

Figure 5-24: Computed upper (thick line) bound lobes using A_{cr}=25μm and lower bound lobes (thin line) of $\varphi_{st}=45^0$, $\varphi_{ex}=145^0$, and with four cutting teeth; stable (circles), unstable (crosses) and finite amplitude stability (triangles) points obtained from numerical simulation

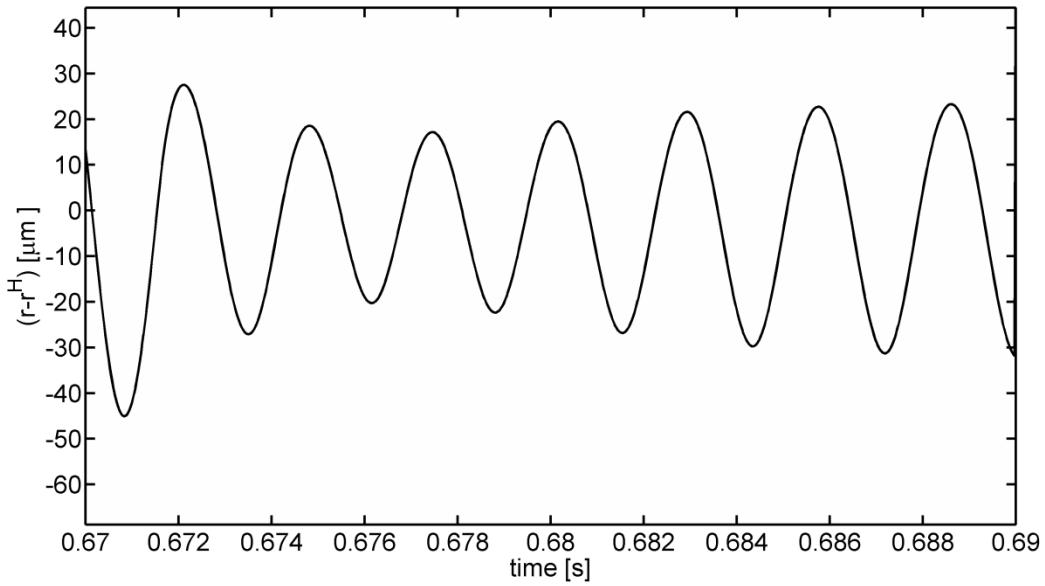

Figure 5-25: The regeneration component of tool deflection in the radial direction during one tooth-passing period at steady state, 750 rpm, b=1mm of $\varphi_{st}=45^0$, $\varphi_{ex}=145^0$, and four cutting teeth

5.8 Summary

The basic formulation of the Multi Frequency approach, MFS, was extended in this work to include the effect of process damping at higher harmonics. It has been long argued in the literature that the zero order is sufficient to establish the stability lobes for most milling operations, and that higher harmonics are only needed in cases of shallow immersion cuts. In this work, it was demonstrated that, even for non-shallow cuts, these higher harmonics are needed at lower cutting speeds and higher damping levels.

The linear viscous damping model of process damping was also added in the formulation of the Semi Discretization Method. SDM was found to yield excellent results throughout the tested speed range, provided that a sufficient number of discretization points within the tooth period are utilized. The effect of this number on the accuracy of the computed stability boundary was investigated. It was found that larger number of divisions is required at lower speeds and higher damping. Accordingly, a conservative large number of divisions was utilized in this work to assess the performance of MFS and SDM. Even with that large number, SDM was more accurate and generally faster in establishing the stability lobes than with MFS. For instance, on a PC with a 2.2 GHz processor, the lobes in Figure 5-5 for ½ immersion up-milling example were calculated in 40, 290 and 690 seconds using zero, zero

+ first, and zero+ first + second order MFS, respectively. While the accuracy improved by adding higher harmonics, the computation time increased drastically. In comparison, it took only 100 seconds to compute the same lobes accurately using SDM.

In this chapter, an effective procedure was also developed to better recognize the onset of instability from time domain simulations. This was accomplished by running the simulation with and without the regenerative component of the chip thickness, and identifying the onset of instability from the vibration associated with the regeneration component only. This method of simulation will be used in the remainder of the thesis to distinguish stable from unstable milling.

Moreover, it was found that at higher levels of structural damping, the stability of the process increases at low speed (beyond the obvious increase due to the elevated level of damping). This was demonstrated on a theoretical example with unusually high modal damping ratios of 7 and 7.8% and in the absence of any damping due to tool/workpiece interaction. This finding could help design tools to machine particular materials, like Titanium, at low speeds.

Besides establishing the stability lobes for milling, the occurrence of finite amplitude stability in this operation due to process damping was studied as well. The results of numerical simulation showed that finite amplitude stability is feasible in milling if the thinnest part of the harmonic component of chip was nonzero. Then, the lower and upper bounds of finite amplitude stability region were developed using SDM and amplitude dependent process damping model. The accuracy of the presented upper and lower bounds were examined by conducting a series of cutting experiments. While the experimental results showed a great agreement with the lower bound, they also revealed that the accuracy of the upper bound depends on the correct approximation of A_{cr}.

Chapter 6
Modeling of Chatter in Flank milling

In this chapter, the Semi Discretization Method, SDM, is employed to model chatter in flank milling using cutters with helical teeth. Process damping is included in the model using the equivalent viscous damper approach. The development is demonstrated first in straight cutting of plain surfaces. Stability lobes are established for these surfaces using an effective flank wear that also accounts for tool radial runout. A new approach of presenting the stability of the cut at different locations along the toolpath is developed; it is designated as the stability maps. The stability maps are established for 5-axis flank milling of three surfaces. Unlike stability lobes, stability maps are toolpath specific, and are verified in this study using numerical simulations and cutting experiments.

In the next two sections, the coordinate systems and toolpath planning strategy used in this chapter are described briefly. In Section 6.3, the governing equations for tool vibration are derived; a 2 degree of freedom (2 DOF) vibratory system will be employed to represent the dynamics of the system. The system's flexibility is restricted to the tool side, and the workpiece will be assumed rigid. A nonlinear mechanistic model will be used to formulate the cutting forces. The start and exit angles and the actual feedrate at each cutter location are calculated in Sections 6.4 and 6.5, respectively. Next, the Semi Discretization Method (SDM) for the helical teeth and including process damping will be presented in Section 6.6. In Section 6.7, the presented method will be illustrated in straight cutting of flat surfaces to establish the stability lobes; stability maps will also be presented in this section. The accuracy of stability lobes and maps for flat surfaces is verified by conducting cutting experiments. In section 6.8, the developed method will be applied to examining the stability of the cut at each cutter location in 5-axis flank milling of three curved surfaces. These predictions are verified using experimental measurements and numerical simulations. Finally, stability maps are established for the flank milling cases and shown to agree with numerical simulations over a wide range of spindle speed.

6.1 Coordinate System

In tool path planning of 5-axis flank milling, tool position is determined in a coordinate system attached to the workpiece, C_{wp}. This coordinate system is shown in Figure 6-1. Two other coordinate frames are used in this chapter: the tilt/rotary table frame C_{tr} and the tool C_t frame. C_{tr} is attached to

the tilt/rotary table center and does not rotate with the table. This frame is used to calculate the tool and workpiece relative motion, which determines the actual feedrate. C_t is attached to the tool tip, and it does not rotate with tool. This frame is suitable for following the dynamics of the tool, and was used in the previous sections to describe tool vibration (XYZ). In this part the flexibility is assumed to be dictated by the tool. In cases where thin blades and the like are being machined, the flexibility of the workpiece should also be taken into account.

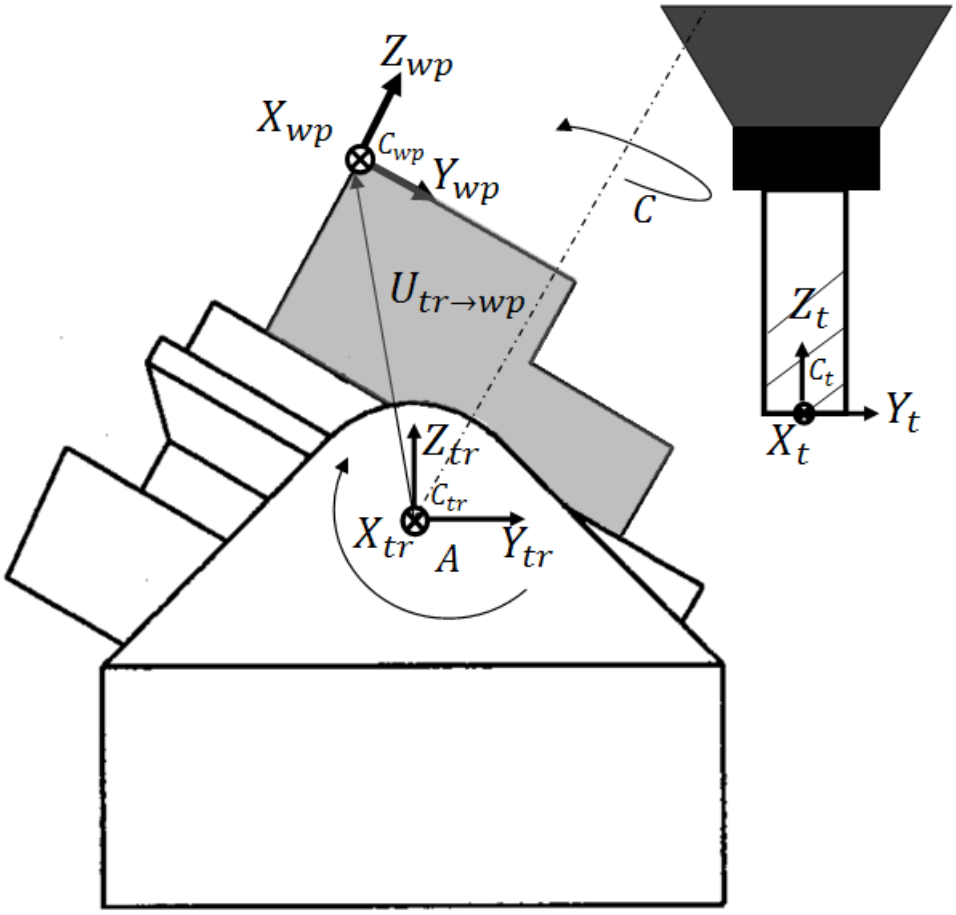

Figure 6-1: Coordinate frames of tilt/rotary table, workpiece and tool

6.2 Tool Path Planning

Knowing the parametric formulation of two curves $\mathbf{R}(v)$ and $\mathbf{S}(v)$ on a surface in C_{wp}, Bedi *et al.* [53, 54] placed a cylindrical tool on the surface such that the tool would be tangent to both curves at the same parametric coordinate v, as shown in Figure 6-2. Since the tool is tangent to the guiding

curves (rails), they are precisely machined. However, overcut might yet happen at other points on the surface.

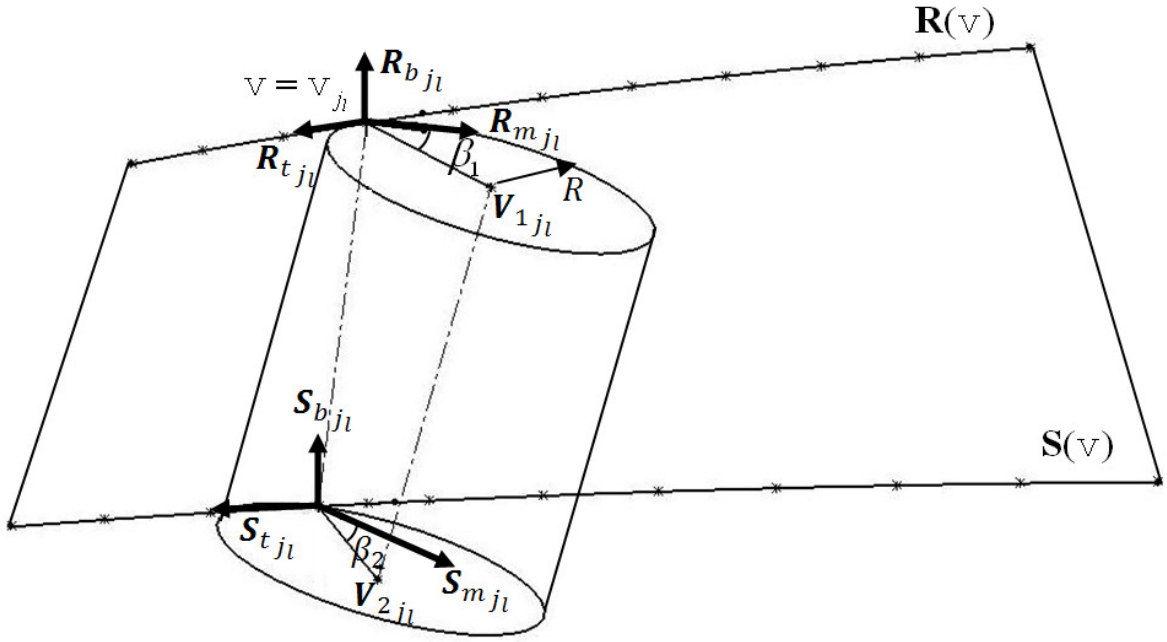

Figure 6-2: Tool path planning strategy: cylindrical tool tangent to two curves on the surface

Details of the derivations to find the tool locations and tool axis orientations along the path are available in [53 and 54]. For the sake of completeness, these derivations are briefly recapitulated below.

Applying the tangency condition at each tool position, v_{j_l} ; j_l=*1..N*$_l$, as illustrated in Figure 6-2, results in the following set of nonlinear algebraic equations:

$$\begin{cases} p_1 \cos\beta_1 + q_1 \sin\beta_1 = R \\ p_2 \cos\beta_2 + q_2 \sin\beta_2 = R \end{cases} \qquad (6.1)$$

where

$$p_1 = (\mathbf{R}_{j_l} - \mathbf{S}_{j_l}) \bullet \mathbf{R}_{m_{j_l}} + \mathbf{S}_{b_{j_l}} \bullet \mathbf{R}_{m_{j_l}} R \sin\beta_2 + \mathbf{S}_{m_{j_l}} \bullet \mathbf{R}_{m_{j_l}} R \cos\beta_2$$

$$q_1 = (\mathbf{R}_{j_l} - \mathbf{S}_{j_l}) \bullet \mathbf{R}_{b_{j_l}} + \mathbf{S}_{b_{j_l}} \bullet \mathbf{R}_{b_{j_l}} R \sin\beta_2 + \mathbf{S}_{m_{j_l}} \bullet \mathbf{R}_{b_{j_l}} R \cos\beta_2$$

$$p_2 = (\mathbf{R}_{j_l} - \mathbf{S}_{j_l}) \bullet \mathbf{S}_{m_{j_l}} + \mathbf{R}_{b_{j_l}} \bullet \mathbf{S}_{m_{j_l}} R \sin\beta_1 + \mathbf{R}_{m_{j_l}} \bullet \mathbf{S}_{m_{j_l}} R \cos\beta_1$$

$$q_2 = (\mathbf{R}_{j_l} - \mathbf{S}_{j_l}) \bullet \mathbf{R}_{b_{j_l}} + \mathbf{R}_{b_{j_l}} \bullet \mathbf{S}_{b_{j_l}} R \sin\beta_1 + \mathbf{R}_{m_{j_l}} \bullet \mathbf{S}_{b_{j_l}} R \cos\beta_1 .$$

In this equation, $\boldsymbol{R}_{jl}$ and $\boldsymbol{S}_{jl}$ are the values of the curves $\boldsymbol{R}(\mathrm{v})$ and $\boldsymbol{S}(\mathrm{v})$, respectively, at v_{j_l}, and $(\boldsymbol{R}_{tjl}, \boldsymbol{R}_{bjl}, \boldsymbol{R}_{mjl})$ and $(\boldsymbol{S}_{tjl}, \boldsymbol{S}_{bjl}, \boldsymbol{S}_{mjl})$ are the Frenet frames at the tangent points [80]. R is the radius of the cutter. The numerical solution of Equation (6.1), for each value of v_{j_l}, yields the two unknown angles β_2 and β_1. These are the angles between the surface normal and the lines connecting the tool center to the contact points on the guiding curves. Since these angles are located in the planes normal to the guiding curves, one can use them to calculate the coordinates of two points on the tool axis, $\boldsymbol{V}_{1jl}$ and $\boldsymbol{V}_{2jl}$. Having calculated $\boldsymbol{V}_{1jl}$ and $\boldsymbol{V}_{2jl}$, the tool position and orientation are now fully defined at location j_l. This process is repeated at all locations, $j_l=1..N_l$, to generate the cutter location file, CL, along the path.

Having calculated the coordinates of two points on the tool axis, $\boldsymbol{V}_{1jl}$ and $\boldsymbol{V}_{2jl}$, the tool orientation vector is obtained as the vector connecting these two points: $\boldsymbol{a}(v)=\boldsymbol{V}_2(\mathrm{v})-\boldsymbol{V}_1(\mathrm{v})$. The magnitude of this vector represents the axial depth of cut: $b\equiv|\boldsymbol{a}(\mathrm{v})|$.

It was shown by Bedi *et al.* [54] that the tool axis will sweep a ruled surface $\mathbf{S}(\mathrm{u},\mathrm{v})$, where u is the parametric variable along the tool axis. On the other hand, the imprint of the tool on the workpiece, which is the machined surface, will not necessarily be a ruled surface. This imprint is referred to as the "grazing" surface; it is determined by shifting the surface swept by the tool axis, $\mathbf{S}(\mathrm{u},\mathrm{v})$, in the direction normal to it by the radius R. Accordingly, the analytical formulation of the grazing surface is written as:

$$\mathbf{G}(\mathrm{u},\mathrm{v}) = \mathbf{S}(\mathrm{u},\mathrm{v}) + \frac{\left(\dfrac{d\mathbf{S}(\mathrm{u},\mathrm{v})}{d\mathrm{v}} \times \mathbf{a}(\mathrm{v})\right)}{\left|\dfrac{d\mathbf{S}(\mathrm{u},\mathrm{v})}{d\mathrm{v}} \times \mathbf{a}(\mathrm{v})\right|}.R. \quad (6.2)$$

For a surface made in several passes, the grazing surface left in the previous cut, say $\mathbf{G}_p(\mathrm{u},\mathrm{v})$, will represent the original material to be removed to generate the machined surface $\mathbf{G}(\mathrm{u},\mathrm{v})$ in the current pass. In this paper, $\mathbf{G}(\mathrm{u},\mathrm{v})$ will be the finishing pass. Both $\mathbf{G}(\mathrm{u},\mathrm{v})$ and $\mathbf{G}_p(\mathrm{u},\mathrm{v})$ will be utilized to compute the start and exit angles of the cutting edges into the stock, as will be shown in Section 6.4.

6.3 Dynamic Model

The dynamic model of the system is shown in Figure 6-3 and is described in the tool coordinate system. The structural model has two orthogonal modes in the X_t and Y_t directions. The workpiece is assumed rigid as well as the tool in the axial direction. In Figure 6-3, K_x, M_x and C_x are the modal stiffness, mass and damping coefficients in the X_t direction, respectively. Likewise, K_y, M_y and C_y are the modal stiffness, mass and damping coefficient in the Y_t direction. These parameters are obtained from impact modal testing performed at the free end of the tool. The modal parameters are assumed not to change at different cutter locations throughout the toolpath.

The equation governing the vibration of the tool in the X_t and Y_t directions, $\boldsymbol{p}$, is

$$\mathbf{M}\ddot{\mathbf{p}} + \mathbf{K}\mathbf{p} + \mathbf{C}\dot{\mathbf{p}} = \mathbf{F}; \quad \mathbf{M} = \begin{bmatrix} M_x & 0 \\ 0 & M_y \end{bmatrix}; \quad \mathbf{K} = \begin{bmatrix} K_x & 0 \\ 0 & K_y \end{bmatrix}; \quad \mathbf{C} = \begin{bmatrix} C_x & 0 \\ 0 & C_y \end{bmatrix} \tag{6.3}$$

In this equation, $\boldsymbol{F}$ is the vector of total cutting forces and is calculated by adding together the elemental cutting forces along the tool axis, as explained below.

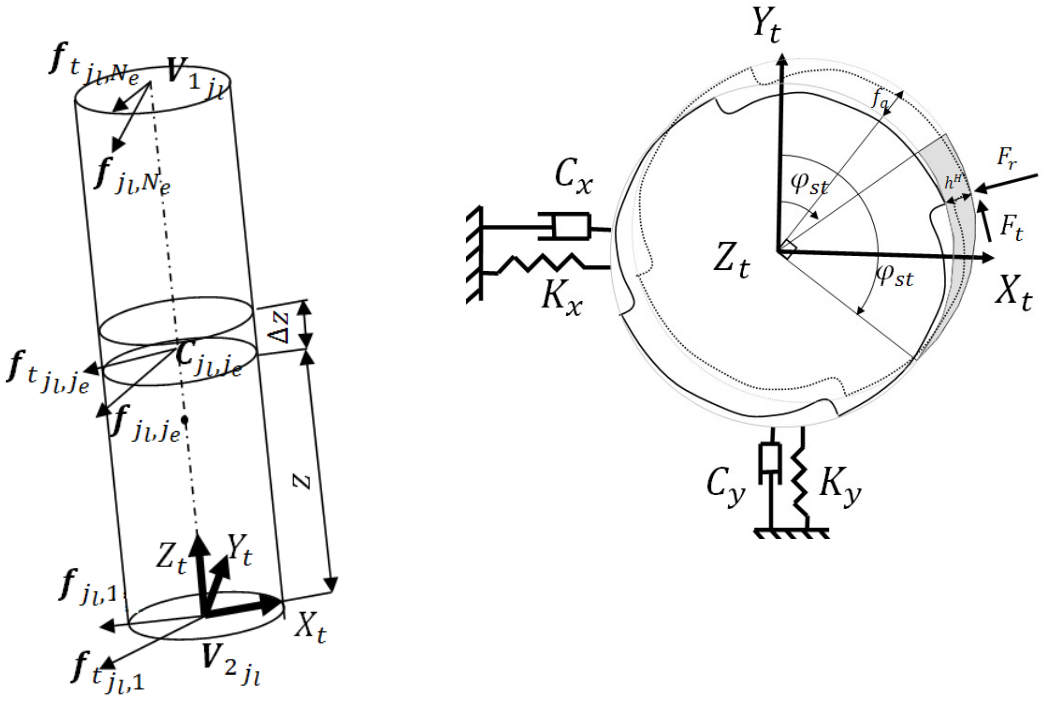

Figure 6-3: (a) Discretizing engaged length of the tool and feed vectors. (b) Dynamic model, chip thickness, and start and exit angles of the axial element j_e

Figure 6-3 (a) shows the engaged part of the tool at position j_l; $j_l = 1..N_l$. The distance between $\boldsymbol{V}_{1jl}$ and $\boldsymbol{V}_{2jl}$ determines the axial engagement of the tool:

$$b_{j_l} = \left| \mathbf{V}_{2j_l} - \mathbf{V}_{1j_l} \right| \tag{6.4}$$

The tool is divided into N_e disks of equal thickness, $\Delta z = b_{jl}/N_e$. The center of the j_e^{th} disk at position j_l is designated $\boldsymbol{C}_{jl,\,je}$. This center is $\boldsymbol{V}_{1\,jl}$ at the top disk, and $\boldsymbol{V}_{2\,jl}$ at the bottom disk; these designations were kept the same as those used by Bedi *et al.* [53, 54]. In the following, however, the subscripts j_l and j_e will be dropped whenever extra subscripts are needed to describe variables, or wherever it is intuitive to follow those variables. At each disk, $j_e = 1..N_e$, the position of cutting tooth, $j_c = 1..N_c$, is determined by its angular position φ with respect to Y_t according to:

$$\phi = \Omega t + (j_c - 1).\frac{2\pi}{N_c} + \frac{(2j_e - 1).\Delta z \tan\psi}{R} \tag{6.5}$$

where N_c is the number of teeth, ψ is the tool helix angle, and Ω is the spindle rotational speed. Notice that subscripts of some variables are dropped whenever the definition of the variable is obvious. For example, the angle φ could have subscripts to define the tooth, and the elemental disk, but that is easily understood. If φ falls between the start, φ_{st}, and exit, φ_{ex}, angles, then the j_c^{th} tooth is engaged in the cut. The start and exit angles in 5-axis machining vary at each cutter location and at each elemental disk. The calculation of these angles will be addressed in Section 6.4.

The elemental tangential and radial forces are calculated using the following force model:

$$\begin{aligned} F_t &= F_{ts} + F_{tp} \\ F_r &= F_{rs} + F_{rp} \end{aligned} \tag{6.6}$$

F_{ts} and F_{rs} are the incremental tangential and radial shear forces acting on the j_c^{th} tooth respectively, and similarly F_{tp} and F_{rp} are the ploughing forces.

The ploughing forces are modeled using the equivalent viscous model established in Chapter 4:

$$\begin{aligned} &F_{rp} = g(\varphi) C_{eq} \dot{r}; \quad C_{eq} = K_{sp} C_d . \frac{\Delta z}{\cos\psi}; \quad g(\varphi) = \begin{cases} 1 & \varphi_{st} < \varphi < \varphi_{ex} \\ 0 & \varphi_{st} > \varphi \quad or \quad \varphi > \varphi_{ex} \end{cases} \\ &F_{tp} = g(\varphi) \mu . F_{rp} \end{aligned} \tag{6.7}$$

where r is the tool radial deflection at the axial element j_e and tooth j_c, and '˙' designates the first degree time derivative. In this chapter, the damping shape factor, C_d , is $0.25W^2$, where W is the tool wear. This implies that small amplitude vibration is assumed. For a cutter with helical teeth one would expect the wear to vary from one tooth to the next as well as along the tooth edge. This is further complicated by tool runout. In the present model a uniform wear land of a constant value will

be assumed for all the elemental disks. The value of W will be designated "effective wear" and will be estimated from experimental evidence. The estimation of effective wear and its effect on the predicted stability borders will be discussed in Section 6.7.

In the previous chapters, the shear forces were assumed to be linear functions of the uncut chip thickness and the cutting force coefficients were estimated empirically. Yet, the estimated coefficients are shown to be nonlinear functions of the uncut chip thickness [14] themselves. Due to the additional rotational axis in 5-axis machining, the feedrate, and consequently the uncut chip thickness, varies at each cutter location and each elemental disk. Accordingly, instead of applying the linear mechanistic model of previous chapters, the following nonlinear mechanistic force model is used to simulate the shear forces:

$$F_{ts} = g(\varphi) K_t . h^{\alpha_t} . \Delta z, \quad F_{rs} = g(\varphi) K_r . h^{\alpha_r} . \Delta z \tag{6.8}$$

where h is the instantaneous chip thickness. α_t, α_r, K_t and K_r are the constant cutting force coefficients, which are estimated experimentally. For aluminum alloy 6061-T6 [17], they were estimated at:

$$\begin{aligned} K_t &= 1250 \frac{N}{mm^2}, \alpha_t = 0.933 \\ K_r &= 568 \frac{N}{mm^2}, \alpha_r = 0.789 \end{aligned} \tag{6.9}$$

In Equation (6.8), to obtain the radial and tangential shear forces in N using the coefficients of Equation (6.9), one needs to insert the chip thickness, h, and element thickness, Δz, in mm. The instantaneous chip thickness, h, consists of a harmonic component, h^H, due to the tool feed motion, and a regeneration component, h^{reg}, due to the vibration in subsequent teeth engagement:

$$h = h^H + h^{reg}; h^H = f_a \sin\theta, h^{reg} = r - r^T, \theta = \begin{cases} \varphi - \varphi_{st} & upmilling \\ \varphi_{ex} - \varphi & downmilling \end{cases} \tag{6.10}$$

where f_a is the feed/tooth on element j_e at cutter location j_l. The chip harmonic component, over the elemental disk engagement in the cut, is shown with the gray area in Figure 6-3. The regenerated part of the chip thickness at each angular position is produced due to the tool vibration in the current cut and the undulations left on the surface machined by the preceding tooth. Keeping track of workpiece surface undulations in 5-axis machining is not an easy task. In the current work, the tool vibration during the preceding tooth engagement will be taken as the surface undulation. This assumption is

reasonable as long as the tool tangential speed is much higher than the feed motion, which is the situation here.

The tool radial displacement, r, is composed of the displacements in the X_t and Y_t directions according to:

$$r = \mathbf{r}(\varphi)\mathbf{p}; \mathbf{r}(\varphi) = [\sin\varphi \quad \cos\varphi]; \mathbf{p} = \begin{bmatrix} x(t) \\ y(t) \end{bmatrix} \tag{6.11}$$

Substituting the uncut chip thickness from Equation (6.10) in Equation (6.8) results in the following:

$$\begin{aligned} F_{ts} &= g(\varphi) K_t \left(f_a \sin\theta + r - r^T \right)^{\alpha_t} \\ F_{rs} &= g(\varphi) K_r \left(f_a \sin\theta + r - r^T \right)^{\alpha_r} \end{aligned} \tag{6.12}$$

Landers and Ulsoy in [17] employed the nonlinear force model in the frequency domain calculation of stability lobes. For this reason, they linearized the cutting force model around the harmonic part of chip thickness:

$$\begin{aligned} F_{ts} &\approx g(\varphi) K_t \left(f_a \sin\theta \right)^{\alpha_t} + g(\varphi) \hat{K}_t \left(r - r^T \right); \hat{K}_t = \alpha_t K_t \left(s_t \sin\theta \right)^{\alpha_t - 1} \\ F_{rs} &\approx g(\varphi) K_r \left(f_a \sin\theta \right)^{\alpha_r} + g(\varphi) \hat{K}_r \left(r - r^T \right); \hat{K}_r = \alpha_r K_r \left(s_t \sin\theta \right)^{\alpha_r - 1} \end{aligned} \tag{6.13}$$

In Equation (6.13), the first terms of radial and tangential forces do not affect the stability of the cut. Therefore, by neglecting these parts, one can express the shear forces as

$$\begin{aligned} F_{ts} &= g(\varphi) \hat{K}_t \left(r - r^T \right) \\ F_{rs} &= g(\varphi) \hat{K}_r \left(r - r^T \right) \end{aligned} \tag{6.14}$$

Equation (6.14) is a linear mechanistic model, for which the cutting force coefficients, $\hat{K}_t$ and $\hat{K}_r$, vary at each elemental disk, $j_e = 1..N_e$, and tooth rotation angle, φ.

Combining the shear and ploughing forces from Equation (6.14) and (6.7), respectively, the total tangential and radial cutting forces on the cutting tooth j_c of the j_e element is obtained as:

$$\begin{aligned} F_t &= g(\varphi) \hat{K}_t \left(r - r^T \right) + g(\varphi) \mu C_{eq} \dot{r} \\ F_r &= g(\varphi) \hat{K}_r \left(r - r^T \right) + g(\varphi) C_{eq} \dot{r} \end{aligned} \tag{6.15}$$

Substituting the tool radial displacement from Equation (6.11) in Equation (6.15) returns the tangential and radial cutting forces in terms of tool deflection in the X_t and Y_t directions:

$$\begin{Bmatrix} F_t \\ F_r \end{Bmatrix} = g(\varphi)\begin{bmatrix} \hat{K}_t \\ \hat{K}_r \end{bmatrix}\mathbf{r}\left(\mathbf{p}(t)-\mathbf{p}(t-T)\right) + g(\varphi)\begin{bmatrix} \mu \\ 1 \end{bmatrix} C_{eq}\mathbf{r}\dot{\mathbf{p}} \tag{6.16}$$

These forces are projected onto the X_t and Y_t directions:

$$\begin{Bmatrix} F_x \\ F_y \end{Bmatrix} = \mathbf{T}(\varphi)\begin{Bmatrix} F_t \\ F_r \end{Bmatrix}; \mathbf{T}(\varphi) = \begin{bmatrix} -\cos\varphi & -\sin\varphi \\ \sin\varphi & -\cos\varphi \end{bmatrix} \tag{6.17}$$

The total cutting forces are computed by the summation of the elemental forces acting on all cutting teeth, $j_c=1..N_c$, of all elemental disks, $j_e=1..N_e$:

$$\mathbf{F} = \sum_{j_e=1}^{N_e}\sum_{j_c=1}^{N_c}\begin{Bmatrix} F_x \\ F_y \end{Bmatrix} \tag{6.18}$$

By inserting Equation (6.16) into Equation (6.17), and then the result into Equation (6.18), the total cutting forces are calculated in terms of the tool deflections, $\boldsymbol{p}$:

$$\begin{aligned}
&\mathbf{F} = \Delta z\mathbf{A}(\Delta\mathbf{p}) + \mathbf{B}\dot{\mathbf{p}};\\
&\Delta\mathbf{p} = \mathbf{p}(t)-\mathbf{p}(t-T)\\
&\mathbf{A}_{j_c,j_e} = g(\varphi)\mathbf{T}(\varphi)\begin{bmatrix} \hat{K}_t \\ \hat{K}_r \end{bmatrix}\mathbf{r}(\varphi); \mathbf{B}_{j_c,j_e} = g(\varphi)C_{eq}\mathbf{T}(\varphi)\begin{bmatrix} \mu \\ 1 \end{bmatrix}\mathbf{r}(\varphi);\\
&\mathbf{A} = \sum_{j_e=1}^{N_e}\sum_{j_c=1}^{N_r}\mathbf{A}_{j_c,j_e}, \mathbf{B} = \sum_{j_e=1=1}^{N_e}\sum_{j_c=1}^{N_r}\mathbf{B}_{j_c,j_e}
\end{aligned} \tag{6.19}$$

By substituting the total cutting force, $\boldsymbol{F}$, as a function of tool deflection in the X and Y directions, $\boldsymbol{p}$, from Equation (6.19) in Equation (6.3), the equation governing the vibration of the 2 DOF system is obtained as a DDE with time-varying coefficients. In Section 6.6, SDM will be used to determine the stability of the system described by this DDE. Before doing so, the calculation of start and exit angles, as well as the actual feedrate at each elemental disk and each cutter location, will be explained in the next two sections.

6.4 Start and Exit Angles

The start, φ_{st}, and exit, φ_{ex}, angles associated with each elemental disk depend on the grazing surface generated in the previous cut, $\mathbf{G}_p(\mathrm{u},\mathrm{v})$, and the grazing, or the machined surface, $\mathbf{G}(\mathrm{u},\mathrm{v})$, in the current cut. This is illustrated in Figure 6-4 for the down-milling operation. In this case, φ_{st} is determined by the intersection of the disk with $\mathbf{G}_p(\mathrm{u},\mathrm{v})$, whereas φ_{ex} is found at the tangent (grazing

point) of the disk with the machined surface $\mathbf{G}(\mathtt{u},\mathtt{v})$. Both the tangent and intersection points are determined in the workpiece coordinates, C_{wp}. They have to be transferred to the tool coordinates, C_t, to compute the entry and exit angles as explained below.

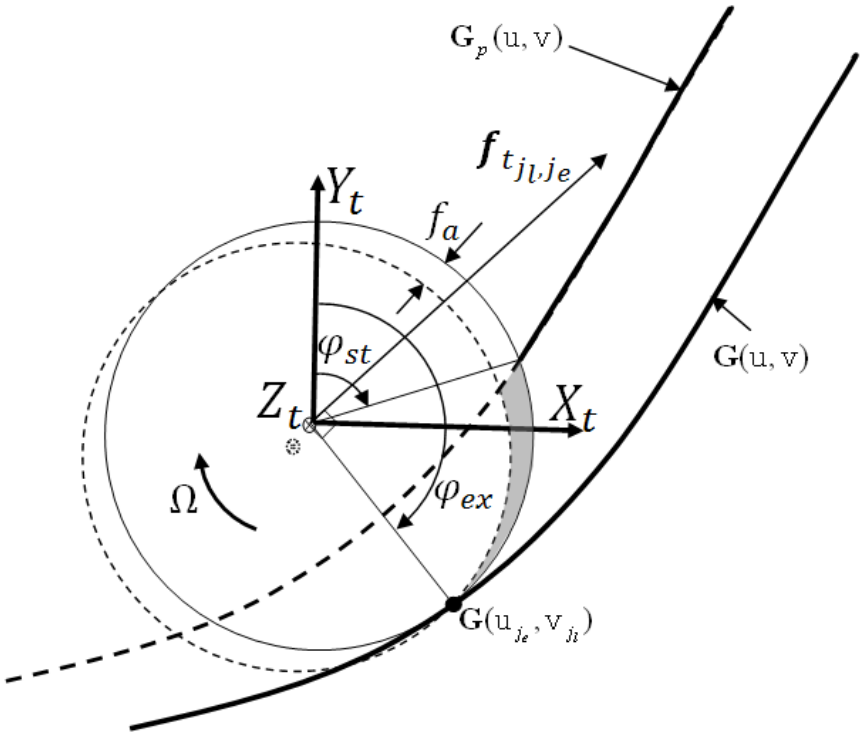

Figure 6-4: Start and exit angles for down-milling

The tangent point is obtained by simply substituting, in Equation (6.2), the $\mathtt{u}_{j_e}$, and $\mathtt{v}_{j_l}$ parameters corresponding to the elemental disk j_e and tool movement step j_l. This yields $\mathbf{G}(\mathtt{u}_{j_e},\mathtt{v}_{j_l})$. As indicated in Figure 6-4, its corresponding Cartesian coordinates are X_{ex}, Y_{ex} and Z_{ex} in C_{wp}. The subscript "*ex*" refers to exit. While obtaining the tangent point is straight-forward enough, finding the intersection point between the elemental disk and the surface grazed in the previous cut is more involved. This is illustrated with the help of Figure 6-5.

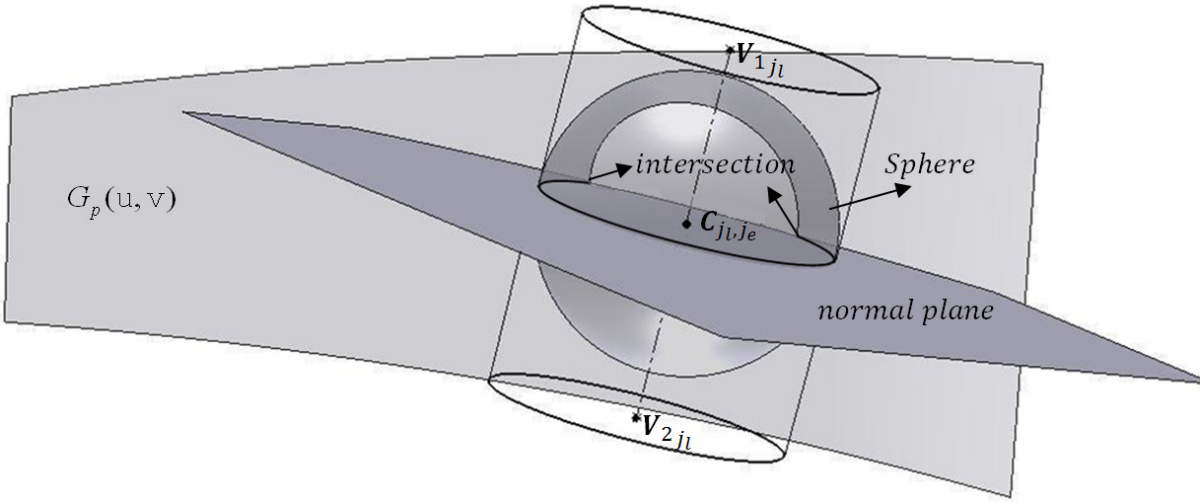

Figure 6-5: Intersection of sphere and normal plane with the surface generated in the previous cut

The intersection point can be thought of as the intersection point of three geometrical entities: a sphere, whose center coincides with the disk center, $\boldsymbol{C}_{jl,je}$, and its radius equal to the tool radius; the plane of the disk that contains $\boldsymbol{C}_{jl,je}$ and is normal to the tool axis; and the surface, $\mathbf{G}_p(u,v)$, grazed in the previous cut. Mathematically, this intersection is obtained by solving the following equations:

$$\begin{aligned} &\mathbf{G}_p(u,v).\mathbf{a}(v_{j_l}) - \mathbf{C}_{j_l,j_e}.\mathbf{a}_v(v_{j_l}) = 0 \\ &\left\|\mathbf{G}_p(u,v) - \mathbf{C}_{j_l,j_e}\right\|^2 - R^2 = 0 \end{aligned} \qquad (6.20)$$

The numerical solution of Equation (6.20) yields two intersection points, as shown in Figure 6-5. Knowing the initial conditions and the direction of motion of the tool, the proper intersection point is selected. The Cartesian coordinates of this intersection point will be designated X_{st}, Y_{st}, and Z_{st} where the subscript "*st*" refers to start. Again, this intersection point is obtained in C_{wp}.

Since the simulation of the dynamics is done in the tool coordinate system, the exit $(X_{ex},Y_{ex},Z_{ex})_{wp}$ and entry $(X_{st},Y_{st},Z_{st})_{wp}$ points in C_{wp} must be transferred to (X_{ex},Y_{ex},Z_{ex}) and (X_{st},Y_{st},Z_{st}), respectively, in C_t. This transformation is conducted according to the expression in Equation (6.21):

$$\begin{bmatrix} X \\ Y \\ Z \\ 1 \end{bmatrix}_t = \mathbf{R}_{XZ}\mathbf{R}_{t\to wp}\begin{bmatrix} X \\ Y \\ Z \\ 1 \end{bmatrix}_{wp} \tag{6.21}$$

where;

$$\mathbf{R}_{XZ} = \begin{bmatrix} 1 & 0 & 0 & 0 \\ 0 & \cos A & \sin A & 0 \\ 0 & -\sin A & \cos A & 0 \\ 0 & 0 & 0 & 0 \end{bmatrix}\begin{bmatrix} \cos C & \sin C & 0 & 0 \\ -\sin C & \cos C & 0 & 0 \\ 0 & 0 & 1 & 0 \\ 0 & 0 & 0 & 0 \end{bmatrix},$$

$$\mathbf{R}_{t\to wp} = \begin{bmatrix} 1 & 0 & 0 & -V_2^x \\ 0 & 1 & 0 & -V_2^y \\ 0 & 0 & 1 & -V_2^z \\ 0 & 0 & 0 & 1 \end{bmatrix}$$

A and *C* are the tilt and rotary angles, and (V_2^x, V_2^y, V_2^z) are the Cartesian coordinates of the tool tip in C_{wp}. Having obtained (X_{ex}, Y_{ex}, Z_{ex}) and (X_{st}, Y_{st}, Z_{st}) following the above transformation, the start and exit angles, which are measured from the axis Y_t of the tool coordinate frame C_t, are obtained from Equation (6.22).

$$\varphi_{st} = \tan^{-1}\frac{X_{st}}{Y_{st}}, \varphi_{ex} = \tan^{-1}\frac{X_{ex}}{Y_{ex}} \tag{6.22}$$

6.5 Chip Thickness

h is the uncut chip thickness at the tooth j_c, elemental disk j_e, and tool location j_l. It consists of harmonic, h^H, and regenerated, h^{reg}, components, as expressed in Equation (6.10). The harmonic part depends on the feedrate, f_a, which varies at each cutter location and elemental disk. The calculation of actual feedrate is addressed in this section.

Due to the tilt and rotary axes, the feedrate vector for each disk is different [62, 69]. This is indicated in Figure 6-3(a). This feedrate vector is the relative velocity vector between the tool and the workpiece; for disk j_e, it can be determined from:

$$\mathbf{f}_{j_l, j_e} = \frac{\mathbf{C}_{j_l+1, j_e} - \mathbf{C}_{j_l, j_e}}{\Delta\bar{t}} \tag{6.23}$$

where $\Delta\bar{t}$ is the time it takes for the disk center to move from the j_l^{th} to the $(j_l+1)^{th}$ position. This time is determined by the programmed feedrate and the interpolation strategy that the post-processor uses for the synchronization of linear and rotational axes. In the DECKEL-MAHO 5-axis machining center, TNC 430 used in the current work, the processor employs the pseudo-distance parameter (of inconsistent units) for interpolation, as follows:

$$ds = \sqrt{\Delta X_{tr}{}^2 + \Delta Y_{tr}{}^2 + \Delta Z_{tr}{}^2 + \Delta \mathtt{A}^2 + \Delta \mathtt{C}^2} \quad (6.24)$$

where:

$$\begin{bmatrix} \Delta X_{tr} \\ \Delta Y_{tr} \\ \Delta Z_{tr} \end{bmatrix} = (\mathbf{V}_{2_{j_l+1}} - \mathbf{V}_{2_{j_l}})_{tr} \quad (6.25)$$

V_{2jl} is the tool tip location at step j_l with respect to the tilt/rotary frame C_{tr}. Notice that, in our setup, the increment (V_{2jl+1}-$V_{2\,jl}$) in C_{tr} is the same as ($V_{2\,jl+1}$-$V_{2\,jl}$) measured relative to a fixed datum (home position) on the machine [81]. To apply Equation (6.24), $V_{2\,ji}$; $j_l = 1..N_l$ must be transformed first from C_{wp} to C_{tr}. For this change, the transformation in Equation (6.26) is applied:

$$\begin{bmatrix} X \\ Y \\ Z \\ 1 \end{bmatrix}_{tr} = \mathbf{R}_{XZ}.\mathbf{R}_{tr\to wp}.\begin{bmatrix} X \\ Y \\ Z \\ 1 \end{bmatrix}_{wp} \;;\; \mathbf{R}_{XZ} = \begin{bmatrix} 1 & 0 & 0 & 0 \\ 0 & \cos\mathtt{A} & \sin\mathtt{A} & 0 \\ 0 & -\sin\mathtt{A} & \cos\mathtt{A} & 0 \\ 0 & 0 & 0 & 0 \end{bmatrix}\begin{bmatrix} \cos\mathtt{C} & \sin\mathtt{C} & 0 & 0 \\ -\sin\mathtt{C} & \cos\mathtt{C} & 0 & 0 \\ 0 & 0 & 1 & 0 \\ 0 & 0 & 0 & 0 \end{bmatrix},$$

$$\mathbf{R}_{tr\to wp} = \begin{bmatrix} 1 & 0 & 0 & -U^{x}_{tr\to wp} \\ 0 & 1 & 0 & -U^{y}_{tr\to wp} \\ 0 & 0 & 1 & -U^{z}_{tr\to wp} \\ 0 & 0 & 0 & 1 \end{bmatrix} \quad (6.26)$$

In Equation (6.26), $\mathtt{A}$ and $\mathtt{C}$ are in degrees and $U_{tr\to wp}$ is the vector, as shown in Figure 6-1, which goes from the origin of C_{tr} to that of C_{wp}.

Having calculated the pseudo-distance parameter, the elapsed time to move from position j_l to j_l+1 is obtained from:

$$\Delta\bar{t} = \frac{ds}{f_{program}} \quad (6.27)$$

where $f_{program}$ is the programmed feedrate. Substituting $\Delta\bar{t}$ in Equation (6.23), we get $\mathbf{f}_{j_l,j_e}$. In this study, a straight cylindrical tool is used, and thus only the component of $\mathbf{f}_{j_l,j_e}$ perpendicular to the tool

axis, $\mathbf{f}_{t_{j_l,j_e}}$, contributes to the chip thickness. As such, the chip thickness expression presented here is a simplification of that developed by Ferry and Altintas [62] for tapered endmills. The subscript "*t*" refers to the "tangent" to the tool. This tangent feed component determines the feed per tooth, f_a. Equation (6.28) gives this feed per tooth acting on disk j_e at tool position j_l. Notice that, in Equation (6.28), full subscripts are included for clarification:

$$f_{a,j_l,j_e} = \frac{\left|\mathbf{f}_{t_{j_l,j_e}}\right|}{N_c}; \mathbf{f}_{t_{j_l,j_e}} = \mathbf{f}_{j_l,j_e} - \left(\mathbf{f}_{j_l,j_e}.\mathbf{a}(\nu_{j_l})\right)\frac{\mathbf{a}(\nu_{j_l})}{\left|\mathbf{a}(\nu_{j_l})\right|} \tag{6.28}$$

6.6 Stability Analysis Using SDM

The cutting forces obtained in Equation (6.19) are substituted in Equation (6.3), and the resulting DDE is rearranged in the following state space form:

$$\dot{\mathbf{q}} = \mathbf{L}\mathbf{q}(t) + \mathbf{R}\mathbf{q}(t-T); \quad \mathbf{q} = \begin{Bmatrix} \mathbf{p} \\ \dot{\mathbf{p}} \end{Bmatrix}$$

$$\mathbf{L} = \begin{bmatrix} \mathbf{0} & \mathbf{I} \\ \Delta z \mathbf{M}^{-1}\mathbf{A} - \mathbf{\Omega} & \mathbf{M}^{-1}\mathbf{B} - \xi \end{bmatrix}; \quad \mathbf{R} = \begin{bmatrix} \mathbf{0} & \mathbf{0} \\ \Delta z \mathbf{M}^{-1}\mathbf{A} & \mathbf{0} \end{bmatrix}; \quad \xi = \begin{bmatrix} \frac{C_x}{M_x} & 0 \\ 0 & \frac{C_y}{M_y} \end{bmatrix}; \quad \mathbf{\Omega} = \begin{bmatrix} \frac{K_x}{M_x} & 0 \\ 0 & \frac{K_y}{M_y} \end{bmatrix}$$

(6.29)

The presented state space equation follows the same format as Equation (5.25), with the difference between the two equations being in the formation of the directional coefficient matrices, ***A*** and ***B***. In Equation (6.29), they are made of the elemental matrices obtained from each axial disk j_e=*1..*N_e. For each disk, the start and exit angles vary, as do the cutting force coefficients at each angular position of cutting tooth. After calculating the directional coefficient matrices, they are applied in the SDM procedure explained in Section 5.4 to determine the stability of cut. In the next section, the method will be illustrated in the machining of flat surfaces using straight cuts. The results will be presented in the form of stability lobes, and the stability map concept will be introduced.

6.7 Milling of Flat Surfaces Using Helical Tool

In this section, SDM is used to develop stability lobes and maps of milling of flat surfaces at different radial immersions. A set of cutting experiments is also carried out to verify the accuracy of the presented method in the prediction of cutting stability. The tool used in the experiments was a 4-flute 25.4 mm diameter HSS endmill with helical teeth mounted on a DECKEL-MAHO 5-axis machining center. The following parameters were identified from the modal analysis of the frequency response functions, FRF, measured at the free end of the tool, using hammer impact:

$$\begin{aligned} f_x &= 338Hz, K_x = 1.8\times10^7 \frac{N}{m}\zeta_x = 0.03 \\ f_y &= 350Hz, K_y = 0.9\times10^7 \frac{N}{m}\zeta_y = 0.03 \end{aligned} \tag{30}$$

As the workpiece was aluminum alloy 6061-T6, the cutting force coefficients of Equation (6.9) are used. Also, K_{sp} for the aluminum alloy was reported at 1.5×10^{14} N/m^3 in [35].

6.7.1 Stability Lobes

In 3-axis machining, the tilt and rotary angles of utilized machine are kept at zero; hence, the feedrate remains constant throughout the toolpath and is the same along the tool axis. The start and exit angles, φ_{st} and φ_{ex}, are determined with respect to the tool radial immersion, and f_a, the feed/tooth, follows the programmed feedrate. In the conducted flat surface milling experiments the feedrate was maintained at 0.05 mm/tooth. Note that although constant feedrate, f_a, is used in this part, the variation in the instantaneous chip thickness is still considered in establishing the lobes.

At each point in a grid of spindle speeds and axial depths of cut, the maximum eigenvalue of the transition matrix of Equation (5.31) is calculated, and the stability criterion is applied. Then, the stability lobes are established by plotting the contour of stability outcome on the grid. Figure 6-6 shows the stability lobes of ½ immersion up-milling operation. Three sets of stability lobes are established at wear land W=40, 60 and 80 μm.

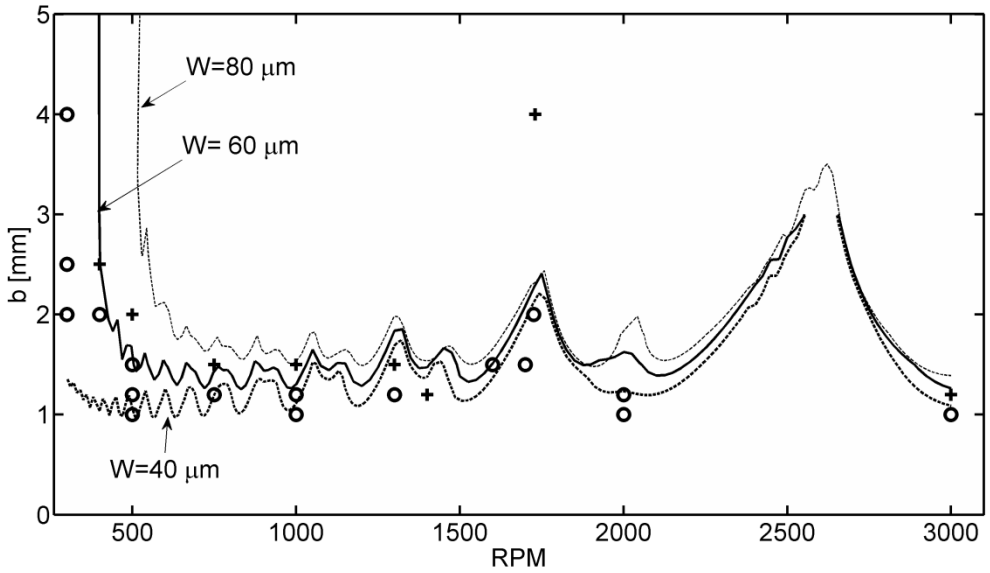

Figure 6-6: Stability lobes of ½ immersion up-milling computed for different wear: W=0.04mm (dashed line), W=0.06mm (solid line), and W=0.08mm (dotted line); Experimentally measured stable (circles) and unstable (crosses) points

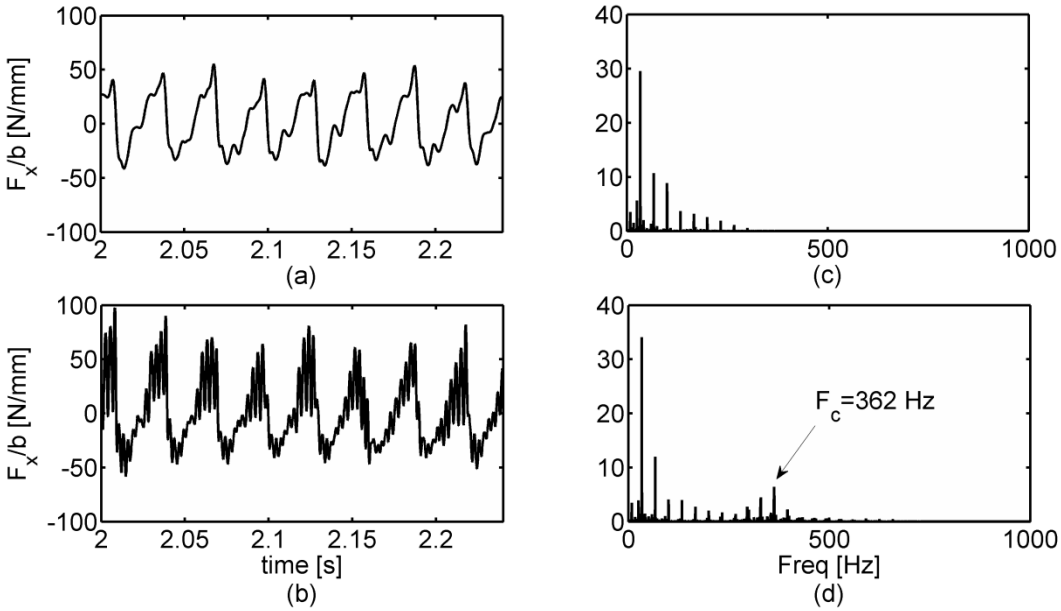

Figure 6-7: Time traces of measured cutting forces in ½ immersion up-milling at 500 RPM and: (a) *b*=1.5mm, (b) *b*=2mm, and the corresponding power spectra at: (c) at *b*=1.5mm, (d) *b*=2mm

The stability of the cut is also examined experimentally at the points shown with the crosses and circles in Figure 6-6. The cutting forces were recorded using a Kistler 9255 table dynamometer, and the force signal was employed to determine if the cut was stable, o, or unstable, +. Examples of the recorded stable and unstable forces are shown in Figure 6-7. The spindle speed was 500 RPM, and the forces were normalized by the axial depth of cut. The frequency spectra of the demonstrated signals are shown in parts (c) and (d). According to the frequency spectra, the amplitude of the force at the chatter frequency, f_c, is close to 10N/mm at b=2mm, and zero at b=1.5mm. The former is shown as an unstable cut (with a cross) in Figure 6-6, and the latter as stable (with a circle).

Comparing the experimentally measured stable and unstable points with the computed lobes, it can be seen that they agree, for the most part, with the borders predicted using W=60μm. This agreement is a source of concern, considering the fact that a sharp tool was utilized in the cutting tests. One must keep in mind, however, that there could be other sources of damping in the cut besides the indentation mechanism. Also, tool runout was not included in the model. In the present experiments, the radial runout of the tool was measured at 15μm. This value of runout relative to the feed/tooth of 50 μm could affect the stability limit by disturbing the natural regeneration of the chip thickness, according to the study carried out by Grenon [82]. There is a need either to modify the model to explicitly include tool runout, or to compile more experimental evidence to provide better estimates of process damping values for typical tools and set ups. Such investigations were not conducted in the present work and could be a subject for future research.

Nonetheless, W=60μm was used as the effective tool flank wear to calculate the stability lobes of ¼ and ⅛ immersion up-milling, shown in Figure 6-8 and Figure 6-9, respectively. With the exception of a few points, in both cases the calculated lobes agree reasonably well with the measured stable and unstable points. This provides a further justification for the approach of employing an effective wear value that is established empirically. The agreement also verifies the accuracy of the presented method in the prediction of stability borders in milling with helical teeth and including process damping.

Having verified the formulation using cuts with simple uniform geometry, a new concept is developed next to present the stability of a cut of varying geometry. Rather than establishing the stability lobes, which show the limit width of cut versus speed, a stability map will be established for known toolpath and workpiece/engagement geometry versus speed. First, the stability map will be established for symmetric flat surface to show the close association between stability maps and stability lobes.

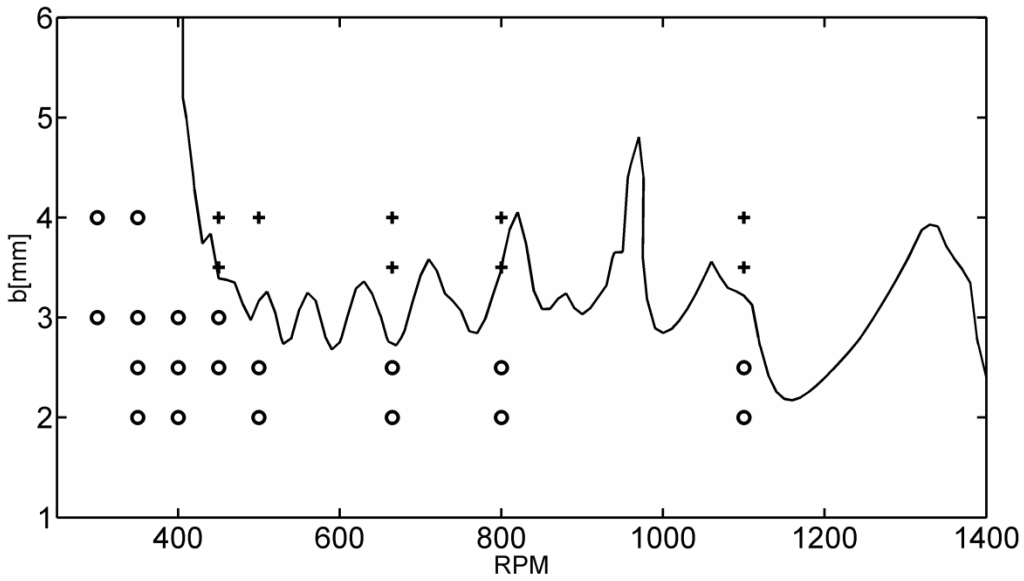

Figure 6-8: Computed stability lobes of ¼ immersion up-milling, and experimentally measured stable (circles) and unstable (crosses) points

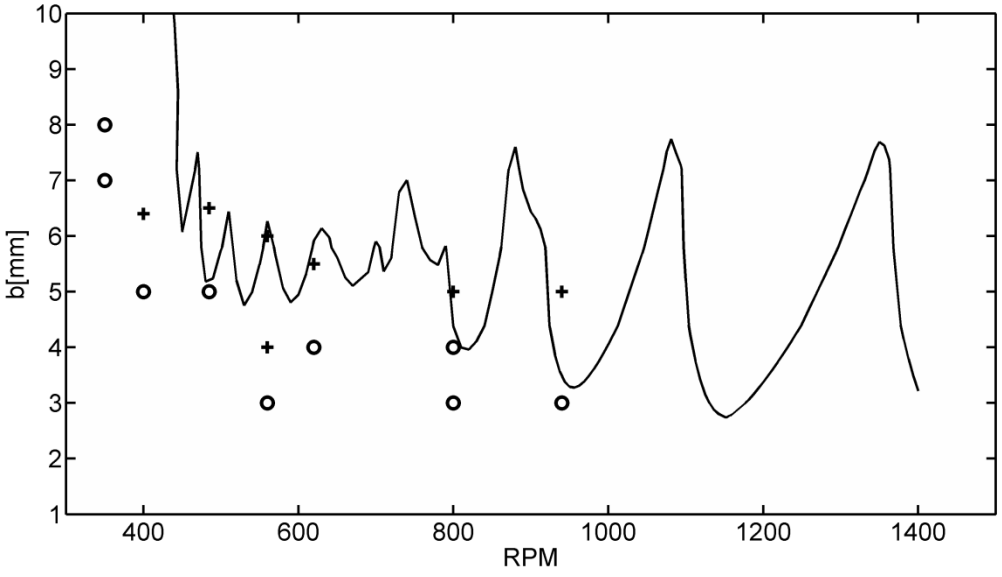

Figure 6-9: Computed stability lobes of ⅛ immersion up-milling, and experimentally measured stable (circles), and unstable (crosses) points

6.7.2 Stability Maps

Figure 6-11 shows the cutting forces recorded while ⅛ immersion up-milling of the flat surface illustrated in Figure 6-10. The feedrate was kept at 0.05 mm/tooth in the Y_t direction , and the axial depth of cut varied between 1 and 6 mm along the 200 mm long toolpath.

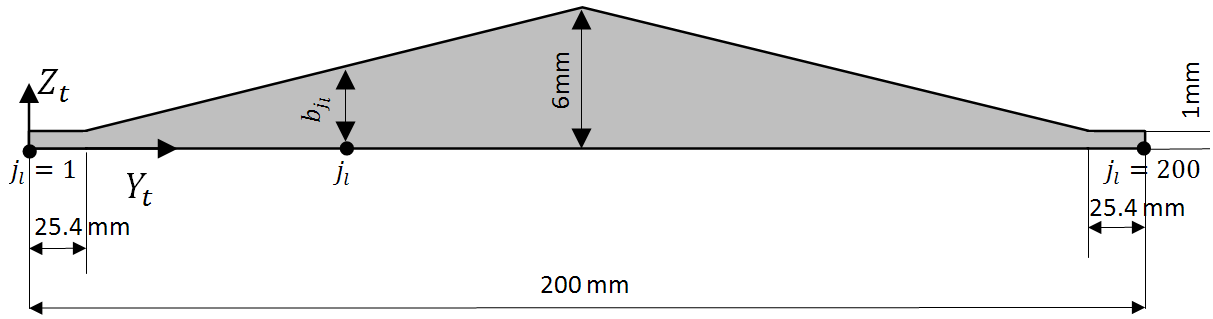

Figure 6-10: The triangular flat surface geometry

In Figure 6-10, the total length of the cut is 200 mm. The stability of the cut will be evaluated at increments of 1 mm along the toolpath. Accordingly, j_l=1..200 along the path would indicate cutter location. With respect to the geometry of the surface, the tool tip has moved j_l mm in Y_t direction at the j_l th cutter location, and its axis is aligned with the Z_t direction. The recorded forces are demonstrated in terms of the cutter location instead of time. The profile of the cutting force at 425 RPM, part (a), follows the variation in the axial depth of cut, which changes from 1mm at either end to 6 mm in the middle, as does the recorded force at 1100 RPM, except for the excessive vibration observed between cutter locations 60 and 140. According to the ⅛ immersion stability lobes established in Figure 6-9, at 425 RPM, the cut is stable for axial depths of cut less than 6 mm, and is unstable for axial depths of cut more than 3mm at 1100 RPM. With respect to the geometry of the flat surface, at cutter location 60, the axial depth of cut exceeds 3mm, and stays above that until cutter location 140.

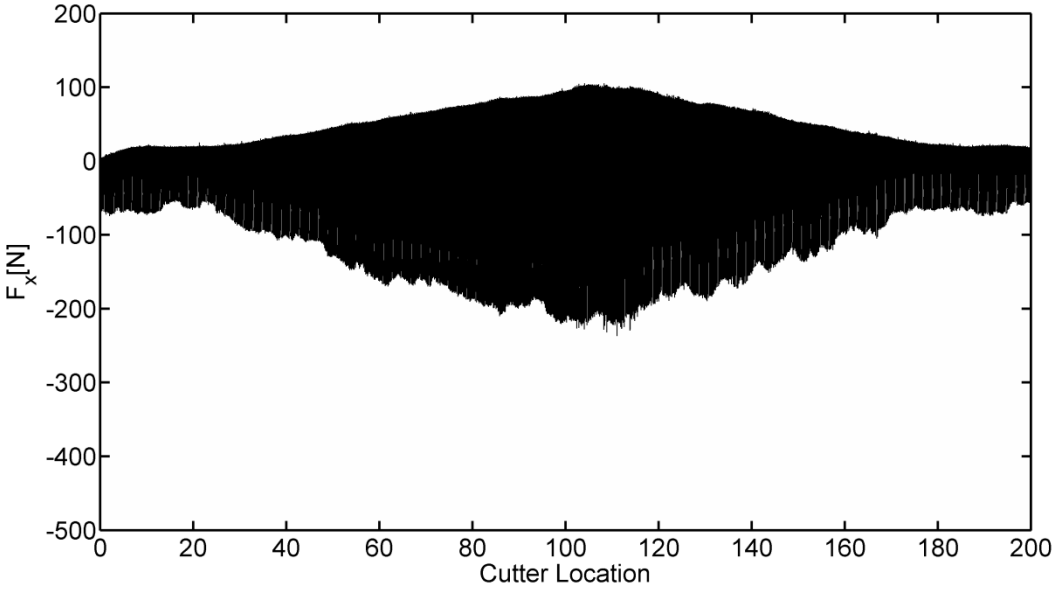

(a)

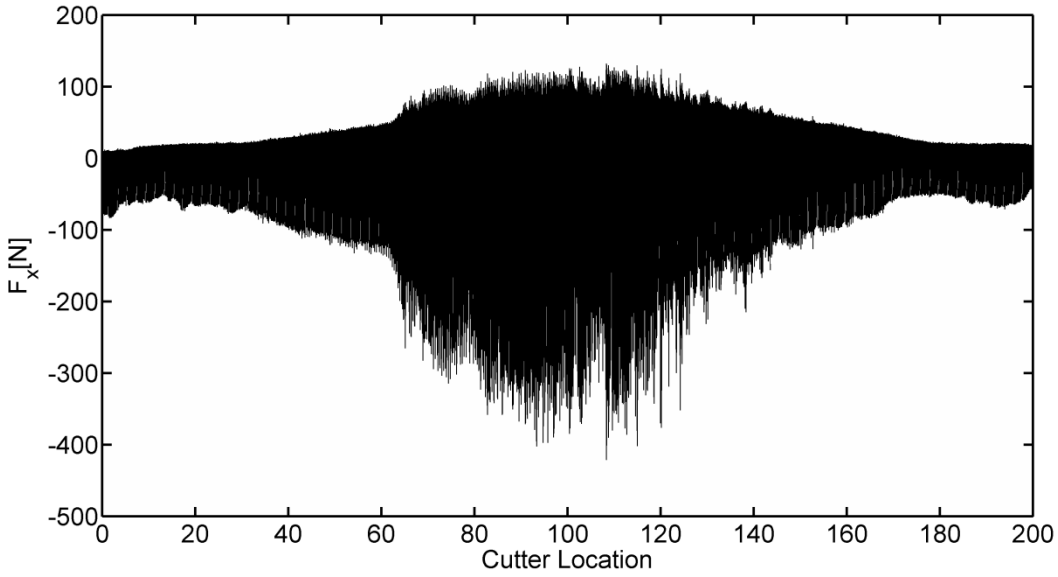

(b)

Figure 6-11: Measured cutting force in the Y_t direction for the triangular surface at: (a) 425 RPM, and (b) 1100 RPM.

The stability of ⅛ immersion up-milling at each cutter location, j_l =1..200, and a grid of spindle speeds is examined by calculating the maximum eigenvalue of the transition matrix in Equation

(5.31). The contour of the instability criterion outcome is plotted in Figure 6-12. The points inside the gray areas are unstable, while the ones inside the white areas are stable. The map is symmetric around the middle of the cut at j_l =100, with the upper half being a mirror image of the lower half; it simply follows the symmetry of the triangular surface. In fact, the lower half of the map, j_l =1..100, is an alteration of the ⅛ immersion stability lobes, shown in Figure 6-9, between b=1 and 6mm, in which the vertical axis of the depth of cut has been replaced by the cutter location number. This diagram will be referred to as the stability map; it shows the stable and unstable cutter locations of a toolpath versus spindle speed.

Cutting experiments of the flat triangular surface were conducted at several spindle speeds. The cutting forces were recorded similar to Figure 6-11 and were used to determine the stable and unstable cutter locations. The results of measurements are also plotted in Figure 6-12. At each spindle speed, the stable cutter locations are marked with circles and the unstable ones with crosses. Excellent agreement is observed between the computed maps and the experimental results.

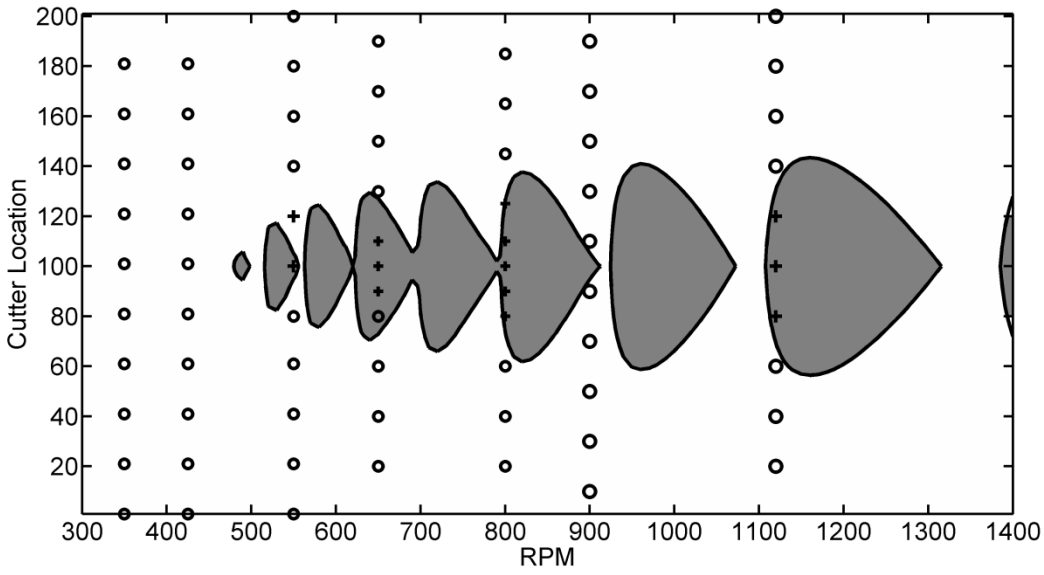

Figure 6-12: Stability maps of ⅛ immersion up-milling of flat triangular surface, and experimentally measured stable (circles) and unstable (crosses) cutter locations

Stability maps were established for ¼ immersion up-milling of the flat triangular surface, as shown in Figure 6-13. Also shown in this figure are the experimentally measured stable and unstable cutter locations throughout the toolpath. Similar to Figure 6-12, the stable cutter locations are marked with

circles and the unstable locations with crosses. The unstable cutter locations all fall inside the gray areas and the stable ones inside the white areas; only at 565 RPM are some stable cutter locations detected inside the gray areas. However, these points are adjacent to the stability borders, and therefore even small fluctuations in spindle speed may cause the vibration to fall in the stable region.

Having verified the developed method in milling the triangular flat surface at 2 immersions, the method will be applied next to 5-axis flank milling of three curved surfaces.

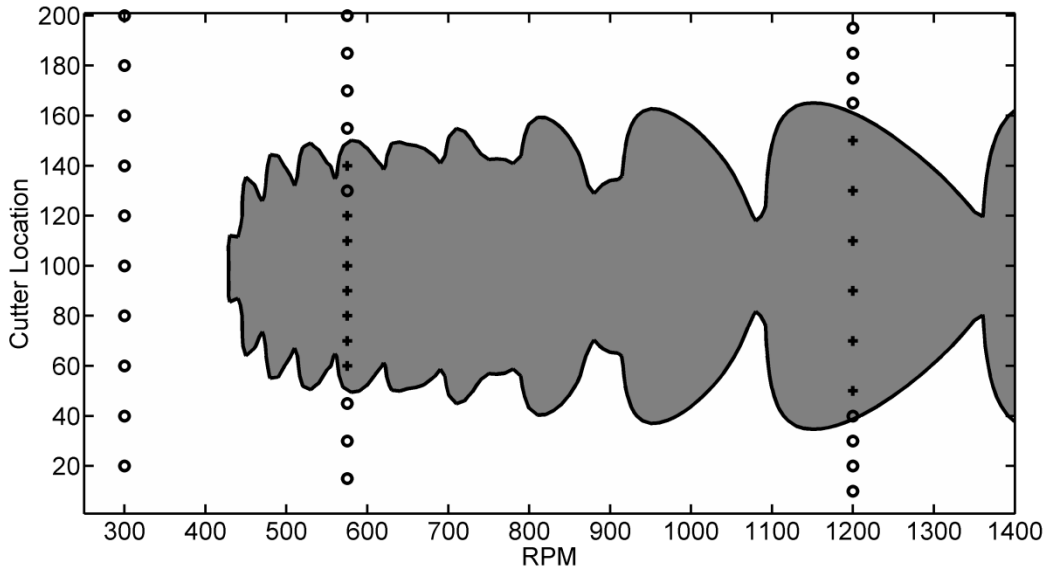

Figure 6-13: Computed stability map of ¼ immersion up-milling of the flat triangular surface, and experimentally measured stable (circles) and unstable (crosses) cutter locations

6.8 5-Axis Flank Milling

In this part of the study, a time domain simulation is used to investigate chatter in 5-axis flank milling of three curved surfaces. The cutting forces and torques during the finishing pass of three curved surfaces are also measured to examine the accuracy of the simulations. SDM is then used to determine the stability of the cut at each cutter location, and the stability map associated with each surface is established and verified by numerical simulations.

The basic surface chosen for testing is constructed using two quadratic Bezier curves, $\boldsymbol{L}_1(\nu)$ and $\boldsymbol{L}_4(\nu)$, with the following parametric equations:

$$\mathbf{L}_1(v)=\sum_{l=0}^{2}\mathbf{P}_l B^2{}_l(v);\mathbf{P}_0=\begin{bmatrix}35\\-15\\0\end{bmatrix},\mathbf{P}_1=\begin{bmatrix}65\\-45\\0\end{bmatrix},\mathbf{P}_2=\begin{bmatrix}110\\-60\\0\end{bmatrix}$$
$$\mathbf{L}_4(v)=\sum_{l=0}^{2}\mathbf{P}'_l B^2{}_l(v);\mathbf{P}'_0=\begin{bmatrix}50\\0\\-30\end{bmatrix},\mathbf{P}'_1=\begin{bmatrix}65\\-45\\-30\end{bmatrix},\mathbf{P}'_2=\begin{bmatrix}95\\-75\\-30\end{bmatrix} \quad (6.31)$$

where $B_l^2(v)$, $i=1..3$, are the quadratic Bezier basis functions. $\boldsymbol{L}_1(v)$ and $\boldsymbol{L}_4(v)$ are plane curves; they are defined in C_{wp} and their coordinates are in millimeter. $\boldsymbol{L}_1(v)$ and $\boldsymbol{L}_4(v)$ are separated in the Z_{wp} direction by 30mm, which translates into surface height of 30mm. Two other surfaces are also tested; one is bounded by the curves $\boldsymbol{L}_3(v)$ and $\boldsymbol{L}_4(v)$ and its height is 5mm, and the other is bounded by $\boldsymbol{L}_1(v)$ and $\boldsymbol{L}_2(v)$, with a height of 15mm, where $\boldsymbol{L}_2(v)$ and $\boldsymbol{L}_3(v)$ are constructed out of $\boldsymbol{L}_1(v)$ and $\boldsymbol{L}_4(v)$, as shown in Equation (6.32).

$$\mathbf{L}_2(v)=\left(\frac{1}{2}\right)\mathbf{L}_1(v)+\left(\frac{1}{2}\right)\mathbf{L}_4(v)$$
$$\mathbf{L}_3(v)=\left(\frac{1}{6}\right)\mathbf{L}_1(v)+\left(\frac{5}{6}\right)\mathbf{L}_4(v) \quad (6.32)$$

A top view in the direction of Z_{wp} of the bounding curves of the three surfaces is given in Figure 6-14. For each tested surface, the bounding curves, e.g., $\boldsymbol{L}_1(v)$ and $\boldsymbol{L}_4(v)$, would correspond to $\boldsymbol{R}(v)$ and $\boldsymbol{S}(v)$, respectively, shown in Figure 6-2. Table 6-1 lists $\boldsymbol{R}(v)$ and $\boldsymbol{S}(v)$ combinations of the three test surfaces, along with their heights.

For each test surface, the tool path is generated by rolling a 25.4mm diameter, 4-flute cylindrical tool with 30° helix angle on its corresponding top and button curves. For force calculations and chatter prediction, the surface machined in the previous path, $\boldsymbol{G}_p(u, v)$, is generated using the same tool path, with the exception that it is offset by a constant amount of 2mm in the Y_{wp} direction, to produce the machined surface $\boldsymbol{G}(u, v)$ in the current cut. This relationship is given in Equation (6.33).

$$\mathbf{G}_p(u,v)=\mathbf{G}(u,v)+\begin{bmatrix}0\\2\\0\end{bmatrix} \quad (6.33)$$

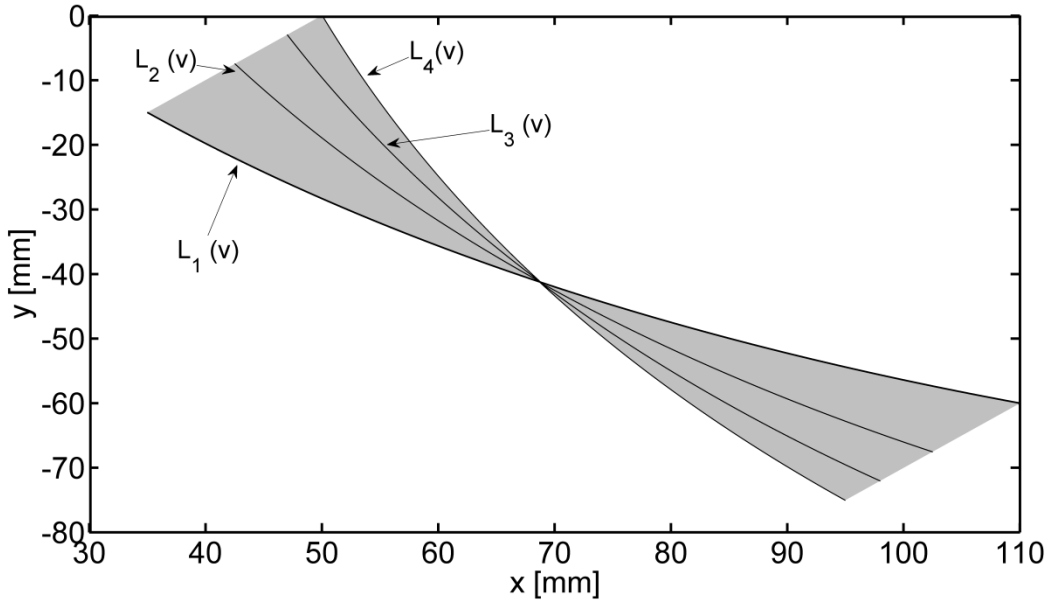

Figure 6-14: Top view of test surfaces, with their generating curves (rails)

Table 6-1: Geometry of test surfaces

Test surface	$\mathbf{R}(v)$	$\mathbf{S}(v)$	Surface height (mm)
1	$\mathbf{L}_3(v)$	$\mathbf{L}_4(v)$	5
2	$\mathbf{L}_1(v)$	$\mathbf{L}_2(v)$	15
3	$\mathbf{L}_1(v)$	$\mathbf{L}_4(v)$	30

6.8.1 Numerical Simulation and Experimental Results

For the numerical simulation, the engaged part of the tool is divided into 60 elemental disks. At each tool position along the path, φ_{st} and φ_{ex} are calculated for all the disks using the method presented in Section 6.4. For instance, Figure 6-15 shows these angles at a point midway along the path used to machine Surface 3. As can be seen, these angles vary for disks at different heights from the tool tip. For the same disk, these angles also vary from one tool position to the next.

The tool used was 25.4 mm in diameter, with four teeth at a helix angle of 30^o. The spindle speed was set at 1750 RPM, and the programmed feedrate was 2000 mm/min. The actual feedrate for each elemental disk was calculated following the procedure presented in Section 6.5. As an example, the actual feedrate at the tool tip for test surface 3 is shown in Figure 6-21(a); its maximum value is only 750 mm/min at the end of the tool path, while it drops drastically to a mere 145 mm/min in the

middle section of the cut. The feedrate is used to calculate the feed/tooth and the resulting harmonic component of the chip thickness, as explained in Section 6.5. The regenerated component of the chip thickness is calculated from the vibrations associated with the previous time step. With the chip thickness now available, the cutting forces acting on each tooth are calculated, along with the ploughing forces using the indentation model. They are then resolved along the tool coordinates X_t and Y_t, summed up for all teeth engaged in the cut, for all disks, to account for the total forces acting on the tool at one position. These forces are then applied to the tool dynamic model to compute the resulting vibration. In essence, beyond finding the chip thickness and the entry and exit angles, the procedure of simulating chatter in the time domain is the same as that already available in the previous chapters, and so the details of the simulation procedure will not be repeated here.

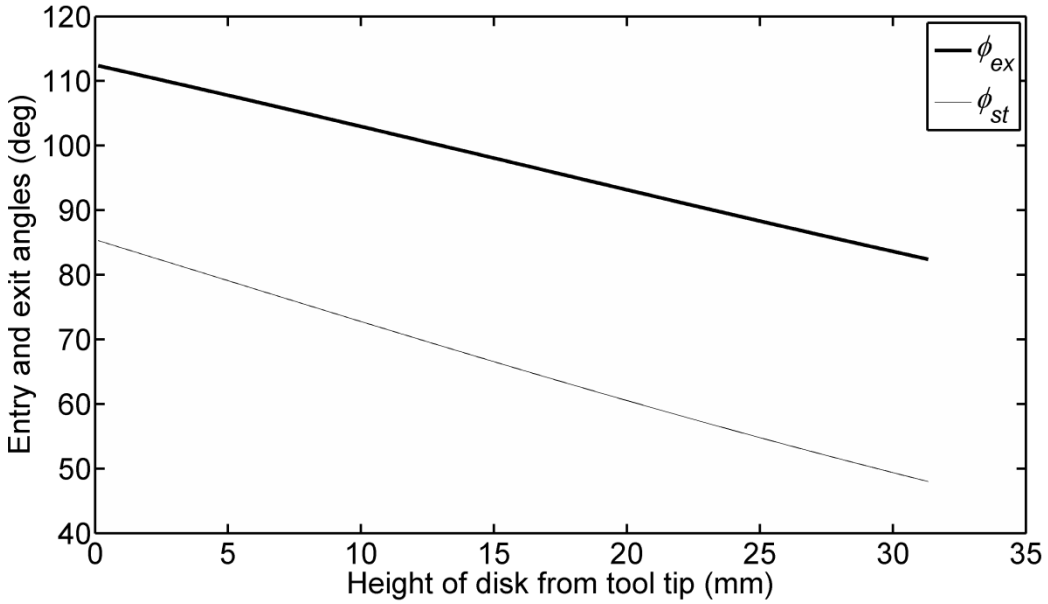

Figure 6-15: Start, φ_{st}, and exit, φ_{ex}, angles for all of the elemental disks of the tool, at midpoint along the tool path to generate Surface 3

The same three surfaces were also machined on the 5-axis DEECKEL-MAHO machining centre, employing the same cutting conditions: spindle speed=1750 RPM and programmed feedrate= 2000 mm/min. An impact test was used to measure the receptance at the tool tip, as is shown in Figure 6-16. The modal parameters are extracted by the curve fitting of the measured receptances; the fitted curves are shown in this figure, as well. The extracted modal parameters are also reported in Table 2.

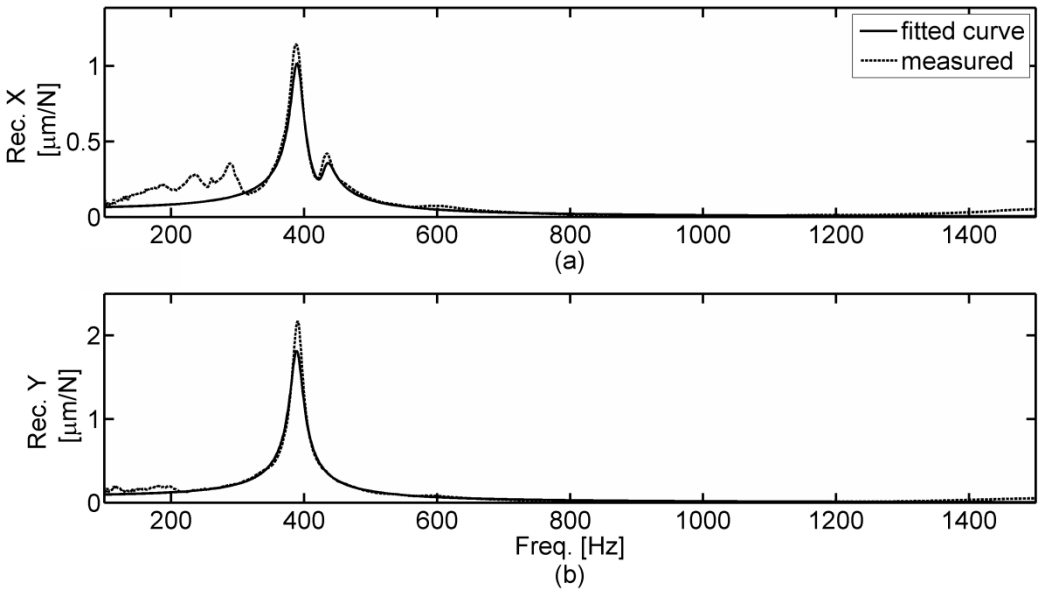

Figure 6-16: Measured receptances in the X_t and Y_t directions, and the curve fitted on them to extract the modal parameters

In the tested frequency range, the frequency response function shows two modes in the X_t direction and only one mode in the Y_t direction.

Table 2: The modal parameters of the tool in the X_t and Y_t directions.

		K[N/m]	f_n *[Hz]*	ξ
X	*Mode 1*	2×10^7	*390*	*0.02*
	Mode 2	0.87×10^8	*433*	*0.02*
Y		1.1×10^7	*389*	*0.02*

Since only one degree of freedom in considered at each direction, the most flexible mode of direction X_t is taken into account and the one at 433Hz is neglected in the modeling. The low natural frequencies reported here are associated with the tool and rotary dynamometer assembly as they are mounted in the machine. A Kistler rotary dynamometer was mounted in the spindle. For each surface, the workpiece was first prepared for the finishing pass by following a tool path that is offset by 2 mm in Y_{wp} from the final path. This, in effect, left 2mm radial depth of cut that had to be removed in the finishing pass.

The simulated and measured cutting forces and torque associated with the first test surface (height 5mm) are shown in Figure 6-17. There are differences at the beginning and end of the plots between the simulated and measured values; these differences are attributed to extra material at these locations associated with the tool leading in and out of the stock that were not included in the simulation. It should also be mentioned here that, in machining this narrow surface, 5 mm, at the low immersion of 2mm, tooth impacts and tool runout would contain significant harmonics that could excite the structural modes and possibly get magnified because of the dynamic response of the dynamometer itself. As can be seen, in the spectrum of the un-filtered data in Figure 6-18(a), the 11^{th} and 13^{th} harmonics of the tool rotational speed are magnified compared to the lower harmonics. For this reason, a low pass filter was applied, as shown in Figure 6-18 (b), to reduce the effect of the "magnification factor" and bring them closer to the higher harmonics of the forces generated in the simulation. This is evident by comparing the spectrum of the filtered measured force in Figure 6-18(b) with the corresponding spectrum obtained from the simulation in Figure 6-18(c). Fortunately, the filtering was only needed for the measured forces associated with the 5 mm surface, and no filtering was applied for the measured forces when machining the 15 and 30 mm surfaces. No filtering was applied for the measured torques for the three surfaces. With the above in mind, we can see the close agreement between the measured and simulated torque and force plots. Close ups of the measured and simulated torque and forces obtained around the middle of the tool path is also included in Figure 6-17; again, excellent agreement can be seen. No chatter was observed, either in simulation or in experiment, while machining Surface 1. To assess the role of process damping, the simulation was also run for this surface without including the ploughing forces. Figure 6-19 shows the simulated torque in this case; it indicates machining instability in the mid section of the tool path where the feedrate drops to a low level. This obviously contradicts the experimental evidence presented in Figure 6-17 and shows, beyond a doubt, the importance of including the process damping in the simulation model for the present surface and cutting conditions.

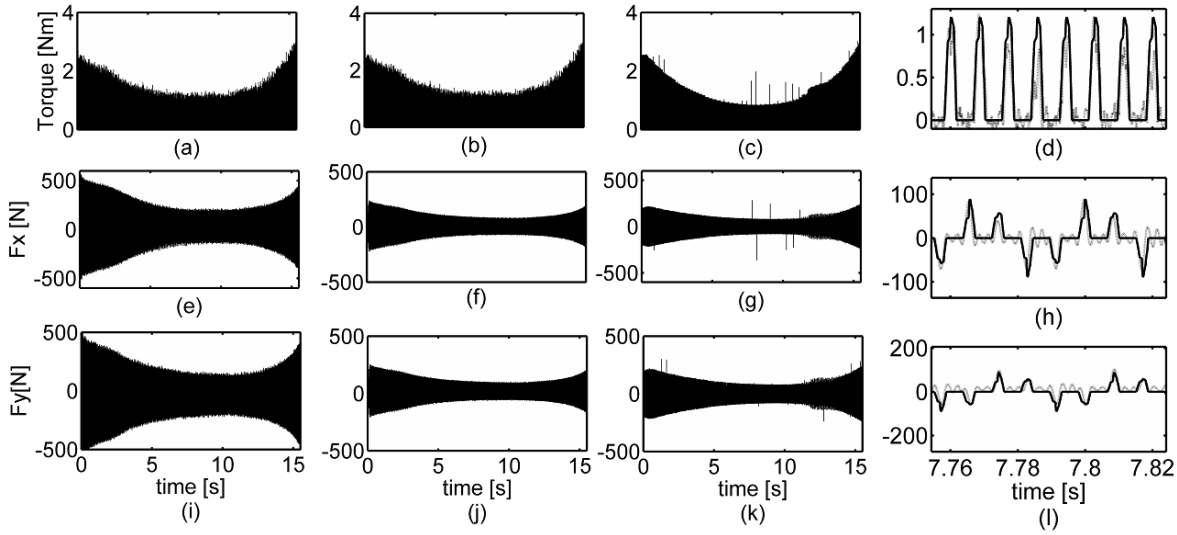

Figure 6-17: Measured (a, e, i and b), measured and filtered (f and j), and simulated (c, g and k) torque and cutting forces in machining test surface 1, height 5mm; close up (d, h and l) of torque and cutting forces at middle of tool pass; simulated (solid line); measured and filtered (dotted line)

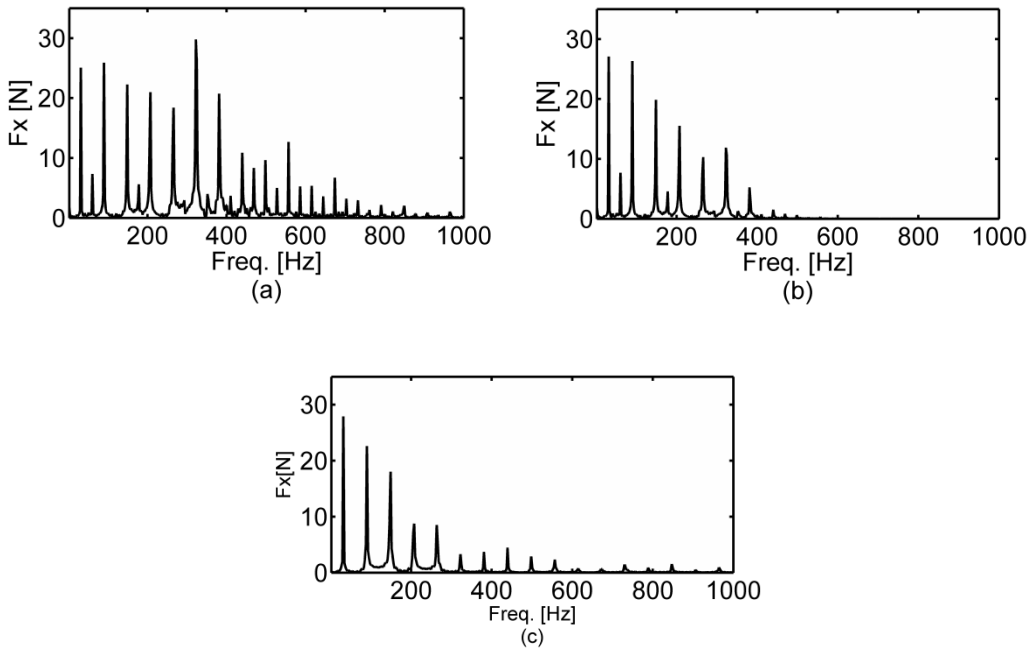

Figure 6-18: Power spectra of: a) un-filtered measured (b) filtered measured, and (c) simulated force in machining Surface 1, height 5mm

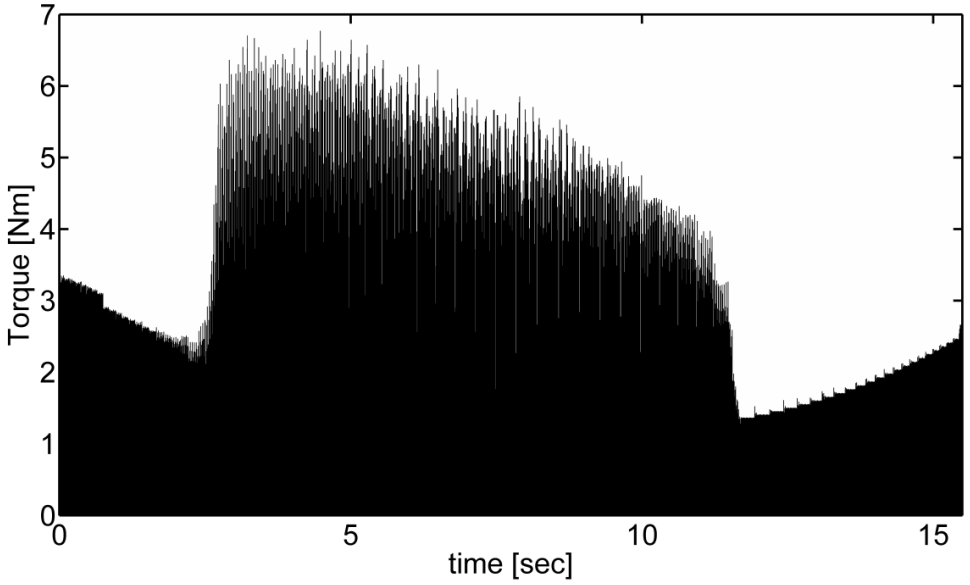

Figure 6-19: Simulated torque without including process damping in machining test Surface 1

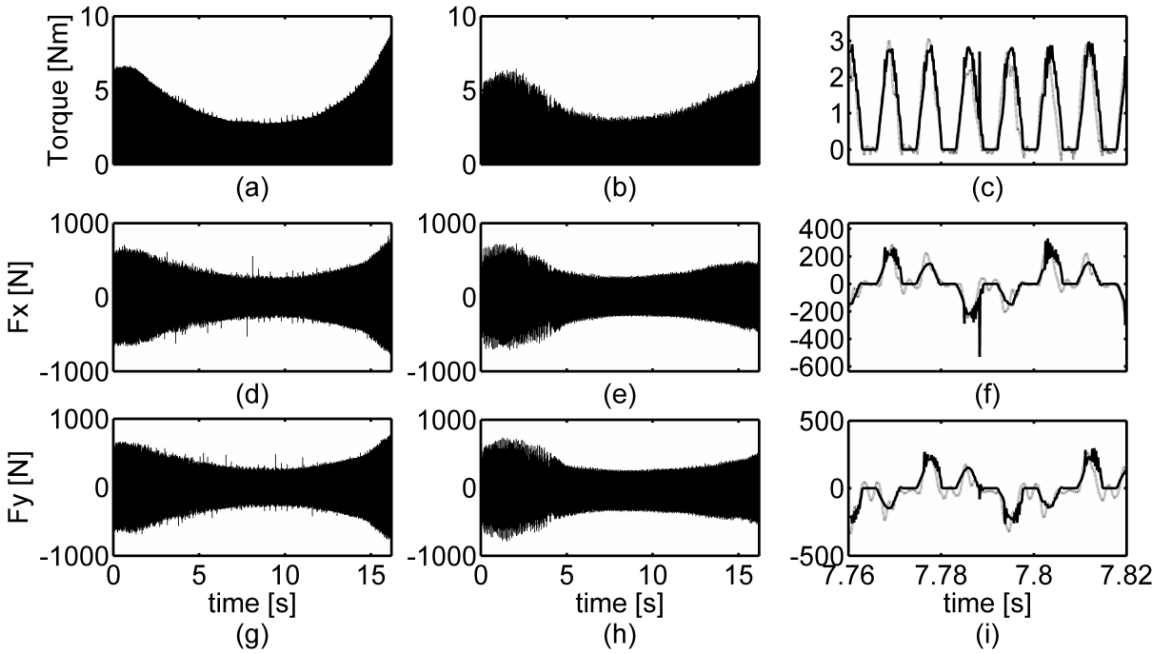

Figure 6-20: Measured (b, e and h) and simulated (a, d and g) torque and cutting forces in machining test Surface 2, height 15 mm, (c, f and i); close up of torque and cutting forces at middle of tool pass; simulated (solid line); measured (dotted line)

The simulated and measured torque and cutting forces obtained in machining test surface 2, height 15 mm, are shown in Figure 6-20. Here, there was no need to filter the measured force signals. As can be seen, the agreement between simulated and measured torque and forces is excellent, and no chatter was detected in machining this surface.

Results of simulation and experimental work for test surface 3, height 30mm, are shown in Figure 6-21 and Figure 6-22. Chatter occurred in machining this surface. In Figure 6-21(a), the feedrate computed at the tool tip is plotted against the distance traveled along the tool path. It can be seen that the feedrate throughout the travel is well below the programmed feedrate of 2000 mm/min. In particular, the feedrate drops drastically around the midpoint, where there was a considerable rotary motion combined with little translation of the tool. Figure 6-21(b) shows the same feedrate along the path, this time plotted against travel time. Figure 6-21(c, d) show the simulated and measured torques, respectively. Apart, from the beginning and end of the plots, the agreement is good. Figure 6-22 shows the measured and simulated forces obtained in machining this surface. Figure 6-22 (a) and (b) show the simulated components while figures (c) and (d) show the corresponding measured values. Close ups of the measured and simulated forces, superimposed on one another, are shown in Figure 6-22 (e) and (f). Two regions are indicated in Figure 6-22(a) and (c); part A around the middle of the path, and part B close to the end. The power spectra of the simulated and measured time traces of these regions are shown in Figure 6-22 (g), (h), and Figure 6-22 (i), (j), respectively. The power spectra of the simulated and measured forces in region B show the rotational speed and its 3^{rd} and 5^{th} harmonics. No chatter was observed in this region. On the other hand, chatter was detected in the power spectra of region A, where the tool vibration modes modulated by the rotational speed are clearly visible at 420 Hz and 478 Hz. In this region, the feedrate, and consequently the chip thickness, become so small and the dynamic cutting force coefficient so large, that machining instability takes place. Such observation was also made by Ismail and Ziaei [64] in 5-axis machining of a turbine blade.

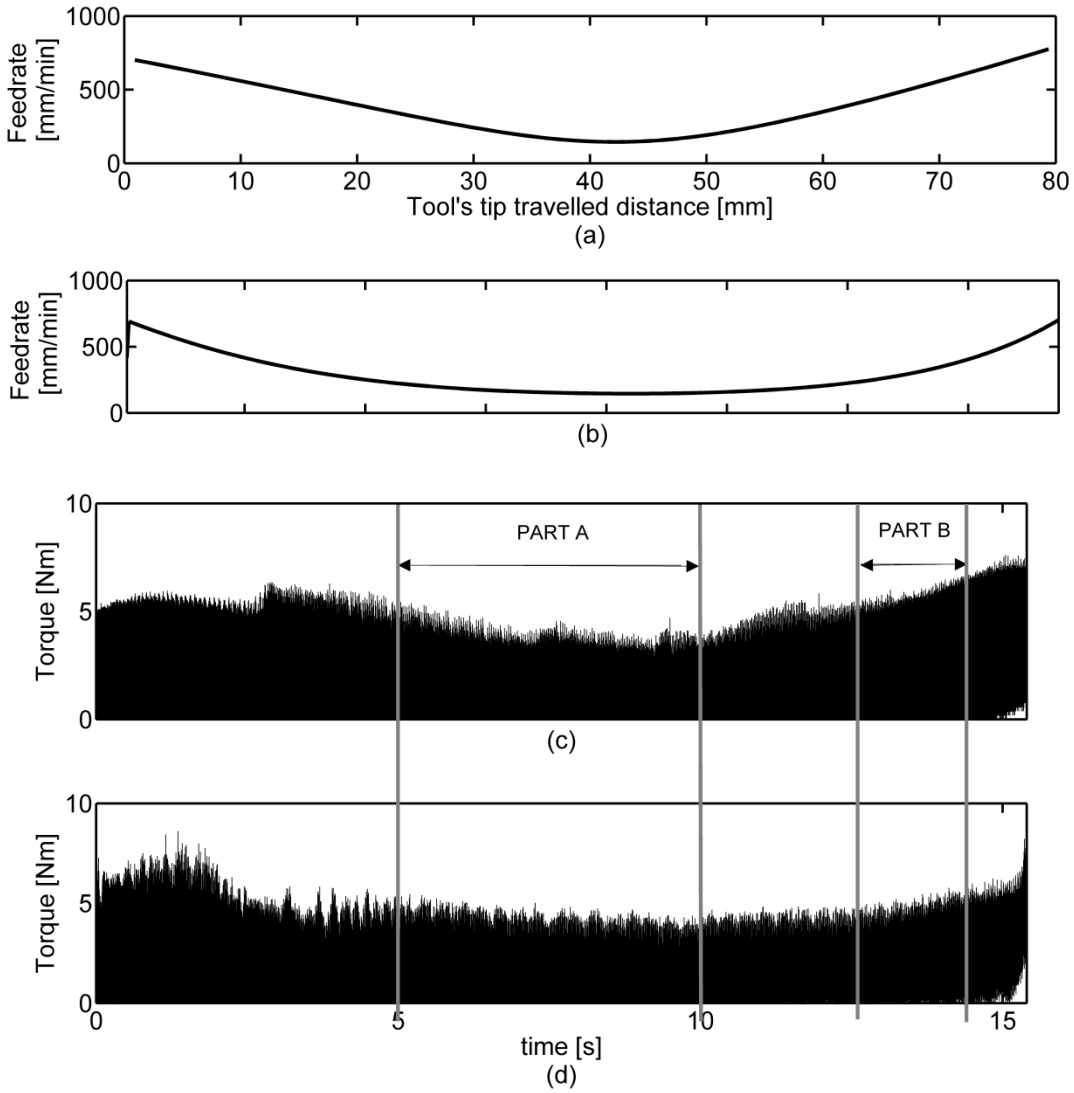

Figure 6-21: Results for test Surface 3, height 30 mm, a) feedrate at the tool tip versus distance travelled along tool path, b) feedrate at the tool tip versus time, c) simulated torque, d) measured torque

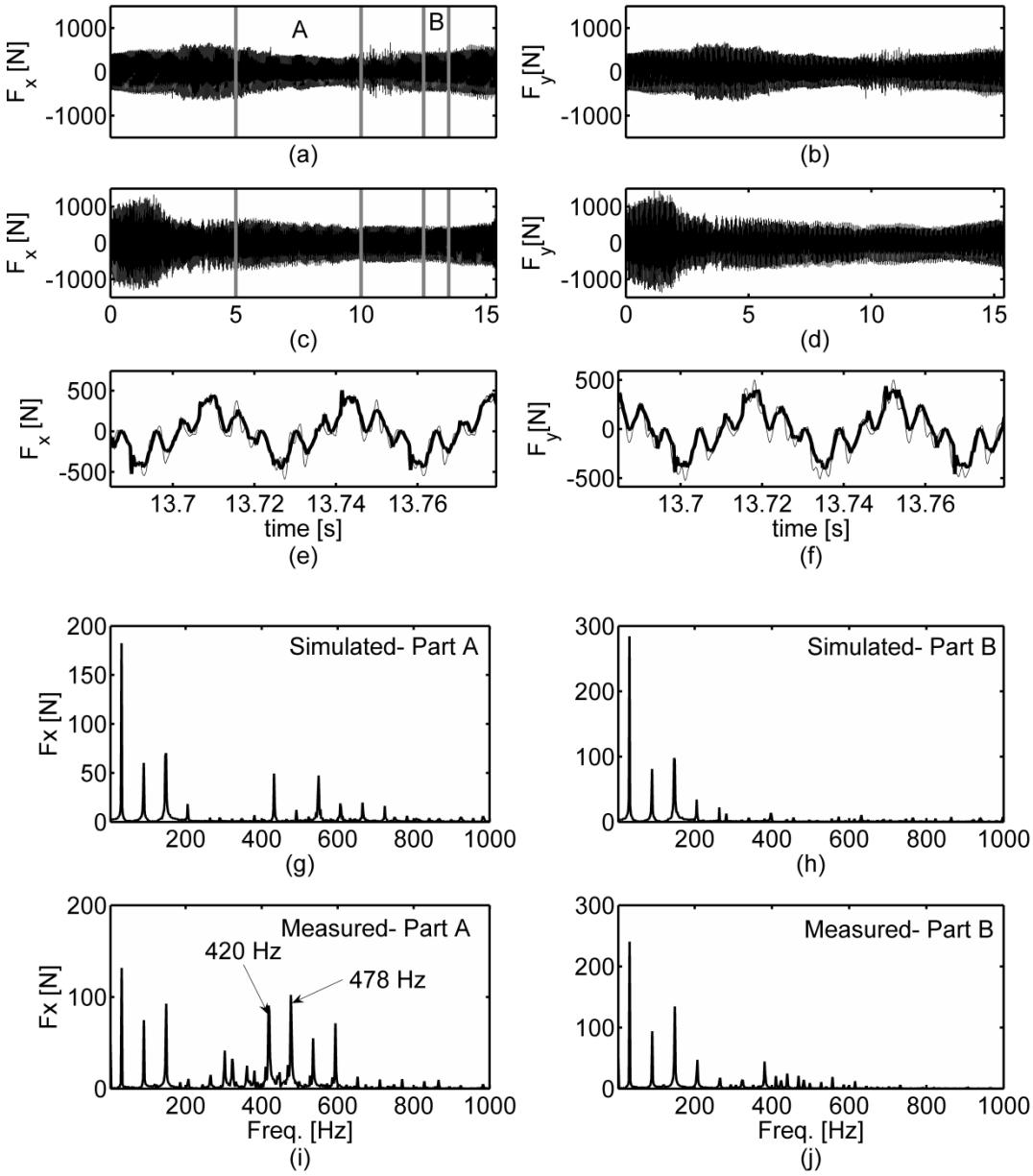

Figure 6-22: Simulated (a, b) and measured (c, d) cutting forces in the X and Y directions; (e, f) close ups of the measured (thin line) and simulated (thick line) forces; power spectra of the simulated (g, h) and measured (i, j) cutting forces in regions A and B

6.8.2 SDM Results and Stability Maps

The SDM is applied to study the stability of tool vibration while it travels along the toolpath of three surfaces. At each cutter location the maximum eigenvalue of the transition matrix is calculated from

Equation (5.31). Notice that the actual feedrate and start and exit angles vary at each cutter location and at each axial elemental disk.

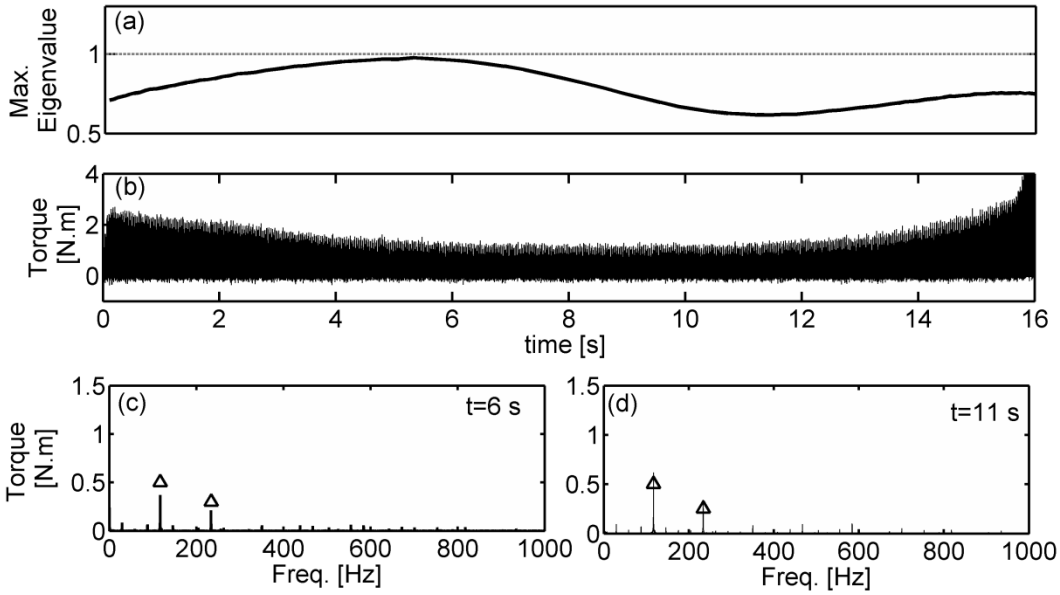

Figure 6-23: Flank milling of Surface 1, height 5 mm: (a) computed maximum eigenvalue of the transition matrix, (b) measured cutting torque, (c), and (d) the frequency spectra of the measured cutting torque at t=6 sec and 11 sec

Figure 6-23 (a) shows the calculated eigenvalues along the toolpath of Surface 1 of 5mm height. According to this figure, the maximum eigenvalue never exceeds 1, indicating a stable cut at all of the cutter locations. This agrees with the measured cutting torque in (b). Figure 6-23(c) and (d) show the frequency spectra of the measured torque at the midway of the toolpath, at t=6 sec, and at the end, at t=11 sec. Neither spectrum exhibits vibration at the chatter frequency. The eigenvalues calculated for Surface 2 are shown in Figure 6-24(a). Except around the middle of the toolpath where the maximum eigenvalue merely exceeds 1, it stays below 1 in almost all of the cutter locations. The measured cutting torque while machining Surface 2 and its frequency spectra at t=6 sec and t=10 sec are shown in (b), (c) and (d), respectively. They show that the whole cut was stable, which agrees closely with the stability predicted by SDM.

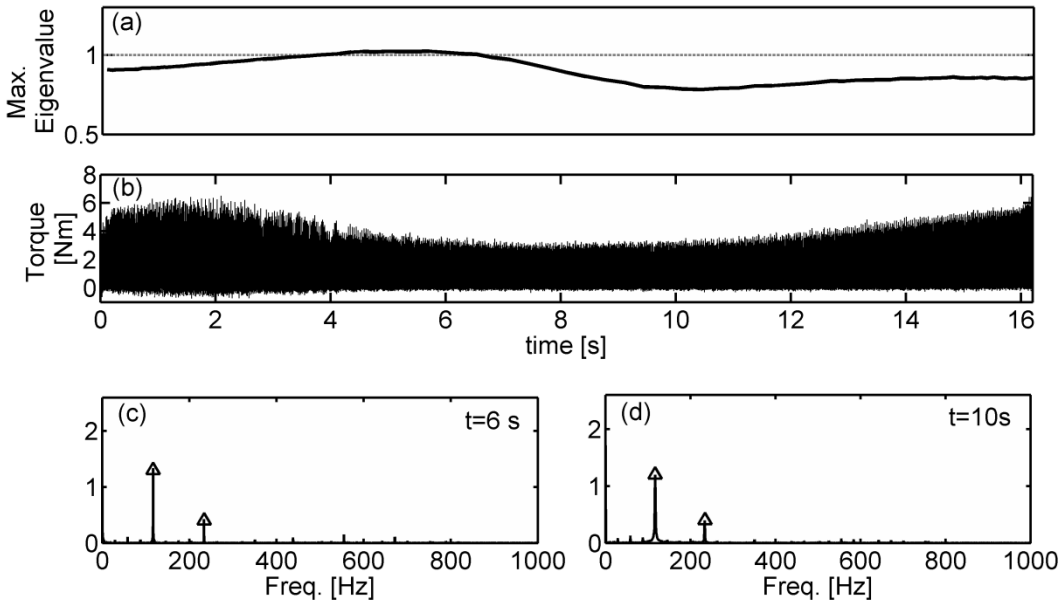

Figure 6-24: Flank milling of Surface 2, height 15 mm; (a) computed maximum eigenvalue of the transition matrix, (b) measured cutting torque, (c), and (d) the frequency spectra of the measured cutting torque at t=6 sec and 10 sec

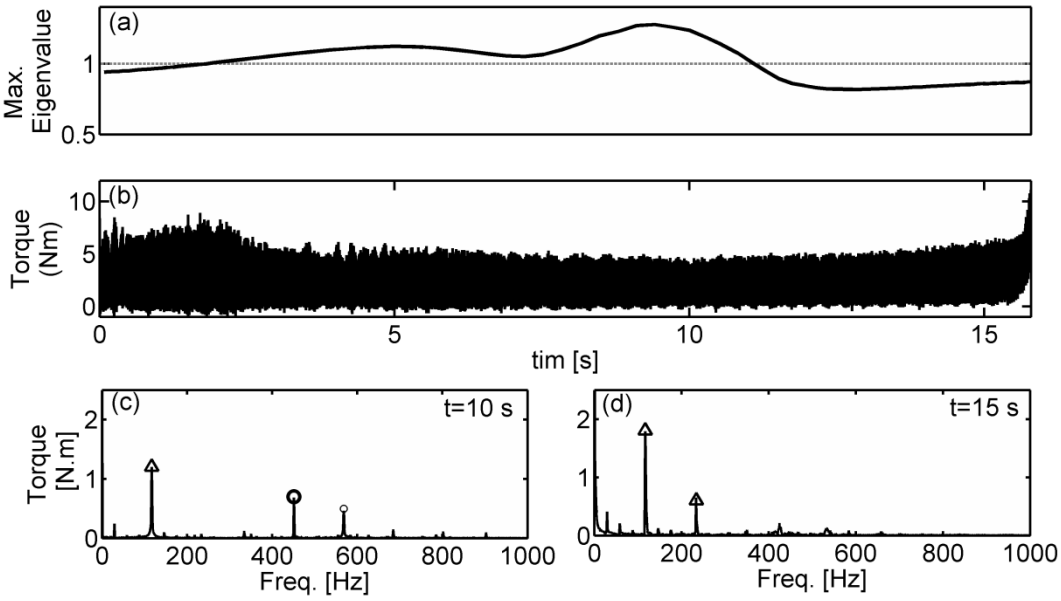

Figure 6-25: Flank milling of Surface 3, height 30 mm; (a) maximum eigenvalue of the transition matrix (b) measured cutting torque (c, and d) the frequency spectra of the measured cutting torque at t=10 sec, and 15 sec, respectively, for Surface 3

For Surface 3 of height 30 mm, the curve of maximum eigenvalue is shown in Figure 6-25(a). It stays below 1 at the beginning and end of toolpath, but fairly exceeds 1 at the middle of the toolpath. This curve predicts a stable cut at the beginning and end, and an unstable cut in the middle section. It agrees well with the cutting tests. The torque spectrum at the midway of toolpath, t=10sec, shows clear peaks at the chatter frequency, which is depicted by circles in part (c) of the figure. These peaks disappear at the end of toolpath at t=15sec.

The maximum eigenvalue of the transition matrix was calculated at each cutter location for a grid of spindle speeds to plot the stability map for each surface. Note that the feedrate values at each spindle speed would change to preserve the feedrate profile shown in Figure 6-21. Figure 6-26 shows the stability map of Surface 1. The points inside the gray areas are unstable, and the points inside the white areas are stable. At 1750 RPM, the cut is stable throughout the entire toolpath, which agrees with the experimental results. However, by increasing the spindle speed, the effect of process damping decreases and unstable region appears at 2300 RPM. By further increasing the spindle speed, the size of unstable regions increases. Nevertheless, there remain some entirely stable channels, such as those around 2800 RPM or between 4500 and 6000 RPM.

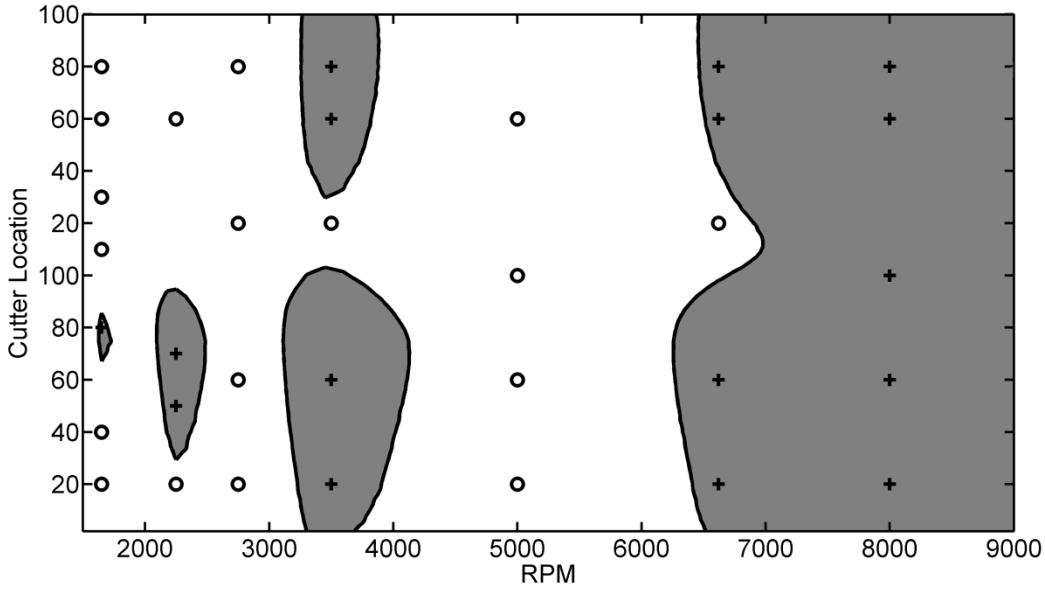

Figure 6-26: Computed stability map of Surface 1 of height 5 mm, and numerically simulated stable (circles) and unstable (crosses) points

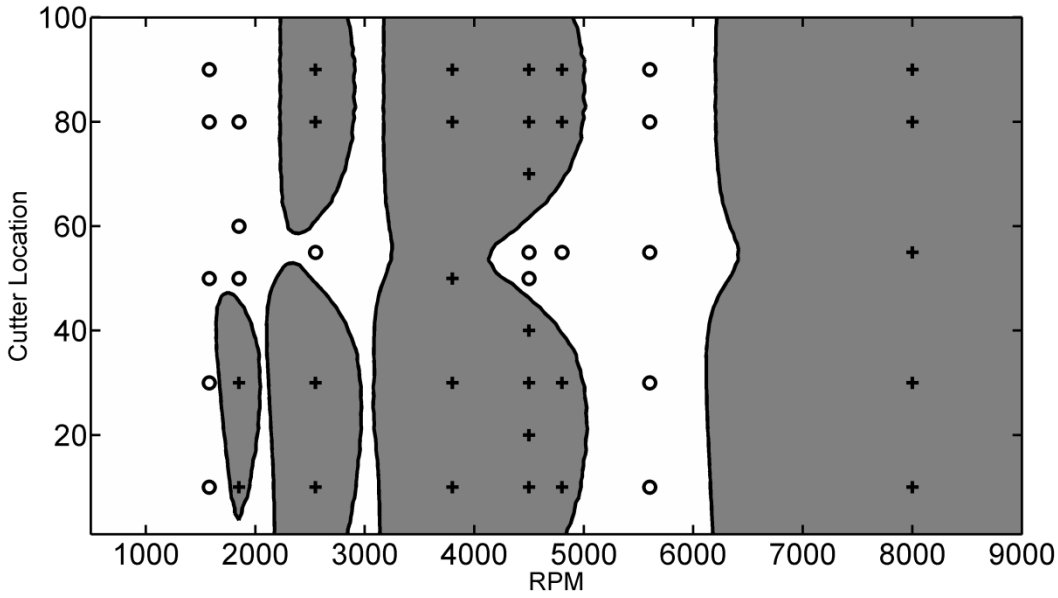

Figure 6-27: Computed stability map of Surface 2 of height 15 mm, and numerically simulated stable (circles) and unstable (crosses) points

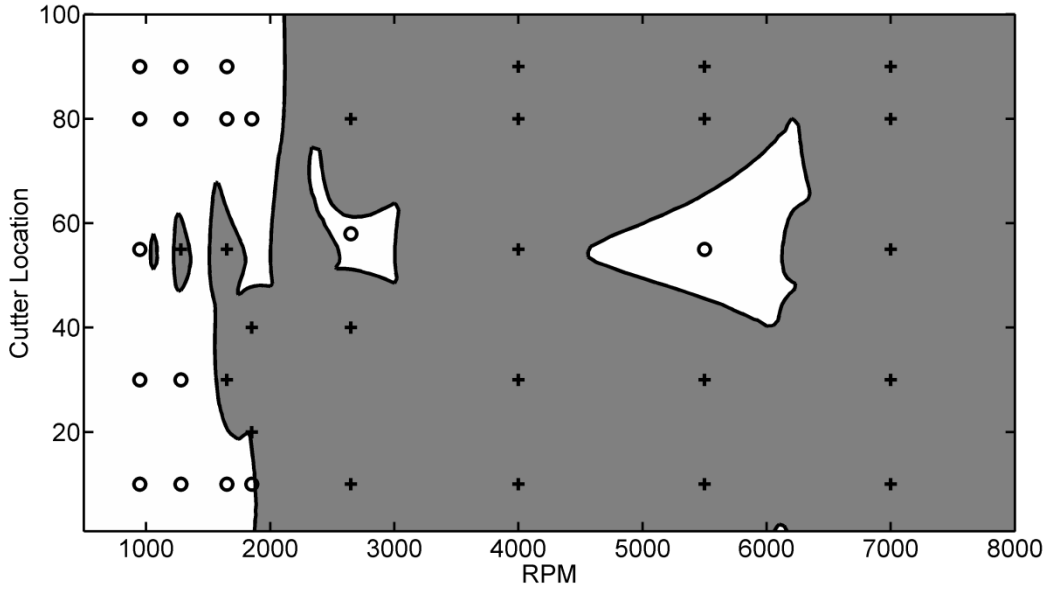

Figure 6-28: Computed stability map of Surface 3 of height 30 mm, and numerically simulated stable (circles) and unstable (crosses) points

The stability map of Surface 2 is shown in Figure 6-27. At 1750 RPM, the cut is stable for most of the toolpath. Only at the middle is it close to the border of instability. By increasing the speed, the unstable regions emerge and increase in size. There are some stable channels (e.g., between 5000 and 6000 RPM), albeit narrower than those observed in Surface 1.

Figure 6-28 shows the stability map of surface 3 of height 30 mm. At around 1750 RPM, the unstable regions start to appear around the midway of the toolpath, but the cut is stable at the beginning and end. By increasing the cutting speed, the unstable regions grow. After 2000 RPM, the cut is unstable during the entire toolpath, except for the two stable regions around 3000 RPM and between 5000 and 6000 RPM. Note that these two regions appear as closed areas inside the unstable region. The numerical simulation was executed at 5500 RPM, and the computed torque is shown in Figure 6-29. Excessive oscillations are observed both at the beginning, 0<t<2.1, and at the end of the toolpath, 3.9<t<4.9, but the middle of cut is stable, as predicted by the map.

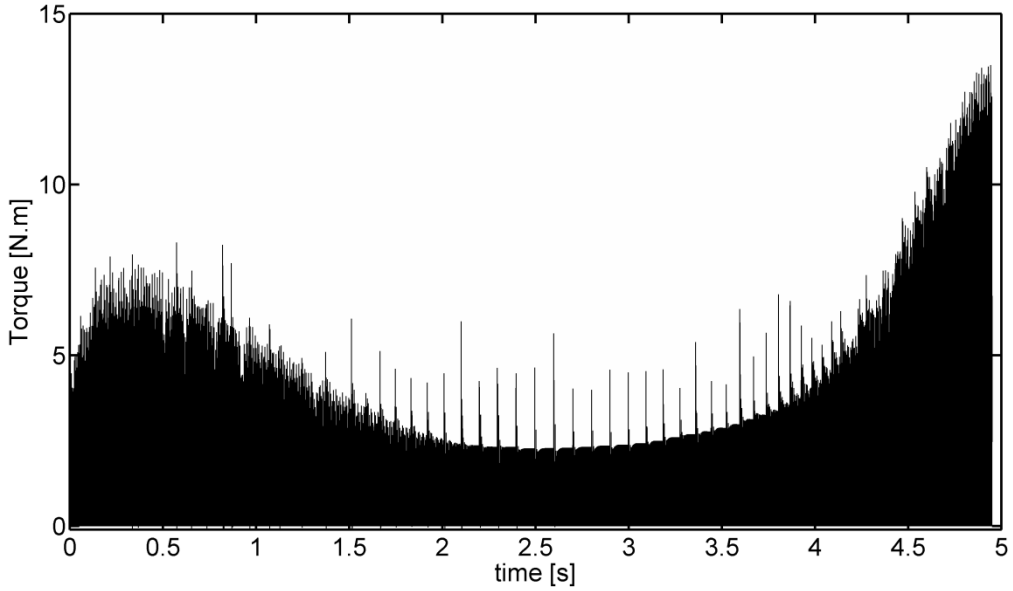

Figure 6-29: The cutting torque obtained by the numerical simulation of machining Surface 3 at 5500 RPM

Also shown in Figure 6-26, Figure 6-27, and Figure 6-28 are the results of numerical simulations at a set of spindle speeds and cutter locations. The circles show the stable points, and the crosses mark the unstable points. In each case, the regeneration component of tool displacement in the Y_t direction was extracted following the method presented in the previous chapter. Examples of simulation results at the 30th cutter location of surface 1 and (a) 5000 RPM, stable point, and (b) 3500 RPM, unstable point, are given in Figure 6-30. Here, y is the total tool deflection and y^H is the harmonic component,

and thus $y\text{-}y^H$ indicates the regeneration component. At the stable point, the amplitude of the regeneration component of tool deflection dies down to zero, while at the unstable point it increases and stabilizes when the tool jumps out of the cut [74]. The stability at all points, shown with circles and crosses in Figure 6-26, Figure 6-27, and Figure 6-28, was determined in a similar fashion. The results of numerical simulations further verify the accuracy of the stability maps.

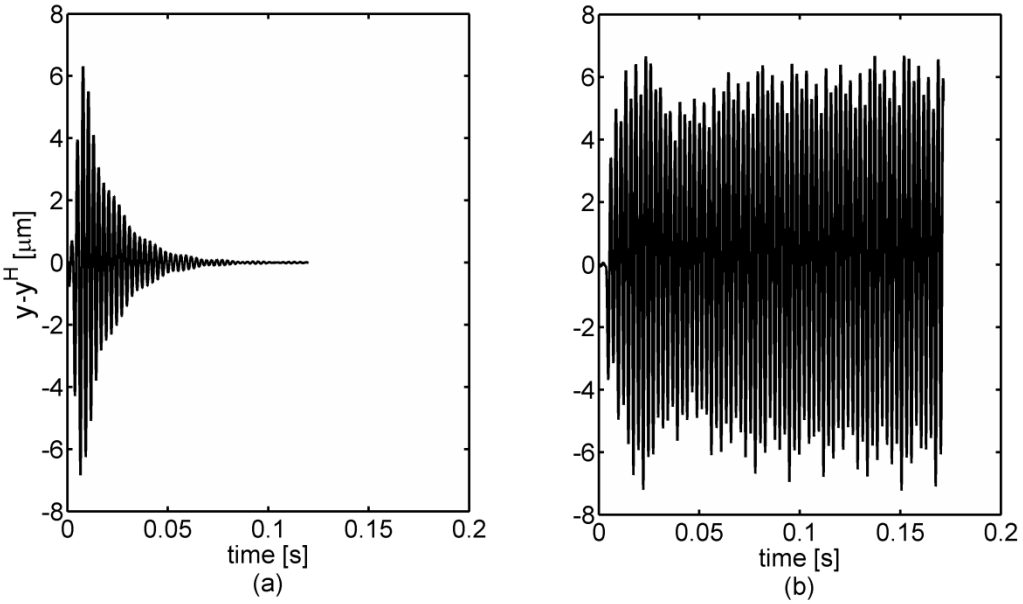

Figure 6-30: Results of numerical simulations for Surface 1 of height 5 mm; regeneration component of tool deflection in Y direction at cutter location 30 for: (a) 5000 RPM and (b) 3500 RPM

The stability maps can be used in toolpath planning or in selecting the spindle speed to avoid chatter. As an example, Figure 6-31(a) shows the cutting torque obtained from numerical simulation of machining Surface 2 at 4500 RPM. To maintain the feedrate profile employed at 1750 RPM, the programmed feedrate was increased proportionally to $f_{programmed}$=5143 mm/min. However, it might not always be possible to maintain the same feedrate profile while changing the spindle speed if one or more of the feed axes hits a saturation point. In this work, it is assumed that no saturation point is reached. For Surface 1, one can predict the stable and unstable cutter locations from the stability map in Figure 6-27; there, all of the cutter locations of the toolpath are unstable except for those between positions 42nd and 64th. The simulated cutting torque shows chatter vibration at the first and final two seconds of the toolpath; otherwise, it is stable in between. This agrees with the stability map. The map, however, shows all the cutter locations to be stable at 5500 RPM. The numerical simulation was

repeated at 5500 RPM and the programmed feedrate was changed accordingly to $f_{programmed}$=6285 mm/min. The simulated torque is illustrated in part (b), which shows the chatter disappearing at the beginning and end, as planned.

According to the stability maps, an entirely stable toolpath can be achieved by using different spindle speeds at different cutter locations (by moving between the gray areas). Yet, one should notice that, changing the spindle speed during the flank milling of blades or impellers might result in a bad surface finish. Therefore, the spindle speed is recommended to be set at a value inside one of the stability channels, and then, be kept constant at that speed for the entire toolpath.

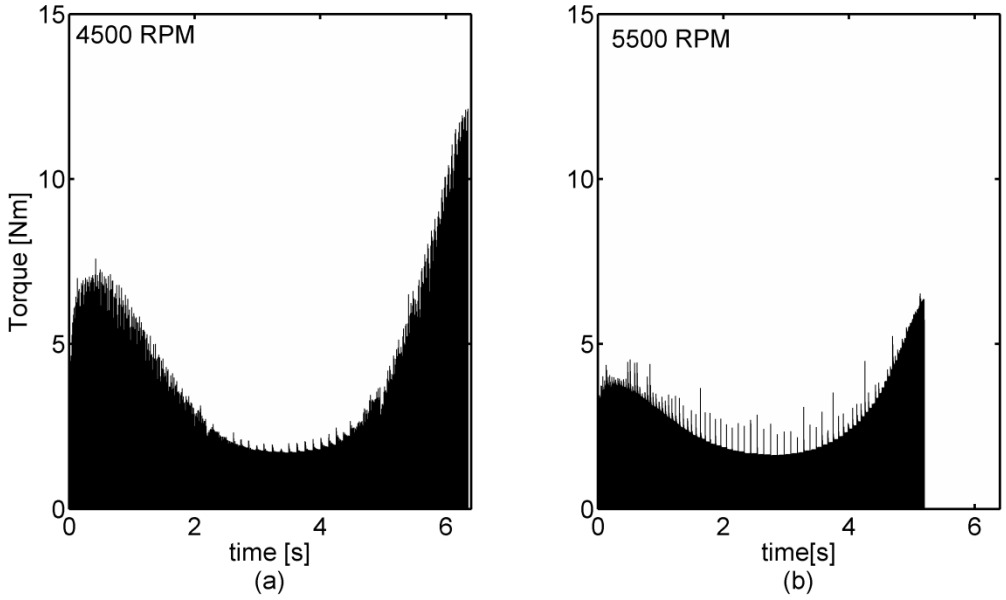

Figure 6-31: Numerically simulated torque while machining Surface 2 at height 15 mm with (a) 4500 RPM, unstable at the beginning and end of toolpath, and (b) 5500 RPM, stable along the full toolpath

6.9 Summary

A discretized time domain model of chatter was presented for flank milling. The dynamics of the tool was represented by a 2 DOF vibratory system, the shear forces were modeled by a nonlinear mechanistic model to account for the instantaneous chip thickness, and the effect of process damping was considered using the equivalent viscous model of ploughing forces. The Semi Discretization Method was employed to determine the stability of cut at each cutter location of 3- and 5-axis flank milling toolpaths.

The stability lobes of 3-axis flank milling were established using the presented time domain model. Moreover, stability maps were presented in this paper as toolpath-specific stability diagrams that determine the stable and unstable cutter locations along the toolpath at each spindle speed. The stability maps thus provide an effective means for optimizing the cutting parameters to achieve higher productivity in flank milling without encountering machining chatter. They are also computationally more efficient than the numerical simulation. For example, while the simulation of each case in Figure 6-31 took eight hours on a PC with a 2.2 GHz processor, the entire stability map in Figure 6-27 was generated in two hours.

Chapter 7
Conclusions and Future Work

In the first part of this thesis, presented in Chapters 3 and 4, the effect of process damping on machining chatter was investigated. The conducted investigation led to establishing stability lobes for continuous cutting that depend on the vibration amplitude. These lobes define the finite amplitude stability region where the vibration stabilizes at certain amplitudes without tool/workpiece disengagement.

Time and frequency domain methods along with the equivalent viscous model of process damping were employed in the second part of the thesis, in Chapters 5 and 6, to determine the stability of the cut in milling. For illustration of the developed method, stability lobes in straight cutting of flat surfaces were established. This led to establishing "stability maps" as a new concept that presents the stability in milling of general surfaces along planned toolpaths. The main contributions of this work are summarized below.

7.1 Contributions

a) *Experimental confirmation of the phenomenon of finite amplitude stability due to the non-linearity associated with process damping.*

In the conventional assessment of chatter using linear models, the machining is either stable or unstable; the vibration amplitude dies down to zero in the former and it increases until the tool disengages from the workpiece periodically in the latter. Previous numerical studies showed that the transition from the fully stable to fully unstable cut occurs gradually over a range of widths of cut due to the nonlinearity associated with process damping. This phenomenon, however, was not studied experimentally until it was addressed successfully in the current work. The experimental investigation provided a much-needed insight into the chatter phenomenon by helping to better assess the stability of the cut, and to explain a major source of uncertainty involved in linear process damping models. In fact, the accuracy of two linear process damping models, existing in the literature, was re-examined in light of the new results. The analytical model, based on small amplitude assumption, was found to be accurate only if it was used to predict the lower border between the stable and finite amplitude stability cuts. The other model, extracted from experimental data, was found to be accurate only if it was used to predict the stability where the tool/workpiece

disengagement occurs at the same amplitude at which the sinusoidal excitation of the tool was carried out in the identification tests of the damping coefficients.

The results of the experimental investigation were published in [83].

b) Developing a new formulation for the equivalent viscous model of process damping.

The equivalent viscous damper approach has been used in the literature to represent process damping. The coefficient of the equivalent damper was either extracted from experimental data collected at specific vibration amplitude and tool geometry, or it was approximated using the assumption of small amplitude vibration. In either case, employing the damping model to compute the stability borders led to errors in establishing the stability lobes.

In this work, a new formulation was presented for the equivalent viscous model of process damping. The new damping formulation includes two independent parts: the first part was referred to as the "damping shape factor"; it depends on geometrical entities only that include: the wear land and clearance angle of the cutting edge, the vibration amplitude and wavelength of the undulations left on the machined surface. The second part, the specific indentation force and coulomb friction coefficients, depends on the mechanical properties of the workpiece. While the second part can be obtained from experimental work reported in the literature, the formulation of the first part was developed in this work. One can compute quickly the coefficient of the equivalent viscous damper at different wear, tool clearance angle, wavelength, and vibration amplitude for a wide range of geometries.

Having developed the new amplitude-dependent formulation of process damping, it was integrated into the frequency domain method for establishing stability lobes. It enabled estimating the lobes at specific amplitudes. It is a novel approach to the commonly used stability lobes where the vibration amplitude is not defined. The lobes associated with small amplitudes define the lower bound of a finite amplitude stability region due to process damping, and the ones associated with the feedrate define the upper bound. Using the new approach, stability bands could be defined rather than "single border" boundary stability lobes.

The formulation of the equivalent damper and computing the amplitude-dependent lobes was published in a journal article [84].

c) *Formulating the Semi Discretization Method (SDM) and Multi Frequency Solution (MFS) in the presence of process damping to establish stability lobes in milling.*

The equivalent viscous damper was integrated into two commonly used methods of computing the stability lobes in milling: Multi-Frequency Solution (MFS) and Semi-Discretization Method (SDM). In the literature, SDM and zero order MFS were shown to lead to similar stability lobes, except for highly interrupted cuts where the higher harmonics of MFS had to be included for accurate prediction of stability. In this thesis, the inclusion of the higher harmonics in MFS was shown to be necessary at low speed and high damping, even if the cut was not highly interrupted.

The stability lobes in milling including the effect of process damping were established and verified experimentally in this work. An article has been submitted to the Journal of Machine Tools and Manufacturing on formulating the MFS and SDM in the presence of process damping.

The formulation of SDM and MFS including process damping was published in a journal article [85].

d) *Modeling chatter in 5-axis flank milling*

A dynamic model was developed in this thesis to simulate chatter in 5-axis flank milling. The tool/workpiece engagement geometry and actual feedrate were computed by post-processing the designed toolpath, and then they were integrated into the numerical simulation of tool vibration while it travels along the 5-axis toolpath. Comparing the results of numerical simulation with the experimental evidences verified the accuracy of the developed dynamic model. It also showed the important role of process damping in stabilizing the vibration in flank milling; the effect of process damping was included in the simulation using the indentation force model. The results of numerical simulation and experimental measurements were published in [86].

e) *Determining the stability of the cut in flank milling using SDM, and introducing the stability maps*

The SDM was used to determine the stability of the cut in flank milling. In the first step, the stability lobes in milling using tools with helical teeth were developed for straight cuts of plane surfaces. In developing the stability lobes, the effect of process damping was included using the equivalent viscous model, and the effect of instantaneous chip thickness was considered using a nonlinear mechanistic model. In the second step, the stability of the cut at each cutter location of a known 5-axis toolpath was determined using the developed SDM formulation. The developed method of

determining the stability of the cut is computationally efficient and thus one can repeat the analysis at different spindle speeds and feedrates for optimization purposes. This was not viable when using the numerical simulations, due to their long computation time.

For straight cuts where the geometry of the cut and feedrate stay constant throughout the toolpath, stability lobes are used to determine the stable and unstable depth of cut at each spindle speed. In 5-axis flank milling the geometry of the cut and actual feedrate vary at each cutter location, and therefore, stability lobes are difficult to establish. In this work, "stability maps" were presented as a novel method of demonstrating the stability of the cut in 5-axis flank milling; they determine the stability of the cut at each cutter location of 5-axis flank milling toolpaths over a range of spindle speeds. Having designed the toolpath, the tool/workpiece engagement and actual feedrate at each cutter location are computed using the various methods available in the literature. These data are then integrated into the SDM formulation presented in this thesis to produce the stability maps for a particular toolpath. The stability maps provide a practical means to adjust the cutting parameters, such as spindle speed and feedrate and avoid machining chatter throughout the toolpath. These maps can be established for the machining of curved surfaces.

7.2 Future Work

a) *Modifying the formulation of equivalent viscous damper with respect to the complexities involved the geometry of cutting edges.*

In computing the coefficient of equivalent viscous damper, the complex geometry of the cutting edge was neglected and only the flank wear was represented by a flat wear land. According to this approximation, process damping is zero for sharp tools, unless the clearance angle is smaller than the surface undulation slope. Nevertheless, experimental evidence shows the effect of process damping at low cutting speed, even for sharp tools at relatively lower undulations slope. Therefore, one needs to rectify the geometric modeling of the cutting edge in computing the coefficient of the equivalent damper. For instance, the hone radius of the cutting edge was neglected in this thesis. Although the hone radius is negligible for worn tools, ignoring it for sharp tools causes inaccuracies. The effect of the hone radius was compensated by an effective flank wear that was determined experimentally. Better modeling of the geometry of the cutting edge can result in eliminating the need for determining effective wear from experimental data.

b) *Including the effect of run-out in the formulation of SDM in milling using tools with helical teeth*

In this thesis, a constant effective tool wear was estimated from experimental measurements to account for the variable wear along the helical teeth of the milling tool. The estimated value of the effective wear, 60μm, in the experiments was higher than expected for the sharp tool used in the cutting. This was explained by the effect of tool runout. Such runout is inevitable for cutters with multiple teeth and it tends to increase the stability of the cut. Therefore, considering the effect of runout in the formulation of SDM presented in this work would result in more realistic approximations of tool wear.

c) *Determining the stability of the cut in flank milling using tools with more complex geometries*

In the machining of blades and impellers, the typical axial engagement of the tool is higher than the values studied in this work. The higher engagement is achieved by using stiffer tools such as conical and tapered endmills. Using tools with alternating helix or uneven pitch has further contributed to the stability of the cut in flank milling. In this thesis, the cutter used for flank milling was a cylindrical endmill with helical teeth. This tool was utilized to simplify the geometry of the cut and concentrate on the concepts and methodologies investigated herein. Extending the presented modeling to tools with more complicated geometries that are common in the machining of curved surfaces can make it more useful in a wider range of engineering applications.

d) *Employing the stability maps in increasing productivity by optimizing the cutting parameters*

The main purpose of developing the chatter predictive models is to identify the chatter-free range of machining parameters, and then to adjust them within that range to achieve higher production. In this thesis, stability maps were developed to determine the chatter-free spindle speeds associated with the designed toolpath and feedrate. One can integrate these maps in procedures to maximize the material removal rate and to define the chatter-free range of optimized cutting parameters. Computationally, generating these maps is efficient, and accordingly, they are suitable for determining the stability of the cut at a range of cutting parameters such as spindle speed and feedrate in the optimization procedure.

Moreover, stability maps determine the unstable cutter locations of the toolpath at a range of spindle speeds. They can therefore be used to modify the tool placement strategy at the unstable cutter

locations and avoid chatter. They can also be employed in scheduling the feedrate, or spindle speed, throughout the toolpath.

References

[1] Armarego, E. J. A, Brown, R. H. 1969. The machining of metals. Prentice Hall, Englewood, New Jersey.

[2] Martellotti, M. E. 1941. An analysis of the milling process. Transactions of ASME, 63, 233-251 .

[3] Merchant, M. E. 1945. Mechanics of the metal cutting. I. Orthogonal cutting and a type 2 chip. Journal of Applied Physics, 16, 267-275

[4] Lee, E. H., Shaffer, B. W., 1951. Theory of plasticity applied to the problem of machining. Journal of Applied Mechanics, 18, 405-413.

[5] Palmer, W. B., Oxley, P. L. B. 1959. Mechanics of orthogonal machining. Proceedings of the Institution of Mechanical Engineers, 173, 623-654.

[6] Tlusty, J. 2000. Manufacturing processes and equipment. Prentice Hall, Upper Saddle River, New Jersey.

[7] Altintas, Y. 2000. Manufacturing automation, metal cutting mechanics, machine tool vibrations, and CNC design. Cambridge University Press.

[8] Lazoglu, I. 2003. Sculpture surface machining: a generalized model of ball-end milling force system. International Journal of Machine Tools and Manufacture, 43,453–462.

[9] Gradisek, J., Kalveram, M., Weinert, K.2004. Mechanistic identification of specific force coefficients for a general endmill. International Journal of Machine Tools and Manufacture, 44, 401-414.

[10] Lamikiz, L., Lopez de Lacalle, L. N., Sanchez, J. A., Salgado, M. A. 2004. Cutting force estimation in sculptured surface milling. International Journal of Machine Tools and Manufacture, 44, 1511-1526.

[11] Budak, E., Altintas, Y., Armarego, E. J. A. 1996. Prediction of Milling Force Coefficients From Orthogonal Cutting Data. Journal of Manufacturing Science and Engineering,118, 216-224.

[12] Armarego, E.J.A., Smith, A.J.R., Gong, Z.J. 1990. Four Plane Facet Point Drills — Basic Design and Cutting Model Predictions. CIRP Annals - Manufacturing Technology, 39, 41-45.

[13] Armarego, E.J.A., Whitfield, R. C. 1990. Computer Based Modeling of Popular Machining Operations for Force and Power Prediction. CIRP Annals - Manufacturing Technology, 34, 65-69.

[14] Koenigsberger, F., Sabberwal, A. J. P. 1961. An investigation into the cutting force pulsations during milling operations. International Journal of Machine Tool Design and Research, 1, 15-33.

[15] DeSilva C.W. 2005. Regenerative Chatter in Machine Tools, Vibration and Shock Handbook. CRC Press, Boca Raton, FL, Chap. 35.

[16] Yellowly, I. 1985. Observations on the mean values of forces, torque and specific power in the peripheral milling process. International Journal of Machine Tool Design and Research, 25, 337-346.

[17] Landers, R. G. , Ulsoy, A. G. 2008. Nonlinear Feed Effect in Machining Chatter Analysis. Journal of Manufacturing Science and Engineering, 130, 1-8.

[18] Kline, W.A., DeVor, R.E., 1983, The effect of runout on cutting geometry and forces in end milling, International Journal of Machine Tool Design and Research, 23, 123-140.

[19] Kline, W.A., DeVor, R.E., Lindberg, J.R. 1982. The prediction of cutting forces in end milling with application to cornering cuts. International Journal of Machine Tool Design and Research, 22, 7-22.

[20] Tobias, S.A., Fishwick, W. 1985. A Theory of Regenerative Chatter. The Engineer, London.

[21] Tlusty, J., Polacek, M. 1963. The Stability of Machine Tools Against Self Excited Vibrations in Machining. International Research in Production Engineering, 465-474.

[22] Tobias, S.A. 1965. Machine Tool Vibration. Blackie and Sons Ltd, London.

[23] Koenigsberger, F., Tlusty, J. 1967. Machine Tool Structures, Stability Against Chatter. Pergamon Press.

[24] Opitz, H., Bemardi, F. 1970. Investigation and Calculation of the Chatter Behavior of Lathes and Milling Machines. CIRP Annals - Manufacturing Technology, 18, 335-343.

[25] Altintas, Y., Budak, E. 1998. Analytical Prediction of Chatter Stability in Milling—Part I: General Formulation. Journal of Dynamic Systems, Measurement, and Control, 120, 22-30

[26] Insperger, T., Stépán, G. 2002. Semi-discretization Method for Delayed Systems. International Journal for Numerical Methods in Engineering, 55, 503–518.

[27] Merdol, S. D., Altintas, Y. 2004. Multi Frequency Solution of Chatter Stability for Low Immersion Milling. Journal of Manufacturing Science and Engineering, 126, 459-467.

[28] Sisson, T.R., Kegg, R. L. 1969. An Explanation of low-speed chatter effects. Journal of Engineering for Industry, 951-958.

[29] Huang, C. Y., Junz Wang, J. J. 2007. Mechanistic Modeling of Process Damping in Peripheral Milling. Journal of Manufacturing Science and Engineering, 129, 12-20.

[30] Peters, J., Vanheeck, P., Van Brussel, H. 1972. The measurement of the Dynamic Cutting Forces. CIRP Annals, 21, 129-136.

[31] Tlusty, J. 1978. Analysis of the State of Research in Cutting Dynamics. CIRP Annals-Manufacturing Technology, 27, 583-589.

[32] Tlusty, J., Heczko, O. 1980. Improving tests of damping in the cutting process. Proceedings of the 8th North American Manufacturing Research Conference, 372-376

[33] Altintas, Y., Eynian, M., Onozuka, H. 2008. Identification of dynamic cutting force coefficients and chatter stability with process damping. CIRP Annals-Manufacturing Technology, 57, 371-374.

[34] Wu, D. W. 1989. A New Approach of Formulating the Transfer Function for Dynamic Cutting Process. Journal of Engineering for Industry, 111, 37-47.

[35] Elbestawi , M. A., Ismail, F., Du, R., Ullagaddi, B. C. 1994. Modeling machining dynamics including damping in the tool-workpiece interface. Journal of Engineering for Industry, 116, 435-439.

[36] Lee, B. Y., Trang, Y. S., Ma, S. C. 1995. Modeling of the process damping force in chatter vibration. International Journal of Machine Tools and Manufacture, 35, 951-962.

[37] Abrari, F., Elbestawi, M. A., Spence, A. D. 1998. On the dynamics of ball end milling: modeling of cutting forces and stability analysis. International Journal of Machine Tools and Manufacture, 38, 215-237.

[38] Ahmadi, K., Ismail, F. 2009. Modeling of machining chatter in ball-end milling including process damping. Proceedings of the 12th CIRP Conference on Modeling of Machining Operations, Donostia-San Sebastian, Spain.

[39] Chiou, Y. S., Chung, E. S., Liang, S. Y. 1995. Analysis of tool wear effect on chatter stability in turning. International Journal of Mechanical Sciences, 37, 391-404.

[40] Chiou, R. Y., Liang, S. Y. 1998. Chatter stability of a slender cutting tool in turning with tool wear effect. International Journal of Machine Tools and Manufacture, 38, 315-327.

[41] Budak, E., Tunc, L. T. 2009. A New Method for Identification and Modeling of Process Damping in Machining. Journal of Manufacturing Science and Engineering, 131, 1–10.

[42] Budak, E., Tunc, L.T. 2010. Identification and Modeling of Process Damping in Turning and Milling Using a New Approach. CIRP Annals - Manufacturing Technology, 59, 403-408.

[43] Kurata, Y., Merdol, S. D., Altintas, Y., Suzuki, N., Shamoto, E. 2010. Chatter Stability in Turning and Milling with in Process Identified Process Damping. Journal of Advanced Mechanical Design, Systems, and Manufacturing, 4, 1107-1118.

[44] Eynian, M., Altintas, Y. 2010. Analytical Chatter Stability of Milling With Rotating Cutter Dynamics at Process Damping Speeds. Journal of Manufacturing Science and Engineering, 132, 1-14.

[45] Bachrathy, D., Stepan, G. 2010. Time-periodic Velocity-dependent Process Damping in Milling Processes. CIRP-PMI 2nd conference proceedings, Vancouver.

[46] Choi, B. K., Jerard, R. B. 1998. Sculptured surface machining: Theory and application. Kluwer Academic.

[47] Liu, X. W. 1995. Five-axis NC cylindrical milling of sculptured surfaces. Computer-Aided Design, 27, 887-894

[48] Rehsteiner, F., Renker, H. J. 1993. collision-free five –axis milling of twisted ruled surface, Annals of CIRP-Manufacturing Science, 42, 457-461

[49] Elber, G., Fish, R. 1997. 5-axis freeform surface milling using piecewise ruled surface approximation. Journal of Manufacturing Science and Engineering, 119, 383-387

[50] Redonnet, J. M., Rubio, W., Dessein, G. 1998. Side milling of ruled surfaces: optimum positioning of the milling cutter and calculation of interference. International Journal of Advanced Manufacturing Technology, 14, 459-465

[51] Rubio, W., Lagarrigue, P., Dessein, G., Pastor, F. 1998. Calculation of tool paths for a torus mill on freeform surfaces on five-axis machines with detection and elimination of interface. International Journal of Advanced Manufacturing Technology, 14, 13-20

[52] Tsay, D. M., Her, M. J. 2001. Accurate 5-axis machining of twisted ruled surfaces. Journal of Manufacturing Science and Engineering, 123, 731-738

[53] Menzel, C., Bedi, S., Mann, S. 2004. Triple tangent flank milling of ruled surfaces. Computer-Aided Design, 36, 289-296

[54] Bedi, S., Mann, S., Menzel, C. 2003. Flank milling with flat end milling cutters. Computer-Aided Design, 35, 293-300

[55] Bohez, E. L. J., Senadhera, S. D. R., Pole, K., Duflou, J. R., Tar, T. 1997. A Geometric Modelling and Five-Axis Machining Algorithm for Centrifugal Impellers. Journal of Manufacturing systems, 16, 422-463.

[56] Chiou, J. C. J. 2004. Accurate tool position for 5-axis rule surface machining by swept envelope approach. Computer Aided Design, 36, 967-974.

[57] Stute, G., Storr, A., Sielaff, W. 1979. NC programming of ruled surface for five axis Machining. Ann CIRP-Manufacturing Science, 28, 267-271.

[58] Monies, F., Redonnet, J. M., Rubio, W., Lagarrigue, P. 2000. Improved Position of a conical mill for machining ruled surfaces: application to turbine blades. Journal of Engineering Manufacture, 214, 625-634.

[59] Monies, F., Rubio, W., Redonnet, J. M., Lagarrigue, P. 2001. Comparative study of interference caused by different position settings of a conical milling cutter on a ruled surface. Proceedings of the Institution of Mechanical Engineers, Part B: Journal of Engineering Manufacture, 215, 1305-1317.

[60] Gong, H., Cao, L. X., Liu, J. 2005. Improved positioning of cylindrical cutter for flank milling ruled surfaces. Computer Aided Design, 37, 1205-1213.

[61] Chu, C. H., Chen, J. T. 2006. Tool path planning for five-axis flank milling with developable surface approximation. International Journal of Advanced Manufacturing Technology, 29, 707-713.

[62] Ferry, W. B., Altintas, Y. 2008. Virtual five-axis flank milling of jet engine impellers-Part I: Mechanics of five-axis flank milling. Journal of Manufacturing Science and Engineering, 130.

[63] Larue, A., Altintas, Y. 2005. Simulation of flank milling process. International Journal of Machine Tools and Manufacture, 45, 549-559

[64] Ismail, F., Ziaei, R. 2002. Chatter suppression in five-axis machining of flexible parts. International Journal of Machine Tools and Manufacture, 42, 115–122

[65] El-Mounayri, H., Elbestawi, M. A., Spence, A. D., Bedi, S. 1997. General Geometric Modeling Approach for Machining Process Simulation. International Journal of advanced Manufacturing Technology, 13, 237-247

[66] Fussell, B. K., Jerard, R. B., Hemmett, J. G. 2003. Modeling of cutting geometry and forces for 5-axis sculptured surface machining. Computer-Aided Design, 35, 333-346

[67] Jerard, R. B., Drysdale, R. L., Hauck, K., Schaudt, B., Magewick, J. 1989. Methods for Detecting Errors in Numerically Controlled Machining of Sculptured Surfaces. IEEE Computer Graphics and Applications, 26-39.

[68] Bailey, T., Ruget, Y., Spence, K., Elbestawi, M.A. 1995. Open-architecture controller for die and mold-machining. Proceedings of the American Control Conference Seattle, Washington.

[69] Roth, D., Ismail, F., Bedi, S. 2003. Mechanistic modeling of the milling process using an adaptive depth buffer. Computer-Aided Design, 35, 1287-1303.

[70] Ozturk E., Budak, E. 2007. Modeling of 5-axis milling processes. Machining Science and Technology, 11, 287- 311.

[71] Ozturk, E., Ozlu, E., Budak, E. 2007. Modeling dynamics and stability of 5-axis milling processes. 10th CIRP International Workshop on Modeling of Machining Operations.

[72] Ferry, W. B. S. 2008. Virtual five-axis flank milling of jet engine impellers. PhD dissertation, University of British Columbia.

[73] Shin, H. M., Tobias, S. A. 1984. Theory of Finite Amplitude Machine Tool Instability. International Journal of machine Tool design research, 24, 45-69.

[74] Tlusty, J., Ismail, F. 1981. Basic Non-Linearity in Machining Chatter. CIRP Annals-Manufacturing Science, 30, 299-304.

[75] Chandiramani, N. K., Pothala, T. 2006. Dynamics of 2-dof regenerative chatter during turning. Journal of sound and vibration, 290, 448-464

[76] Jemielniak, K., Widota, A. 1989. Numerical simulation of non-linear chatter vibration in turning. International Journal of Machine Tools and Manufacturing, 29, 239–247.

[77] Clancy, B. E., Shin, Y. C. 2002. A comprehensive chatter prediction model for face turning operation including tool wear effect. International Journal of Machine Tools and Manufacture, 42, 1035–1044

[78] Tlusty, J., Ismail, F. 1983. Special Aspects of Chatter in Milling. ASME Journal of Acoustics, Stress, and Reliability in Design, 105, 24-32.

[79] Inman, D.J. 1994. Engineering Vibration. Pearson Prentice Hall.

[80] Farin, G. 2002. Curves and Surfaces for CAGD. fifth ed., Morgan Kaufmann, San Francisco.

[81] Roth, D. 2004. Mechanistic modeling of 5-axis machining. PhD Dissertation, University of waterloo.

[82] Gernon, B. 1988. A study of geometric constraints in machining instability. Masters Thesis, University of waterloo.

[83] Ahmadi, K., Ismail, F. 2010. Experimental investigation of process damping nonlinearity in machining chatter. International Journal of Machine Tools and Manufacture, 50, 1006-1014

[84] Ahmadi, K., Ismail, F. 2011. Analytical Stability Lobes Including Nonlinear Process Damping Effect on Machining Chatter, International Journal of Machine Tools and Manufacture, 51, 296-308.

[85] Ahmadi, K., Ismail, F. 2011. Stability Lobes in Milling Including Process Damping and utilizing Multi Frequency and Semi Discretization Methods. International Journal of Machine Tools and Manufacture, (accepted for publication)

[86] Ahmadi, K., Ismail, F. 2010. Machining Chatter in Flank Milling. International Journal of Machine Tools and Manufacture, 50, 75–85.